THE EFFECTS OF TRADE WIND INVERSION VARIABILITY ON HIGH ELEVATION CLIMATES IN HAWAIʻI

A DISSERTATION SUBMITTED TO THE GRADUATE DIVISION OF
THE UNIVERSITY OF HAWAIʻI AT MĀNOA IN PARTIAL FULFILLMENT
OF THE REQUIREMENTS FOR THE DEGREE OF

DOCTOR OF PHILOSOPHY

IN

GEOGRAPHY

MAY 2015

By

Ryan James Longman

Dissertation Committee

Thomas Giambelluca, Chairperson
Henry Diaz
Camilo Mora
Tomoaki Miura
Ross Sutherland

ACKNOWLEDGEMENTS

I would like to thank the United States Army Corp of Engineers, the Commission on Water Resource Management and the Pacific Island Climate Science Center for the funds used to support my Ph.D. graduate research assistantship. I am also grateful to Haleakalā National Park, the Pacific Island Climate Change Cooperative, and the Pacific Island Ecosystem Research center for providing additional funding for project development. I am sincerely grateful to Abby Frazier and Mike Nullet who have aided my research efforts on countless occasions. Special thanks Ross Sutherland who believed that I could be a good teacher and gave me the opportunity to prove it. Sincere thanks to Camilo Mora for showing me that a global analysis was within my reach. I thank Henry Diaz for pushing me forward on all fronts and Tomoaki Miura for his commitment to help me see this degree through to the end. I express my deepest gratitude to my adviser Tom Giambelluca who has opened my eyes to a set of skills that I never knew I possessed and a world of possibilities that I never knew existed. I am most thankful to my wife Christina who has been a consistent source of encouragement and support through my academic journey. I also thank my sons Kainoa and Kelani who have shown me the true meaning of fulfillment and who have given me all the motivation that I needed to complete this degree in a timely manner.

ABSTRACT

The primary objective of this dissertation is to characterize the spatial and temporal variability of climate at high elevation in Hawai‘i and to identify the proximal causes of observed change. First, up to 25 years (1988-2013) of climate data obtained from 11 weather stations located within the HaleNet climate network on Maui, Hawai‘i, were used to characterize the climate along a 2030-m leeward and 810-m windward elevation transect. Ten climate variables were assessed for trends occurring over the period of record at each station for the 6-month dry (May-October) and wet (November-April) seasons. In general a drying trend was identified along both leeward and windward transects during the dry season. At the five highest elevation sites (2120 to 2990 m), significant increases in solar radiation (2 to 4% decade^{-1}), vapor pressure deficit (9 to 10% decade^{-1}), potential evapotranspiration (3 to 7% decade^{-1}), and the number of zero rainfall days (4 to 5% decade^{-1}), and significant decreases in relative humidity (-3 to 5% decade^{-1}), and rainfall (-3 to -8% decade^{-1}) were identified at two or more of these sites over the period of record. Increases in Trade Wind Inversion (TWI) frequency of occurrence and or decreases in TWI base height were identified as potential agents driving these changes. A second part of this research is to test this hypothesis. To accomplish this, forty years (1973-2013) of radiosonde data obtained from the atmospheric sounding stations located at Hilo and Līhu‘e were used to calculate TWI frequency, base height and strength variability over time. Results indicate a 16% average increase in TWI frequency of occurrence beginning in the early 1990’s. TWI frequency was significantly correlated with the vertical wind velocity variable “omega” obtained from 4 reanalysis data sets, suggesting that observed increases in TWI frequency are a result of increased atmospheric subsidence over the Hawai‘i region. Increased TWI frequency has resulted in 16 and 40% average decreases in high elevation rainfall for the dry and wet

seasons, respectively. The upward shift in TWI frequency is not explained by phase changes in the El Niño Southern Oscillation (ENSO) or the Pacific Decadal Oscillation (PDO). Over shorter time periods, however, such as the post-TWI shift period (1991-2013), both ENSO and PDO indices were found to be significantly correlated with TWI frequency, but the sign of the relationship is opposite for the two season. The final component of this research is to identify the role that ENSO and PDO have on TWI frequency of occurrence on ~20 year time scales and to quantify the subsequent effects that TWI variability has on climate variables at mid and high elevations in Hawai‘i. Results show that, during the dry season, mean TWI frequency is higher during the cool phases of ENSO and PDO relative to the warm phases and an opposite relationship is observed in the wet season. Cool phase ENSO and PDO conditions that have dominated over the most recent period of record may help to explain a 4% decade^{-1} increase and a 2% decade^{-1} decrease in TWI frequency for the dry and wet seasons, respectively. The opposite response of TWI frequency during the dry and wet seasons helps to explain why high elevation energy and moisture regimes have opposite patterns of change within each season over the same period. The increase in TWI frequency explain some of the observed increases in solar radiation and decreases in rainfall and relative humidity observed at high elevations but much of the variability is still unaccounted for.

TABLE OF CONTENTS

LIST OF TABLES

LIST OF FIGURES

LIST OF ABBREVIATIONS AND SYMBOLS

AMO	-	Atlantic Multi-Decadal Oscillation
CA	-	cloud attenuation of sunlight
DJF	-	December, January, February
ENS	-	4-reanalysis dataset ensemble
ENSO	-	El Niño Southern Oscillation
ECMWF	-	European Center for Medium Range Weather Forecasts reanalysis data
GHG	-	Green house gases
HC	-	Hadley Circulation Cell
HN	-	HaleNet
hPa	-	hectopascal
HST	-	Hawai‘i standard time
K_d	-	incoming shortwave radiation
LCL	-	Lifting condensation level
MEI	-	Multivariate El Niño Southern Oscillation Index
NDRP	-	National Centers for Environmental Prediction – Department of Energy (NCEP/DOE) Atmospheric Model Intercomparision (AMIP-II) reanalysis data
NH	-	Northern Hemisphere
NNRP	-	National Centers for Environmental Prediction - National Center for Atmospheric Research (NCEP/NCAR) reanalysis data
OLR	-	outward longwave radiation
P	-	precipitation
PDO	-	Pacific Decadal Oscillation
PET	-	potential evapotranspiration
RH	-	relative humidity
R_n	-	net radiation
RF	-	rainfall
SLP	-	sea level pressure
SHF	-	soil heat flux
SM	-	soil moisture
SST	-	sea surface temperature
T_a	-	surface air temperature
TMCF	-	tropical montane cloud forest
TWI	-	trade wind inversion
UTC	-	Coordinated Universal Time
VPD	-	vapor pressure deficit
WS	-	wind speed at 2 meters
ZP	-	zero precipitation days
20CR	-	National Oceanic and Atmospheric Administration Cooperative Institute for Research in Environmental Sciences (NOAA/CIRES) reanalysis data

CHAPTER 1. INTRODUCTION

1.1 Introduction and Background

The eight main islands of the Hawaiian archipelago are located in the middle of the Pacific Ocean between 19° and 22° north latitude and 154° and 160° west longitude. The average elevation across the main island chain is ~900 m (A. Frazier, personal communication, January 6, 2001), and Hawai‘i is home to some of largest volcanic mountains in the Pacific Ocean. The highest volcano in the island chain (Mauna Kea) is located on the youngest and southernmost island (Hawai‘i) and extends ~4200 m a.s.l. into the troposphere. Other high elevation mountains include Mauna Loa Volcano (~3400 m a.s.l.), which also located on the Island of Hawai‘i, and Haleakalā Volcano (~3000 m a.s.l.) on the Island of Maui. The topography of these high mountains combined with general and local atmospheric circulation patterns create some of the most spatially diverse climate gradients anywhere in the world.

The climate of Hawai‘i can be characterized by two 6-month seasons; dry season which extends from May to October and a wet season which extends from November to April (Giambelluca and Schroeder, 1998). The general climate around the main Hawaiian Islands is relatively dry, with rainfall over the open-ocean less than 600 mm yr^{-1} (Adler et al., 1990). The islands themselves, however, have much different rainfall characteristics and the wettest location in the island chain (“Big Bog, Maui”), receives over 10,000 mm yr^{-1} while the driest spot (Mauna Kea, Hawai‘i) receives less than 250 mm yr^{-1} (Giambelluca et al., 2012).

The climate in Hawai‘i is strongly affected by the general atmospheric circulation pattern in the tropical and subtropical Pacific, which is dominated by the Hadley Cell. The Hadley Cell is driven by pressure gradient forces that arise from differential heating between the equator and

the poles and the direction of the wind is influenced by the rotation of the planet (Coriolis force). Near the equator, convective and convergent processes lift air and then push it poleward in the upper troposphere, driving this circulation. The air sinks in the sub-tropics between 20-30° latitude and returns to the equator as surface winds. Surface winds are deflected to the right in the northern hemisphere due to the effects of Coriolis force, thus causing persistent northeast trade winds that persist 50-80% of the time in the winter and 85-90% of the time in the summer (Sanderson, 1993). The strong persistence of the summer trades can be explained by the semi-permanent subtropical high pressure ridge that sits to the northeast of the island chain (Gerza et al., 2012). The persistent trade winds move moist air toward the island chain where it is orographically lifted up the mountain providing a consistent source of rainfall along the east-facing slopes (Giambelluca et al., 2012). Typically, clouds from the windward side of the island do not reach the leeward side under normal trade wind conditions (Scholl et al., 2007). The topographic blocking effectsof the mountains alters trade wind patterns and causes relatively dry conditions on the leeward sides on the islands (Leopold, 1949). Thermally-driven local (land-sea) circulation near the coast and along the slopes produces clouds and some precipitation on the leeward sides of the islands, most notably on the Kona Coast of the Big Island, where a summer maximum of rainfall occurs.

Another prominent feature of the Hadley Cell is the trade wind inversion (TWI), which is created from the interaction between subsiding air from the upper troposphere and convection-driven mixing from lower levels (Riehl, 1979; Giambelluca and Nullet, 1991; Cao, et al., 2007). The TWI layer caps convective processes beneath it, limiting the vertical development of clouds on the highest mountains (Leopold, 1949; Riehl 1979; Giambelluca and Nullet; 1991, Cao et al., 2007). The TWI is controlled by large-scale atmospheric circulation and influenced by sea

surface temperature (SST) and fluctuations in the tropical atmosphere on scales from diurnal to multi-year (Cao et al., 2007). Because vertical motions are suppressed by the TWI, cloud cover and precipitation are decreased, and solar radiation is increased at locations above the TWI base height (Giambelluca and Nullet, 1992). Elevation, relative to the mean TWI base height and exposure to prevailing winds are primary factors determining microclimates along the slopes of the highest islands. As a result of interacting forces, ecosystems can range from desert, to tropical rainforest, to alpine shrubland over very short distances.

During the wet season, the trade-wind regime is frequently interrupted by low pressure systems. Among these disturbances are upper level lows, some of which develop closed surface circulations (Kona lows; Caruso and Businger, 2005), and cold fronts associated with mid-latitude cyclones (Giambelluca and Schroeder, 1998). The Hawaiian word “kona” means leeward and is used to describe winds with a southerly or westerly component that replace the trade winds during weather disturbances.

The climate of Hawai‘i is also strongly affected by the Pacific-centered coupled ocean-atmospheric modes of climate variability such as the El Niño-Southern Oscillation (ENSO) and the Pacific Decadal Oscillation (PDO) (Diaz and Giambelluca, 2012). ENSO is a fluctuation in sea surface temperature that originates in the tropical Pacific region and is associated with weather anomalies including severe weather events affecting ecosystems, agriculture, and freshwater supplies worldwide (Collins et al., 2010). An El Niño event is characterized by warming of the “cold tongue” (normally cold surface waters of the eastern equatorial Pacific), and an eastward shift of the “warm pool” (normally warm surface waters of the western equatorial Pacific), with attendant changes in rainfall, a reduction of the equatorial easterly winds and a flattening of the zonal oceanic thermocline slope (Vecchi and Wittenberg, 2010). PDO is a

variation in sea surface temperature patterns in the North Pacific (Mantua et al., 1997). The PDO is well correlated with climate and ecology including sea level pressure, winter land surface temperatures, precipitation and stream flow. ENSO events, which recur on relatively short time scales (2-7 years), and PDO, which varies on decadal time scales have both been shown to be well correlated with rainfall in Hawai‘i (e.g. Chu and Chen, 2005). The effects of ENSO and PDO are not independent of one another and the interacting effects of the two modes can produce different climatic effects that have unique temporal and spatial attributes across the State (Frazier et al., 2012).

1.2 Statement of the Problem

The climate of Hawai‘i is determined by a number of interacting factors that can change through space and time. Variations in high elevation climate in Hawai‘i and their relation to season and location have not been fully analyzed. Prior research has identified links between climate variations and the behavior of the TWI, especially at high elevations (Tran, 1995). ENSO is thought to influence TWI occurrence (Cao et al., 2007) and, hence, affect climate. However, the roles of natural modes of climate variability including ENSO and PDO, and fluctuations in Hadley Cell circulation in driving observed climate variations on Hawai‘i’s mountain slopes are not well understood. Considering this, a detailed analysis of the most reliable and up-to-date observational data and the factors that influence climate variability is needed.

1.3 Purpose of the Study

The purpose of this dissertation is to build on the existing body of research aimed at characterizing high elevation climates in Hawai‘i (Minyard et al., 1994; Tran, 1995; Loope and Giambelluca, 1998; Giambelluca et al., 2014) and detecting change (see Cao et al., 2007; Giambelluca et al., 2008; Diaz et al., 2011; Krushelnycky et al., 2013; Frazier et. al. 2013;

Longman et al., 2014). This research also seeks to identify the proximal causes of observed changes in the high elevation environment. Further, the analysis presented here will test the hypotheses that: (1) observed changes in climate can be explained, in part, by changes in the frequency of occurrence of the TWI and/or changes in the base height of the TWI; and (2) that TWI variability is not completely explained by natural modes of climate variability.

1.4 Structure of the Dissertation and Research Questions

To test these hypotheses I use a series of statistical tools to analyze climatic data obtained from several databases. This dissertation consists of five chapters including; this introduction, three chapters formatted as manuscripts and a concluding chapter. Figures and tables will follow each individual chapter and a master references cited list can be found at the end of the dissertation. A brief description of the dissertation chapters and subsequent research questions for each chapter are provided below.

The primary objective of Chapter 2 is to characterize the general climatology of Haleakalā Volcano (Maui, Hawai‘i) through an analysis of ~25 years of field observations obtained from the HaleNet climate network. I analyze seven measured climate variables and five derived climate variables and characterize results in terms of the spatial (elevation and orientation to the prevailing winds) and temporal (diurnal, seasonal, and annual) behavior of these variables. Period-of-record changes were assessed for 10 climate variables and are described in terms of changes to available energy and moisture over time. Chapter 2 research questions are:

1. What are the spatial characteristics of climate along leeward and windward elevation gradients on Haleakalā Volcano and how do they differ during the dry and wet seasons?

2. What are the diurnal, annual, and inter-annual patterns of climate and how do they differ between dry and wet seasons.

In Chapter 3, TWI data derived from observations at two atmospheric sounding stations, the vertical velocity of wind variable "omega" obtained from four reanalysis products and a 4-model reanalysis ensemble, and rainfall data obtained from 21 high elevation (>1900 m) climate stations are analyzed. Chapter 3 research questions are:

3. Have the previously detected increases in TWI frequency and decreases in TWI base height persisted over the most recent 10 years of observations?
4. Can changes in TWI frequency variability be explained by changes in general atmospheric circulation?
5. What is the role of large scale modes of internal variability, such as ENSO and PDO, in explaining TWI variability over the last ~40 years?
6. How have changes in the TWI frequency of occurrence affected rainfall regimes at high elevations, for the two 6-month, dry and wet seasons in Hawai‘i?

In Chapter 4, a composite of TWI frequency data obtained from two atmospheric sounding stations, solar radiation, rainfall and relative humidity data from as many as three mid-elevation (>950 m and <1900 m) and five high-elevation (>1900 m) HaleNet climate stations and both ENSO and PDO climate indices over the period 1991-2013 are analyzed. Chapter 4 research questions are:

7. What is the response of TWI frequency of occurrence to the three phases of ENSO and the two phases of PDO and are there statistically significant differences in mean TWI frequency during these phases?
8. What is relationship between TWI frequency and seasonal solar radiation, rainfall, and relative humidity at high and mid elevations?
9. What are the temporal patterns of climate variables and climate indices over the past ~2 decades (1991-2013)?
10. Can phase changes in Pacific-centered modes of climate variability explain observed changes to high elevation climates and are observed changes unique in the dry and wet seasons?

In Chapter 5, I summarize the major findings of the chapters and suggest future research paths.

CHAPTER 2. CLIMATOLOGY OF HALEAKALĀ VOLCANO

2.1 Abstract

The steep mountain slopes of Haleakalā Volcano (Maui, HI) support some of the most spatially diverse environments on the planet. Microclimates found across vertical gradients on the mountain slopes can change over relatively short differences in slope exposure and elevation and are strongly influenced by a persistent temperature inversion and northeast trade winds that are characteristic of this region. Eleven climate stations, which comprise the HaleNet climate network, have been monitoring climatic conditions along a 2030-m leeward (960 to 2990 m) and a 810-m windward (1650 to 2460 m) altitudinal transect, beginning as early as June of 1988. Hourly measurements of solar radiation, net radiation, relative humidity, wind speed, temperature, precipitation and soil moisture, and derived variables including potential evapotranspiration, vapor pressure deficit, soil heat flux and daytime cloud attenuation of sunlight are analyzed in this study. This dissertation documents the annual, diurnal and elevational characteristics of these climatic variables as well as their temporal behavior over the period-of-record (~1988 to 2013) in both the 6-month dry (May – October) and wet (November to April) seasons. Results show that the climate gradients along both leeward and windward elevation transects are highly influenced by the trade wind inversion in both dry and wet seasons. Period-of-record trends in the dry-season, show increases in energy and decrease in moisture at high elevations (>2000 m). Significant dry season changes include: decreases in precipitation (5 to 8% decade^{-1}), relative humidity (3 to 5% decade^{-1}) and cloud attenuation of sunlight (-2 to -5% decade^{-1}) and increase in solar radiation (2 to 4% decade^{-1}), vapor pressure deficit (9 to 10 % decade^{-1}), zero precipitation days (4 to 5% decade^{-1}) and potential evapotranspiration (3 to 7% decade $^{-1}$). For the wet-season, an opposite signal of change was observed at high elevation although trends were not as statistically robust as in the dry season.

2.2 Introduction

Climate is the driving factor behind the physical, chemical and biological processes operating within the natural environment. The climatology of a mountain is a composite of a multitude of microclimates that change through space and time. The myriad of microclimates along elevation transects on the high mountains in Hawai‘i determines the local variability in ecosystem processes, species composition, and the distribution of vegetation (Riehl et al., 1951; Parmesan 1996; Giambelluca and Nullet, 1991; Crausbay and Hotchkiss, 2010). Haleakalā Volcano, which is located on the Island of Maui, is the third highest mountain in the Hawaiian archipelago extending 3055 m above sea level. Haleakalā is a shield shaped volcano which originated in the early Pleistocene (0.8 myr) and is still considered to be volcanically active (Sherrod et al., 2007). Though volcanic episodes have lessened, Haleakalā has continued to erupt every 200 to 500 years and its youngest lava flows are thought to have formed between A.D. 1449 and 1633 (Sherrod et al., 2007). The summit of Haleakalā, located at 20°42' N and 156°15' W, overlooks a large crater 12 km long 4 km wide, which has ten cinder cones on its floor and sheets of exposed pyroclastic materials on the outer walls. Maui Island, like most of the main Hawaiian Islands, has distinctly different climates on windward and leeward slopes. Great environmental contrasts occur within short distances as a result of the diverse topography and the influence of general and local circulation patterns. Along the windward exposure of the volcano, the persistent north east trade winds push moist marine air towards mountain slopes where it is orograhically lifted to form a persistent cloud layer and thus a steady source of precipitation. On the leeward side of the mountain, clouds are formed by convective forces that move air up the mountain slopes throughout the day (Leopold, 1949). One of the most striking climatic features affecting the volcano is the trade wind inversion (TWI), a synoptic subsidence inversion that

prevents orographic precipitation or the formation of clouds above its base height (Riehl, 1979; Giambelluca and Nullet, 1991; Cao et al., 2007). Because vertical lifting is suppressed by the presence of TWI, moisture regimes are decreased, and radiative fluxes are increased, at locations above the TWI base height (Giambelluca and Nullet, 1992a). Elevation, proximity to the mean TWI base height and exposure to prevailing winds are all primary factors determining microclimates along the slopes of the volcano. As a result of these environmental characteristics, ecosystems can range from desert, to tropical rainforest, to alpine shrub land over very short distances.

In 1916, the upper portion of Haleakalā Volcano was made part of Hawai‘i National Park. This area, along with subsequent additions, became Haleakalā National Park in 1961 and currently protects 13,444 ha of land, of which 10003 ha are designated as a wilderness area managed under the Wilderness Act of 1964 (NPS, 2015). The park encompasses the summit/"crater" area and its boundary extends down to sea level on the eastern flank of the mountain. More than 90% of the native biota that is found within the park boundaries is endemic to the Hawaiian Islands and nearly 50% is endemic to the Island of Maui (NPS, 2015). Despite the high percentages of native and endemic species found in the park, the introduction of alien plants and animals primarily by anthropogenic activities has led to the decline and in some cases extinction of many native species. The National Park has had a profound impact on the preservation of high-elevation ecosystems through fencing efforts and the removal of feral goats and other invasive alien species (NPS, 2015).

The primary objective of this report is to characterize the general climatology of Haleakalā Volcano through an analysis of field observations obtained from the HaleNet climate network located on the mountain. This climatology will include the spatial and temporal

characteristics of microclimates along two mountain slope transects located on seperate windward and leeward exposures of the mountain. Seven measured variables and five derived variables are analyzed for their spatial and temporal characteristics. Period-of-record changes are assessed for 10 climate variables and described in terms of changes to available energy and moisture. Specific research questions are as follows:

1. What are the spatial characteristics of climate along leeward and windward elevation gradients on Haleakalā Volcano and how do they differ during the dry and wet seasons?
2. How do climate variables change through time? What are the diurnal, seasonal, annual and period-of-record patterns of temporal change?

2.3 Physical Setting

2.3.1 Climate and Vegetation Characteristics

The general climate around the main Hawaiian Islands is relatively dry, with rainfall over the open ocean is less than ~600 mm yr^{-1} (Adler et al., 2003). The islands themselves however, may receive up to 15 times the open-ocean rainfall as a result of the orographic lifting of moist marine air driven by the persistent northeast trade winds (Loope and Giambelluca, 1998). The mean annual cycle of climate in Hawai‘i is usually described in terms of two 6-month seasons (May-Oct and Nov-Apr), which correspond to the traditional dry and wet seasons respectively (Giambelluca and Schroeder, 1998). Trade winds are present between 80-90% of the year, thus dominating surface airflow and weather patterns (Cao et al., 2007). The TWI is created as a result of subsiding air from the upper troposphere interacting with convection-driven air from the surface (Riehl, 1979; Giambelluca and Nullet, 1991; Cao et al., 2007). Both the trade winds and the TWI are associated with the thermally-driven circulation, known as the Hadley Cell, in which

air is lifted near the equator and pushed poleward, where it subsides in the subtropics (Diaz and Bradley, 2005). Hawai‘i lies in the zone of subsiding air within the Hadley Cell circulation.

The TWI layer inhibits the vertical movement of air up the mountain, which causes a sharp contrast in rainfall at high elevations (Giambelluca and Nullet, 1991). These vertical contrasts in precipitation are clearly seen in the mean annual rainfall patterns for East Maui shown in Figure 2.1. The TWI is a prominent feature on the mountain occurring on average 82% of the year at an average base height of 2150 m (Cao et al., 2007).

The complex topography of Haleakalā interacts with atmospheric circulation to produce some of the most spatially complex rainfall patterns in the world (Lyons, 1982; Chu et al., 1993; Schroder, 1993; Giambelluca et al., 2012). Desert-like precipitation minimum zones and extreme wet conditions can be found within a few tens of kilometers distance (Giambelluca et al., 2012). Orographic lifting is a major determinant of rainfall throughout the year in Hawai‘i and the processes that produce orographic cloud precipitation on the windward and leeward sides of the island are separate from one another. On the windward side of the island, trade winds push moist air up the eastern slopes of the mountain, cooling air to the dew point, causing water vapor to condense and eventually form clouds. The trade winds are present between 85 – 95% of the time in the summer and 50 – 80% in the winter (Sanderson, 1993). The strong persistence of the winds in the summer can be explained by the semi-permanent subtropical high-pressure anti-cyclone that sits to the northeast of the island chain (Gerza et al., 2012). The upper part of Haleakalā extends above the TWI, which forces the trade winds around rather than over it (Leopold, 1949). Clouds from the windward side of the island do not reach the leeward side under normal trade wind conditions (Scholl et al., 2007). Instead a diurnal land/sea breeze pattern causes an anabatic movement of air up leeward slopes creating a cloud zone from about

1240 to 1800 m (Giambelluca and Nullet, 1991). However, this process is not sufficient to produce consistent convective showers (Leopold, 1949), therefore leeward slopes are generally dry. During the winter months, the semi-permanent anticyclone is weakened, and the trade winds are frequently interrupted by synoptic disturbances such as upper level troughs, frontal systems, and Kona storms (Giambelluca and Schroeder, 1998;Tu and Chen, 2011). A majority of the annual leeward precipitation is received as a result of these disturbances (Giambelluca and Schroeder, 1998)

The climate of Hawai‘i is strongly affected by Pacific-centered modes of internal climate variability (coupled ocean-atmosphere) including the El Niño Southern Oscillation (ENSO) and the Pacific Decadal Oscillation (PDO; Diaz and Giambelluca, 2012). Both ENSO and PDO are naturally occurring fluctuations in Pacific sea surface temperature (SST). ENSO phases recur on periods of 2 to 7 years and strongly influence winter rainfall patterns in Hawai‘i, where the positive phase (La Niña) is associated with wet conditions and the negative phase (El Niño) is associated with the dry conditions across the State (Chu and Chen, 2005). The patterns associated with positive (negative) phase of the PDO are similar to positive (negative) phases of ENSO, however the PDO signals fluctuate over longer (~20 to 30 yr) time periods (Chu and Chen, 2005).

Climatic zones on the slopes of Haleakalā can be characterized with reference to four atmospheric layers described by Riehl et al., (1951). These four climate zones with the corresponding atmospheric layers in parentheses are: 1) *marine* (sub-cloud), 2) *fog* (cloud), 3) *transitional* (inversion), and 4) *arid* (free atmosphere). The sub-cloud layer extends from sea level to the lifting condensation level (LCL, 600 - 800 m) at which point clouds begin to develop. Typically the LCL is higher on the leeward side due to additional heating of air over its

longer trajectory across the land surface. The cloud layer exists from the LCL to the base of the TWI (mean 2165 m ± 486m s.d.; Cao et al., 2007). The thickness of the inversion is variable (282 m ± 281 m s.d.; Cao et al., 2007) and above this point the stable dry air of the free atmosphere can be found. The height and thickness of the TWI varies in space and time in response to fluctuations in large-scale circulation and surface heating (Giambelluca and Nullet, 1991). This layered system disappears when cyclonic systems disrupt the trade winds and Hadley Cell subsidence.

The vegetation characteristics across elevation gradients on both the windward and leeward orientations of Haleakalā are dependent on several factors, including, substrate, topography, precipitation, available genotypes and the fragmentation and severe modification of native vegetation, especially at lower elevations (Medeiros et al. 1986). The northern and northeastern exposures of windward Haleakalā are subject to persistent orographic rainfall throughout the year. The tropical montane cloud rainforests (TMCFs) found within the fog zone on these slopes are dominated by the native species *Metrosideros polymorpha* (‘ōhi‘a lehua). The upper reaches of the cloud forests have resisted the invasion of alien species and native species have been shown to recover rapidly after the removal of feral ungulates (Loope et al., 1992). Above the cloud zone an abrupt change in physiognomy and species composition of the vegetation occurs in the vicinity of the mean TWI, where the rain forest transitions to grassland and shrubland (Kitayama, and Mueller–Dombois, 1992). This abrupt transition in vegetation at the cloud zones upper limit (forest line) is linked to the TWI’s pronounced discontinuity in moisture availability (Crausbay and Hotchkiss, 2010).

High-elevation wetland systems are also present on the windward side of the mountain. There are several bogs found along the northeast volcanic rift between 1450 and 2270 m

elevation (Loope et al., 1991) and two high-elevation lakes found at 2040 m (Wai‘ele‘ele) and 2100 m (Wai‘ānapanapa; Crausbay and Hotchkiss, 2012). These wetland ecosystems contain a relatively large number of rare species many of which are endemic to the island of Maui.

The presence of clouds has profound effects on the biota within the TMCFs (Delay and Giambelluca, 2010). Cloud droplets are intercepted by leaves, stems and other obstacles within the forest system, adding to soil moisture on both windward and leeward sides of the mountain (Giambelluca et al., 2011). The leeward cloud zone was once extensively dominated by *Acacia koa* and *Metrosideros polymorpha,* much of which has been degraded to grassland by fire and browsing by feral goats and cattle (Medeiros et al., 1986).

A subalpine shrub land zone occurs from ~1800 to ~2400 m, dominated by *Coposma montana, Sophora chrysophylla*, *Styphelia tameiameiae* and *Vaccinium reticulatum*; above ~2400 m, in an alpine zone vegetation is sparse due to the combination of harsh climatic and edaphic conditions (Medeiros et al., 1986). The alpine zone is the habitat for the endemic Haleakalā silversword, (*Argyroxiphium sandwicense* subsp. *macrocephalum*), which grows on cinder flats and rocky cliffs in a area spanning the central to western portions of the crater and up to the summit from 2150 to 2990 m elevation (Krushelnycky et al., 2013). Mean annual rainfall within this zone varies from 1090 to 1520 mm yr^{-1} (Giambelluca et al., 2013) and large diurnal temperature fluctuations with potentially freezing conditions at night and frequently high daytime temperatures (Loope et al., 1992). Early Hawaiian settlers did not use these high-elevation lands extensively, most likely because of the extreme conditions found there (Burney et al., 1995).

2.3.2 The HaleNet Climate Network

High mountains such as Haleakalā Volcano provide a natural laboratory for the study of elevation effects on tropical climate (Giambelluca and Nullet, 1991). Climate variables such as temperature, relative humidity, and precipitation exhibit impressive changes across relatively short distances along the slopes of the mountain. In July of 1983 a climate monitoring network (MauiNet) was established by the University of Hawai‘i College of Tropical Agriculture to support a variety of agricultural research projects. The network consisted of 23 stations ranging from 40 to 1640 m in elevation on the northwest flank of Haleakalā Volcano. MauiNet measurements included solar radiation, temperature, and relative humidity and, at some sites, rainfall, soil temperature, soil moisture and wind. MauiNet was operated by Haruyoshi Ikawa of Department of Agronomy and Soil Science until about 1989.

In June of 1988 the beginnings of the HaleNet climate network were established on the leeward slopes of Haleakalā Volcano with the installation of three climate measurement stations at elevations of 960 – 2130 m. Two climate monitoring stations were collocated with MauiNet sites HN-119 (960 m) and HN-106 (1640 m) and a third station HN-151 (2120) was installed near the Haleakalā National Park Headquarters. This leeward transect of HaleNet stations was expanded further up the mountain in March 1990 with the addition of HN-152 (2590 m) and a summit station HN-153 (2990 m). In June 1992, a second transect was established on the windward side of the island at elevations 1650, 1960, 2260, and 2470 m. These windward stations are all located in remote areas, making access to them difficult without the aid of helicopter transportation. In December 2000, an additional leeward station (HN-141) was installed at 1240 m elevation on the southwest rift of Haleakalā Volcano. In August 2001, a windward station (HN-142) was installed in the Nature Conservancy Waikamoi Preserve located

in the upper Pi‘ina‘au stream drainage basin at 1932 m. Of the eleven stations (Figure 2.2) that once operated in the HaleNet climate network, eight are still in full operation. The Waikamoi station (HN-142), which was installed for a research project on cloud water interception, was removed in August 2003. The Horseshoe Pu`u station (HN-163) at 1960 m elevation was discontinued after being badly damaged in 1996 by lightning and high winds. The Pu`u Pahu station (HN-106) at 1650 m elevation was vandalized in 2003 and now only collects rainfall data. The entire network has a vertical coverage 810 m (1650 – 2460 m) and 2030 m (960 – 2990 m) along the windward and leeward slopes respectively (Figure 2.3).

HaleNet stations have been recording microclimatic data for as long as ~27 years (1988 to 2015; Table 2.1) are in continued operation. The data collected at these stations includes measurements of net and solar radiation, temperature, wind speed and direction, relative humidity, precipitation, soil temperature, soil heat, and soil moisture. Recent upgrades to the active stations still in operation include the addition of 4-component net radiometers, which provide measurements of downward and upward longwave and shortwave radiation. All of these climate variables can be analyzed independently or in combination to derive additional variables such as potential evaporation.

The stations within the network provide data relevant to the four atmospheric layers described by Riehl (1951). These layers can be delineated according to levels of the cloud base and the TWI base, both of which can vary through space (vertical and horizontal) and time (e.g., dry season vs. wet season). The marine (sub-cloud) zone which extends from sea level to the mean cloud base level ~1000 m on the leeward slope is best represented by station HN-119 (960 m). This zone is almost always below the cloud base. Air in this layer is well mixed with temperature and relative humidity profiles strongly influenced by upwind sea surface conditions.

The fog (cloud) zone, which extends from the mean cloud base level to lower limit of the TWI is represented best by leeward stations HN-141 (1240 m), HN-106 (1640 m) and windward station HN-164 (1650 m). This zone experiences frequent cloudy conditions, which correspond to the lowest receipts of energy and highest amounts of moisture on either transect. This zone is also influenced by the rapid upslope movement of moist air during the day and the frequent downward flow of dry air from the upper atmosphere, which produces high variability in humidity and radiation.

The transition (inversion) zone covers a range of heights beginning at the TWI base height and extending through the inversion. Within this zone any of the four atmospheric layers can be present at a given time. Fluctuations in the inversion can produce rapid changes in relative humidity of 60% or more over a few minute time period (Giambelluca and Nullet, 1991). HaleNet stations HN-151 (2120 m) on the leeward transect and HN-162 (2260) on the windward transect are most representative of this zone.

The arid (free atmosphere) zone extends above the upper limit of the inversion zone. The air found in this layer originated from the upper troposphere and is typically dry. This air is isolated from ocean moisture when the TWI is present making it relatively cloud free. The upper slopes of Haleakalā, which penetrate into the arid zone, are exposed to high levels of radiation and low rainfall amounts. HaleNet stations HN-152 (2590 m) and HN-153 (2990 m) on the leeward slope and HN-161 (2460 m) on the windward slope most effectively capture the characteristics of the free atmosphere zone. During periods of TWI absence or an unusually high TWI base height, moist air originating from lower elevations can reach these stations.

2.4. Methods

2.4.1 HaleNet Instrumentation

Solar radiation (W m^{-2}) was measured with Eppley model 8-48 (Eppley Laboratory, Newport, RI, USA) thermopile pyranometer measuring global solar radiation and sampled at a 10 s interval. Beginning in January, 2011 a Hukseflux (Manorville NY, USA) model NR01 four-component net radiation sensor was installed at all of the stations still in operation. Net radiation (W m^{-2}) was measured with a Radiation Energy Balance Systems (REBS; Seattle WA, USA), Model Q*6. In June of 1994 three stations (HN-106, HN-119, and HN-151) Model Q*6 were upgraded to Model Q*7, and in July of 1999 all of the net radiometers were replaced with the Model Q*7.1. Beginning in January 2011 net radiation was calculated as the sum of the difference between upward and downward long and short wave transmissions recorded with the Hukseflux NR01. Air temperature (°C) and Relative humidity (%) were monitored with Vaisala Model (Helsinki, Finland) HMD-30-YB sensors and in July of 1999 these sensors were replaced with the Vaisala Model HMP-45-C. Wind speed (m s^{-1}) was measured with a Qualimetrics (Sacramento CA, USA) Model 2011 at the leeward stations and a Met One (Shanghai, China) Model 014A 3-cup anemometers. In July of 1999 all these instruments were replaced with a Met One Model 034A and in January 2011 a R.M. Young (Traverse City, MI) Model 05106 propeller type anemometer. Soil moisture was measured with a Cambell Scientific Inc. (Logan, UT, USA) model CS615/CS616 reflectometer. Soil Heat was measured with a REBS model HFT-3 heat plate. Data for all variables were sampled at 10 s intervals and recorded hourly using a LI-COR (Lincoln, NE, USA) LI-960 data logger (before mid-July 1999), a Campbell Scientific, Inc. CR10X data logger (after mid-July 1999) and Campbell Scientific CR2990 data logger as of January 2011.

2.4.2 Data Quality and Control

HaleNet data used in this report were subjected to a series of quality control and quality assurance procedures before they were made available for analyses. First, all the data are plotted as a time series and visually screened for outliers and unrealistic consecutive values (e.g. Air temperature drops from 28˚ to 9˚ in one hour). Second, the relationships between variables that are highly correlated are compared (e.g. solar radiation and net radiation). Third, variable data were compared between nearby stations. Finally, to improve the overall accuracy and homogeneity of the HaleNet data, a series of error detection, correction, and homogenization techniques were developed for some of the measured variables. Application of these techniques was necessary to correct for the effects instrument calibration drift and the abrupt data shifts resulting from adjustment of data logger coefficients following sensor recalibration.

For solar radiation (K_d) measurements, methods were developed to homogenize hourly K_d time series based on comparison of clear-sky radiation observations against estimates derived from a clear-sky radiation model. In-homogeneities in the record are identified based on shifts in pyranometer response in relation to the model estimates, and corrected to produce a homogeneous time series. A detailed description of this method is given in Longman et al. (2013).

Net radiation (R_n) data were corrected and homogenized using several methods. First the data were corrected using a procedure that adjusted data obtained from early versions of the REBS net radiometers Q*6 and Q*7, to be consistent with the sensor calibration approach recommended by the manufacturer beginning with model Q*7.1. This correction involved the use of separate calibration factors for positive (daytime) and negative (nighttime) values, and a wind correction. If no wind speed value was available for a given time period, the mean station

wind speed was used for the correction. Finally, the R_n data were homogenized so that values obtained from the different sensors that were in place over the period of record were in agreement with one another. To accomplish this, the hourly R_n/K_d ratio was used to identify inconsistencies within a given data set by examining how this ratio changed over time. The principle behind the adjustment is that the R_n/K_d ratio should be consistent over time and any apparent shifts or trends indicate a change in the sensor. R_n data can then be corrected based on the relationship between R_n/K_d ratios for a given time period and the R_n/K_d ratios obtained during a reference period. The mean ratio from the time period when recently installed Hukseflux net radiometers were in place was used as the R_n/K_d ratio reference period. All other time periods were corrected based on this value. The adjustments were checked by comparing adjusted REBS sensor data with Hukseflux data for a time period when both sensors operated at each site simultaneously. Based on this comparison, it was conclude that adjusted daytime radiation values were in close agreement with the reference data. However, adjusted nighttime (negative) Rn values were not in agreement with the reference data. Therefore, a simple adjustment of nighttime values was applied based on comparison of the new and old sensors during the period of overlapping observations.

An assessment of wind speed data revealed several homogenization issues: 1) sensors installed at different heights during the period of record; 2) changes in the low-wind threshold due to the degradation of the instruments bearings; and 3) changes in sensor type. These issues were addressed by: 1) adjusting wind speed to a common sensor height based on an assumed logarithmic profile, setting zero plane displacement and roughness length as a function of the vegetation height (e.g. Thomas et al., 2005); 2) identifying and correcting data affected by worn bearings in the anemometer. After adjusting for sensor height differences, each station time

series was divided into two groups representing periods during which instrument bearings were assumed to be good (reference data) and periods when the bearings appeared to have been faulty. The bad-bearing periods were identified as periods with repeated cases of zero as the recorded wind speed. Experience shows that completely calm conditions are very rare at all stations. The end of these bad-bearing periods almost always coincided with the replacement of the bearings or sensor as indicated in the field notes. Using rank regression, parameter values for the Weibull distribution were determined based on the reference data set. Data were then adjusted for bad-bearing periods, by setting the wind speed at each time interval according to its cumulative frequency, using the inverse Weibull cumulative frequency function with settings from the reference data set. For intervals with measured zero wind speed (which have indistinguishable cumulative frequencies), the order of the Weibull-generated values was randomized before cumulative frequencies were assigned. Comparison of frequency distributions for reference bad-bearing periods showed that only the lower wind speed measurements are significantly affected by the bearing degradation. Therefore, only wind speeds less than 1.5 m s^{-1} were corrected using this method.

An assessment of relative humidity data from the HaleNet stations revealed several problems related to calibration drift. Fortunately, HaleNet stations experience saturated conditions (RH = 100%) more or less frequently, and these periods can be used as reference points to correct the calibration drift. First, the data were examined at each station during periods when the sensor calibration was thought to be accurate to establish the length of the time window needed to provide a high confidence in the occurrence of saturated conditions at the site. The length of the required time window ranged from 6 (HN station 164) to 60 (HN station 153) days. Maximum measured relative humidity was identified using a moving window that encompassed

of the appropriate length for each station. Data with calibration drift errors were adjusted according to the following equation:

$$RH_{adj} = RH * \left(\frac{100}{RH_{max}}\right) \quad (1)$$

where: RH_{adj} is the adjusted hourly relative humidity, RH is the measured hourly relative humidity, and RH_{max} is the maximum hourly value within the current time window. Each adjusted time series was graphed and visually checked. Rainfall at each station was graphed alongside the RH time series to provide additional information useful in conducting the visual consistency check.

2.4.3 Derived Variables

2.4.3.1 Potential Evapotranspiration

Potential Evapotranspiration (PET) can be defined as the rate at which a vegetated surface, not limited by moisture availability, loses water to the atmosphere (Dunne and Leapold, 1978). Several methods have been developed to calculate PET (e.g. Penman, 1948; Thornthwaite 1948; Priestley and Taylor, 1972), however the Penman-Monteith (Monteith, 1965) method is recommended by the FAO for calculating PET whenever the required input data are available (Gong et al., 2006). The Penman-Monteith method requires measurements of air temperature, wind speed, relative humidity and net radiation. This method also includes a thermodynamic (energy required to evaporate water) and aerodynamic (the turbulent transport of water vapor away from the evaporating surface), component that accounts for the effects of vegetation on thermodynamic and aerodynamic processes (Howell and Evett, 2004; Bonan, 2008;). This method was used to calculate PET (mm hr^{-1}) at 8 HaleNet stations where sufficient data were available. The Penman-Monteith equation can be expressed as:

$$\lambda E = \frac{\Delta(R_n - G) + \frac{\rho C_p}{r_a}(e_*[T_a] - e_a)}{\Delta + \gamma} \quad (2)$$

where λE is the evaporation expressed as a latent heat flux (W m^{-2}), Δ is the slope of the saturation vapor pressure versus temperature curve (kPa $°C^{-1}$), R_n the net radiation flux density at the surface (W m^{-2}), G the sensible heat flux density from the surface to the soil (assumed to be negligible over a 24-hr period), ρ is the density of air (kg m^{-3}), C_p the specific heat of moist air at constant pressure (1004 J kg^{-1} K^{-1}), $e_*[T_a]$ is the saturation vapor pressure (kPa) at ambient air temperature (T_a, °C), e_a is the actual vapor pressure of the air (kPa), r_a is the aerodynamic resistance to turbulent heat and/or vapor transfer from the surface to the reference height (z) above the surface [s m^{-1}], γ is the pyschrometric constant (kPa $°C^{-1}$).

The resistance to transfer of heat and water vapor from the evaporating surface into the air above is represented by the aerodynamic resistance term, estimated here using the following relationship (Allen et al., 1998):

$$r_a = \frac{\left[\ln\left(\frac{(z_a - ZPD)}{z_0}\right)\right]^2}{k^2 U_Z} \quad (3)$$

where z_a height of wind measurements (m), ZPD zero plane displacement height (m), z_0 roughness length governing momentum transfer of heat and vapour [m], k is the von Karman's constant, 0.41, u_z wind speed at height z (m s^{-1}). To provide reference-surface PET estimates, the terms ZPD and z_0 were held constant at all of the stations at values of 0.1005 and 0.015 respectively, which are representative of a short grass cover.

2.4.3.2 Vapor Pressure Deficit

Saturation vapor pressure can be defined as the equilibrium vapor pressure under the existing environmental conditions of temperature (Murray 1967). Saturation vapor pressure

increases non-linearly with higher temperature and can be expressed by a sixth-order polynomial developed by Lowe (1977);

$$e_* = \mathrm{A_0} + \mathrm{T_a}\left(\mathrm{A_1} + \mathrm{T_a}\left(\mathrm{A_2} + \mathrm{T_a}\left(\mathrm{A_3} + \mathrm{T_a}\left(\mathrm{A_4} + \mathrm{T_a}(\mathrm{A_5} + \mathrm{A_6}\mathrm{T_a})\right)\right)\right)\right) \quad (4)$$

where A_0 is 6.107800, A_1 is 4.436519E-1, A_2 is 1.428946E-2, A_3 is 2.650648E-4, A_4 is 3.031240E-6, A_5 is 2.034081E-8, A_6 is 6.136821E-11.

Vapor pressure is defined as the part of the total atmospheric pressure contributed by the ambient water vapor content. Vapor pressure can be derived from RH as:

$$e_\mathrm{a} = \mathrm{RH}\left(\frac{e_*}{100}\right) \quad (5)$$

where, RH is the relative humidity.

The vapor pressure deficit (VPD) is the difference between the saturation vapor pressure and the actual vapor pressure:

$$\mathrm{VPD} = e_* - e_\mathrm{a} \quad (6)$$

VPD is an indication of the dryness of the air and the potential for evaporative fluxes.

2.4.3.3 Soil Heat Flux

The flux of sensible energy into or out of the soil (soil heat flux, G) is an important component of the surface energy balance especially in areas with sparse or no vegetation (Giambelluca et al., 2014). Spatial and temporal variations in G are driven by available energy at the surface, which is influenced by surface characteristics and atmospheric conditions. At each HaleNet station, G is estimated based on measurements from two soil heat flux transducers placed at a 8 cm depth and estimated changes in sensible heat stored in the soil above the transducers based on measurements of soil moisture and soil temperature:

$$\mathrm{G} = \mathrm{F} + \mathrm{S} \quad (7)$$

where F is the average of soil heat flux at 0.8 cm and S is the change in sensible heat storage in the upper 8-cm soil layer:

$$S = \left(\frac{\Delta T_{Soil}}{TI}\right) D \left((\rho_b C_s) + \theta\, \rho_w\, C_w\right) \quad (8)$$

where ΔT_{soil} is the change in temperature in the upper 8 cm of soil from the previous hour (°C), TI is the time interval (s), D is the vertical thickness of the soil layer above the heat plate (m), ρ_b is the bulk density of the soil (kg m^{-3}), C_s is the specific heat for mineral soil (J kg^{-1} K^{-1}), θ is the volumetric soil moisture content (m^3 m^{-3}), ρ_w is the density of water (kg m^{-3}) and C_w is the specific heat of water (J kg^{-1} K^{-1}).

2.4.3.4 Cloud Attenuation of Sunlight

To determine the reduction of global radiation by clouds, measured global radiation values are compared to clear-sky estimates derived from the REST2 clear-sky radiation model (Gueymard, 2008). The two-band REST2 clear-sky radiation model (Gueymard, 2008) can predict instantaneous or short-term (hourly or sub-hourly) global radiation based on a limited number of inputs that describe the local and current, atmospheric and environmental conditions. Methods for parameterizing clear-sky radiation models, specifically in Hawai‘i, have been described elsewhere (Gueymard, 2012; Longman 2012). For this study, REST2 model inputs are held constant at their respective long-term means. In a previous study, we analyzed the effects of temporal averaging of model atmospheric transmission parameters (Longman et al. 2012). The results showed that holding model inputs constant at their mean annual value gave better results than using temporally varying (daily or monthly) parameter estimates for prediction of clear-sky radiation at a range at a sample of the HaleNet stations. The use of fixed input parameter values was also mandated for this study by the fact that measured atmospheric parameters were not available for the entire period of record.

To calculate the cloud attenuation of sunlight, mean hourly solar radiation for each month in the record was divided by the long-term mean REST2 modeled clear-sky solar radiation for the appropriate calendar month. This analysis was applied only to data between the hours of 9:00 AM and 5:00 PM (HST) to eliminate any topographical shading effects during times of low sun angles. The hourly percent of cloud attenuation of sunlight is expressed as:

$$\mathrm{CA} = 100 - \left(\frac{\mathrm{Kd_h}}{\mathrm{CS_h}}\right) * 100 \quad (9)$$

Where, CA is the cloud attenuation of sunlight, Kd_h is measured hourly solar radiation and CS_h is the modeled clear-sky hourly solar radiation. Monthly means are calculated as the average of the seven mean hourly CA values for each month.

2.4.3.5 Data Aggregation and Temporal Assessment Methods

Hourly HaleNet data are aggregated in several ways. The period-of-record mean diurnal cycles are calculated for each month with at least 15 days of data by averaging the monthly mean hourly values. Mean monthly values are derived from the mean monthly diurnal cycles. The 6-month dry and wet season and annual means are calculated by averaging the appropriate mean monthly values. Dry and wet season aggregated values are used to show spatial patterns related to elevation along leeward and windward transects. Period-of-record trends are assessed using the seasonal anomalies. These anomalies were calculated as the average of the departure of each monthly value from the appropriate period-of-record monthly mean. Anomaly values were included for a given season-year only if at least 50% of the data were available.

Precipitation (rainfall) was aggregated as follows to avoid extreme biases associated with missing data in the temporal analysis:

$$\mathrm{p_{i,j}} = \frac{\mathrm{p_{sum\_i,j}}}{m_{i,j}} \mathrm{N_i} \quad (10)$$

where $p_{i,j}$ is the monthly rainfall total, $p_{sum\_i,j}$ is the sum of daily rainfall for days with good data, $m_{i,j}$ is the number of observation days in a month, N_i is the number of days in the month, and the subscripts i and j stand for month and year, respectively. Monthly mean precipitation was calculated as:

$$P_{POR\_i} = \frac{P_{sum\_i}}{M_i} N_i \quad (11)$$

where P_{POR_i} is the period-of-record mean precipitation for month i and P_{sum_i} is the sum of precipitation for month i for all months with ≥ 15 days of data, M_i is the number of days with precipitation observations included in P_{sum_i}. Precipitation anomalies are calculated as:

$$P_{anom\_i,j} = p_{i,j} - P_{POR\_i} \quad (12)$$

where $P_{anom\_i,j}$ is the monthly precipitation anomaly for month i and year j. For months with ≥ 15 days of data, a zero precipitation statistic was calculated as:

$$ZP_{i,j} = \frac{NZP_{i,j}}{m_{i,j}} * 100 \quad (13)$$

where ZP is equal to the percentage of days with zero precipitation in month i and year j, NZP is the number of days of good data with zero precipitation, and the subscripts i and j stand for month and year, respectively.

Period-of-record trends are analyzed and tested for statistical significance using linear regression model. Statistical significance at the 90% significance level ($p \leq 0.1$), using the null hypothesis that the trend is zero. Time series are assessed for the period of record for each variable at each station. Time series start dates vary with station (Table 1) and variable. Time series end dates are typically October 2013 with the exception the variables potential evapotranspiration and cloud attenuation of solar radiation (October 2011) at all stations and all variables at the HN-106 station (October 2003).

Period of record trends are assessed for each of the two seasons for all time series with n ≥ 15 seasonal values. Following this criteria we exclude all of the time series from HN-141, all of the time series from HN-106 (except for precipitation) and all time series data of soil heat flux and soil moisture. We express relative change in a given variable over the period of record as:

$$Trend_{X\_k} = \frac{b_{X\_k}}{X_{POR\_k}} * 100 \quad (14)$$

where $Trend_{X\_k}$ is the period-of-record trend as a percentage of the mean for variable X and season k; b_{X_k} is the slope of the trend line derived from linear regression in per year units for variable X and season k; X_{POR_k} is the period-of-record mean of variable X and season k.

In total, 10 climate variables obtained from data collected from as many as 8 HaleNet stations are analyzed for period-of-record change for both dry and wet seasons. Changes over time are characterized using the linear model (lm) statistical function in the R open source statistical package. The linear model used in this analysis does not account for the effects of temporal autocorrelation. In a preliminary analysis, 128 climate variable time series were tested for temporal autocorrelation using the Durbin-Watson statistical test (Durbin and Watson, 1971). Of the 128 time series tested, 15 (11.7%) we significant at $\alpha = 0.05$ and 5 (3.9%) were significant at $\alpha = 0.01$ and no consistent patterns among stations or variables were identified. Based on these results it was decided to not include a temporal autocorrelation correction in the linear model.

2.5 Spatial and Temporal Assessment

The complete record of HaleNet data is analyzed and results are presented for each variable. A description of the HaleNet data with regards to the temporal (diurnal and annual) and spatial (elevation and exposure to the prevailing winds) behavior of seven observed and four derived variables is presented and discussed for all HaleNet stations where sufficient data are available. We analyze the mean annual cycle of each variable as well as the spatial and temporal

characteristics of the 6-month dry and wet seasons. High-elevation stations are those located above 2000 m and mid-elevation stations are located between 900 and 2000 m (Table 2.1). Period-of-record trends are assessed only for the stations that were established by June 1992 and are currently still in operation (i.e. 8 stations).

2.5.1 Solar Radiation

The amount of solar radiation reaching the surface of the Earth is modulated by several factors including latitude, time of day, time of year, topography and the optical properties of the atmosphere. Latitude of a given location governs the angle at which the sun's rays strike the Earth and therefore the amount of solar radiation arriving at the surface at any point throughout the day. Near the equator, the sun is always high overhead at midday and the days and nights are nearly equal in length throughout the year. Since Haleakalā Volcano is located ~20°N of the equator, the annual day length cycle has a range of approximately 2.5 hours. The annual cycle of solar radiation for each HaleNet station is shown in Figure 2.4. The seasonal changes are related to day length changes, the annual march of solar declination affecting the angle of incidence of direct radiation, and variations in cloud cover characteristics. Differences among stations are due mainly to elevation effects on clear sky radiation (under clear skies, solar radiation increases with elevation as the optical thickness of atmosphere is reduced) and spatial differences in cloud cover. The annual peak of solar radiation occurs in June for the four highest elevation stations located above the mean TWI level (2160 m) and in July for the five stations located at or below this point (Table 2.2). The minimum values occur in either November or December although the values for these months were very similar at all stations.

The diurnal solar radiation patterns for the dry and wet seasons are shown in Figure 2.5. For all stations, solar radiation increases sharply in the morning with relatively little attenuation

by clouds. For the highest elevation stations located at or above the mean TWI, solar radiation peaks at 12:00 or 13:00. This pattern is indicative of generally clear conditions at these elevations throughout the day with some influence of clouds occurring at leeward stations. At the mid-elevation stations, clouds that move progressively upslope during the day begin to reduce solar radiation significantly by late morning, especially for the leeward stations. The most notable change occurs within the cloud zone at leeward station HN-141(1240 m) where radiation is 30% lower at 13:00 PM than at 10:00 AM (Figure 2.5). Local sea-land and mountain-valley wind regimes can interact with the general trade wind flow and promote cloud development on the leeward side of the islands (Leopold, 1949). The presence of the TWI effectively caps the vertical development of clouds thus the highest-elevation stations show relatively cloud free conditions throughout the day.

For the mid-elevation station HN-164 (1650 m) on the windward exposure diurnal differences in cloud effects are not as clearly identifiable, which can be explained by the consistent presence of clouds throughout the day. Diurnal patterns for all stations are similar in the dry and wet seasons. However, less influence of clouds is seen during the wet season at mid-elevation leeward stations.

The dry and wet season spatial profiles of solar radiation for 3 windward and 6 leeward stations are shown in Figure 2.6. Solar radiation gradients along the transects show similar patterns with a distinct minimum occurring in the center of the cloud zone ~1650 m and the highest irradiance occurring at the highest elevation station along both transects. For the dry season, radiation at the highest station on each transect (2990 m and 2460 m for leeward and windward transects, respectively) is almost twice as much as the radiation measured within the cloud zone (Table 2.2). This contrast is much less pronounced in the wet season profiles.

2.5.2 Cloud Attenuation of Sunlight

Global solar radiation passing through the Earth's atmosphere is modulated by aerosols, trace gases and clouds. Because of Hawai'i's mid-oceanic location and distance from continental aerosol source areas, variability in atmospheric transmissivity is relatively low, especially in the free atmosphere above stations at high elevations (Longman et al., 2012). At the surface, clouds are the primary factor determining the attenuation of global radiation. Annually, the cloud attenuation of insolation (CA) can be as low as 4% at the summit and as high as 56% in the heart of the cloud zone all within the same month (Figure 8; Table 4). Annual CA minimums (i.e. sparse cloud cover) occur between December and January for all but one of the leeward stations (2990 m). Despite being in the middle of the wet season these months have the lowest cloud cover frequency across the islands (Barnes, 2013). The timing of the highest mean monthly CA (i.e. abundant cloud cover) is more spatially variable. For mid-elevation leeward stations, maximums occur between April and June, which corresponds to the time of the highest TWI frequency and base height (Figure 3), thus promoting cloudy conditions at low elevations. For high elevation leeward stations, the highest CA occurs between September and November, which is the transition period from the dry to wet season, a period of decreasing TWI frequency. Windward CA maximums occur in March and April, corresponding to some of the wettest months of the year at those locations (Giambelluca et al., 2013).

Diurnal profiles for the dry season (Figure 9) show a noticeable increase in afternoon cloud attenuation at all leeward stations with the greatest afternoon cloudiness occurring within the cloud zone (1640 m). Windward diurnal cycles are relatively constant throughout the day for this season. Wet season diurnal patterns (Figure 10) are similar to those of the dry season; however, in general, much clearer conditions are observed throughout the day.

Vertical profiles of CA show the decreasing effects of cloud cover with elevation above the cloud zone. Between 1640 and 2990 along the leeward transect cloud cover is reduced by 47 and 32% for the dry and wet seasons respectively. Along the windward transect decreases in cloud cover between 1650 and 2460 are 30 and 26% for dry and wet seasons, respectively.

2.5.3 Net Radiation

The difference between the absorbed and emitted radiation at all wavelengths is termed "Net Radiation" (R_n). At the surface, incoming (downward) shortwave (solar) and longwave (atmospheric) radiation add energy, while outgoing (upward) reflected shortwave and emitted longwave radiation remove energy. As a quantitative measure of the chief source of energy for all environmental processes, R_n is a fundamentally important variable in determining local climate and hydrological flows. R_n at the surface is used to heat the biomass, soil and overlying air and to evaporate water. Net radiation is positive during the day and negative at night, and generally higher during the summer than the winter. Across the globe, R_n is positive at low latitudes and negative at high latitudes. These variations in time and space drive the diurnal and annual cycles in climate and help explain the global distribution of climates. The same effects can be seen at the local scale, especially where extreme spatial gradients in radiation are found. Therefore, knowledge of the spatial and temporal variations in R_n is essential for understanding natural processes on Haleakalā.

The annual R_n peak for the HaleNet stations occurs in July at six stations and June at three stations (Figure 2.10; Table 2.4) although differences were very small between the two months (1 to 8 W m^{-2}). R_n minimums occurred in December for all nine stations analyzed. The annual cycles of R_n follow those of the solar radiation cycles with the higher values occurring

during the high-sun, dry season months and lower values occurring in the low-sun, wet season months.

The diurnal patterns of R_n for the dry and wet seasons resemble solar radiation patterns during the daylight hours (Figure 2.11). At night, longwave radiation loss to space increases with elevation along both transects, as indicated by the greater negative values. Mid-elevation sites are often beneath a cloud layer that persists after dark. As a result, longwave radiation loss is reduced, but increases in the early morning hours as the sky begins to clear. For the high-elevation stations, which are typically above the cloud layer, longwave radiation tends to decrease throughout the night as the ground cools. In general, there is a much greater nighttime longwave radiation loss along the leeward transect.

R_n increases with elevation along the windward transects for both seasons (Figure 2.12). Vertical profiles of R_n do not show consistent relationships with elevation along the leeward transect. The effects of clouds and clear atmosphere changes with elevation do not explain all of the variability. Differences in R_n can be explained by additional factors including albedo, and surface temperature. Vegetation should have an effect on decreasing surface temperature (less longwave outgoing radiation) and lowering surface albedo (less shortwave outgoing radiation) thus explaining higher R_n along the windward transect which is more vegetated and potentially explaining the increased R_n at HN-141 (1240 m) which is located within a leeward dry-land forest preserve (Medeiros and von Allmen, 2006).

2.5.4 Temperature

Much of the solar radiation transmitted through the atmosphere is absorbed at the Earth's surface, increasing its temperature. The surface, in turn, warms the lower atmosphere through conduction and longwave radiation emission (by the surface) and absorption (by the air). Surface

air temperature (T_a) on a mountain slope is determined by R_n, but also by the temperature of the free atmosphere at a given elevation.

Hawai‘i has the consistently small annual T_a cycle characteristic of marine tropical climates (Figure 2.13). The differences between the coldest and warmest months (Table 2.5) is small (2.6 to 3.7 °C) with the highest mean monthly T_a values occurring primarily in August (September for 1650 m station) and lowest values occurring in February for all of the leeward stations and the mid elevation windward station and in March and April for the 2260 m and 2460 m high-elevation windward stations, respectively. The differences in the timing of the lowest monthly T_a values on the windward transect are most likely explained by variations in cloud cover.

The diurnal temperature cycles at all stations are marked by an abrupt change at sunrise and sunset and (Figures 2.14). During the dry season, when cloudy conditions are most common in the afternoon hours, temperature is relatively stable across the leeward transect between 1240 and 2120 m due to the well-mixed air within the cloud zone. The stations located below (above) this zone exhibit a more pronounced diurnal cycle and are much cooler (warmer) to the presence (absence) of clouds. For the wet season, clearer conditions promote a more distinct elevation-dependent relationship although the effects of clouds are still apparent. Again, the onset of afternoon clouds is most noticeable at the stations located within the heart of the cloud zone on both transects, marked by a distinct temperature decrease between 11:00 and 12:00 h.

A clear pattern of decreasing temperatures with increasing elevation is seen, although the rate at which temperatures decrease is not constant along each transects (Figure 2.15). Increases in temperature with elevation that occur within the TWI layer are not directly identifiable at this vertical resolution and are smoothed out by vertical fluctuations in the TWI level. However,

temperature lapse rates (the rate of temperature decrease with elevation) indicate a clear relationship between elevation and the stations affected by the inversion and the moist conditions that exist within the cloud zone below it. Temperature lapse rates occurring on the leeward transect below HN-141 (1240 m) and above HN-152 (2590 m) are greater than temperature lapse rates occurring between these points. These lower lapse rates can be explained, in part, by the release of latent energy within the cloud zone, so that rising air cools and the wet adiabatic lapse rate (approximately half of the dry adiabatic lapse rate) within the cloud. In addition the effects of increased temperature due to the presence of the inversion may have a dampening effect on on lapse rates. Since the air is generally unsaturated below the LCL and above the TWI, lapse rates are greater there. The presence of the TWI and the subsequent increase in T_a at some point along the gradient has a dampening effect on the lapse rates as well.

The data indicate noticeably lower temperatures at windward stations compared with leeward stations at similar elevations. For example, stations located at 1640 m and 1650 m on leeward and windward exposures, respectively, have an annual T_a difference of 1.4˚C despite a 10 m difference in elevation. Under normal moist adiabatic conditions the temperature lapse rate would be 0.64˚C per 100 m (2. 6˚C) between these two sites which is 1.2˚C greater than observed. Warmer leeward T_a is driven primarily by a difference in partitioning of net radiation. On the Windward side of the island, where moisture is not limited, a high portion of net radiation is partitioned to latent energy which has a cooling affect on the atmosphere. On the leeward side of the island, where moisture is limited, a large portion of net radiation is partitioned to sensible heat energy, which has a warming effect on the atmosphere.

It is also interesting to note that the two leeward stations located within the cloud zone HN-141 (1240 m) and HN-106 (1640 m) which have only a 0.5˚ difference in mean annual T_a

despite a vertical elevation difference of 400 m. This is most likely explained by the surface characteristics affecting the partitioning of available energy at the two sites. Active forest restoration at Auwahi (HN-141) appears to have lowered the air temperature there (see section 8.1).

2.5.5 Relative Humidity

Relative humidity (RH) is the ratio of water vapor in the air to the maximum amount of water vapor the air can hold. RH is a determining factor in the evaporation rate and once RH reaches100%, air is considered saturated and cannot absorb any additional water vapor. RH is determined by both the amount of water vapor in the air and the air temperature (which determines the water vapor content at saturation). Because air can hold more water vapor at higher temperatures, an inverse relationship exists between RH and air temperature. On the mountain slopes of Haleakalā the relationship between relative humidity and temperature is much more complex, especially when considering the dominant effects of the TWI on moisture regimens at high elevations. The mean annual cycles of relative humidity at HaleNet stations are not very distinct (Figure 2.16). All of the stations experience their lowest mean monthly values in either January or December; however, the timing of the highest monthly values varies with elevation (Table 2.6). For the mid-elevation stations highest relative humidity is found between April and June, corresponding to a time of frequent TWI conditions. For high-elevation stations maximums occur between the months of September to November. These months correspond to times of decreased TWI frequency and for September the highest TWI base height. Stations located well below the inversion show fairly flat annual cycles. In general, difference between the highest and lowest mean monthly values increases with elevation and the greatest differences

are found on the windward transect at high elevations. The smallest differences in monthly relative humidity occur within the cloud and marine zones located beneath the TWI.

Diurnal cycles of RH for the dry and wet seasons have distinct patterns for windward and leeward sites (Figure 2.17). On the leeward exposure, beginning in the cloud zone, relative humidity increases in the mid-morning and decreases in the late afternoon. Increases in RH are explained by the transport of moisture by upslope winds during the daylight hours. At HN-119 (960 m) located just below the cloud zone relative humidity decreases in the afternoon hours due to the increase in temperature. In the evening hours, relative humidity increases as temperature decreases. For windward station HN-164 (1650 m) located in the heart of the cloud zone, relative humidity remains relatively constant throughout the day suggesting that the effects of the air temperature cycle (which is very muted to start with) are offset by a cycle in water vapor content (higher during the day to offset the higher saturation vapor pressure) because of consistently moist conditions driven by orographic cloud development.

In general, mean annual relative humidity decreases with elevation along both transects annually (Figure 2.18). The highest relative humidity values are found at the windward cloud zone station and, in general, windward stations have higher relative humidity than leeward stations at similar elevations. The lowest relative humidity values are found at the highest leeward stations located well above the mean TWI base, where air is arid due to the isolating effects of the TWI which impedes the movement of moist marine air to high elevations.

2.5.6 Vapor Pressure Deficit.

The capacity of the air to hold water vapor is controlled by the air temperature. While relative humidity is a measure of the moistness of the air, expressed as a ratio of the water vapor content (e.g., the vapor pressure) to the saturation water vapor (e.g., the saturation vapor

pressure), vapor pressure deficit (VPD) is a measure of the dryness of the air given as the saturation water vapor minus the vapor pressure.

The mean annual cycle of VPD has different patterns depending on location (Figure 2.19). A pronounced annual cycle with summer maximums are observed at the highest elevation leeward sites and a less pronounced annual cycle with winter maximum are observed along the windward transect and within the leeward cloud zone. For the highest-elevation stations maximums occurring in June and minimums occurring in March correspond to the highest and lowest frequency of the TWI respectively (Cao et al., 2007). Despite the low temperatures found at high elevations, the predominantly dry-conditions found above the TWI are driving some of the highest VPD across the network.

The diurnal cycle of vapor pressure deficit at each station (Figure 2.20) varies across elevation, exposure and time. For leeward stations located above and below the cloud zone, VPD follows a pattern similar to diurnal temperature profiles (Figure 2.21), where VPD increases as the air begins to warm. For leeward stations located within the cloud zone (1650 – 2120 m), a marked afternoon decrease in VPD becomes apparent as the air becomes saturated. For leeward stations, VPD is fairly constant throughout the day.

Decreases in VPD are found on the leeward transect between 960 and 1650 m due to increases in humidity within the cloud zone. As relative humidity decreases from 1650 to 2590 an increase in VPD is observed. At the highest elevations cold temperatures drive decreases in VPD from 2590 to 2990 m. Leeward transects show a general increase in VPD with height.

2.5.7 Wind Speed

The highest mountains of the Hawaiian Islands are also some of the windiest places in the archipelago. At more than 3000 m elevation, the summit area of Haleakalā is exposed to the

stronger winds found in the free atmosphere at that level. At lower elevations, winds are reduced by friction with the surface. The wind characteristics at any particular site are highly variable due to the surface topography (i.e. vegetation and relief), orientation to the prevailing trade winds and the exposure of the instrumentation. For the HN stations analyzed in this study no clear annual wind speed (WS) cycle was observed (Figure 2.22). However, the three windward stations and the leeward summit station had their highest mean monthly values in either June or July (Table 2.8), which corresponds to the period of highest trade wind frequency (Cao et al., 2007). Three of the five remaining leeward stations had their highest monthly wind speeds in January (960 m, 1640 m and 2590 m); August (1240 m), and December (2120 m).

Diurnal cycles of wind speed are most pronounced at leeward mid-elevation stations where winds diminish around the times of reversals in the direction of thermal slope winds in the mid-morning and early evening (Figure 2.23). During the day, slopes and overlying air are warmed, and the warm air moves convectively upslope. At night when the air cools and becomes dense, it moves downslope under the influence of gravity. The marked depressions in the diurnal cycle are indications of when these up and down slope shifts occur. At windward stations, a distinct decrease in wind speed is seen in the afternoon hours at all of the stations, but most notably at the highest elevations. The drivers behind this decrease are not completely understood.

In general, mean annual wind speed increases with elevation in both the dry and wet seasons and along both windward and leeward gradients (Figure 2.24). The exception to this is the 1240 m station on the leeward transect, which has higher wind speeds than the station above it (1640 m) during the dry season (Table 2.8). This may be explained by the greater instrument exposure at the 1240 m station and the convergent effect of winds that wrap around the north and south exposures of the mountain connecting at this location. In general, leeward wind speed is

greater in the summer and the winter. Wind speed on the windward side of the island is rather consistent throughout the year and the greatest wind speeds are found on the windward summit station located at 2460 m.

2.5.8 Precipitation

In Hawai‘i, the interaction of mountainous topography, the persistence of the trade winds, the heating and cooling of the land and the consistent presence of the TWI create some of the most spatially diverse rainfall patterns found anywhere in the world (Giambelluca et al., 2013). Understanding mean rainfall patterns is important for a variety of resource management issues in Hawai‘i, including the assessment and protection of freshwater resources and the successful management of native ecosystems. Rainfall can be highly variable from year to year; however, the long-term mean annual cycle is in agreement with the traditional understanding of the Hawaiian wet and dry seasons (Figure 2.25). As expected, the highest mean monthly precipitation occurs in the wet season and the lowest monthly values occur in the dry season (Table 2.9). For the highest elevation stations, monthly precipitation peaks in March and in December and minimums were found in May and June which correspond with the months of lowest and highest TWI frequency of occurrence, respectively (Cao et al., 2007). Windward stations are consistently wetter than leeward stations throughout the year.

Diurnal profiles are unique for both leeward and windward exposures. On the Leeward exposure, there is a distinct afternoon maximum at all of the stations in the dry season and an afternoon maximum at the three mid elevation stations in the wet season (Figure 2.26). On the windward exposure there are distinct minimums in the afternoon hours. These observations are consistent with the general rule that rainfall peaks during the night over oceans and during the afternoon over the land.

Precipitation gradients along the slopes of Haleakalā have many unique spatial characteristics (Figure 2.27). Along the leeward transect there is very little change in precipitation with elevation. This is most likely explained by the fact that the leeward transect does not follow a straight line up the mountain and also that most of the stations are located in close proximity to the same isohyets (Figure 2.1). Along the windward transect precipitation is much greater than the leeward transect and there is a consistent decreases with elevation. Windward stations run perpendicular through several isohyets along the transect. During both the dry and wet seasons, precipitation is lowest at the 960 m station positioned directly below the cloud zone (Table 2.9). The highest rainfall totals are found at HN-164 (1650 m) in the heart of the windward cloud zone. Rainfall at this station is the highest of anywhere in the State (Giambelluca et al., 2013).

2.5.9 Soil Moisture

Soil moisture (SM) is an important control on plant vitality. The moisture content of the soil depends on a number of factors including rainfall amount, soil properties, hill slope angle, plant transpiration and evaporation from the soil. Annual cycles of soil moisture are most pronounced at leeward mid-elevation stations located at or beneath the mean TWI observed throughout the dry season (Figure 2.28). For leeward stations located above the TWI, decreases in dry season soil moisture are identifiable but not as pronounced as the mid-elevation stations. For windward stations no apparent annual cycle was identified, with predominantly wet conditions observed throughout the year. For all stations, maximum values occur in the wet season and minimums occur in the dry season (Table 2.10).

Differences in soil moisture are found across the elevation gradient (Figure 2.29). Slight increases in soil moisture are found between the 960 and 1640 m leeward stations as gradients

transition into the cloud zone and steady decreases as gradients transition out of the cloud zone along the leeward transect. There is very little difference between the two highest elevation stations, which are located in areas with highly porous soils and little vegetation cover. In general, the leeward transect exhibited uniform spatial patterns with slightly higher values in the wet season. The largest difference between seasons occurs at the 2120 m station, which has the highest precipitation along the leeward transect (Figure 2.27) as well as one of the largest differences in dry and wet season precipitation among the stations (Table 2.9). For the windward transect, soil moisture decreases with increasing elevation but conditions are similar in the two seasons.

2.5.10 Soil Heat Flux

Soil heat flux (SHF) is the gain or loss of stored sensible heat energy within the soil. The rate at which this exchange occurs between the surface and the underlying soil depends on the temperature gradient and thermal conductivity of the soil (Bonan 2008). Spatial and temporal variations in soil heat flux are driven by net radiation and surface characteristics (Giambelluca et al., 2014). Annual soil heat flux (Figure 2.30) is in general agreement with expected patterns related to net radiation (Figure 2.10). In general, soil temperature increases during the warmer half of the year, which happens to correspond to the dry season in Hawai‘i, in response to a period of positive soil heat flux (Table 2.11). Similarly, the reduction of soil temperature during the cool (wet) season is a manifestation of negative soil heat flux. The annual cycle of SHF is most pronounced at the three highest elevation stations, where the highest mean monthly values occur between May and June and the lowest monthly means occur between November and December. These three stations also have the largest annual cycle for net and solar radiation. Stations located at mid elevations show annual cycles that are less pronounced. It is interesting to

note that the highest mean monthly SHF at the 2120 m station occurs in March, which corresponds directly with the month of low TWI frequency (Cao et al., 2007).

Diurnal soil heat flux (Figure 2.31) is in general agreement with expected patterns related to net radiation (Figure 2.11). Patterns are similar in the two seasons, however, the range in values is greater in the dry season, because of the higher daytime net radiation. On the leeward side of the island, the effects of clouds can be clearly identified by a marked decrease during the afternoon hours at mid elevations. For windward stations, where persistently cloudy conditions prevail (1650 to 2260 m), the diurnal cycle of SHF is the least pronounced.

2.5.11 Potential Evapotranspiration

Potential evapotranspiration (PET) is used as a metric to describe the influences that climate has on plant transpiration, wet-canopy evaporation, and soil evaporation. In any environment PET can be used as a proxy to understand plant water relations. The moisture content and temperature of the air, the intensity of the wind, and the available energy at the surface are all factors that determine the rate at which water evaporates (Dunne and Leopold, 1978). The annual cycle of PET (Figure 2.32) is similar to the annual cycle of solar radiation with the highest mean monthly values occurring in either June for the highest-elevation stations or July for the mid-elevation stations and the lowest monthly values occurring in either November or December (Table 2.12). Annual cycles are the most pronounced at the high-elevation sites located above the mean TWI where fluctuations in available energy and moisture regimens are the greatest throughout the year. Mid-elevation stations located within the cloud and sub-cloud zones experience a less pronounced annual cycle due to the consistently high humidity and damped radiation cycle.

Diurnal profiles of PET are similar to solar and net radiation profiles with low values occurring in morning, increase at sunrise, and decrease after the solar zenith hour (Figure 2.33). The increases in clouds and subsequent decrease in PET are observed at the leeward mid-elevation stations especially during the dry season when the TWI frequency is higher. Afternoon clouds limit the amount of energy received at the surface, decrease daytime temperatures, and increase the relative humidity, all of which contribute to lower PET. These effects are most notable at the 1640 m station in the heart of the leeward cloud zone.

Increases in elevation are associated with increases in PET along both windward and leeward transects (Figure 2.34). An exception to this is found at leeward station HN-106 (1640 m) where there is a slight decrease in PET is observed during the dry season. This is explained by dry season decreases in net radiation (Table 2.4) and similar relative humidity (Table 2.6) observed at the 960 m and 1640 m station, as discussed earlier. In general lower PET values are found at the mid-elevations where humidity is high and available energy is reduced by cloud attenuation of sunlight. Windward PET profiles show consistent decreases in PET with increases in elevation. The range in dry and wet season minimum and maximum mean monthly values increases with elevation above the cloud zone and the largest difference occurs at the leeward summit station (Table 2.12).

2.6 Period of Record Change in Climate Variables

The long-term (period-of-record) trends in climate variables for the eight of the HaleNet stations are shown in this section. Seasonal anomalies were assessed for six of the measured (K_d, R_n, T_a, RH, WS, and P) and three of the derived (VPD, PET, and CA) variables discussed in section 4 as well as the zero precipitation days variable (ZP; discussed in section 3.4). Data were subdivided and assessed by season, elevation and exposure to the prevailing trade winds. Mid-

elevation leeward stations include HN-119 (960 m), and HN-106 (1640 m; for P and ZP only). The mid-elevation windward station is HN-164 (1650 m). High-elevation leeward stations include HN-151 (2120 m), HN-152 (2590 m) and HN-153 (2990 m). High-elevation windward stations include HN-162 (2260 m), HN-161 (2460 m). The variables were evaluated for trends based on the period of record of data at each station (Table 2.1). Linear regression was used to characterize the behavior of climate variables over time and only time series with at least 15 years of data were used in this analysis.

Period-of-record trends in K_d vary with elevation and season (Figure 2.35). Statistically significant increases in dry season solar radiation (0.7 to 1.2 W m^{-2} yr^{-1}) were found at four of the five high- elevation stations located at or above the mean TWI base height (Table 2.13). Non-significant decreases in K_d were found below the TWI mean base height and a statistically significant decrease (-0.6 W m^{-2} yr^{-1}) is found at the leeward mid-elevation station located just below the cloud zone at HN-119 (960 m). For the wet season, regression slopes were negative at all stations except HN-151 (2120 m) station on the leeward transect and only mid-elevation station HN-164 (1650 m) on the leeward transect was identified as statistically significant (-1.2 W m^{-2} yr^{-1}). A comprehensive analysis of high-elevation, long-term trends in solar radiation can be found in Longman et al. (2014).

Period-of-record changes in CA were assessed for 7 HaleNet stations during the dry and wet seasons (Figure 2.36). For the dry season, increase in CA were identified at mid elevation station HN-119 (960 m) on the leeward transect (0.2 % yr^{-1}) and significant decreases in CA were found at HN-151 (2120), HN-152 (2590 m) and HN-153 (2990 m) at high elevation on the leeward transect (-0.2 to -0.3 % yr^{-1}) and at the windward summit station HN-161(2460 m)(-0.5

% yr^{-1}) (Table 2.15). For the wet season, increases in CA were found at all of the stations analyzed, significant at the mid elevation windward station HN-164 (1650 m)(0.4 % yr^{-1}).

Period-of-record changes in R_n were assessed for six stations during the dry season and five stations during the wet season (Figure 2.37). Decreases in R_n were found in both the dry and wet seasons. A statistically significant dry season decrease in R_n (-0.5 W m^{-2}) was identified at lowest elevation (960 m) leeward station in the network (HN-119)(Table 2.15). For the wet season statistically significant decreases in R_n were found at HN-119 (960 m), HN-151 (2120 m), and (HN-153) 2990 m (-0.8, -0.5, and -0.7 W m^{-2} yr^{-1}, respectively).

Period-of-record changes in T_a were assessed for seven stations during the wet and dry seasons (Figure 2.38). Decreases in T_a were identified at all of the stations analyzed for both dry and wet seasons (except for HN-151 (2120 m) during the dry season). Statistically significant decreases in Ta (-0.04 to -0.08˚C yr^{-1}) were identified at three windward locations and at the leeward summit station (Table 2.16). During the wet season significant decreases were identified at all of the stations (-0.02 to -0.08 ˚C yr^{-1}) except for HN-151 (2120 m).

Period-of-record changes in RH were assessed for six stations during the dry and wet seasons (Figure 2.39). For the dry season decreasing trends were identified at all elevations. Statistically significant decreases (-0.3 to -0.5% yr^{-1}) were identified at three of the four high elevation stations analyzed HN-151 (2120 m), HN-161 (2460 m) and HN-152 (2590 m)(Table 2.17). For the wet season the highest elevation stations showed an increase in RH, significant at windward station HN-161 (2460 m) (0.3 % yr^{-1}).

Period-of-record changes in VPD were assessed for six HaleNet stations during the dry and wet seasons (Figure 2.40). For the dry season increases in VPD were found at 5 of the 6 stations analyzed (Table 2.18) with a significant increases identified at HN-119 (2120 m, 0.02

mb yr^{-1}), HN-151 (2120 m, 0.04 mb yr^{-1}) and HN-152 (2590 m, 0.04 mb yr^{-1}). For the wet season, a significant increase in VPD was identified at the leeward 960 m station (0.02 mb yr^{-1}) and significant decreases were identified at HN-152 (2590 m) and HN-153 (2990 m) on the leeward transect (-0.03 and -0.05 mb yr^{-1}, respectively).

Period-of-record changes in WS were assessed for six HaleNet stations during the dry and wet seasons (Figure 2.41). During the dry season, a significant increase in wind speed was observed at the leeward summit station (0.04 m s^{-1} yr^{-1}) and slight decreases in WS were observed along the windward transect, significant at HN-162 (2260 m)(-0.05 m s^{-1} yr^{-1}; Table 2.19). For the wet season decreases in WS were observed at all of the stations except the leeward summit station at HN-153 (2990 m), significant at HN-119 (960 m; -0.02 m s^{-1} yr^{-1}) and HN-152 (2590 m; -0.04 m s^{-1} yr^{-1}) on the leeward transect and HN-162 (2260 m; -0.06 m s^{-1} yr^{-1}) on windward transect.

Period-of-record changes in P were assessed for eight HaleNet stations during the dry and wet seasons (Figure 2.42). For the dry season significant decreases in P (1.1 to 13.1 mm yr^{-1}) were identified at all of the stations except HN-119 (960 m)(Table 2.20). For the wet season, six of the eight stations analyzed show decreasing trends in P, none of which were determined to be significant.

Period-of-record changes in ZP were assessed for seven HaleNet stations during the dry season and 8 stations during the wet seasons (Figure 2.43). For the dry season, increases in ZP were identified at all of the stations except station mid elevation station HN-119 (960 m)(Table 2.21). Statistically significant increases were identified at the four leeward stations found above 1600 m (0.4 to 0.7 % yr^{-1}). For the wet season non-significant decreases in ZP were found at six of the eight stations.

Period-of-record changes in PET were assessed for four HaleNet stations during the dry and wet seasons (Figure 2.44). For the dry season, increases in PET were found along the leeward transect except at HN-119 (960 m)(Table 2.22) and significant trends were identified at the three high-elevation leeward stations HN-151 (2120 m; 0.02 mm d^{-1} yr^{-1}), HN-152 (2590 m; 0.04 mm d^{-1} yr^{-1}) and HN-153 (2990 m; 0.04 mm d^{-1} yr^{-1}). For the wet seasons, decreases in PET were identified across the leeward gradient and significant decreases were found at the lowest (HN-119, 960 m) and highest (HN-153, 2990 m) stations (-0.02 and -0.06 mm d^{-1} yr^{-1}, respectively). PET was not calculated for any of the windward stations due to limitations in available data.

2.7 Discussion

Haleakalā is one of the highest mountains of any oceanic island in the world. The eleven climate variables analyzed in this report show distinct, elevation dependent vertical profiles that are clearly influenced by the combined effects of surface topography, exposure to prevailing winds, and the presence or absence of the TWI. The presence of the TWI creates persistently clear skies conditions at the highest elevations and a moisture rich cloud zone at mid elevations along the mountain slopes. Period-of-record changes in climate are apparent across both leeward and windward gradients and are characterized in this report as the percentage of decadal changes to energy and moisture regimes over time. For the dry season, a mixed signal of changes in energy and a clear decrease in moisture was observed, most notably at the highest elevations (Table 2.23). In terms of energy, significant increases in K_d (3 to 4 % $decade^{-1}$) and decreases in CA (-2 to -5 % $decade^{-1}$) were observed at leeward and windward high-elevation sites. Changes to these parameters suggest decreases in cloud cover at high elevations. Longman et al., (2014) showed through an analysis of satellite derived cloud observations, decreases in dry season high-

elevation cloud cover amounting to 6 - 8 % per decade (1998 -2012). High elevation decreases in cloud cover are most likely explained by either increase in TWI mean frequency of occurrence and/or decreases in TWI mean base height. Reported decreases in CA and subsequent increases in K_d do not explain the observed decreases in T_a reported here. The significant decreases in T_a observed at three windward locations and the leeward summit station may be explained by localized effects such as changes to the wind patterns or they may be part of a large signal of decreased temperatures observed globally over the past ~decade (e.g England et al., 2014). Regarding moisture, a significant drying trend is apparent at all of the stations located above 1000 m. Observations indicate significant decreases in; RH (-3 to -5% decade^{-1}), and P (-3 to -8% yr^{-1}) and increases in VPD (9 to 10% decade^{-1}), PET (3 to 7% decade^{-1}) and ZP (4 to % decade^{-1} found at two or more of the five high elevation stations. In addition, the mid-elevation leeward cloud zone station (HN-106) located at 1640 m showed a significant decrease in P (-5% yr^{-1}) and an increase in ZP (7% decade^{-1}). The windward mid elevation station HN-164 also showed significant decreases in P (-3 % decade^{-1}). The general, the consistency of change among the stations and the abundance of significant trends adds confidence to the conclusion that decadal-scale drying has occurred during the dry season along both leeward and windward transects and potential increases in the TWI frequency of occurrence or changes in the base height during the dry season are possible explanation. In general, agreement was seen among the atmospheric variables analyzed (especially at the high elevation sites) regarding a trend toward dryer conditions over time. For 39 of the 63 dry season time series analyzed (62%), trends were determined to be statistically significant and for the five moisture variables analyzed at high-elevation stations, 15 of the 20 time series (75%) showed significant drying.

For the wet season, many of the climate variables showed decadal trends opposite of the dry season signal (Table 2.24). Regarding energy, decreases in available energy were identified for all of the variables at most of the stations analyzed. Decadal decreases in K_d and increases in CA were found along leeward and windward gradients with significant decreases in K_d (-12.5% decade) and CA (3.9 % decade^{-1}) identified at the mid-elevation windward station HN-164 (1650 m). Significant decreases in R_n (-4 to -8% decade^{-1}) were observed at three of the six stations analyzed and a consistent decreases in T_a (-0.2 to -0.10 °C -decade^{-1}) were found at all stations and determined to be statistically significant at all of the stations except HN-151(Table 2.16). For moisture variables a mixed signal is observed. Decreases in precipitation were observed at all of the stations but regression slopes were small (-1 to -4% decade^{-1}) and not significant. RH increased at 3 of the 4 high elevation stations (Hn151, HN-152, and HN-161) significant at windward station HN-161 (2460 m) and VPD decreased at the same three stations, significant at HN-152 (2590 m) and HN-153 (2990 m). Decreases in available energy and increases in moisture are potentially explained by a decrease in the TWI frequency of occurrence or increases in base height although significant wet season trends were less abundant compared to the dry season.

Decreases in wet season precipitation, which were not in agreement with the other moisture variables, may be explained by factors unrelated to the frequency of occurrence of the TWI. Decreases precipitation may be explained by decreases in heavy rain events (e.g. Elision Timm et. al., 2011).

Many of the changes in climate reported are potentially explained by variations in TWI frequency or base height. Cao et al., (2007) identified a statistically significant increase in TWI frequency of occurrence and a decrease in base height using data ending in year 2003. Whether

or not these trends persisted or abated over the most recent decade of observations is not clear. In addition, the drivers behind TWI variability are not clearly understood. In the subsequent chapters of this dissertation I make an attempt to answer these questions. Again, it is important to note that of the 65 time series analyzed only 22 trends were determined to be statistically significant (34%) and of the five high elevation moisture variables analyzed, a significant wetter signal was observed only at the leeward summit station (HN-153).

2.8 Conclusions

A detailed knowledge of the climate at any given elevation is critically important for a variety of resource management issues, including ground water and surface water development and protection, controlling and eradicating invasive species, protecting and restoring native ecosystems, and planning adaption strategies to address the effects of global warming (Giambelluca et al., 2014). HaleNet climate monitoring and the subsequent analyses of observed climate variability along the slopes of Haleakalā is a tool that can be used by resource mangers in their efforts to protect the native plant and animals that reside there. Also, this data can be used as a proxy to understand how other mountain ecosystems function in the State where measurements are not available. In a recent effort aimed at mapping a number of climate variables at a 250 m resolution for the entire State of Hawai‘i, Giambelluca et al. (2014) have used HaleNet data to calibrate and validate a number of climate models used in the mapping effort. In addition, the growing length of record makes the HaleNet data set increasingly valuable in understanding expected future changes to high-elevation ecosystems in Hawai‘i. Recent research endeavors that have made use of HaleNet observations have addressed changes in temperature (Giambelluca et al., 2008), moisture (Crausbay and Hotchkiss, 2010), vegetation (Krushelnycky et al., 2013, Crausbay et al., 2014), and solar radiation (Longman et al., 2014)

along the slopes of Haleakalā. Changes in moisture may affect vegetation characteristics, promote the spread of invasive species, and decrease water recharge to the aquifers. These changes are amplified by the time scales by which they are occurring. The faster the climate changes, the less time native species will have to react to these changes and the area in which these species have a competitive advantage may shrink.

Hawai‘i may prove to be highly relevant in the discussion on global climate change impacts. The HaleNet data is a resource and a tool that can help us better understand changing signals in the Earth’s climate, especially at high elevations. The atmosphere in Hawai‘i is relatively free from direct anthropogenic disturbances however the high inter-annual and inter-decadal climate variability associated with tropical island locations makes it hard to determine the driving forces behind change. The findings in this Chapter suggest that high-elevation climates in Hawai‘i are changing through time and that these changes are potentially driven by the variability of TWI frequency and/or base height. Time series assessed over ~25 year periods may not be a sufficient amount of time to identify a robust change in climate; however these types of assessments can provide valuable information used to guide future research design. Further research is needed to determine how climates are changing through time and the impacts that these changes have on high elevation ecosystems in Hawai‘i. Undoubtedly, the HaleNet data archive will be an essential tool moving forward with these and other important research questions.

Chapter 2 Tables

Table 2.1: HaleNet climate network station metadata.

Sta ID #	Sta Name	Elev (m)	Albedo	Press. (mb)	LAT	LON	Start Date	End Date	Land Cover Type
HN-119	Kula Ag	960	0.19	905	20.761	156.323	Jun-88	-	grass
HN-106	Pu'u Pahu	1640	0.13	835	20.761	156.280	Jun-88	Oct-03	pasture
HN-141	Auwahi	1240	0.14	875	20.648	156.345	Dec-00	-	dryland forest
HN-151	Park HQ	2190	0.07	789	20.763	156.251	Jun-88		shrub, basaltic outcrop
HN-152	Nene Nest	2590	0.10	747	20.741	156.249	Mar-90		cinder, sparse grass, fern
HN-153	Summit	2990	0.05	713	20.714	156.259	Mar-90	-	cinder
HN-164	Big Bog	1650	0.13	834	20.730	156.095	Jun-92	-	montane wetland
HN-163	Horseshoe Pu'u	1930	0.13	807	20.738	156.111	Jun-92	Nov-96	cloud forest
HN-142	Waikamoi	1960	0.14	804	20.777	156.225	Aug-01	Aug-03	cloud forest
HN-162	Tree Line	2260	0.13	834	20.737	156.127	Jun-92	-	cloud forest, forest line
HN-161	Pohaku Palaha	2460	0.13	758	20.734	156.143	Jun-92	-	Shrub, basaltic outcrop

Table 2.2: Mean annual cycle of solar radiation (W m^{-2}).

Sta ID	Elev	Jan	Feb	Mar	Apr	May	Jun	Jul	Aug	Sep	Oct	Nov	Dec	Annual	Dry	Wet
HN-119	960	163	181	191	210	211	219	225	220	195	175	156	153	191	207	175
HN-141	1240	159	172	184	197	198	203	206	205	194	180	162	151	184	198	171
HN-106	1640	155	169	184	170	180	178	187	185	162	153	141	143	167	174	160
HN-164	1650	138	147	146	153	179	187	191	187	176	142	124	117	157	177	138
HN-151	2120	205	227	237	259	269	280	283	268	238	213	184	187	237	259	216
HN-162	2260	186	202	207	236	263	278	268	262	227	196	164	166	221	249	193
HN-161	2460	218	241	256	289	318	331	323	318	277	244	206	194	268	302	234
HN-152	2590	220	248	274	307	331	338	328	326	281	250	211	200	276	309	243
HN-153	2990	225	259	291	337	357	367	354	344	309	270	221	208	295	333	257

yellow highlighted squares represent the maximum monthly value; blue highlighted squares represent the minimum monthly value; Annual is the average of the 12 monthly values; Dry and Wet are the average 6-month dry and wet season values.

Table 2.3: Mean annual cycle of the cloud attenuation of sunlight (%).

Sta ID	Elev	Jan	Feb	Mar	Apr	May	Jun	Jul	Aug	Sep	Oct	Nov	Dec	Annual	Dry	Wet
HN-119	960	27.2	30.0	37.9	40.1	42.9	40.9	37.7	37.1	39.3	36.2	34.1	28.0	36.0	39.0	32.9
HN-141	1240	30.6	36.0	41.3	43.2	45.3	43.6	42.2	40.9	40.5	37.2	32.7	30.4	38.7	41.6	35.7
HN-106	1640	34.1	39.1	43.8	55.6	55.3	56.4	52.1	50.7	53.9	50.3	45.1	37.0	47.8	53.1	42.4
HN-164	1650	33.3	39.6	46.7	50.3	47.6	44.8	43.7	42.5	40.6	43.2	41.0	40.5	42.8	43.7	41.9
HN-151	2120	13.7	17.9	26.4	28.3	28.8	26.0	23.6	25.5	29.3	27.6	26.0	16.8	24.2	26.8	21.5
HN-162	2260	22.6	27.6	35.6	33.1	28.6	24.3	26.3	25.6	31.3	33.2	35.1	27.3	29.2	28.2	30.2
HN-161	2460	10.3	14.9	21.4	18.7	14.4	11.1	12.6	11.3	17.2	16.6	17.1	15.2	15.1	13.9	16.3
HN-152	2590	7.2	10.6	15.2	13.8	10.4	8.9	10.5	8.8	15.3	13.3	13.5	9.9	11.5	11.2	11.7
HN-153	2990	8.5	9.7	11.8	7.3	5.6	3.7	6.1	5.9	8.8	9.5	13.2	10.5	8.4	6.6	10.2

Table 2.4: Mean annual cycle of net radiation (W m^{-2}).

Sta ID	Elev	Jan	Feb	Mar	Apr	May	Jun	Jul	Aug	Sep	Oct	Nov	Dec	Annual	Dry	Wet
HN-119	960	80	98	110	120	126	130	135	127	110	96	83	72	107	121	94
HN-141	1240	95	115	133	151	153	157	162	161	139	121	104	92	132	149	115
HN-106	1640	81	94	105	104	113	112	120	114	99	92	79	77	99	108	90
HN-164	1650	100	113	118	132	149	160	162	160	147	118	102	88	129	149	109
HN-151	2120	110	124	147	160	171	172	179	171	146	126	107	98	143	161	125
HN-162	2260	102	120	144	167	195	206	203	195	166	138	109	93	153	184	122
HN-161	2460	114	137	165	185	200	209	208	208	181	157	123	107	166	194	138
HN-152	2590	85	115	138	157	171	175	174	168	139	117	93	79	134	157	111
HN-153	2990	110	138	163	184	193	198	199	195	176	145	119	106	161	184	137

Table 2.5: Mean annual cycle of surface air temperature (°C).

Sta ID	Elev	Jan	Feb	Mar	Apr	May	Jun	Jul	Aug	Sep	Oct	Nov	Dec	Annual	Dry	Wet
HN-119	960	15.8	15.5	16.0	16.5	17.4	18.3	18.9	19.2	19.0	18.5	17.6	16.4	17.4	18.5	16.3
HN-141	1240	12.9	12.1	12.8	12.9	14.0	14.5	15.1	15.4	14.9	14.9	14.3	13.5	14.0	14.8	13.1
HN-106	1640	12.3	11.9	12.0	12.2	13.2	14.1	15.2	15.4	14.8	14.6	14.0	12.7	13.5	14.5	12.5
HN-164	1650	11.1	10.6	10.7	10.7	12.0	12.6	13.1	13.2	13.4	13.1	12.6	11.8	12.1	12.9	11.2
HN-151	2120	11.2	10.5	10.6	10.9	12.3	13.4	13.9	13.9	13.0	12.7	12.5	11.4	12.2	13.2	11.2
HN-162	2260	10.6	9.5	9.0	8.9	10.5	11.0	11.3	11.9	11.6	11.3	10.9	10.4	10.6	11.3	9.9
HN-161	2460	9.3	8.4	7.9	8.4	9.8	10.4	10.7	11.1	10.7	10.4	9.9	9.2	9.7	10.5	8.8
HN-152	2590	9.9	9.4	9.4	10.1	11.9	12.8	12.8	13.0	12.3	11.8	11.0	10.2	11.2	12.4	10.0
HN-153	2990	7.2	6.6	6.8	7.8	9.4	10.3	10.2	10.5	10.1	9.5	8.4	7.6	8.7	10.0	7.4

Table 2.6: Mean annual cycle of relative humidity (%).

Sta ID	Elev	Jan	Feb	Mar	Apr	May	Jun	Jul	Aug	Sep	Oct	Nov	Dec	Annual	Dry	Wet
HN-119	960	82.2	81.8	84.3	83.9	84.5	84.7	84.0	83.3	83.4	82.7	83.6	82.1	83.4	83.8	83.0
HN-106	1640	71.3	72.1	79.3	83.9	84.2	85.1	81.7	82.2	83.2	81.6	78.7	73.7	79.7	83.0	76.5
HN-164	1650	86.8	91.1	94.6	97.4	96.1	96.7	96.5	96.6	96.5	96.7	96.3	91.4	94.7	96.5	92.9
HN-151	2120	51.7	56.2	63.3	67.0	64.6	62.3	62.7	65.9	71.1	68.1	64.2	57.5	62.9	65.8	60.0
HN-162	2260	62.9	68.9	80.5	83.4	77.9	81.8	85.5	85.3	87.1	86.2	85.3	69.5	79.5	84.0	75.1
HN-161	2460	54.2	60.5	72.4	72.3	67.5	68.8	72.9	71.4	76.5	76.0	72.6	66.4	69.3	72.2	66.4
HN-152	2590	39.7	42.2	50.2	48.2	43.5	42.1	48.3	49.4	54.4	51.2	52.9	45.2	47.3	48.1	46.4
HN-153	2990	37.6	40.8	44.6	40.8	37.5	35.8	44.4	44.4	48.3	46.0	50.8	43.1	42.8	42.7	42.9

Table 2.7: Mean annual cycle of vapor pressure deficit (mb).

Sta ID	Elev	Jan	Feb	Mar	Apr	May	Jun	Jul	Aug	Sep	Oct	Nov	Dec	Annual	Dry	Wet
HN-119	960	2.3	2.3	2.1	2.3	2.4	2.7	2.9	3.1	3.0	2.9	2.5	2.5	2.6	2.8	2.3
HN-106	1640	2.7	2.5	1.7	1.3	1.5	1.6	2.3	2.2	1.8	1.9	2.2	2.5	2.0	1.9	2.1
HN-164	1650	1.3	0.8	0.6	0.2	0.5	0.4	0.5	0.4	0.4	0.4	0.6	0.8	0.6	0.4	0.7
HN-151	2120	4.1	3.5	2.9	2.8	3.6	4.2	4.2	3.8	2.8	3.2	3.5	3.8	3.5	3.6	3.4
HN-162	2260	3.4	2.8	1.4	1.1	2.3	1.7	1.4	1.6	1.1	1.5	1.3	2.6	1.9	1.6	2.1
HN-161	2460	3.5	2.5	1.9	2.0	2.6	2.6	2.4	2.4	2.4	2.1	2.2	2.8	2.5	2.4	2.5
HN-152	2590	4.6	4.1	3.6	4.1	5.2	5.7	5.3	5.2	4.4	4.4	3.9	4.4	4.6	5.0	4.1
HN-153	2990	3.3	3.0	2.6	3.5	4.4	4.9	4.2	4.3	4.0	3.7	3.0	3.2	3.7	4.3	3.1

Table 2.8: Mean annual cycle of wind speed (m s^{-1}).

Sta ID	Elev	Jan	Feb	Mar	Apr	May	Jun	Jul	Aug	Sep	Oct	Nov	Dec	Annual	Dry	Wet
HN-119	960	1.9	1.7	1.7	1.7	1.6	1.6	1.6	1.6	1.6	1.5	1.5	1.6	1.6	1.6	1.7
HN-141	1240	2.5	2.5	2.7	2.5	2.4	2.6	2.7	2.8	2.6	2.5	2.6	2.7	2.6	2.6	2.6
HN-106	1640	3.0	2.7	2.6	2.3	2.2	2.1	2.2	2.3	2.2	2.2	2.3	2.7	2.4	2.2	2.6
HN-164	1650	2.4	2.5	2.6	2.5	2.4	3.1	3.5	3.4	3.2	2.8	2.8	2.6	2.8	3.1	2.6
HN-151	2120	3.2	3.0	3.3	2.9	2.7	2.9	3.1	2.9	2.6	2.7	3.1	3.4	3.0	2.8	3.1
HN-162	2260	3.6	3.7	3.8	3.8	3.4	4.0	4.0	3.6	3.5	3.7	3.8	4.0	3.7	3.7	3.8
HN-161	2460	5.2	5.1	6.2	5.9	5.2	6.4	6.4	6.1	5.5	5.9	6.0	6.0	5.8	5.9	5.7
HN-152	2590	4.1	3.4	3.6	3.3	3.1	3.1	3.1	3.0	2.8	3.0	3.3	3.7	3.3	3.0	3.6
HN-153	2990	4.4	4.3	4.2	4.4	4.4	4.9	5.0	4.6	4.0	4.3	4.5	4.7	4.5	4.5	4.4

Table 2.9: Mean annual cycle of precipitation (mm).

Sta ID	Elev	Jan	Feb	Mar	Apr	May	Jun	Jul	Aug	Sep	Oct	Nov	Dec	Annual	Dry	Wet
HN-119	960	78	45	78	20	30	17	12	17	20	39	51	74	482	136	346
HN-141	1240	109	42	88	42	54	30	36	27	40	63	51	85	667	250	417
HN-106	1640	105	59	94	30	29	22	21	32	55	56	69	95	667	214	452
HN-164	1650	662	668	1059	816	569	613	686	637	666	891	1114	1063	9445	4063	5382
HN-151	2120	146	110	180	56	50	28	49	56	55	76	122	151	1078	313	765
HN-162	2260	401	414	544	369	248	261	313	278	329	403	511	536	4606	1831	2776
HN-161	2460	257	251	312	165	118	99	133	112	178	193	284	368	2469	834	1635
HN-152	2590	116	83	142	38	35	16	37	43	54	61	114	131	869	245	624
HN-153	2990	151	82	143	30	35	15	24	31	44	66	124	171	915	214	701

Table 2.10: Mean annual cycle of soil moisture (m^3 m^{-3}).

Sta ID	Elev	Jan	Feb	Mar	Apr	May	Jun	Jul	Aug	Sep	Oct	Nov	Dec	Annual	Dry	Wet
HN-119	960	0.36	0.37	0.38	0.35	0.32	0.29	0.24	0.25	0.27	0.25	0.27	0.35	0.31	0.27	0.35
HN-106	1640	0.38	0.41	0.40	0.39	0.39	0.38	0.32	0.28	0.30	0.31	0.33	0.39	0.36	0.33	0.38
HN-164	1650	0.77	0.78	0.79	0.79	0.78	0.78	0.78	0.78	0.78	0.78	0.78	0.78	0.78	0.78	0.78
HN-151	2120	0.34	0.36	0.38	0.33	0.30	0.20	0.14	0.15	0.16	0.20	0.25	0.36	0.26	0.19	0.34
HN-162	2260	0.53	0.55	0.57	0.57	0.55	0.52	0.54	0.56	0.56	0.57	0.58	0.58	0.56	0.55	0.56
HN-161	2460	0.45	0.46	0.47	0.46	0.44	0.38	0.41	0.44	0.45	0.46	0.46	0.47	0.45	0.43	0.46
HN-152	2590	0.13	0.13	0.14	0.11	0.10	0.07	0.06	0.06	0.06	0.08	0.10	0.13	0.10	0.07	0.12
HN-153	2990	0.11	0.10	0.11	0.09	0.09	0.08	0.07	0.08	0.08	0.08	0.10	0.11	0.09	0.08	0.10

Table 2.11: Mean annual cycle of soil heat flux (W m^{-2}).

Sta ID	Elev	Jan	Feb	Mar	Apr	May	Jun	Jul	Aug	Sep	Oct	Nov	Dec	Annual	Dry	Wet
HN-119	960	-1.0	-1.6	-1.0	-1.2	-1.0	-0.9	-0.6	-0.6	-1.0	-1.1	-1.1	-1.3	-1.0	-0.9	-1.2
HN-106	1640	-1.9	-2.3	-0.6	-0.7	0.3	0.2	0.4	-0.2	-1.4	-1.6	-1.9	-3.0	-1.0	-0.4	-1.7
HN-164	1650	-2.9	-2.7	-1.9	-1.9	-1.3	-1.6	-1.6	-1.9	-2.1	-2.3	-2.7	-3.0	-2.1	-1.8	-2.5
HN-151	2120	0.6	1.2	2.8	0.7	1.0	0.5	0.8	0.0	-0.2	-0.6	-1.0	-1.4	0.4	0.3	0.5
HN-162	2260	-0.1	0.3	0.5	0.6	0.5	0.1	0.1	0.1	-0.3	-0.5	-0.6	-0.7	0.0	0.0	0.0
HN-161	2460	-1.6	-0.3	1.1	2.0	2.5	2.0	2.1	1.4	0.5	-0.6	-1.8	-2.1	0.4	1.3	-0.4
HN-152	2590	-2.2	-1.9	-0.8	0.6	2.5	3.0	2.7	1.7	-0.2	-1.6	-2.7	-2.8	-0.1	1.4	-1.6
HN-153	2990	-0.5	0.4	1.3	2.0	2.8	2.5	1.8	1.4	1.0	-1.0	-1.6	-1.3	0.7	1.4	0.0

Table 2.12: Mean annual cycle of potential evapotranspiration (mm d^{-1}).

Sta ID	Elev	Jan	Feb	Mar	Apr	May	Jun	Jul	Aug	Sep	Oct	Nov	Dec	Annual	Dry	Wet
HN-119	960	2.6	3.1	3.4	3.5	3.7	3.9	4.2	4.1	3.5	3.1	2.7	2.4	3.3	3.7	2.9
HN-106	1640	3.8	3.8	3.5	3.2	3.6	3.5	4.0	3.9	3.3	3.2	3.1	3.4	3.5	3.6	3.5
HN-164	1650	2.5	2.7	2.7	2.9	3.5	3.8	3.8	3.7	3.6	2.9	2.5	2.4	3.1	3.6	2.6
HN-151	2120	5.3	5.1	5.4	5.4	5.9	6.4	6.7	6.1	5.0	4.7	4.6	4.7	5.4	5.8	5.1
HN-162	2260	4.2	4.4	4.1	4.6	5.5	5.8	5.5	5.5	4.3	3.9	3.3	4.0	4.6	5.1	4.1
HN-161	2460	5.6	5.6	5.8	6.2	7.3	7.5	6.9	7.2	6.0	5.6	4.8	4.3	6.1	6.7	5.4
HN-152	2590	5.6	5.5	5.9	6.3	7.0	7.2	7.1	6.7	5.4	5.3	4.5	4.7	5.9	6.5	5.4
HN-153	2990	6.1	6.7	7.0	8.0	8.7	9.4	8.9	8.6	7.4	7.0	6.1	6.1	7.5	8.3	6.7

Table 2.13: Temporal trends in seasonal solar radiation over the period of 1988 to 2013.

		Dry-Season					Wet-Season				
Sta.	Elev.(m)	Trend (W m^{-2} yr^{-1})	n	r^2	SE	p	Trend (W m^{-2} yr^{-1})	n	r^2	SE	p
HN119	960	-0.6	25	0.448	0.14	0.000	-0.3	25	0.079	0.24	0.174
HN164	1650	-0.2	20	0.047	0.26	0.360	-1.2	20	0.312	0.41	0.011
HN151	2120	0.8	24	0.491	0.18	0.000	0.1	23	0.009	0.19	0.663
HN162	2260	1.0	15	0.144	0.64	0.162	-1.3	18	0.131	1.08	0.140
HN161	2460	1.1	20	0.372	0.33	0.004	-0.6	16	0.146	0.41	0.145
HN152	2590	1.2	24	0.450	0.28	0.000	-0.1	23	0.000	0.26	0.701
HN153	2990	0.7	23	0.217	0.29	0.025	-0.4	21	0.021	0.26	0.172

Trend is the slope of the regression line, n is the number of seasonal values; r^2 is the coefficient of determination; SE is the standard error of the slope (same units as Trend); p is a measure of statistical significance. Note: red p-values indicated significant trends ($\alpha = 0.1$).

Table 2.14: Temporal trends in cloud attenuation of sunlight over the period of 1988 to 2013.

		Dry-Season					Wet-Season				
Sta.	Elev.(m)	Trend (% yr^{-1})	n	r^2	SE	p	Trend (% yr^{-1})	n	r^2	SE	p
HN119	960	0.2	23	0.383	0.05	0.002	0.1	24	0.074	0.10	0.197
HN164	1650	0.0	19	0.000	0.10	0.978	0.4	17	0.254	0.17	0.039
HN151	2120	-0.2	23	0.396	0.06	0.001	0.2	24	0.033	0.20	0.394
HN162	2260	-0.2	15	0.099	0.19	0.254	0.4	18	0.20	0.21	0.065
HN161	2460	-0.5	18	0.417	0.14	0.004	0.2	17	0.048	0.20	0.400
HN152	2590	-0.3	22	0.350	0.09	0.004	0.2	22	0.056	0.17	0.291
HN153	2990	-0.2	21	0.198	0.09	0.043	0.1	21	0.003	0.26	0.817

Table 2.15: Temporal trends in seasonal net radiation over the period of 1988 to 2013.

		Dry-Season					Wet-Season				
Sta.	Elev.(m)	Trend (W m^{-2} yr^{-1})	n	r^2	SE	p	Trend (W m^{-2} yr^{-1})	n	r^2	SE	p
HN119	960	-0.5	22	0.187	0.22	0.045	-0.8	24	0.423	0.19	0.001
HN164	1650	-0.3	18	0.111	0.26	0.177		14			
HN151	2120	-0.3	20	0.051	0.27	0.339	-0.5	19	0.182	0.27	0.069
HN162	2260		14				-0.4	15	0.037	0.59	0.492
HN161	2460	-0.6	15	0.064	0.61	0.362		12			
HN152	2590	0.1	22	0.004	0.35	0.783	-0.3	22	0.057	0.30	0.285
HN153	2990	-0.4	21	0.089	0.33	0.188	-0.7	21	0.244	0.28	0.023

Table 2.16: Temporal trends in seasonal air temperature over the period of 1988 to 2013.

		Dry-Season					Wet-Season				
Sta.	Elev.(m)	Trend (˚C yr^{-1})	n	r^2	SE	p	Trend (˚C yr^{-1})	n	r^2	SE	p
HN119	960	-0.05	25	0.255	0.02	0.010	-0.03	24	0.134	0.02	0.078
HN164	1650	-0.08	17	0.456	0.02	0.003	-0.04	17	0.193	0.02	0.078
HN151	2120	0.01	21	0.007	0.02	0.726	-0.02	24	0.131	0.01	0.082
HN162	2260	-0.05	16	0.443	0.02	0.005	-0.02	18	0.050	0.02	0.373
HN161	2460	-0.04	20	0.277	0.02	0.017	-0.05	17	0.241	0.02	0.045
HN152	2590	-0.01	22	0.039	0.01	0.381	-0.06	23	0.345	0.02	0.003
HN153	2990	-0.04	23	0.347	0.01	0.003	-0.08	22	0.437	0.02	0.001

Table 2.17: Temporal trends in seasonal relative humidity over the period of 1988 to 2013.

		Dry-Season					Wet-Season				
Sta.	Elev.(m)	Trend (% yr^{-1})	n	r^2	SE	p	Trend (% yr^{-1})	n	r^2	SE	p
HN119	960	-0.1	25	0.117	0.08	0.095	-0.2	24	0.346	0.06	0.003
HN164	1650	0.0	17	0.017	0.05	0.621	0.1	16	0.094	0.10	0.248
HN151	2120	-0.3	22	0.332	0.09	0.005	-0.1	24	0.007	0.14	0.708
HN162	2260		13					14			
HN161	2460	-0.3	20	0.244	0.13	0.027	0.3	17	0.180	0.16	0.090
HN152	2590	-0.5	23	0.345	0.15	0.003	0.1	23	0.023	0.19	0.488
HN153	2990	-0.3	23	0.120	0.17	0.105	0.4	22	0.129	0.21	0.101

Table 2.18: Temporal trends in vapor pressure deficit over the period of 1988 to 2013.

		Dry-Season					Wet-Season				
Sta.	Elev.(m)	Trend (mb yr^{-1})	n	r^2	SE	p	Trend (mb yr^{-1})	n	r^2	SE	p
HN119	960	0.02	23	0.242	0.01	0.017	0.02	24	0.354	0.01	0.002
HN164	1650	0.00	17	0.005	0.01	0.796	-0.01	16	0.053	0.01	0.389
HN151	2120	0.04	21	0.331	0.01	0.006	0.00	24	0.001	0.01	0.867
HN162	2260		12					13			
HN161	2460	0.02	20	0.130	0.01	0.118	-0.03	17	0.127	0.02	0.161
HN152	2590	0.04	22	0.227	0.02	0.025	-0.03	23	0.092	0.02	0.160
HN153	2990	0.01	23	0.011	0.01	0.637	-0.05	22	0.274	0.02	0.013

Table 2.19: Temporal trends in seasonal wind speed over the period of 1988 to 2013.

		Dry-Season					Wet-Season				
Sta.	Elev.(m)	Trend (m s^{-1} yr^{-1})	n	r^2	SE	p	Trend (m s^{-1} yr^{-1})	n	r^2	SE	p
HN119	960	-0.01	24	0.092	0.01	0.150	-0.02	24	0.265	0.01	0.010
HN164	1650		14					14			
HN151	2120	0.00	21	0.002	0.01	0.851	-0.01	22	0.060	0.01	0.272
HN162	2260	-0.05	18	0.652	0.01	0.000	-0.05	19	0.396	0.02	0.004
HN161	2460	-0.02	19	0.069	0.01	0.276	-0.03	16	0.092	0.03	0.255
HN152	2590	-0.02	22	0.200	0.01	0.037	-0.04	21	0.389	0.01	0.003
HN153	2990	0.04	22	0.514	0.01	0.000	0.02	22	0.050	0.01	0.318

Table 2.20: Temporal trends in seasonal precipitation over the period of 1988 to 2013.

		Dry-Season					Wet-Season				
Sta.	Elev.(m)	Trend (mm yr^{-1})	n	r^2	SE	p	Trend (mm yr^{-1})	n	r^2	SE	p
HN119	960	0.3	24	0.018	0.44	0.531	-0.4	24	0.006	0.94	0.713
HN106	1640	-1.1	21	0.178	0.53	0.057	-1.6	21	0.067	1.37	0.257
HN164	1650	-13.1	18	0.274	5.34	0.026	5.5	17	0.020	9.85	0.586
HN151	2120	-1.5	21	0.213	0.65	0.035	-2.4	24	0.081	1.73	0.179
HN162	2260	-5.8	17	0.202	2.96	0.070	0.6	19	0.001	4.36	0.897
HN161	2460	-3.1	21	0.168	1.59	0.065	-0.4	17	0.001	3.14	0.893
HN152	2590	-1.0	23	0.140	0.53	0.078	-1.8	23	0.039	1.95	0.367
HN153	2990	-1.7	21	0.175	0.83	0.059	-2.4	22	0.047	2.38	0.334

Table 2.21: Temporal trends in zero precipitation days over the period of 1988 to 2013.

		Dry-Season					Wet-Season				
Sta.	Elev.(m)	Trend (% yr^{-1})	n	r^2	SE	p	Trend (% yr -1)	n	r^2	SE	p
HN119	960	-0.1	23	0.031	0.10	0.425	-0.1	24	0.017	0.19	0.542
HN106	1640	0.7	19	0.590	0.14	0.000	0.2	20	0.071	0.20	0.257
HN164	1650	0.0	17	0.004	0.10	0.818	0.0	16	0.004	0.22	0.826
HN151	2120	0.5	21	0.244	0.20	0.023	-0.1	23	0.012	0.22	0.620
HN162	2260		14				-0.3	16	0.091	0.29	0.256
HN161	2460	0.1	18	0.019	0.24	0.583	-0.4	15	0.110	0.28	0.227
HN152	2590	0.5	22	0.190	0.23	0.042	-0.2	22	0.026	0.26	0.475
HN153	2990	0.4	20	0.221	0.20	0.037	-0.2	22	0.039	0.26	0.380

Table 2.22 Temporal trends in potential evapotranspiration over the period of 1988 to 2011.

		Dry-Season					Wet-Season				
Sta.	Elev.(m)	Trend (mm d^{-1} yr^{-1})	n	r^2	SE	p	Trend (mm d^{-1} yr^{-1})	n	r^2	SE	p
HN119	960	-0.01	19	0.079	0.01	0.243	-0.02	19	0.345	0.01	0.008
HN164	1650		8					8			
HN151	2120	0.02	18	0.168	0.01	0.092	-0.01	17	0.011	0.02	0.689
HN162	2260		10					10			
HN161	2460		14					11			
HN152	2590	0.04	19	0.268	0.02	0.014	-0.02	19	0.066	0.02	0.288
HN153	2990	0.06	19	0.256	0.02	0.023	-0.05	21	0.208	0.02	0.038

Table 2.23 Percentage changes in all dry season climate variables.

Trend decade^{-1}		ENERGY				MOISTURE				
Dry-Season		KD	CA	RN	WS	RH	VPD	P	ZP	PET
Sta.	Elev.(m)	%	%	%	%	%	%	%	%	%
HN119	960	-2.8	1.7	-4.0	-6.3	-1.3	8.3	2.1	-0.8	-3.0
HN106	1640							-5.0	7.2	
HN164	1650	-1.4		-1.8		-0.2	3.8	-3.2	0.2	
HN151	2120	3.0	-2.1	-1.6	0.5	-3.0	10.4	-4.7	5.0	3.3
HN162	2260	4.0	-2.3		-14.6			-3.1		
HN161	2460	3.6	-4.6	-3.0	-2.6	-3.2	8.7	-3.7	1.3	
HN152	2590	3.9	-2.8	0.6	-6.6	-5.0	8.9	-4.0	5.0	6.3
HN153	2990	2.0	-2.0	-2.4	9.5	-2.9	1.7	-7.8	4.4	6.7

Where, K_d is the solar radiation; CA is daytime cloud attenuation of sunlight; R_n is net radiation; WS is wind speed; RH is relative humidity; VPD is vapor pressure deficit; P is precipitation; ZP is zero precipitation days;; PET is potential evapotranspiration; Blue shaded cells decreases in energy and increases in moisture and Orange shaded cells indicate increases in energy and decreases in moisture; All decadal trends are presented in units of % and significant ($\alpha = 0.1$).

Table 2.24 Percentage changes in all wet season climate variables.

Trend decade-1		ENERGY				MOISTURE				
Wet-Season		KD	CA	RN	WS	RH	VPD	P	ZP	PET
Sta.	Elev.(m)	%	%	%	%	%	%	%	%	%
HN119	960	-3.8	1.3	-8.3	-12.0	-1.9	9.9	-1.0	-1.2	-6.8
HN106	1640							-3.5	2.4	
HN164	1650	-12.5	3.9	-1.1		1.2	-12.6	1.0	-0.5	
HN151	2120	2.0	1.8	-4.2	-2.7	-0.5	0.7	-3.1	-1.1	-1.3
HN162	2260	-17.9	4.2	-3.4	-13.3			0.2	-3.4	
HN161	2460	-9.5	1.7		-5.9	3.0	-11.0	-0.3	-3.6	
HN152	2590	-2.2	1.8	-2.9	-10.4	1.3	-7.3	-2.9	-1.9	-4.2
HN153	2990	-8.6	0.6	-5.1	3.5	3.6	-15.5	-3.4	-2.3	-7.5

Chapter 2 Figures

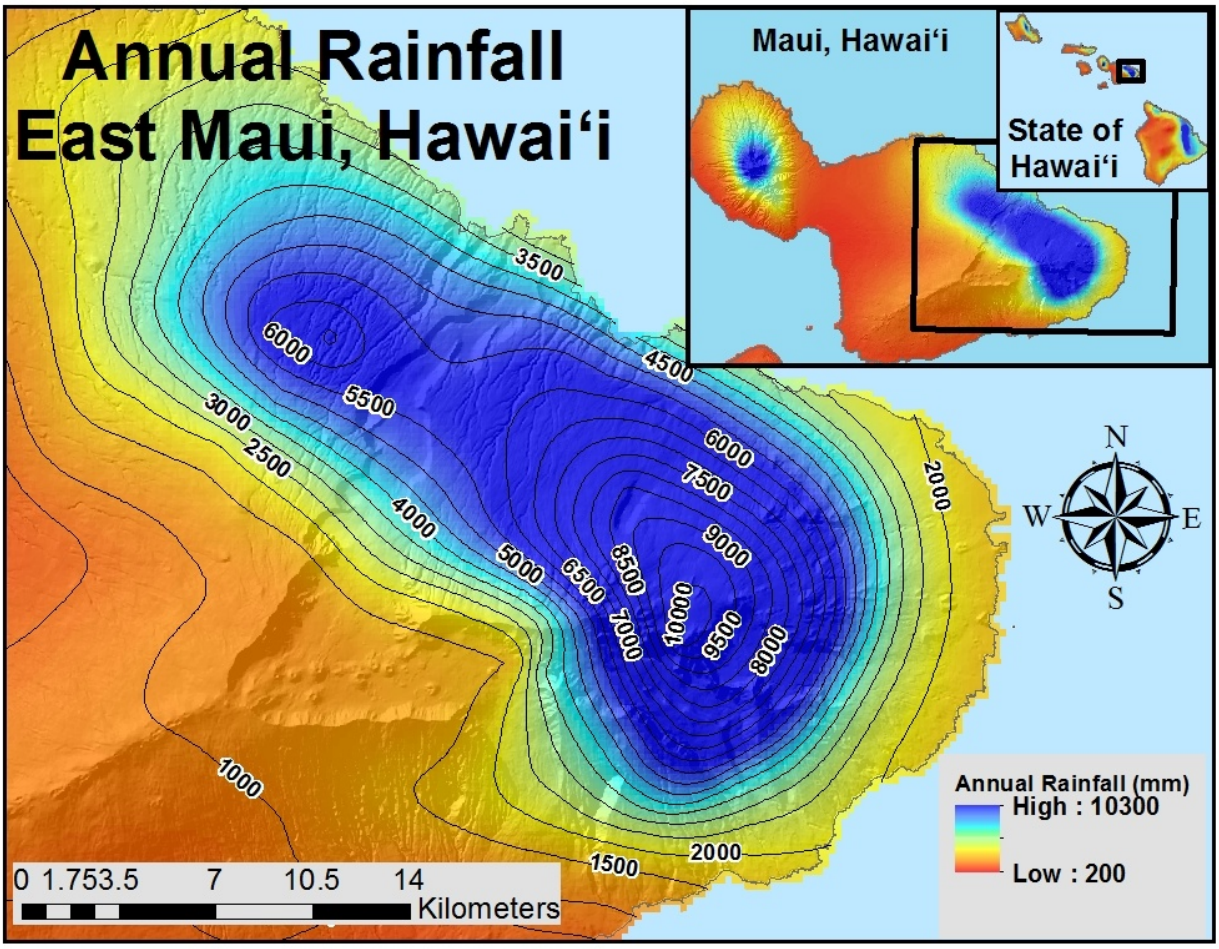

Figure 2.1: East Maui mean annual rainfall.

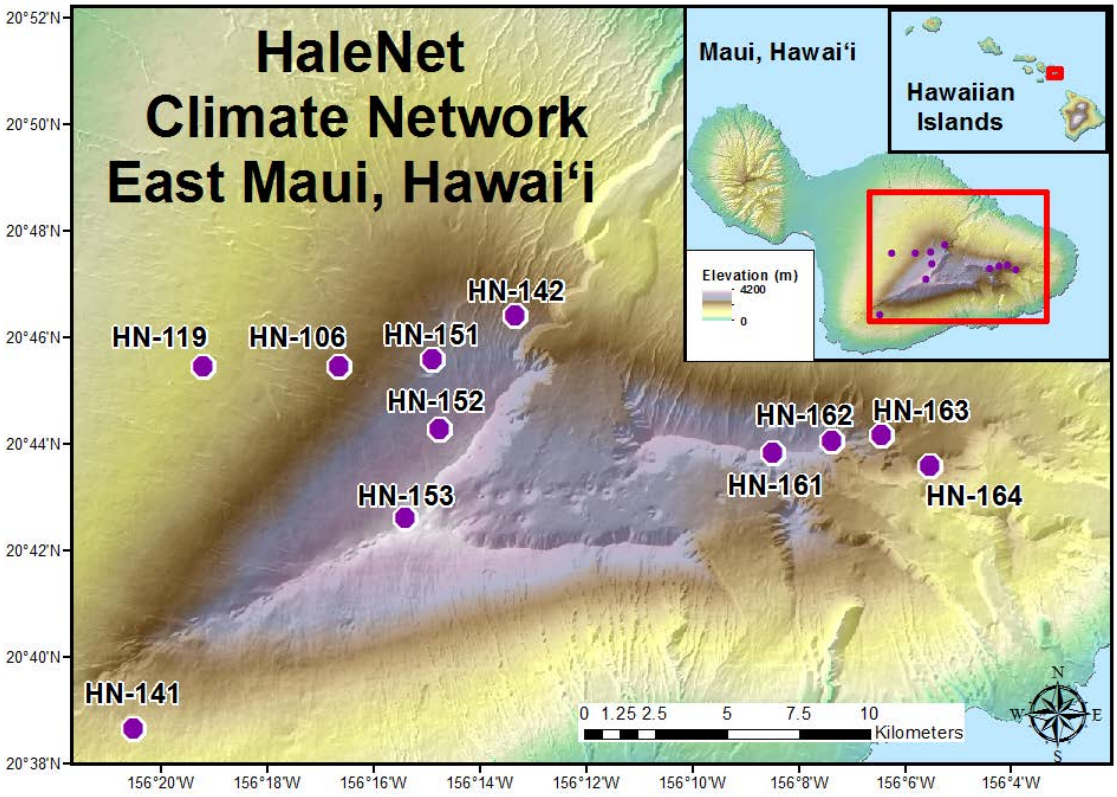

Figure 2.2: The HaleNet Climate Network, East Maui, HI.

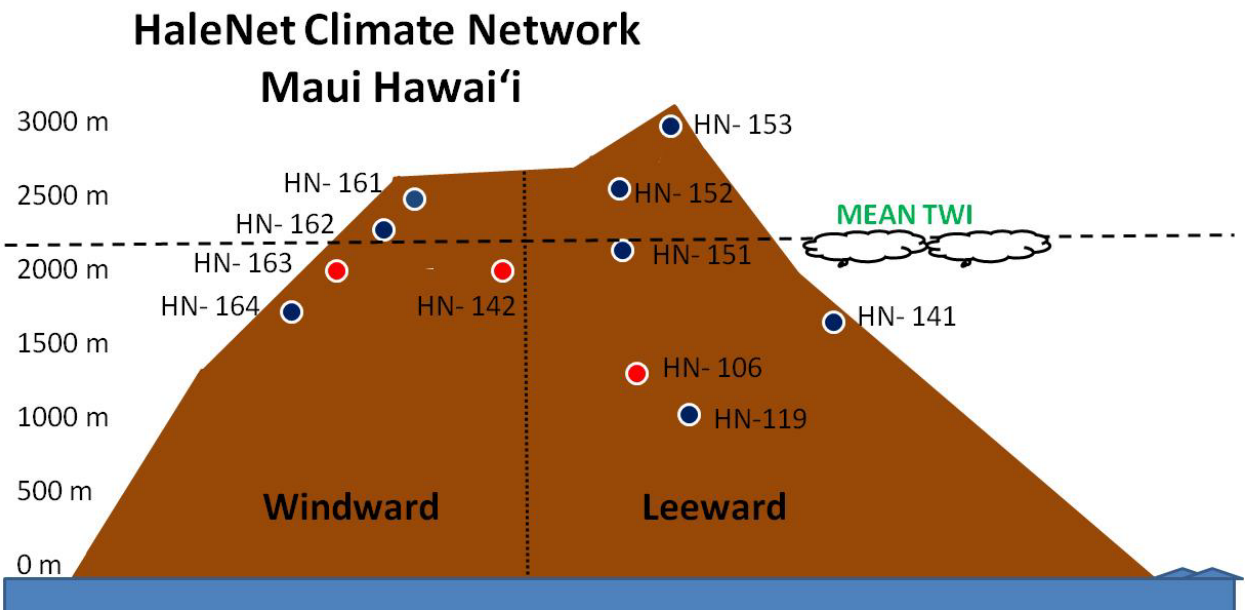

Figure 2.3: Vertical Profile of the HaleNet climate network. Maui Hawai‘i; horizontal orientation of the stations and island topography are not to scale; blue Dots indicate stations that are in full operation; red dots indicate stations that are in partial operation or not operating

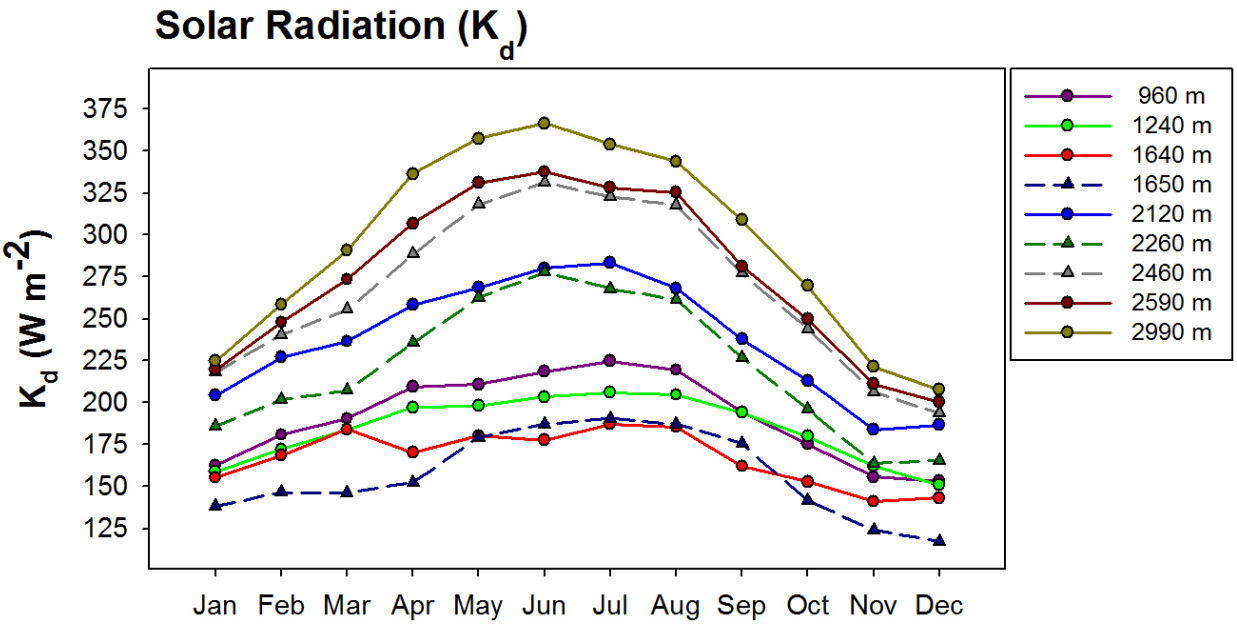

Figure 2.4: Mean annual cycle of solar radiation; solid lines with a circle symbol indicate leeward stations; dashed lines with a triangle symbol indicate windward stations.

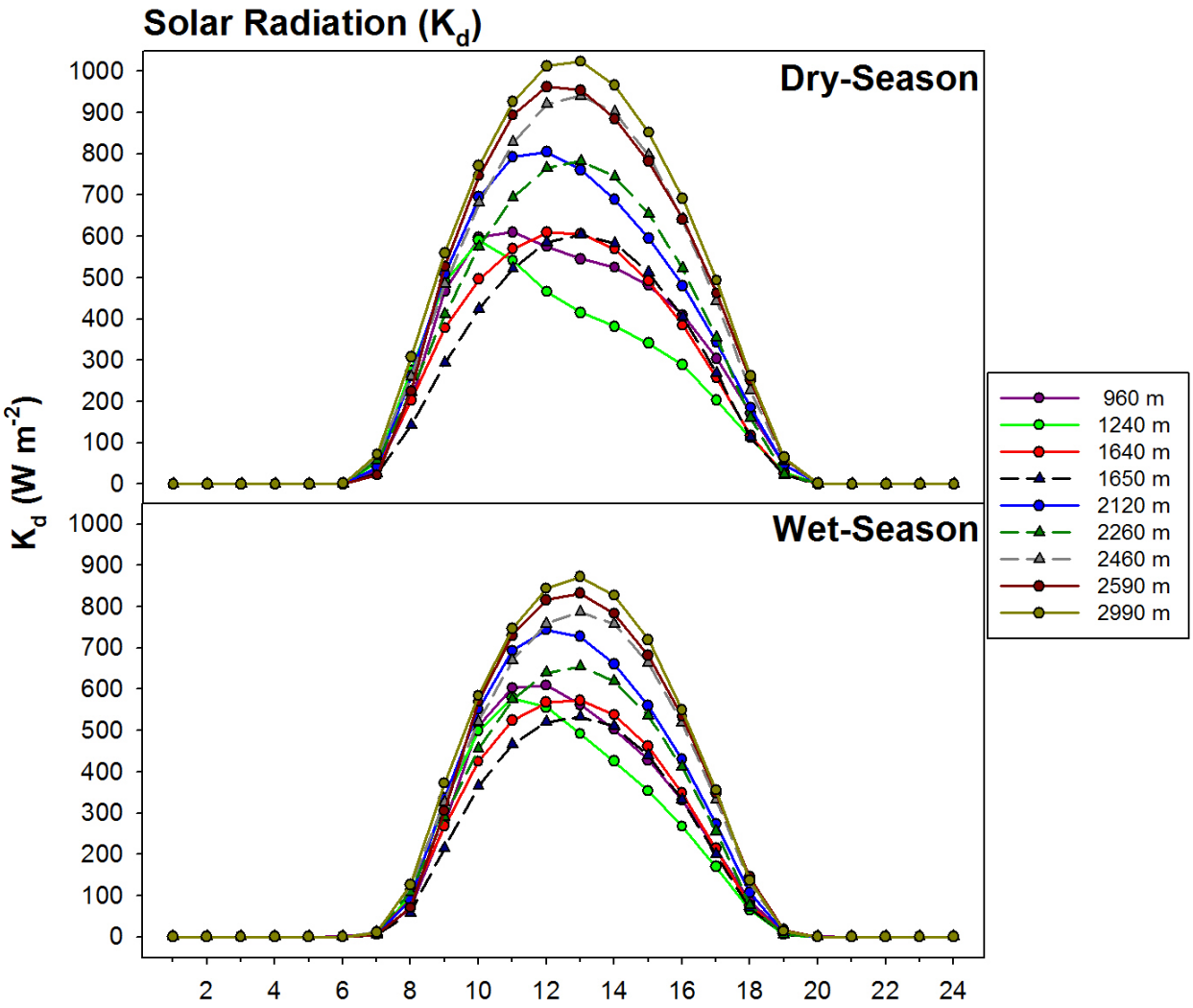

Figure 2.5: Diurnal cycles of solar radiation for the dry (top) and wet (bottom) season; solid lines with a circle symbol indicate leeward stations; dashed lines with a triangle symbol indicate windward stations.

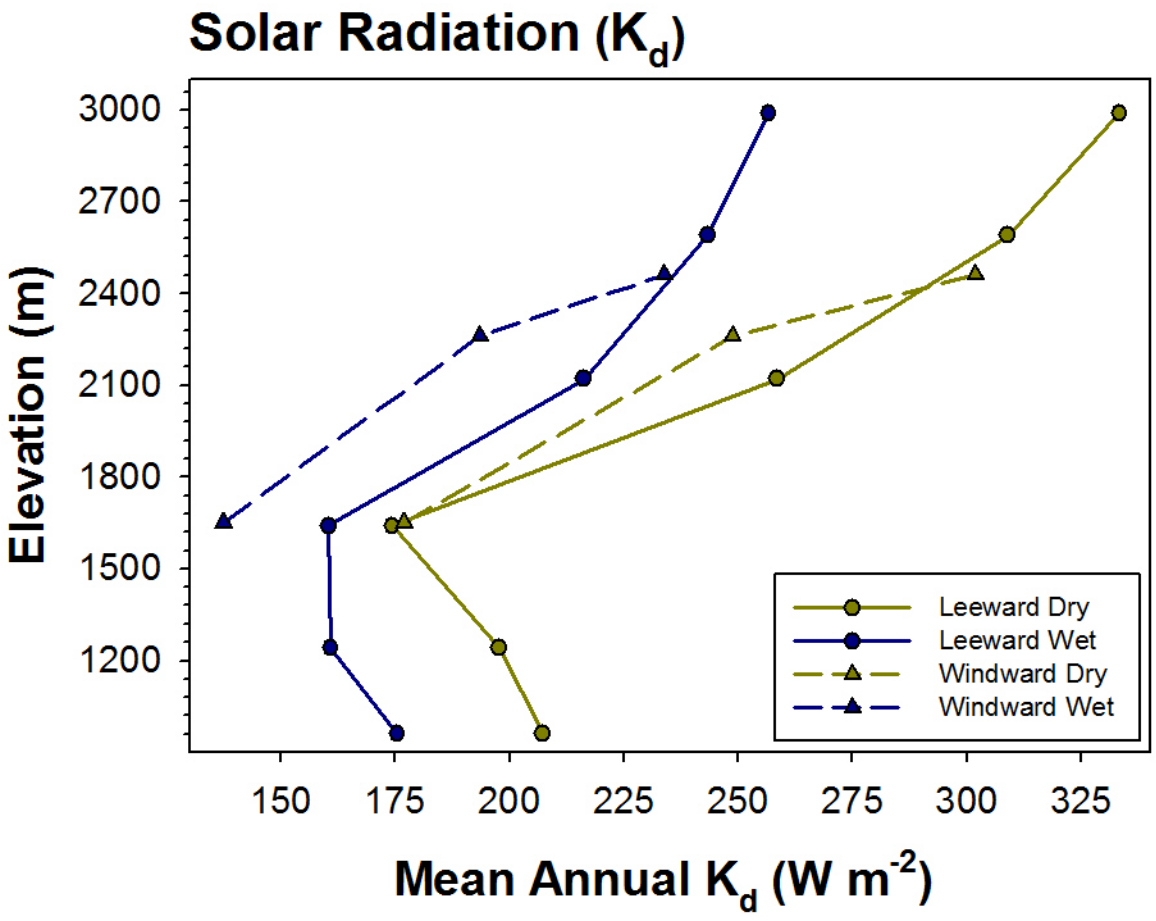

Figure 2.6: Vertical profiles of mean annual solar radiation along leeward (solid line, circle marker) and windward (dashed line, triangle marker) elevation transects for dry (yellow) and wet (blue) seasons.

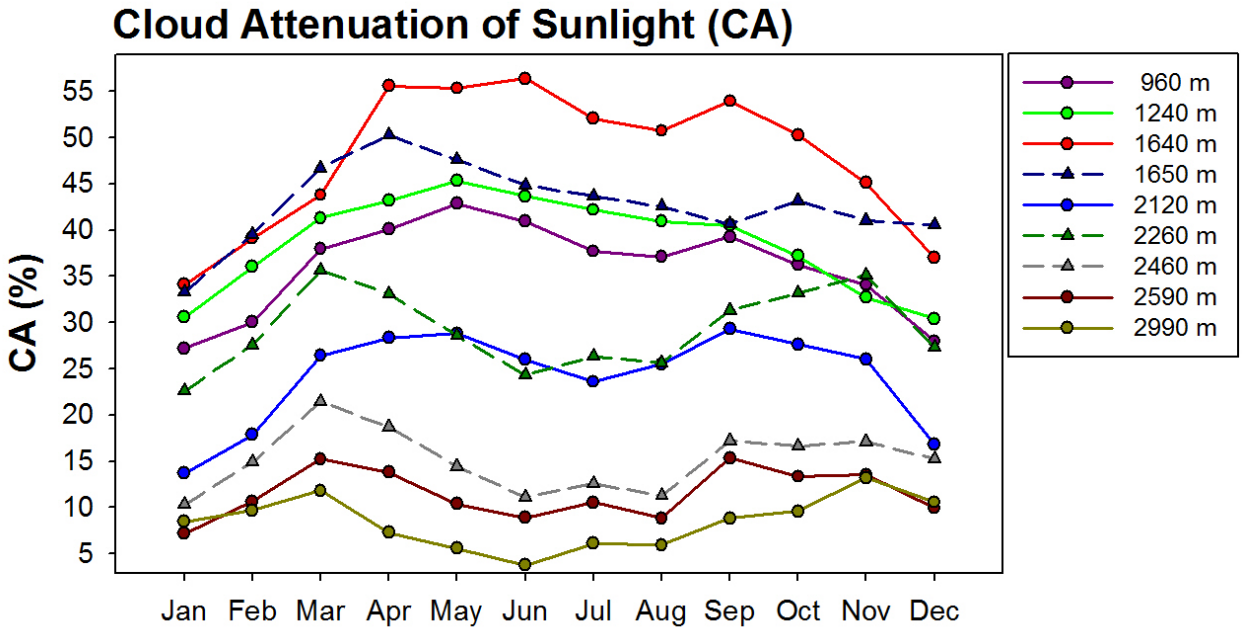

Figure 2.7: Mean annual cycle of daytime cloud attenuation of sunlight; solid lines with a circle symbol indicate leeward stations; dashed lines with a triangle symbol indicate windward stations.

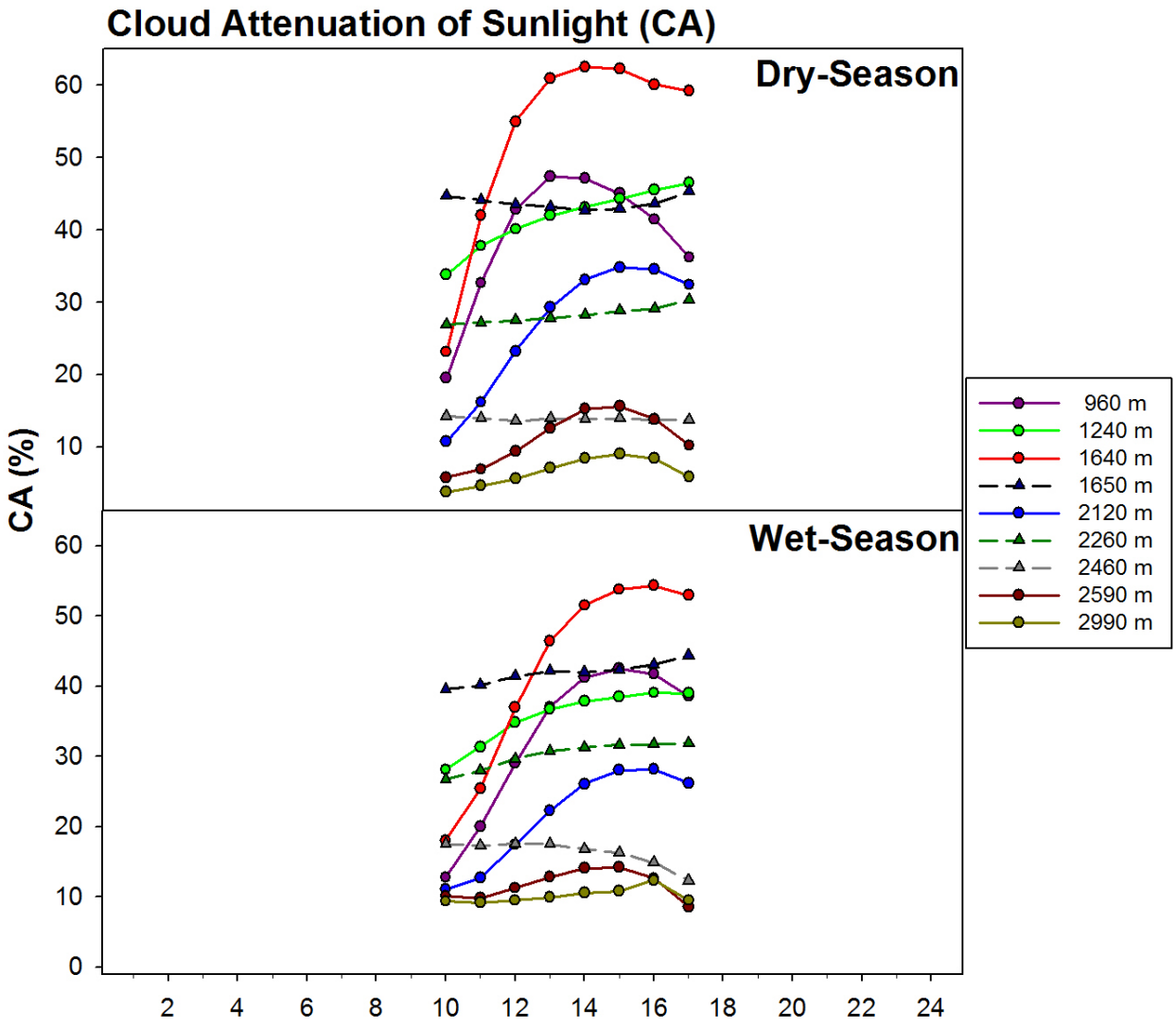

Figure 2.8: Diurnal cycles of cloud attenuation of sunlight for the dry (top) and wet (bottom) season; solid lines with a circle symbol indicate leeward stations; dashed lines with a triangle symbol indicate windward stations.

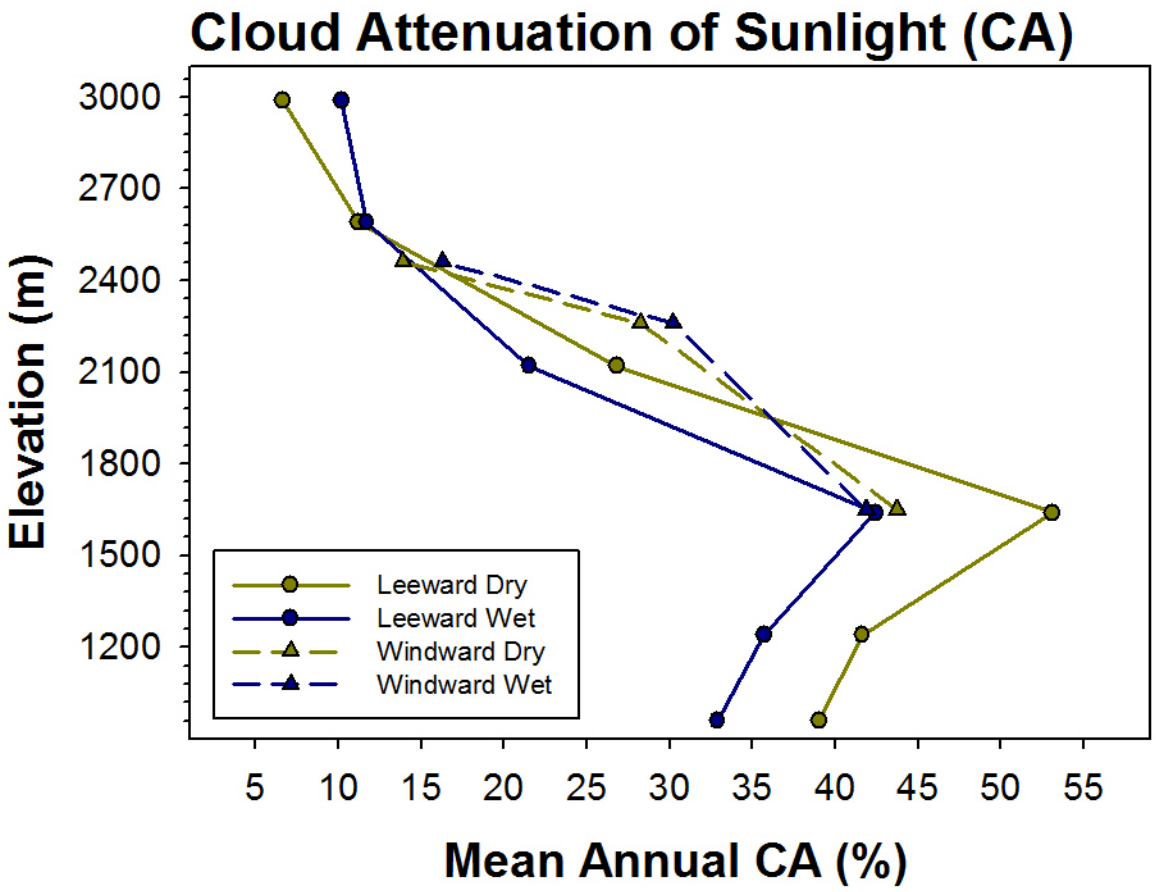

Figure 2.9: Vertical profiles of mean annual daytime cloud attenuation of sunlight along leeward (solid line, circle marker) and windward (dashed line, triangle marker) elevation transects, or dry (yellow) and wet (blue) seasons.

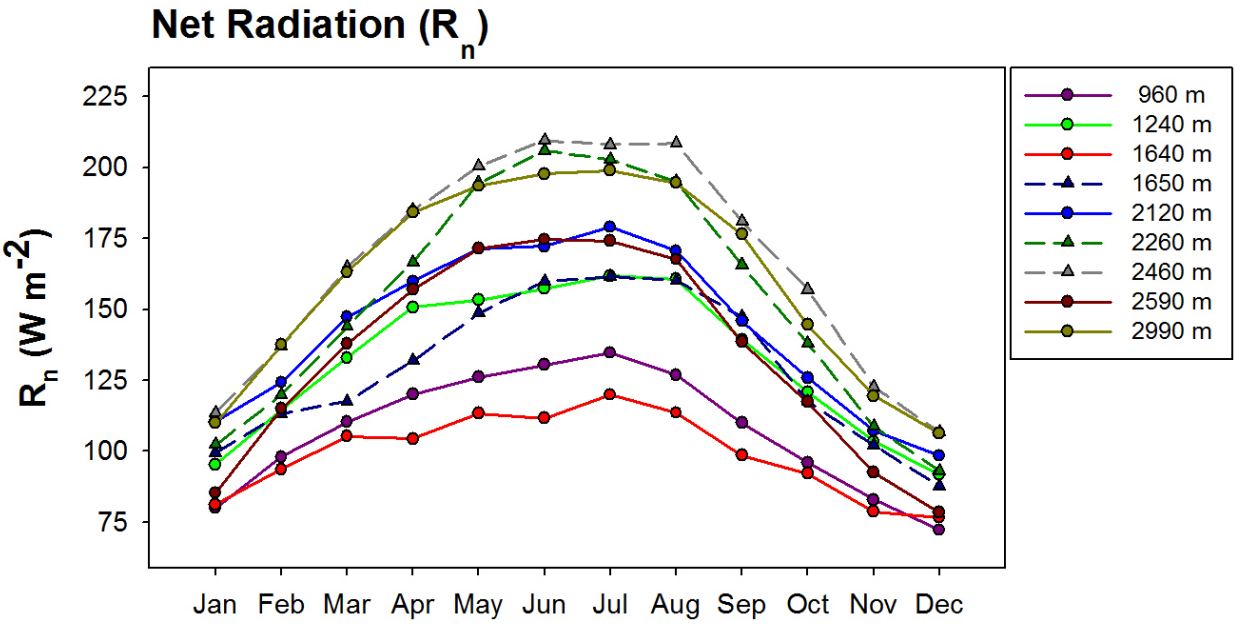

Figure 2.10: Mean annual cycle of net radiation solid lines with a circle symbol indicate leeward stations; dashed lines with a triangle symbol indicate windward stations.

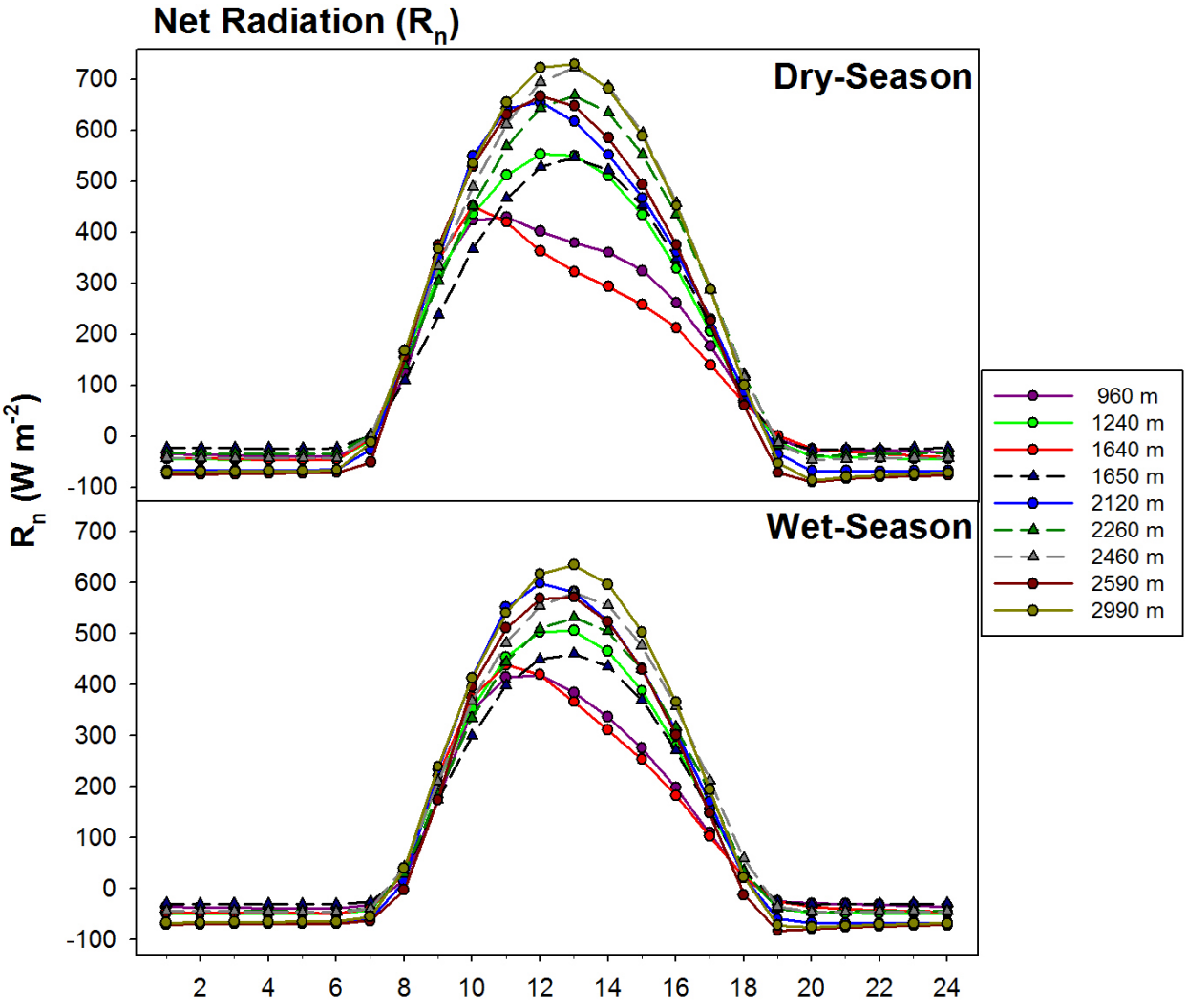

Figure 2.11: Diurnal cycles of net radiation for the dry (top) and wet (bottom) season; solid lines with a circle symbol indicate leeward stations; dashed lines with a triangle symbol indicate windward stations.

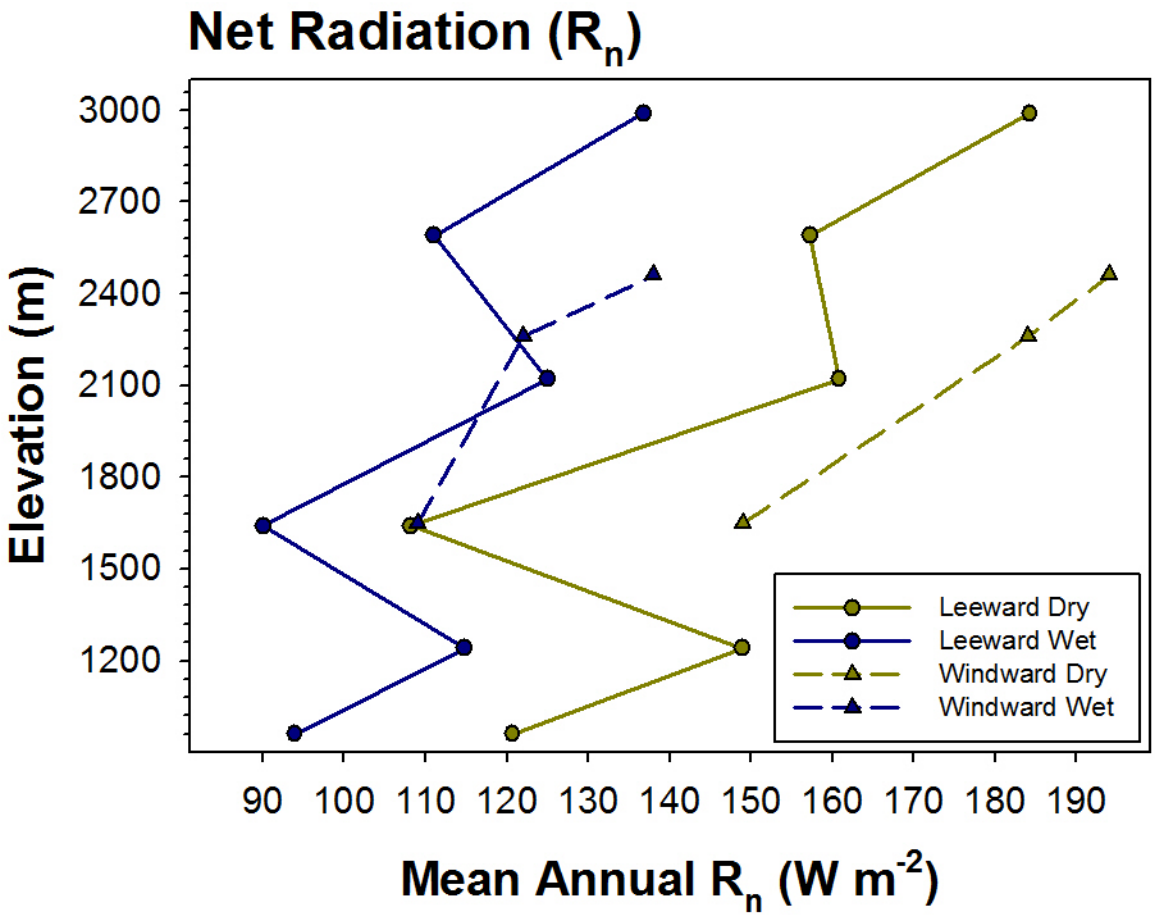

Figure 2.12: Vertical profiles of mean annual net radiation along leeward (solid line, circle marker) and windward (dashed line, triangle marker) elevation transects, or dry (yellow) and wet (blue) seasons.

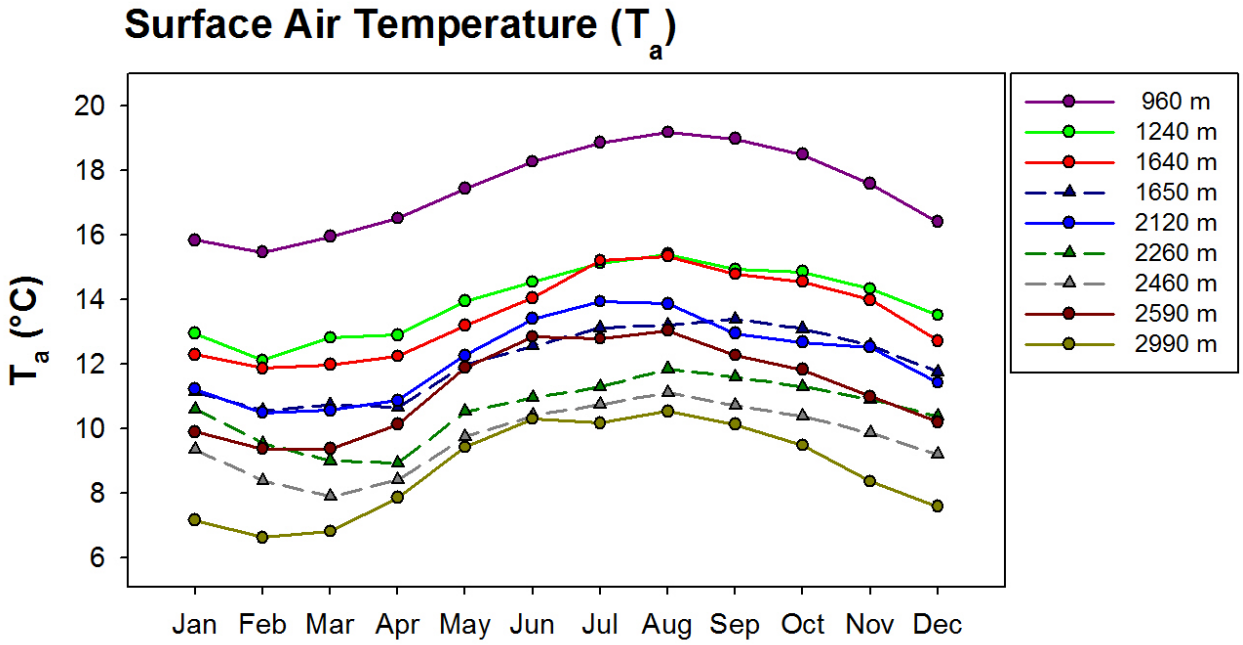

Figure 2.13: Mean annual cycle of surface air temperature
solid lines with a circle symbol indicate leeward stations;
dashed lines with a triangle symbol indicate windward stations.

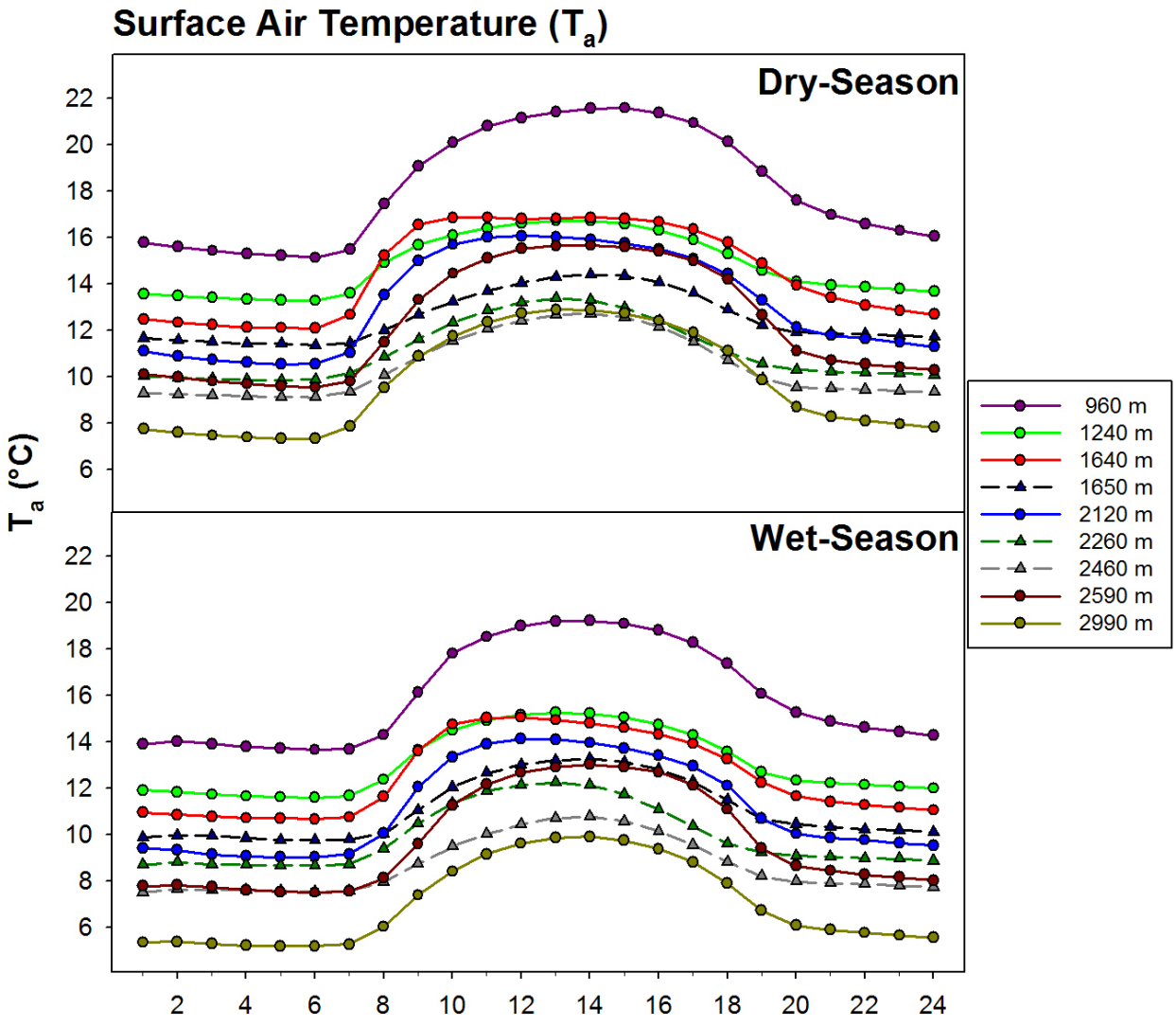

Figure 2.14: Diurnal cycles of surface air temperature for the dry (top) and wet (bottom) season; solid lines with a circle symbol indicate leeward stations; dashed lines with a triangle symbol indicate windward stations

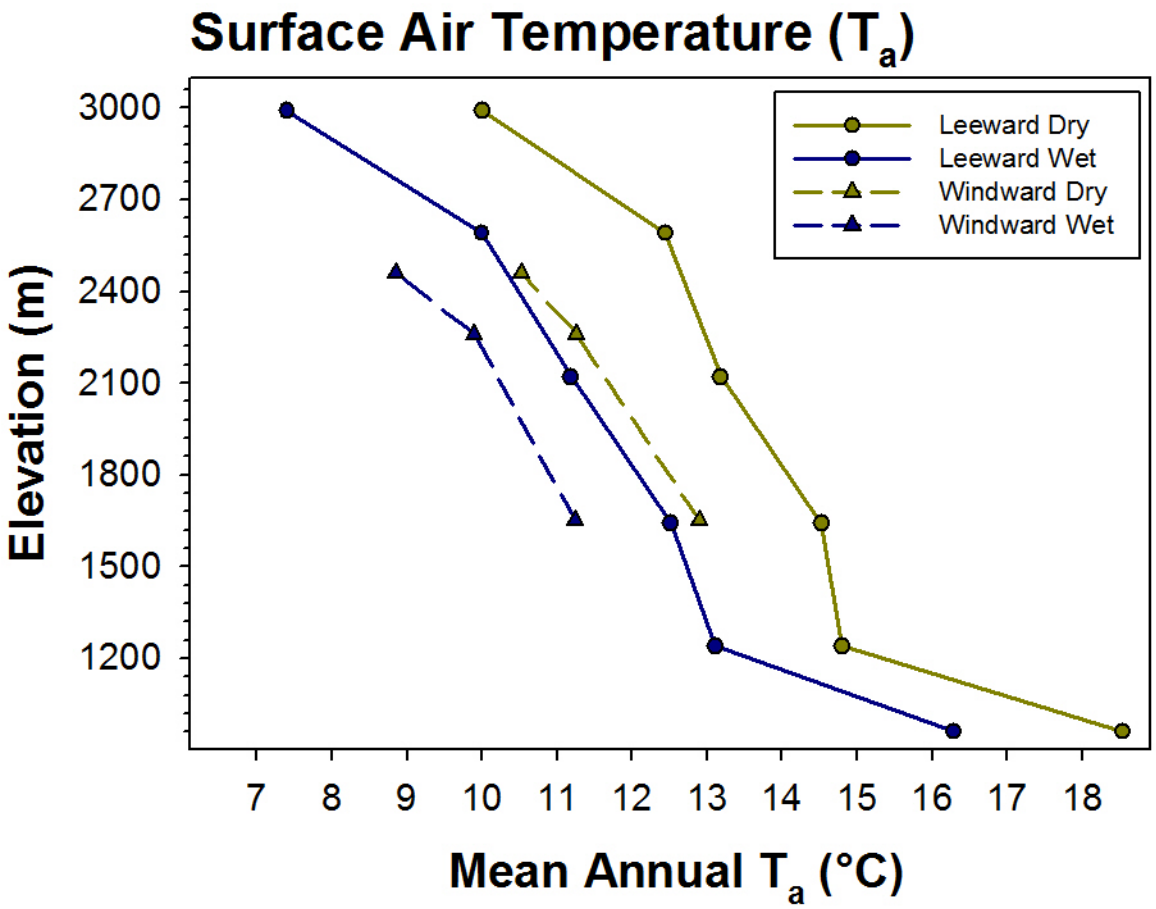

Figure 2.15: Vertical profiles of mean annual surface air temperature along leeward (solid line, circle marker) and windward (dashed line, triangle marker) elevation transects, or dry (yellow) and wet (blue) seasons.

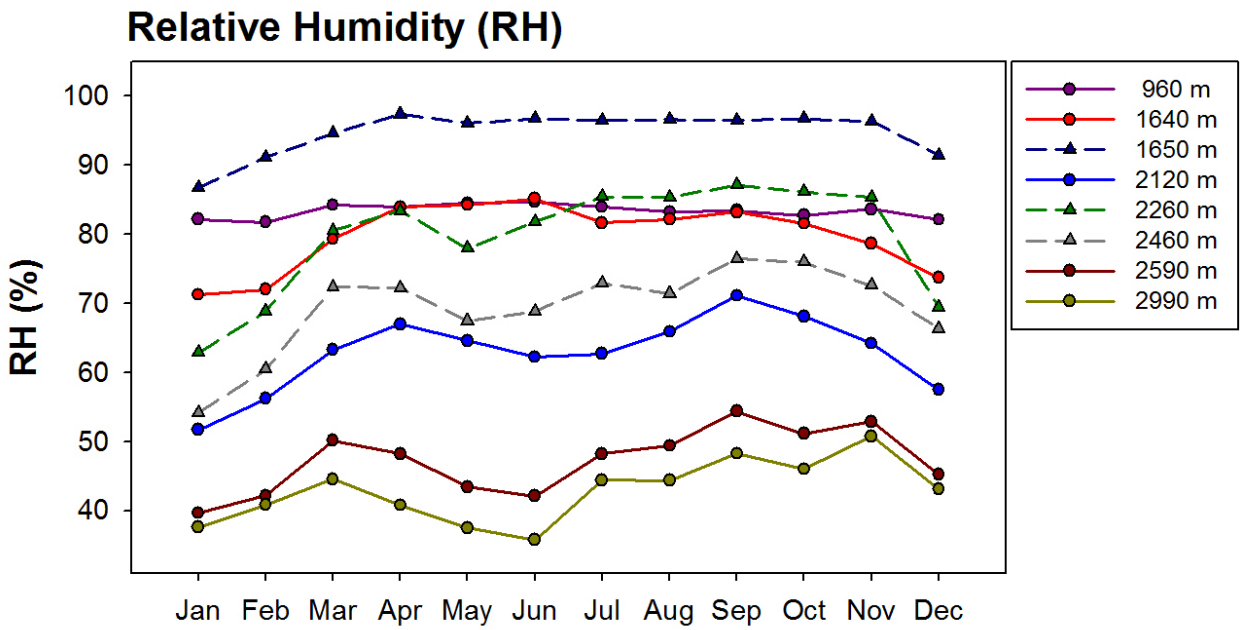

Figure 2.16: Mean annual relative humidity solid lines with a circle symbol indicate leeward stations; dashed lines with a triangle symbol indicate windward stations.

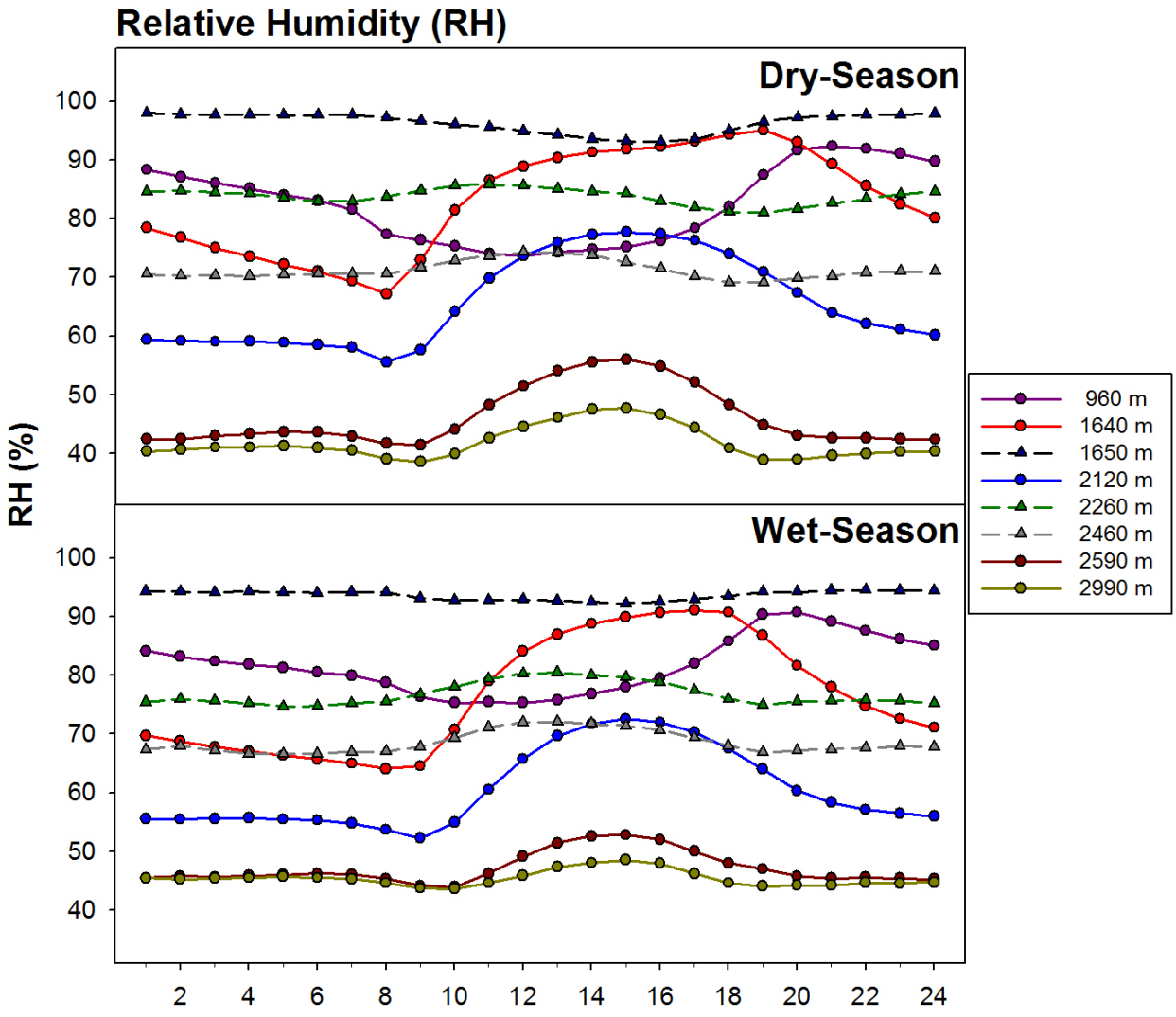

Figure 2.17: Diurnal cycles of relative humidity for the dry(top) and wet (bottom) season; solid lines with a circle symbol indicate leeward stations; dashed lines with a triangle symbol indicate windward stations.

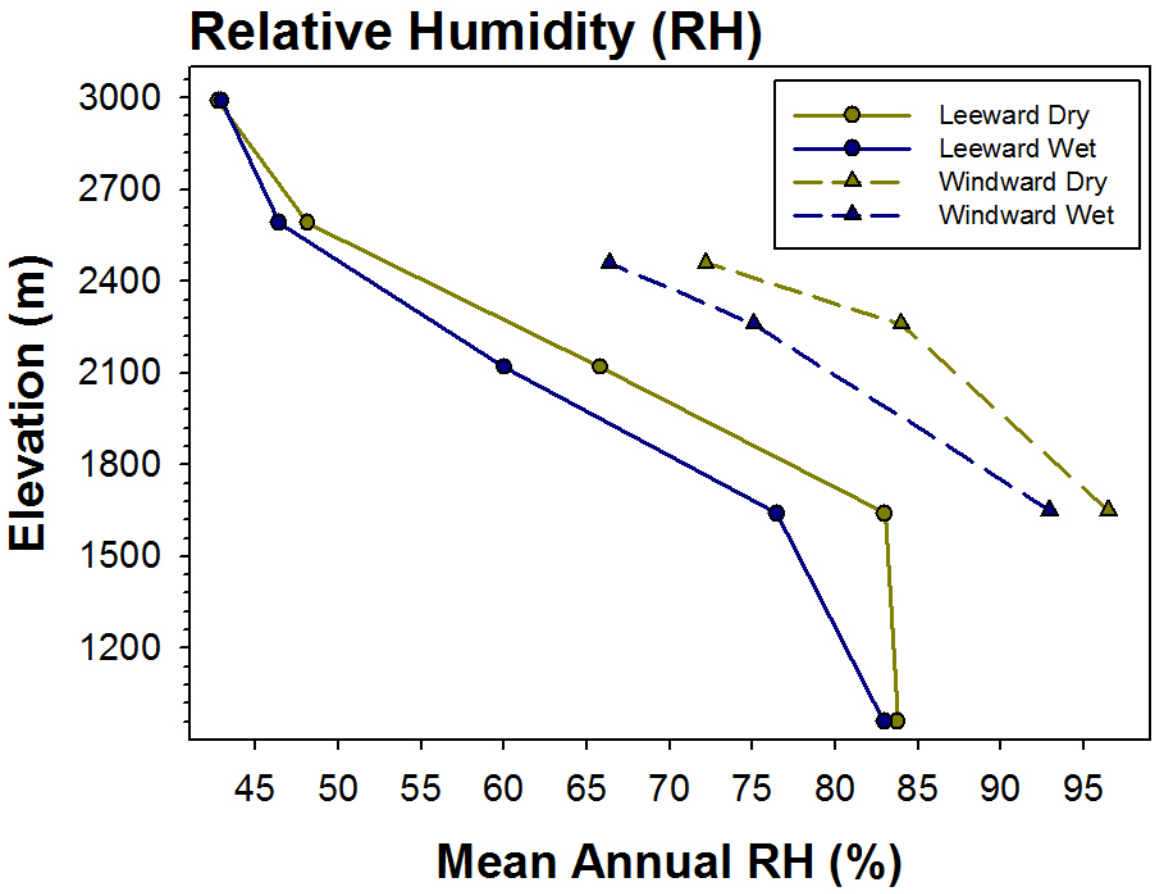

Figure 2.18: Vertical profiles of mean annual relative humidity along leeward (solid line, circle marker) and windward (dashed line, triangle marker) elevation transects, or dry (yellow) and wet (blue) seasons.

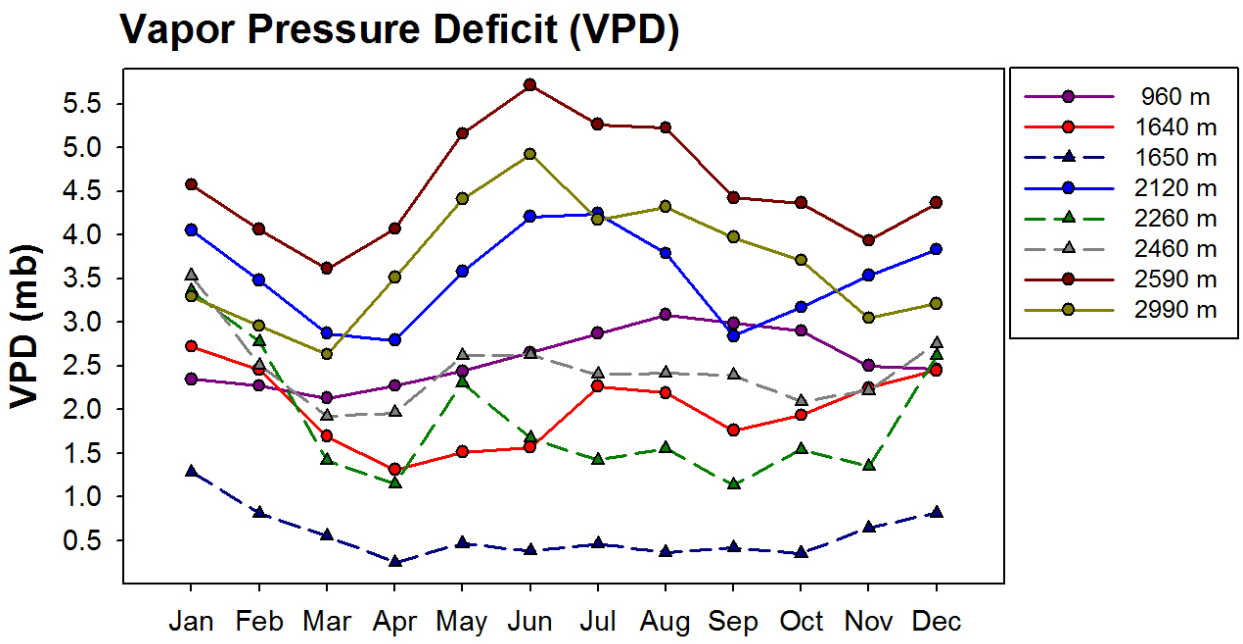

Figure 2.19: Mean annual cycle of vapor pressure deficit solid lines with a circle symbol indicate leeward stations; dashed lines with a triangle symbol indicate windward stations.

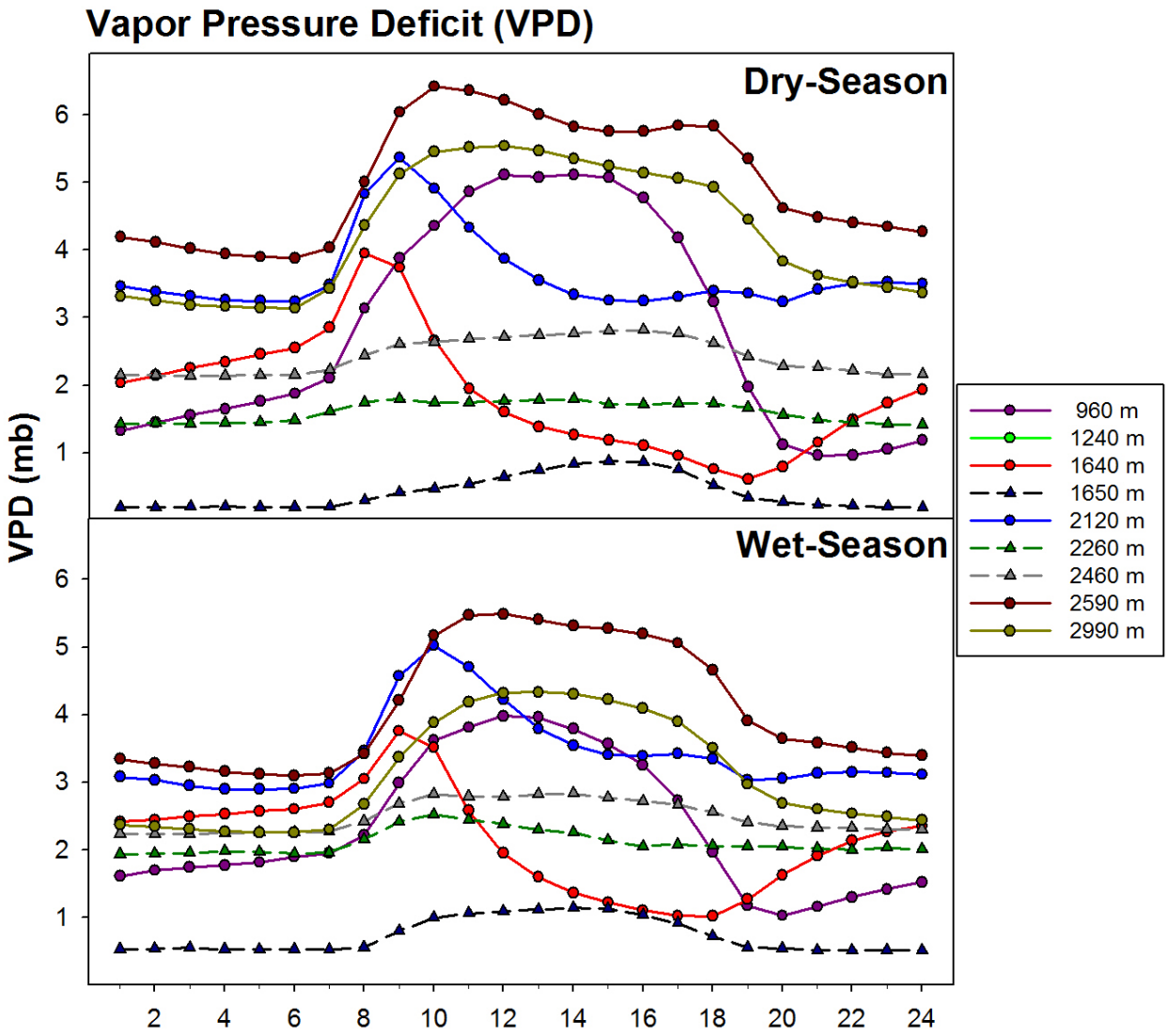

Figure 2.20: Diurnal cycles of vapor pressure deficit for the dry (top) and wet (bottom) season; solid lines with a circle symbol indicate leeward stations; dashed lines with a triangle symbol indicate windward stations.

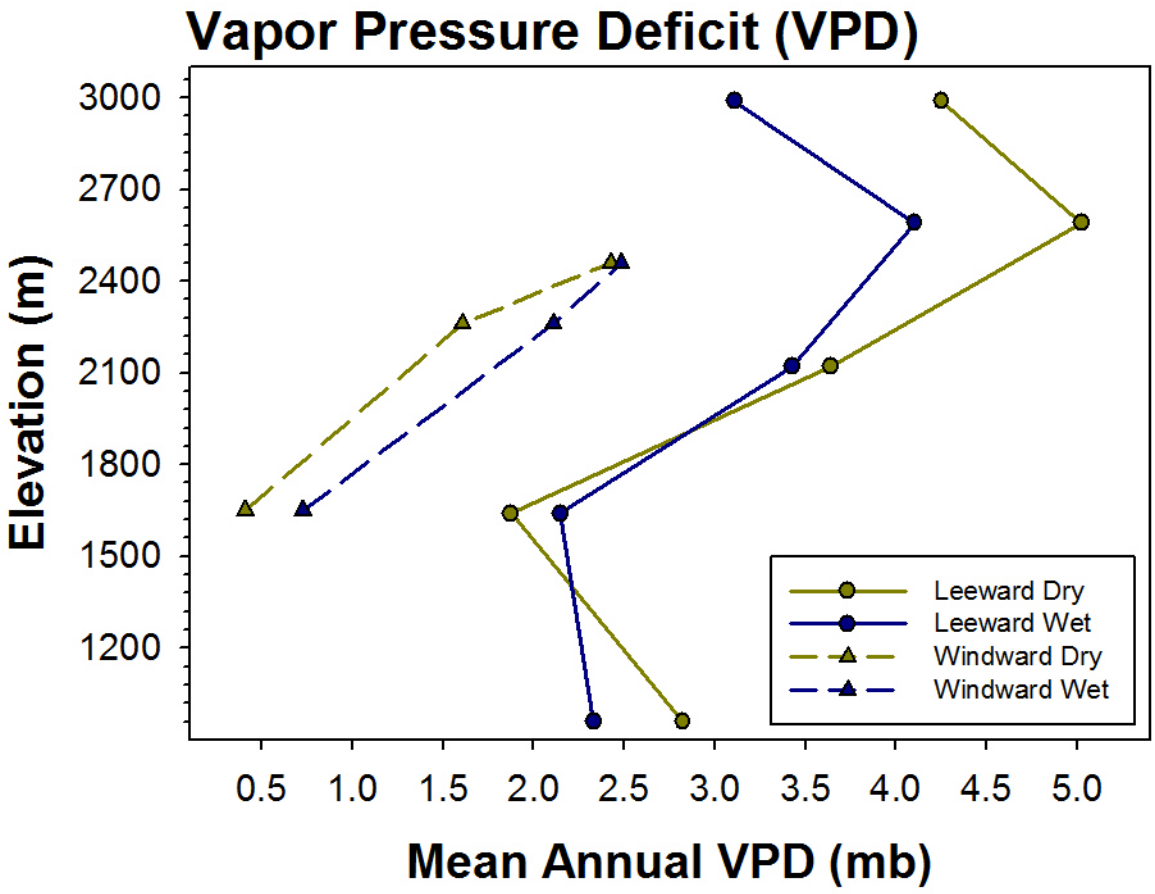

Figure 2.21: Vertical profiles of mean annual vapor pressure deficit along leeward (solid line, circle marker) and windward (dashed line, triangle marker) elevation transects, or dry (yellow) and wet (blue) seasons.

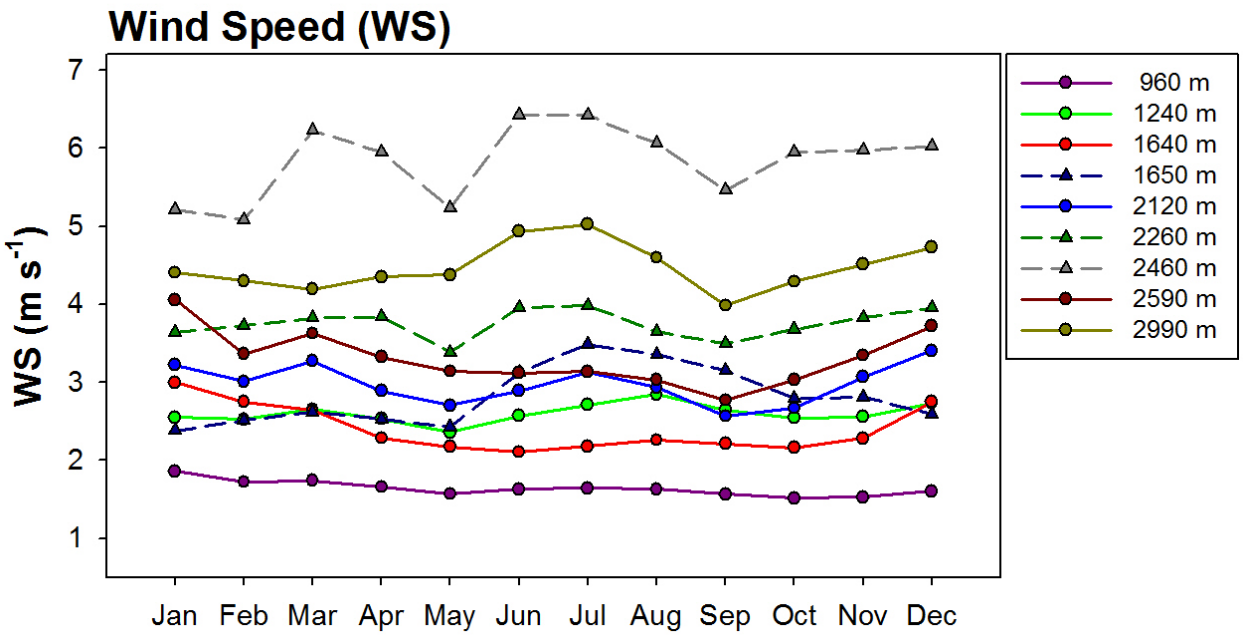

Figure 2.22: Mean annual cycle of wind speed solid lines with a circle symbol indicate leeward stations; dashed lines with a triangle symbol indicate windward stations.

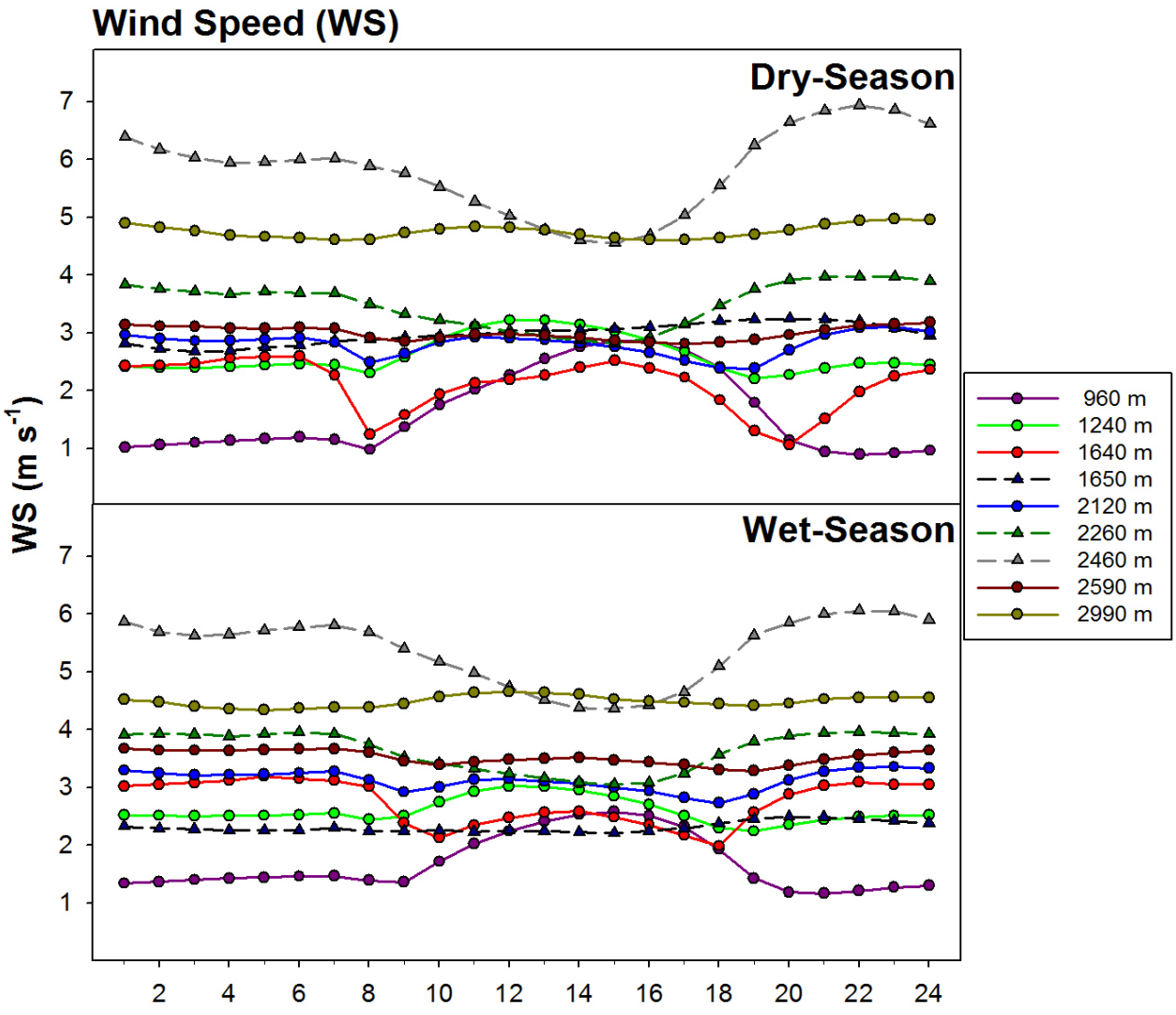

Figure 2.23: Diurnal cycles of wind speed for the dry (top) and wet (bottom) season; solid lines with a circle symbol indicate leeward stations; dashed lines with a triangle symbol indicate windward stations.

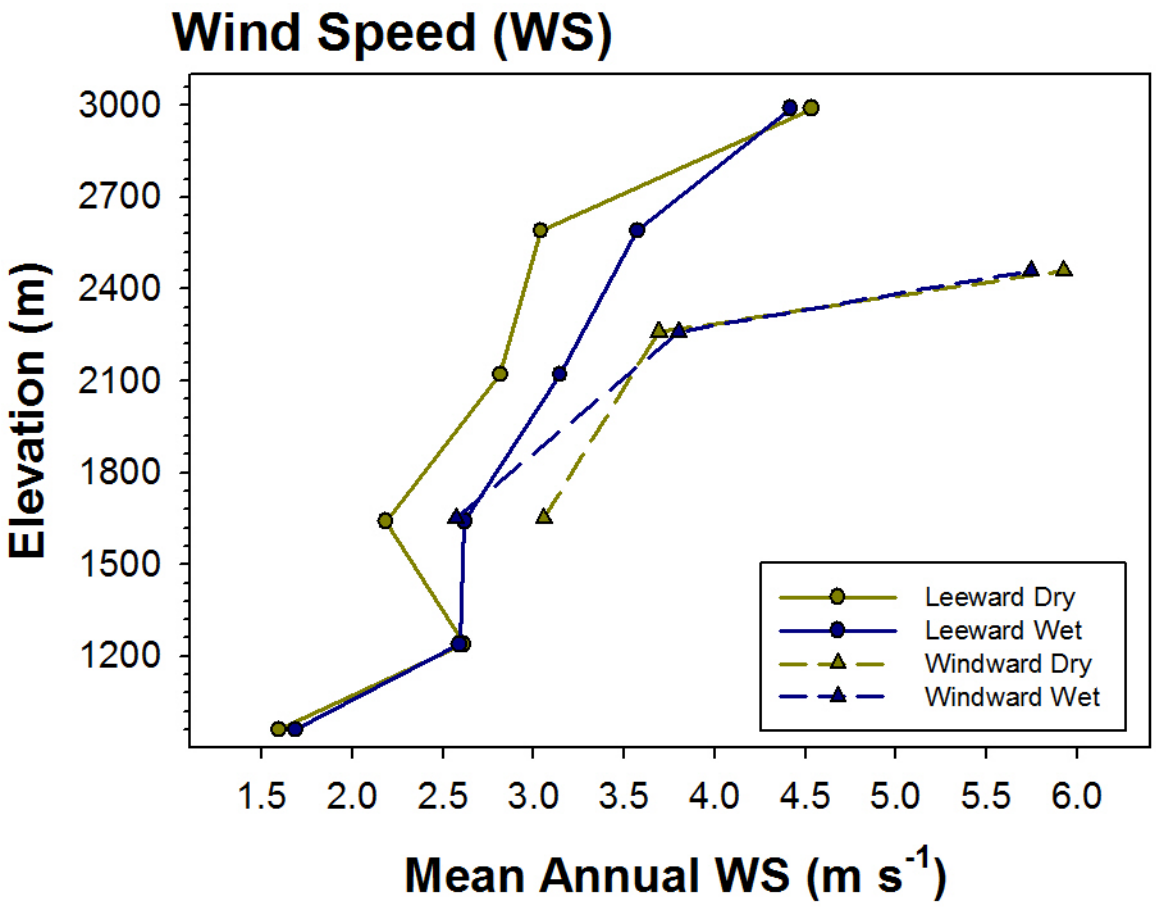

Figure 2.24: Vertical profiles of mean annual wind speed along leeward (solid line, circle marker) and windward (dashed line, triangle marker) elevation transects, or dry (yellow) and wet (blue) seasons.

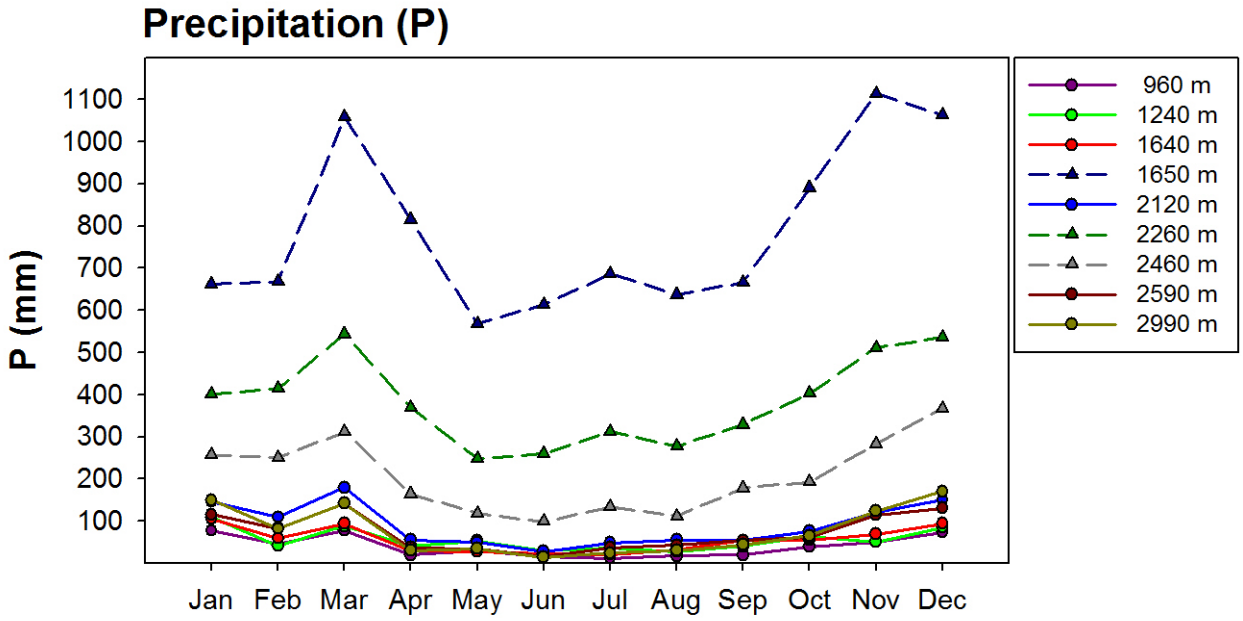

Figure 2.25: Mean annual cycle of precipitation solid lines with a circle symbol indicate leeward stations; dashed lines with a triangle symbol indicate windward stations.

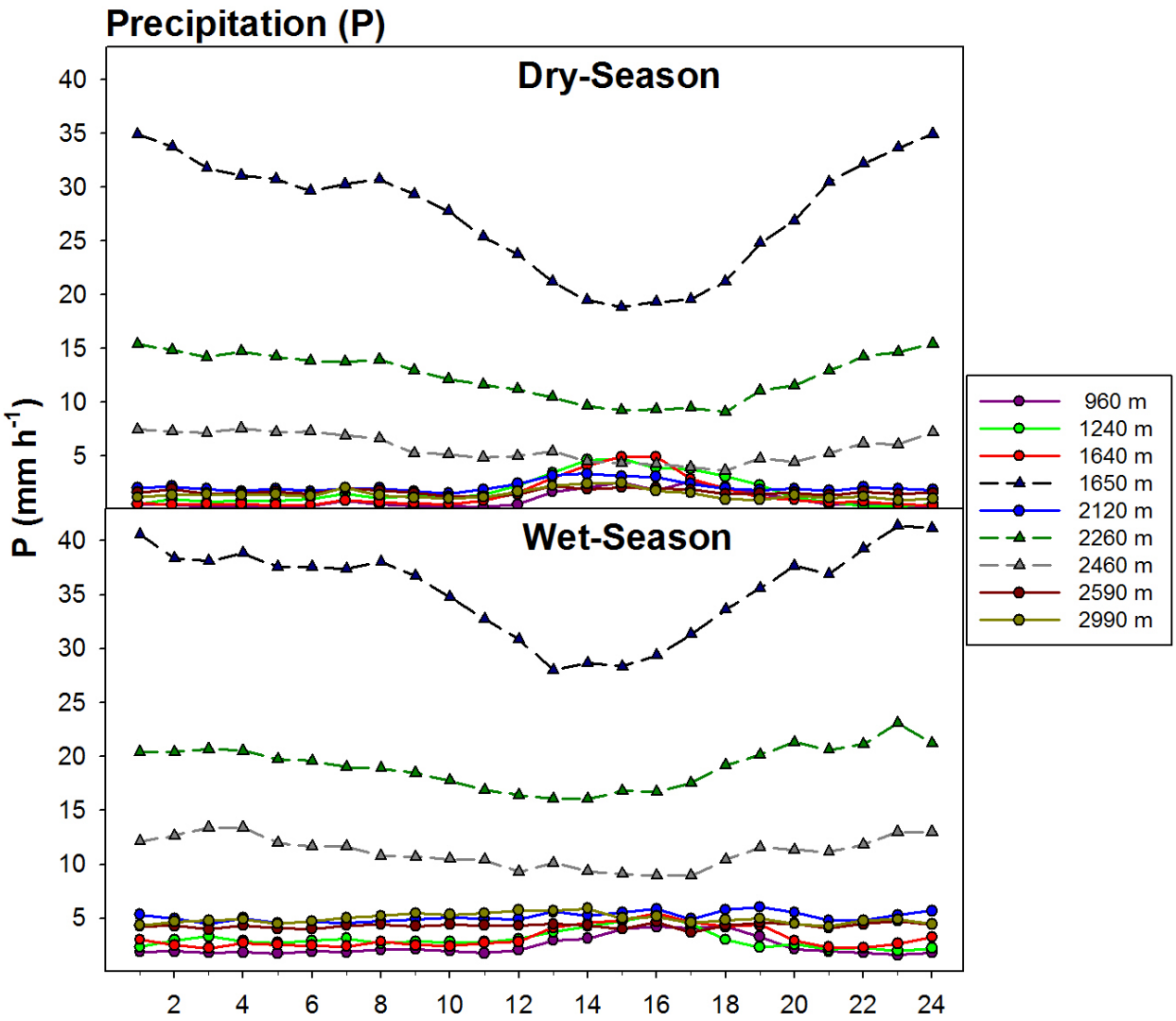

Figure 2.26: Diurnal cycles of precipitation for the dry (top) and wet (bottom) season; solid lines with a circle symbol indicate leeward stations; dashed lines with a triangle symbol indicate windward stations.

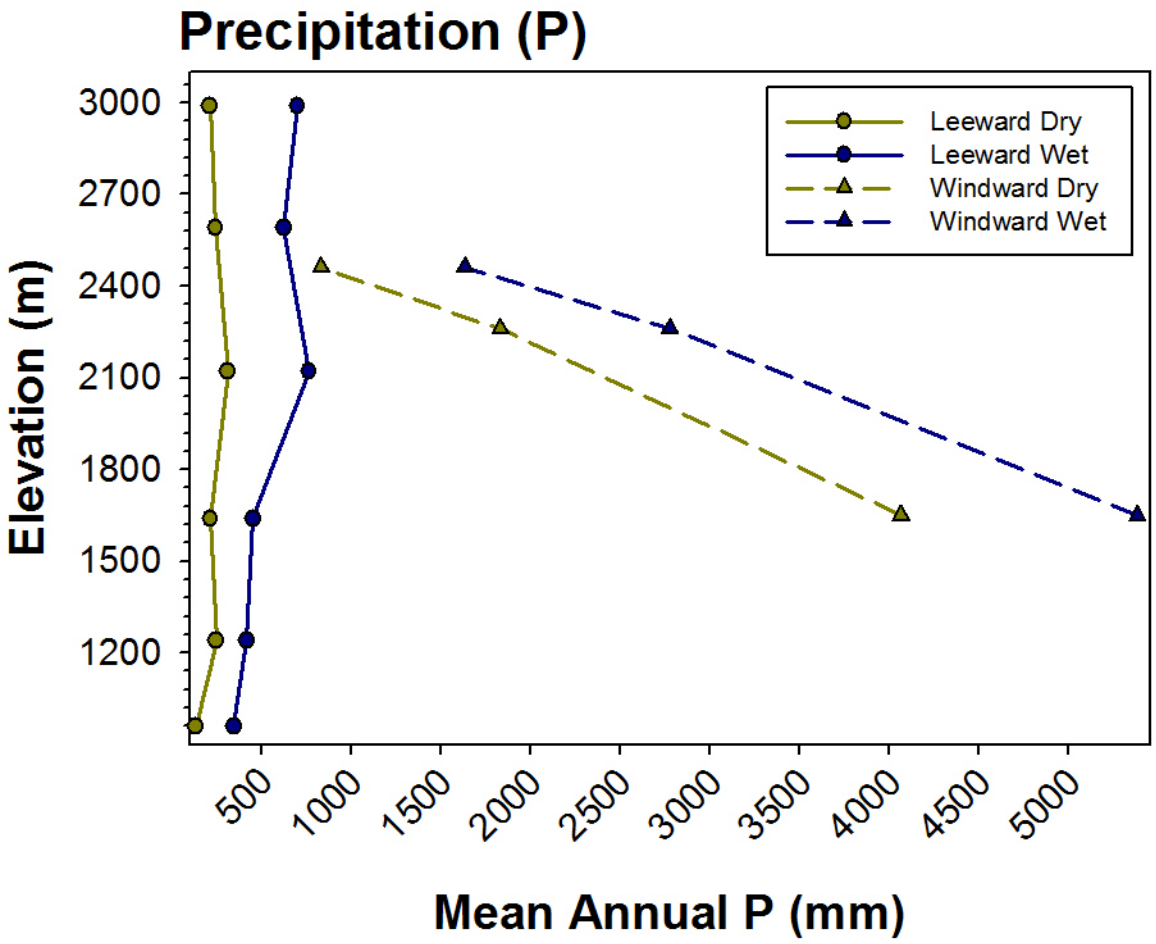

Figure 2.27: Vertical profiles of mean annual precipitation along leeward (solid line, circle marker) and windward (dashed line, triangle marker) elevation transects, or dry (yellow) and wet (blue) seasons.

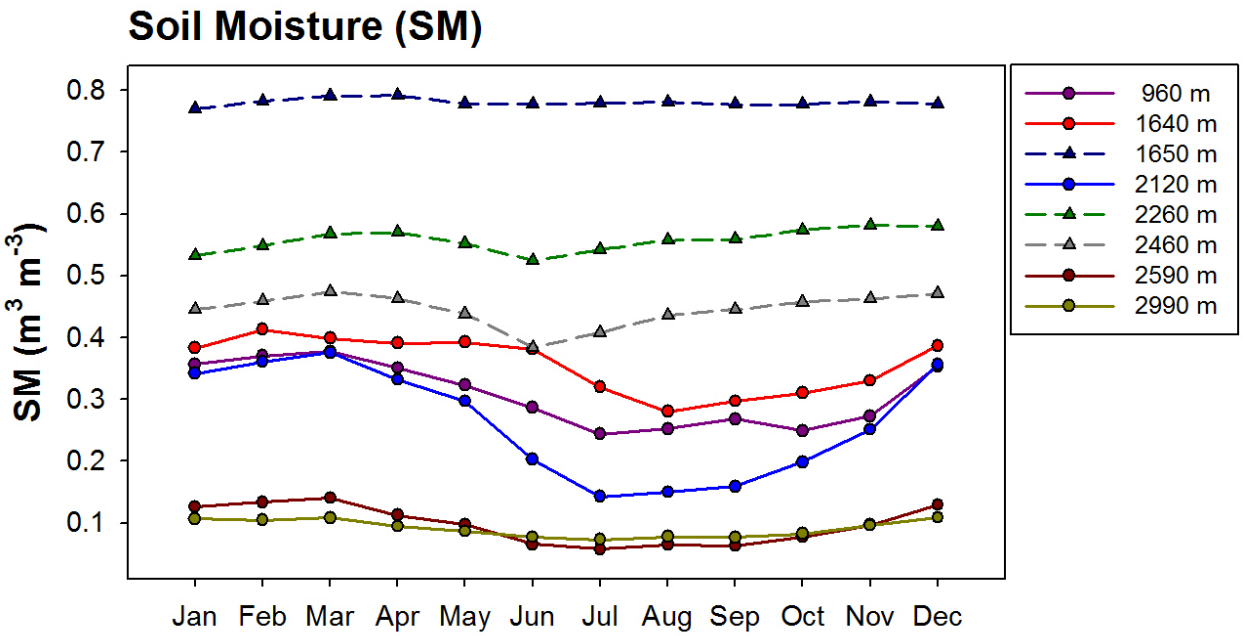

Figure 2.28: Mean annual cycle of soil moisture solid lines with a circle symbol indicate leeward stations; dashed lines with a triangle symbol indicate windward stations.

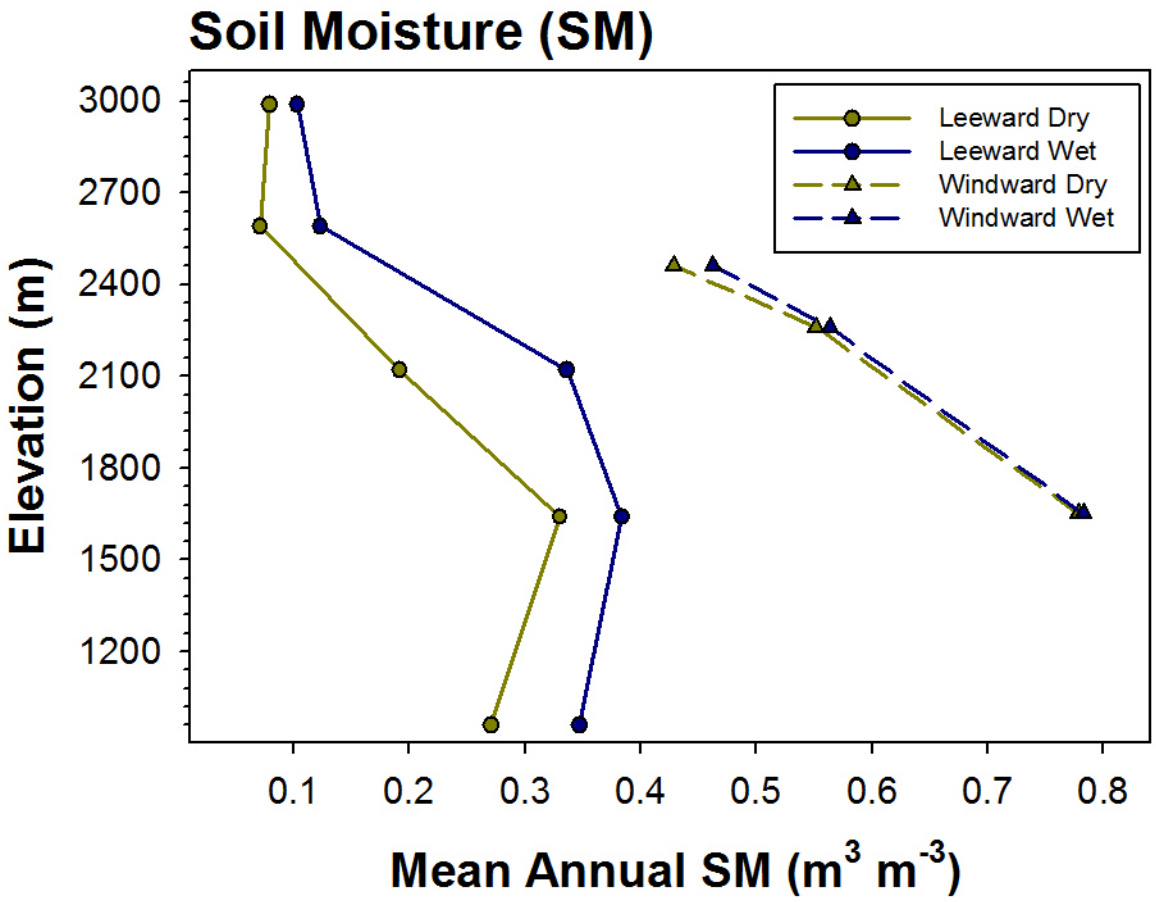

Figure 2.29: Vertical profiles of mean annual soil moisture along leeward (solid line, circle marker) and windward (dashed line, triangle marker) elevation transects, or dry (yellow) and wet (blue) seasons.

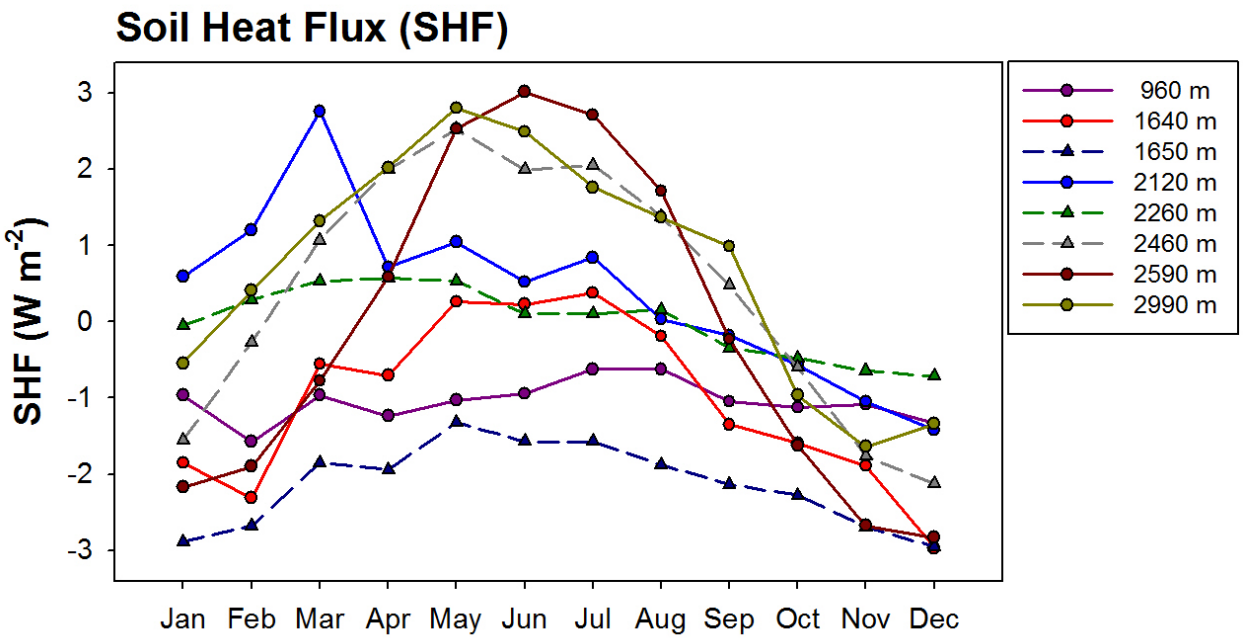

Figure 2.30: Mean annual cycle of soil heat flux solid lines with a circle symbol indicate leeward stations; dashed lines with a triangle symbol indicate windward stations.

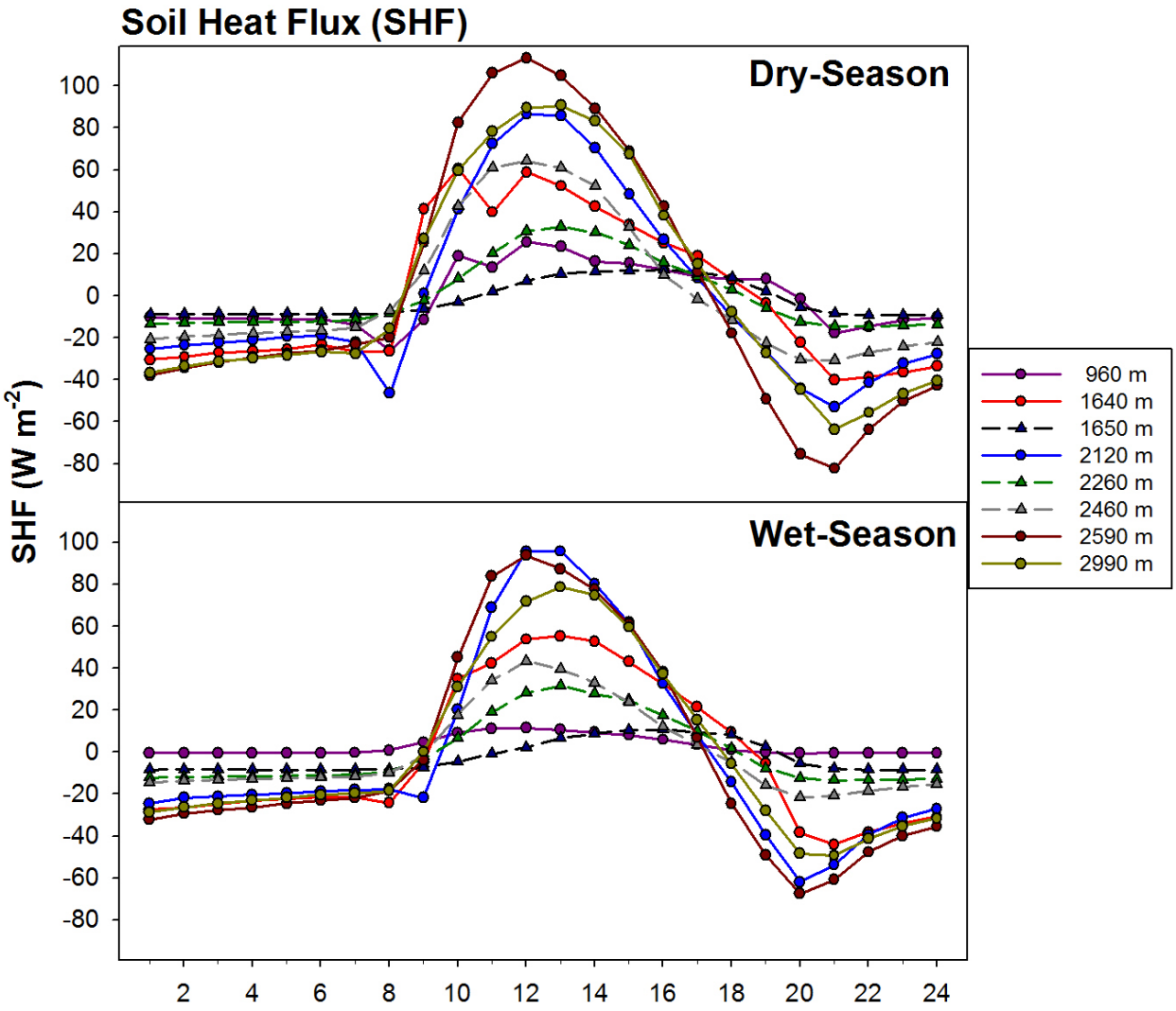

Figure 2.31: Diurnal cycles of soil heat flux for the dry and wet (bottom) season; solid lines with a circle symbol indicate leeward stations; dashed lines with a triangle symbol indicate windward stations.

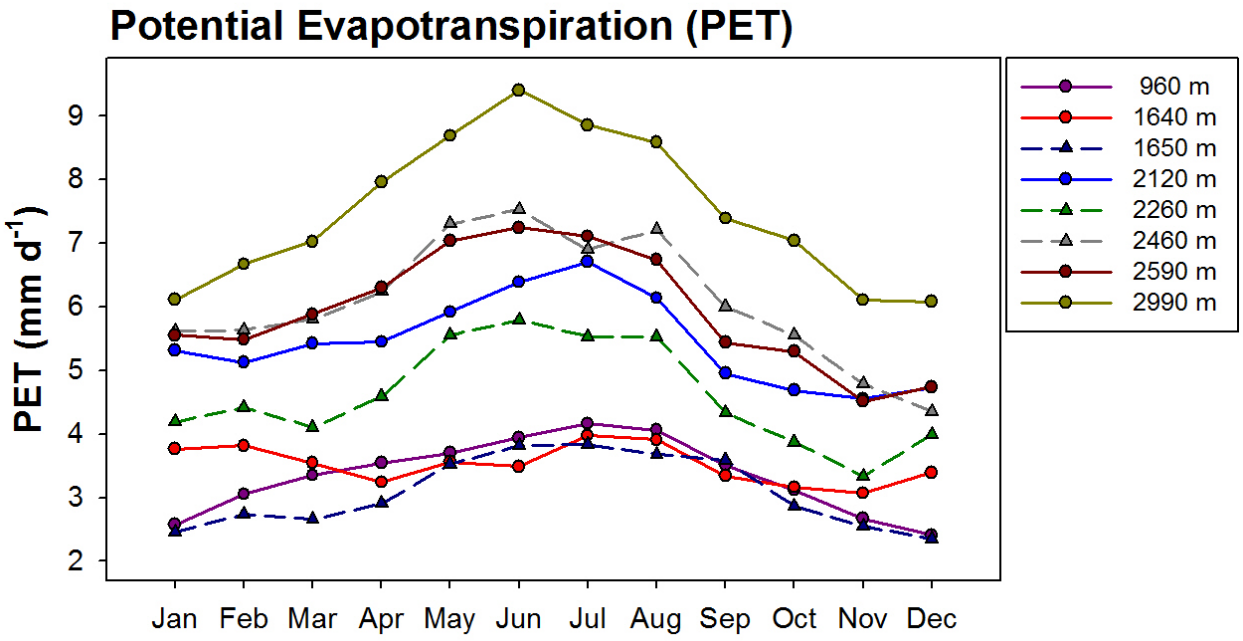

Figure 2.32: Mean annual cycle of potential evapotranspiration solid lines with a circle symbol indicate leeward stations; dashed lines with a triangle symbol indicate windward stations.

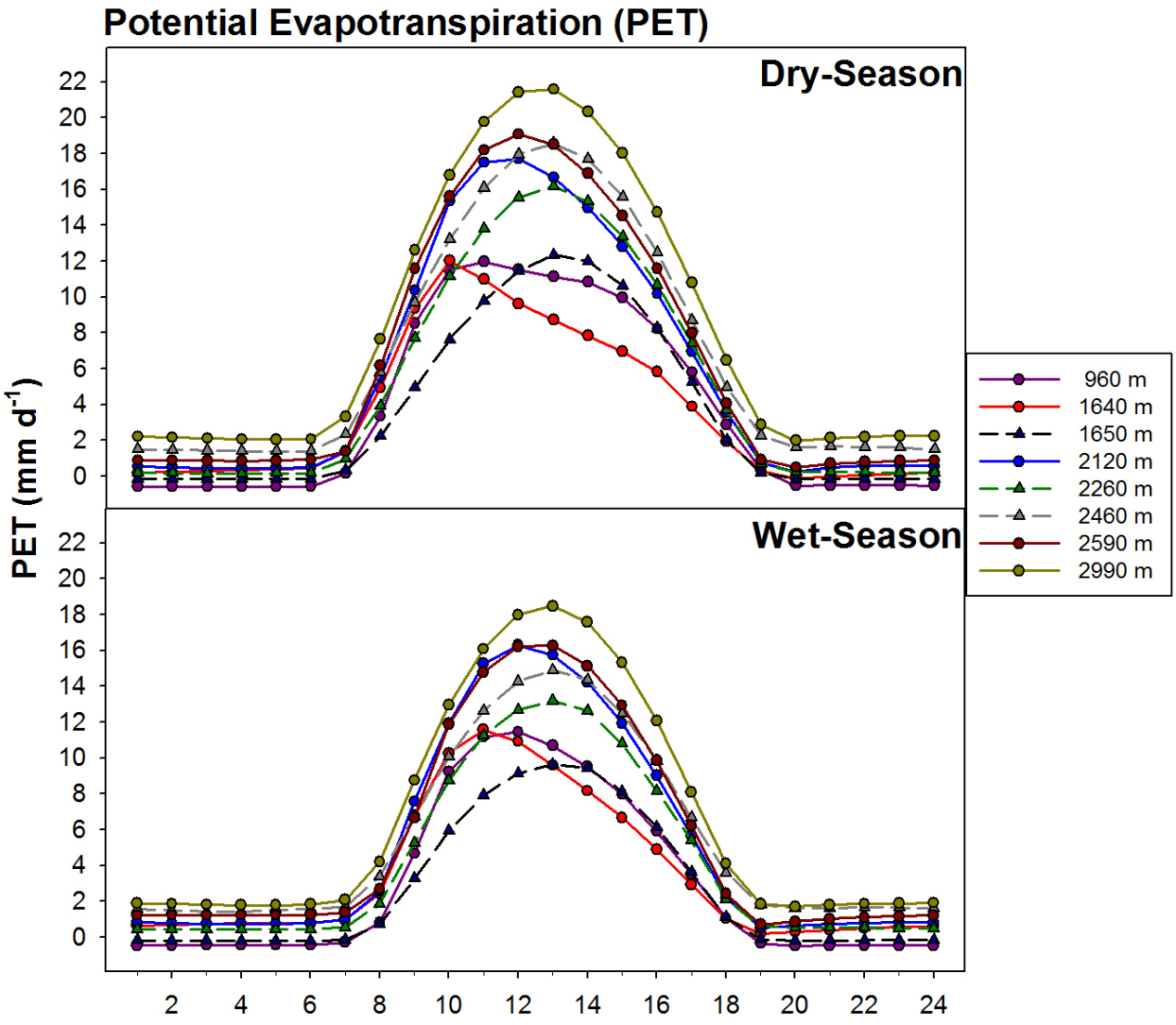

Figure 2.33: Diurnal cycles of potential evapotranspiration for the dry (top) and wet (bottom) season; solid lines with a circle symbol indicate leeward stations; dashed lines with a triangle symbol indicate windward stations.

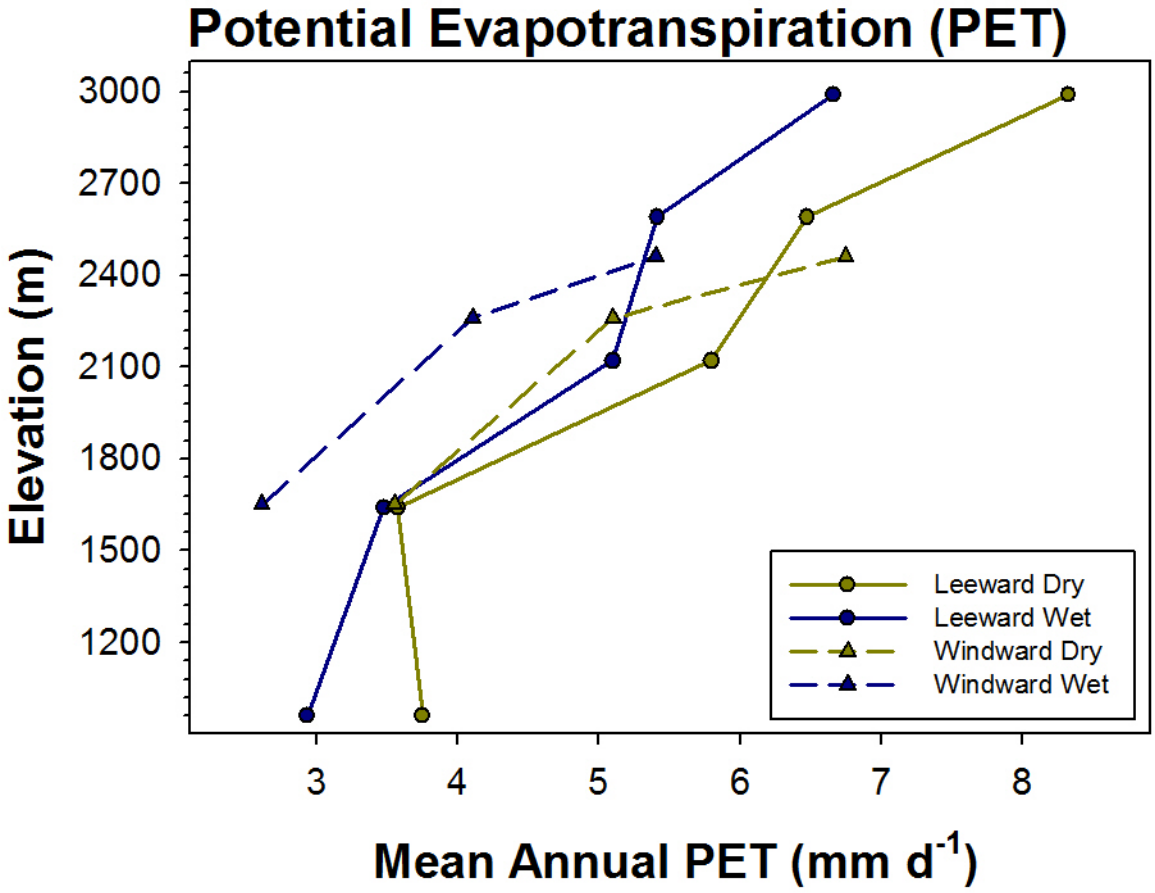

Figure 2.34: Vertical profiles of mean annual potential evapotranspiration along leeward (solid line, circle marker) and windward (dashed line, triangle marker) elevation transects, or dry (yellow) and wet (blue) seasons.

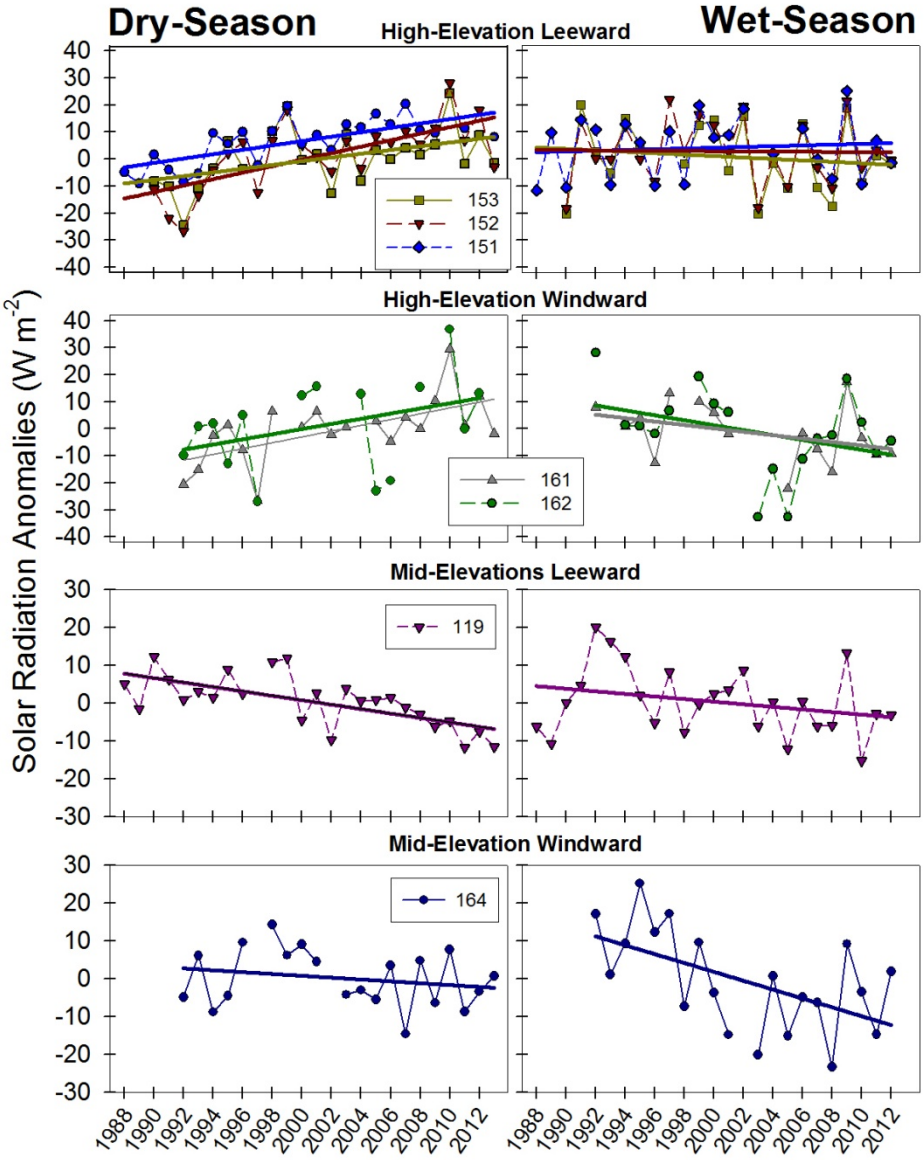

Figure 2.35: Time series of solar radiation during dry (left) and wet (right) seasons (1988 to 2013).

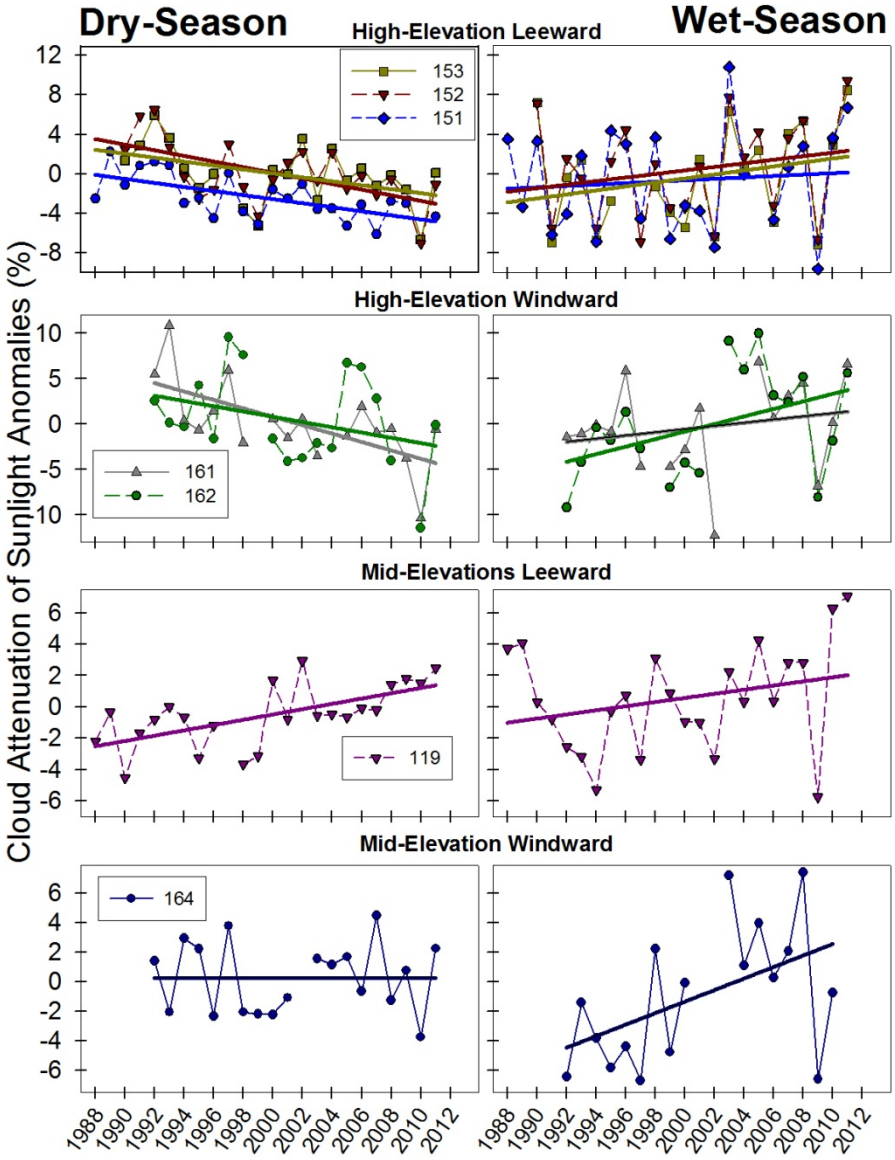

Figure 2.36: Time series of cloud attenuation of sunlight during dry (left) and wet (right) seasons (1988 to 2013).

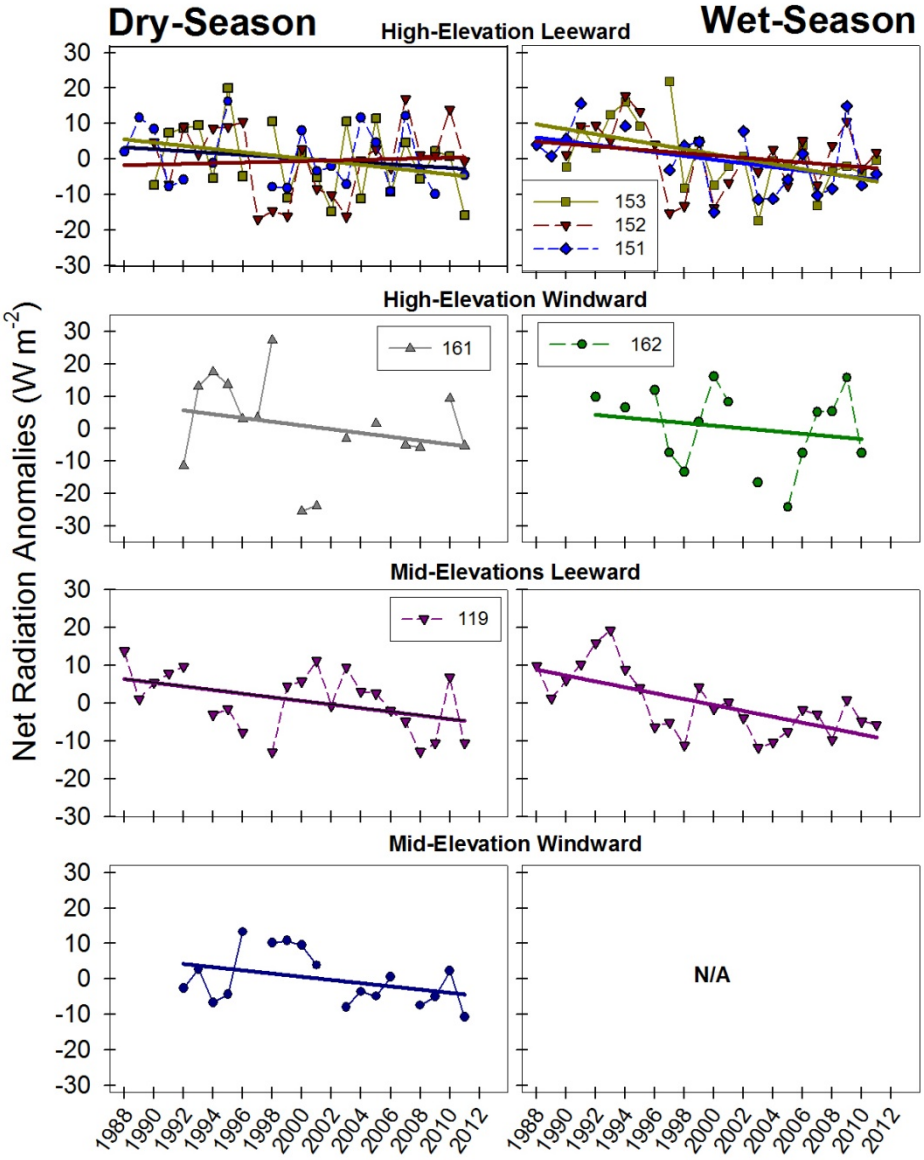

Figure 2.37: Time series of net radiation
during dry (left) and wet (right) seasons (1988 to 2013).

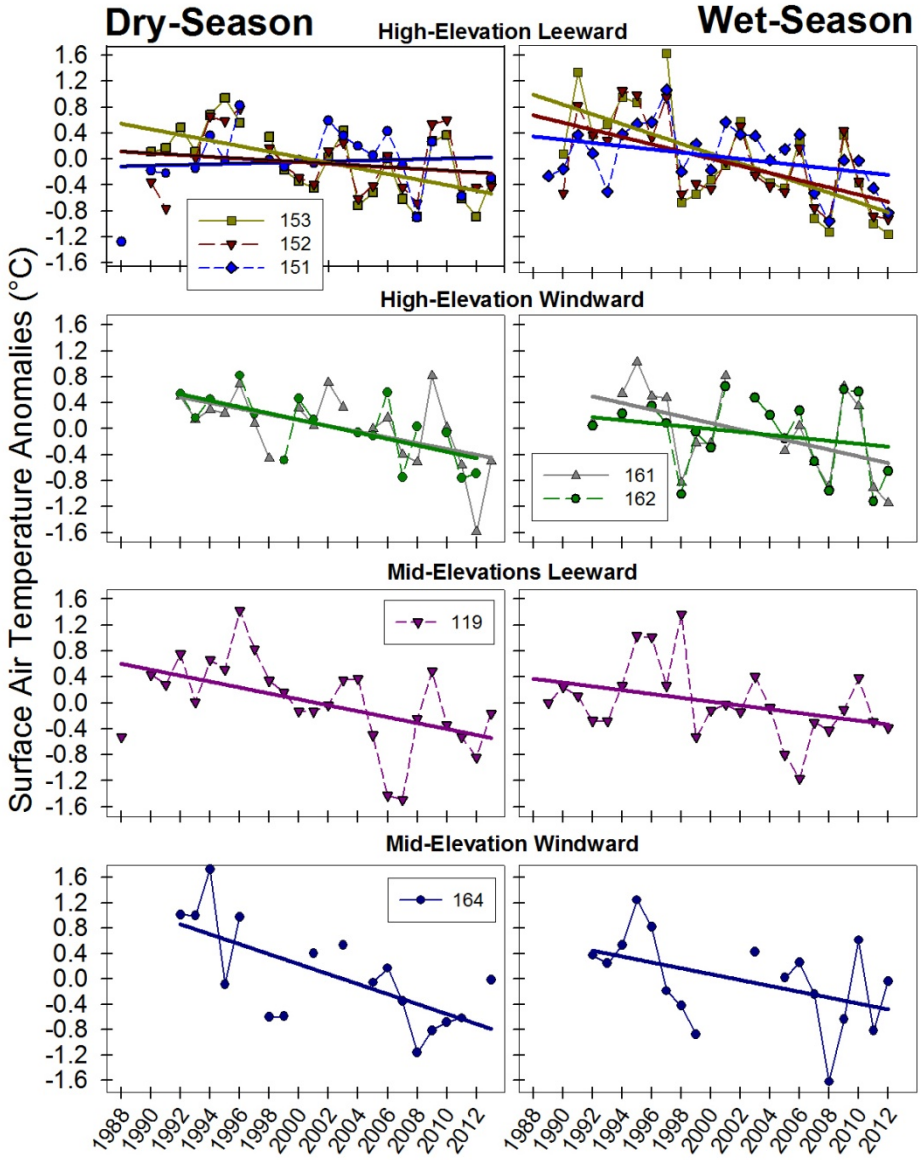

Figure 2.38: Time series of surface air temperature during dry (left) and wet (right) seasons (1988 to 2013).

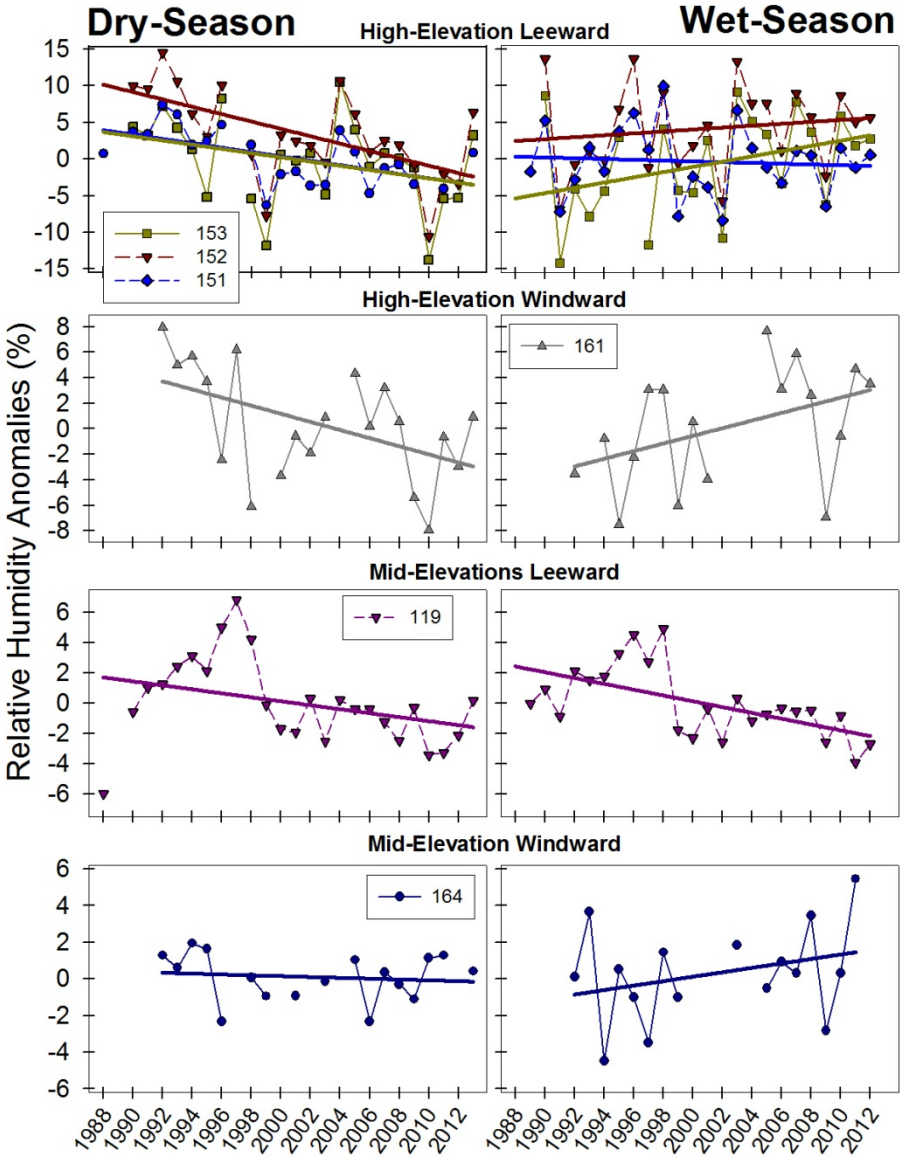

Figure 2.39: Time series of relative humidity during dry (left) and wet (right) seasons (1988 to 2013).

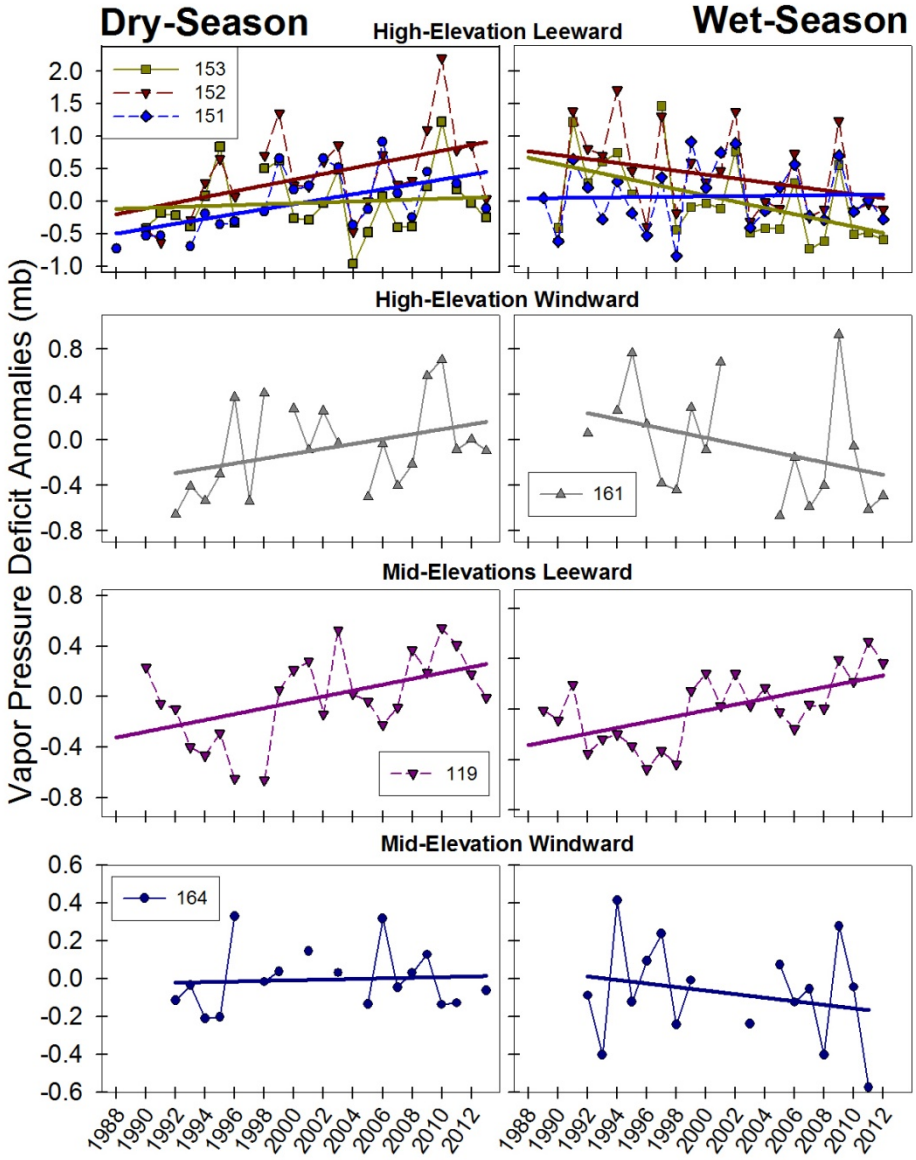

Figure 2.40: Time series of vapor pressure deficit during dry (left) and wet (right) seasons (1988 to 2013).

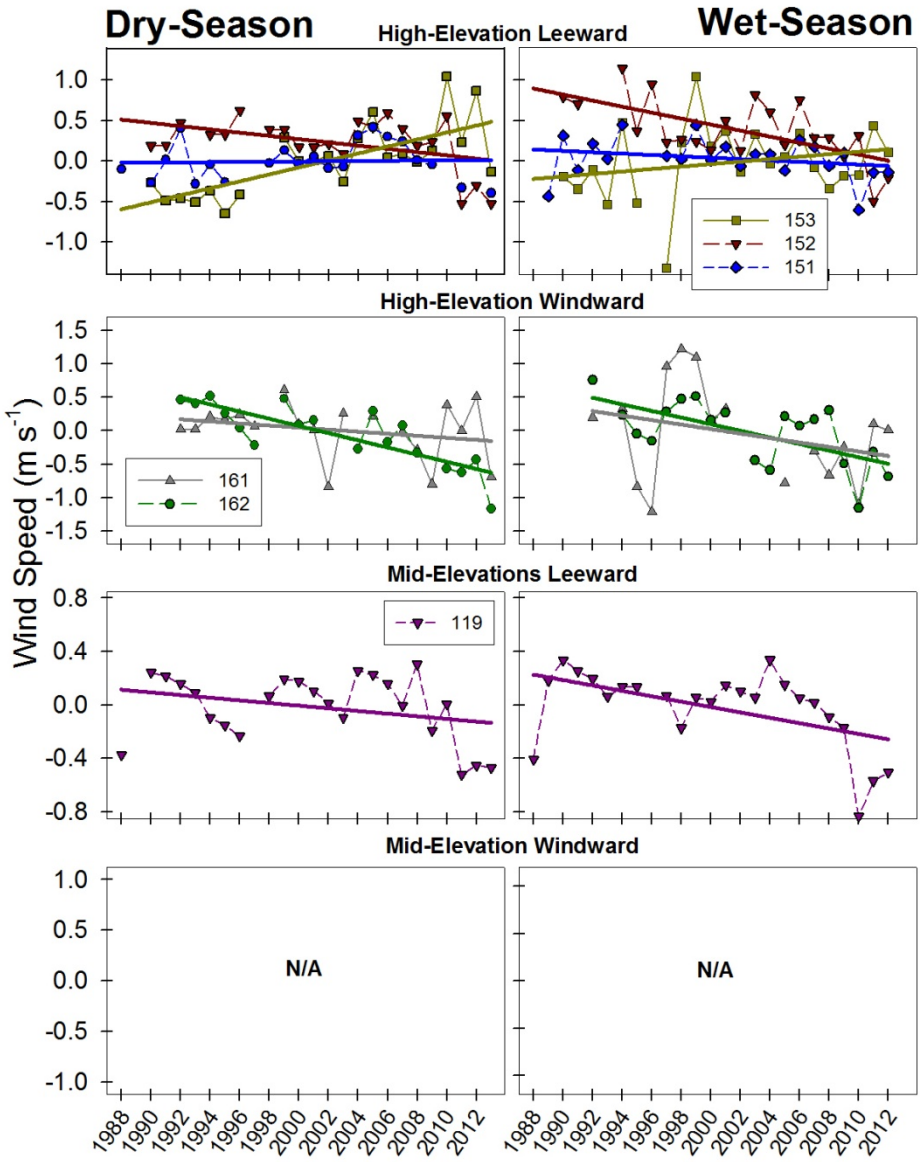

Figure 2.41: Time series of wind speed
during dry (left) and wet (right) seasons (1988 to 2013).

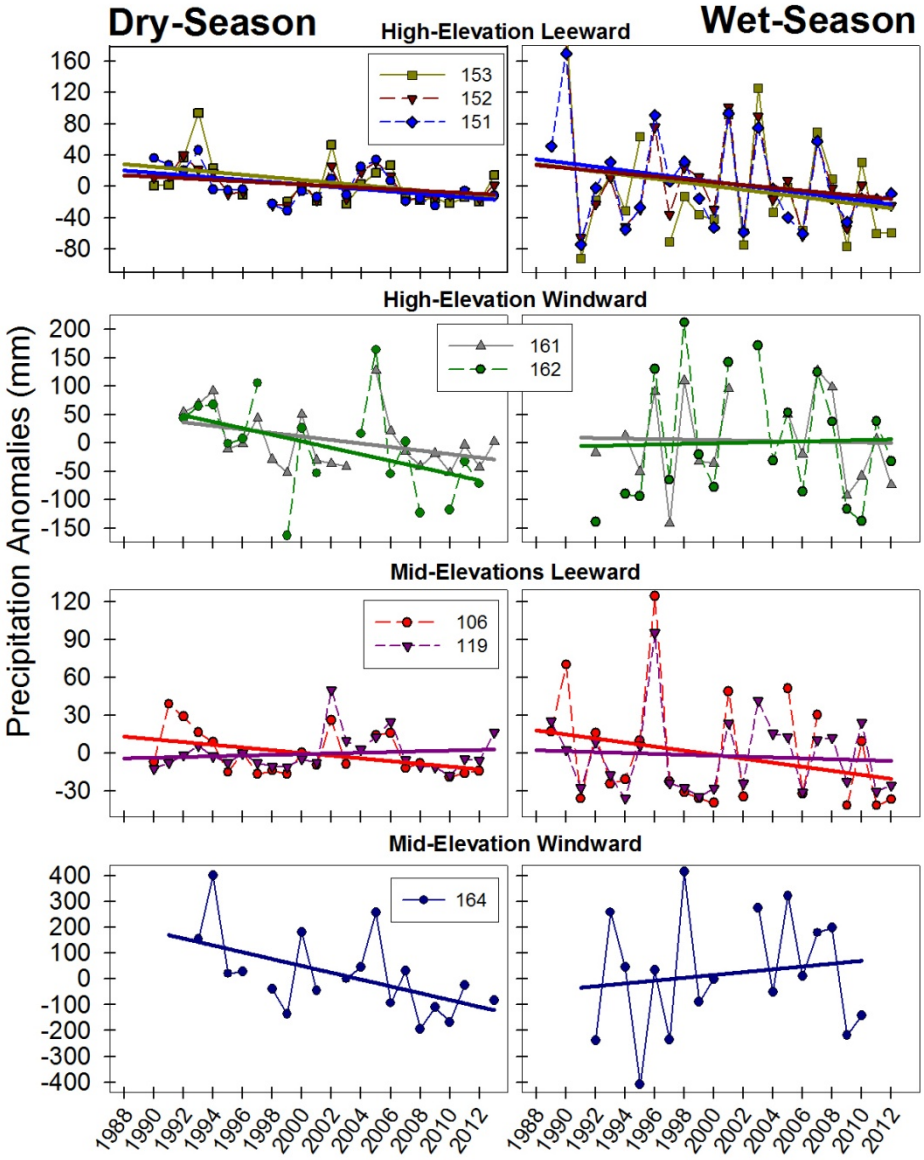

Figure 2.42: Time series of precipitation
during dry (left) and wet (right) seasons (1988 to 2013).

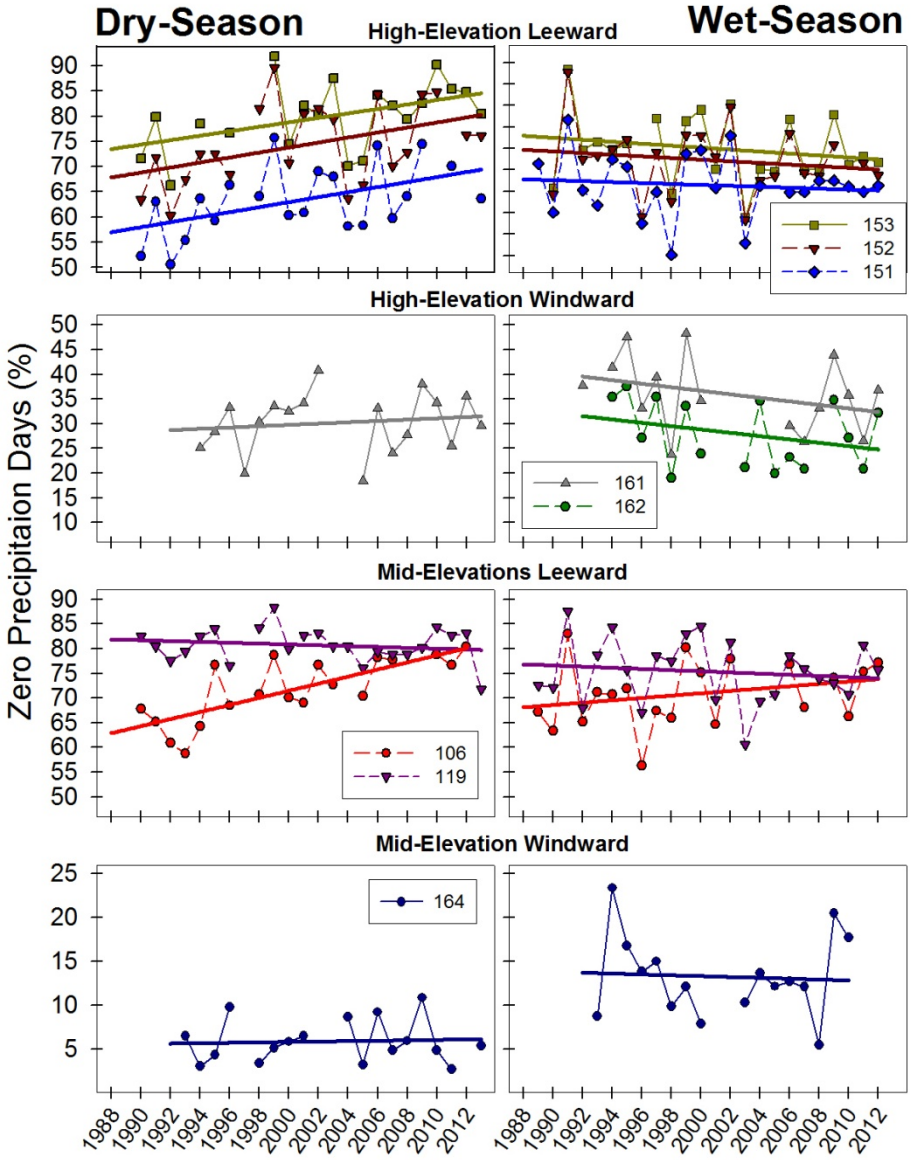

Figure 2.43: Time series of zero precipitation days during dry (left) and wet (right) seasons (1988 to 2013).

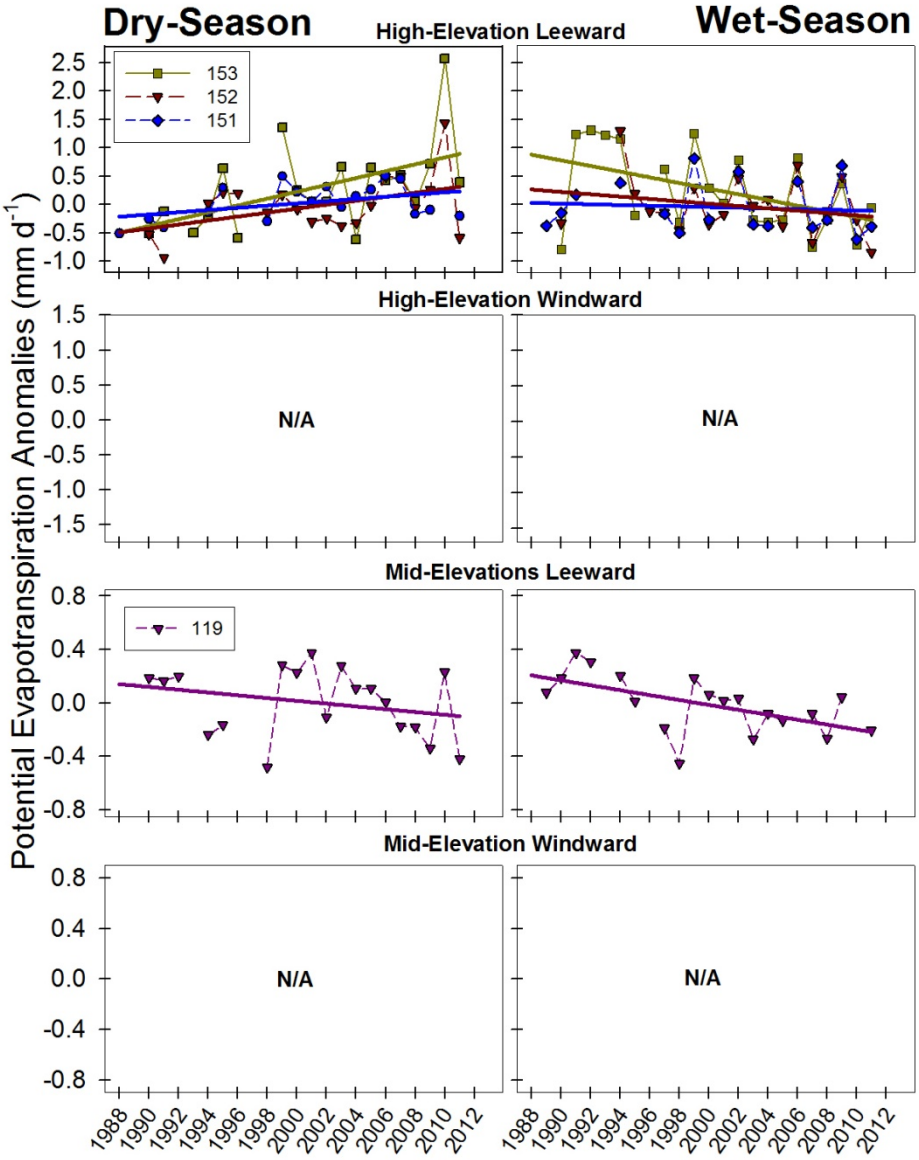

Figure 2.44: Time series of potential evapotranspiration during dry (left) and wet (right) seasons (1988 to 2013).

CHAPTER 3. SUSTAINED INCREASES IN LOWER TROPOSPHERIC SUBSIDENCE OVER THE CENTRAL TROPICAL NORTH PACIFIC DRIVES A DECLINE IN HIGH ELEVATION RAINFALL IN HAWAI‘I

3.1 Abstract

Consistent increases in the strength and frequency of occurrence of the Trade Wind Inversion (TWI) were identified across a ~40-yr period (1973–2013) in Hawai‘i. Change-point analysis indicates that a marked shift occurred in the early 1990s resulting in a 16% increase in the mean TWI frequency between the periods 1973-1990 and 1991-2013, based on the average of changes at two sounding stations and two 6-month (wet and dry) seasons. Regional increases in the vertical wind velocity variable “omega” at the 500 hPa level obtained from four reanalysis data sets were identified over the same ~40 year time period. The post-1990 period mean for the 4-model reanalysis ensemble shows increases in downward vertical velocity of 19% (±11% s.d) and 27 (±14% s.d) for the dry and wet seasons, respectively. Good agreement was found between the time series of TWI frequency of occurrence data and omega (r^2 = 0.23 - 0.46), suggesting that increases in the intensity of Hadley cell subsidence are driving the observed increases in TWI frequency. Correlations between omega and large-scale modes of internal climate variability such as the El Niño-Southern Oscillation (ENSO) and the Pacific Decadal Oscillation (PDO) do not explain the abrupt shift in TWI frequency in the early 1990s. On average post-1990 average rainfall was 3% (±13% s.d.) lower in the dry season and 40% (±21% s.d.) lower in the wet season at 21 high elevation stations in Hawai‘i. Of stations for which rainfall was significantly correlated with TWI frequency average rainfall was 16% lower during the dry season (38% of the stations), and 40% lower during the wet season (100% of the stations), relative to the pre-1991 period.

3.2 Introduction

The effects of climate change in the Hawaiian Islands has received considerable attention in recent years (e.g. Cao et al., 2007; Giambelluca et al. 2008; Timm and Diaz, 2009, Chu et al., 2010; Diaz et al., 2011; Ellison Timm et al., 2011; Bassiouni and Oki, 2012; Diaz and Giambelluca et al., 2012; Krushelnycky et al., 2012; Longman et al., 2014). Increases in temperature (Giambelluca et al., 2008), decreases in precipitation and increased drought occurrence (e.g. Chu and Chen, 2005; Kurk and Levinson; 2008; Diaz and Giambelluca, 2012), particularly at high elevations (e.g. Krushelnycky et al., 2012; Frazier et al., 2013), have been observed in Hawai‘i over the past several decades. However, the driving forces behind these changes are not clearly understood. One possible explanation to decreases in high elevation rainfall is an increase in the frequency of occurrence of the Trade Wind Inversion (TWI). The thermally driven Hadley cell (HC) circulation moves air vertically to a height of about 15 km within the Inter-tropical Convergence Zone, and then poleward to the subtropics, where air descends. The TWI is a result of the HC subsidence interacting with convectively driven air rising from lower levels, which causes a discontinuity in the vertical temperature profile (Riehl, 1979). When the TWI is present, the vertical development of clouds is suppressed and the transport of moisture to high elevation ecosystems above the inversion on Hawai‘i’s highest mountains is inhibited (Giambelluca, 2005).

Several studies have been conducted to document the characteristics of the TWI (e.g. Riehl, 1979; Giambelluca and Nullet, 1991; Cao et al., 2007), and to determine the effects it has on the climate (e.g. Loope and Giambelluca, 1998; Longman et al., 2012) and on ecological processes (e.g. Kitaymama and Mueler_Dombois, 1992; Krushelnycky et al., 2012; Crausbay et al., 2014; Gotsch et al., 2014) at high elevations in Hawai‘i. Cao et al. (2007) identified the TWI

using data from two long-term radiosonde stations in Hawai‘i (Hilo and Līhu‘e) and showed an increase in TWI frequency of occurrence and a decrease in base height for most months analyzed from 1979 to 2003. Whether or not these trends persisted or abated over the next decade has not been determined.

Longman et al. (2014) has shown that dry season solar radiation has significantly increased at all of the four high elevation (>2000 m) stations that were analyzed on the Island of Maui, Hawai‘i, from ~1988–2013, which, at least for the period of high resolution MODIS satellite imagery (since 2001), can be explained by a decrease in cloud cover. Examination of variations in the frequency of occurrence and base height of the TWI is relevant to understanding the causes of the observed trends in cloud cover and solar radiation at high elevations. In addition, it is important to understand the driving forces behind TWI variability including the response to changes in HC circulation and to phase changes in the internal modes of climate variability operating on inter-annual and/or inter-decadal time scales.

A strong body of evidence now exists indicating that the tropical circulation belt has both widened and intensified over the past several decades (Lucas et al., 2013, and references therein). However, the rates of change in extent and intensity are not known with a high degree of certainty (Quan et al., 2014). In addition, opinions in the current literature differ regarding the relationship between widening and intensification. Some modeling efforts have shown an inverse relationship between HC intensity and expansion (e.g. Mitas and Clement, 2006; Lu et al., 2007), while other research has found a positive relationship between these variables (Tanaka et al., 2004; Quan et al., 2004; Nguyen et al., 2013). HC variations are most commonly defined using the mass-weighted zonal mean meridional stream function (e.g. Oort and Yienger, 1996; Trenberth et al., 2000; Quan et al., 2004; Stachnik and Schumacher, 2011). However, they can

also be defined in terms of velocity potential or vertical velocity (omega) at specific pressure levels (Wang, 2002; Tanaka et al., 2004), the meridional component of divergent wind (Song and Zhang, 2007), or variations in meridional atmospheric moisture transport (Sohn and Park, 2010). Changes in HC are also assessed using proxy data such as outward longwave radiation (OLR) (e.g. Hu and Fu, 2007) or sea level pressure (SLP) (e.g. Song and Zhang, 2007).

Changes in HC width and intensity have been explained by multiple climate forcing mechanisms such as, increases in greenhouse gas (GHG) concentrations and associated changes in the sea surface temperature (SST; e.g Staten et al., 2011), stratospheric ozone depletion (e.g. Polvani et al., 2011) and the effects of aerosols (e.g. Allen et al., 2012). Natural variability such as the El Niño Southern Oscillation (ENSO) and the Pacific Decadal Oscillation (PDO) have also been found to affect HC width and intensity (e.g. Mitas and Clement, 2005; Grassi et al., 2012). During the warm (cool) phase of ENSO the HC is narrower (wider) and more (less) intense (Oort and Yienger, 1996). Negative phase PDO conditions have been shown to promote a widening of the tropical belt at least during the equinox seasons (Grassi et al., 2012).

Many of the studies that examine changes to the HC make use of one or more of eight available global reanalysis data products (Davis and Rosenlof, 2012; Lucas et al., 2013). Reanalysis data are global gridded data sets derived using methods that combine meteorological forecast models and observations. The majority of reanalysis products are limited to the satellite era with only 3 of the 8 available reanalysis time series extending back to the pre-satellite era. Reanalysis data are not without their shortcomings and many differences among the datasets have been identified in the literature (e.g. Song and Zhang, 2007; Stachnik and Shumacher, 2011, Nguyen et al., 2012, Lucas et al., 2013). The inclusion or exclusion of satellite data and differences in the physics of the underlying models are potential sources of differences among

the various reanalysis products (Lucas et al., 2013). Throne and Vose (2010) note that because of these systematic differences it is crucial to examine an ensemble of reanalysis datasets to validate a climate change signal.

In this study, I analyze TWI data obtained from two atmospheric sounding stations, the vertical velocity of wind variable "omega" from four reanalysis products and a 4-model reanalysis ensemble, and rainfall data from 21 high elevation (>1900 m) climate stations. The main objectives of this analysis were to determine 1) whether previously detected increases in TWI frequency and decreases in TWI base height persisted after 2003; 2) whether changes in TWI characteristics are significantly correlated with changes in atmospheric general circulation; 3) the role of large scale modes of internal variability, such as ENSO and PDO, in explaining TWI variability; and 4) the effects of changes in TWI frequency on rainfall regimes at high elevations, for the two 6-month seasons in Hawai‘i.

3.3 Data

TWI characteristics were calculated using vertical profiles of temperature and relative humidity obtained at two atmospheric sounding stations in Hawai‘i located at Līhu‘e (21.97˚N, 159.333˚W) on the Island of Kaua‘i and Hilo (19.72˚N, 155.05˚W) on Hawai‘i Island (Figure 3.1). The 2:00 PM HST (0:00 UTC) soundings from each station from 1973 to 2013 were used in this analysis to identify TWI characteristics over the period of record. Atmospheric sounding data are maintained by the University of Wyoming and can be accessed at (http://weather.uwyo.edu/upperair/sounding.html).

Omega, the Lagrangian tendency of air pressure, dp/dt (Pa s^{-1}), is a measure of the vertical wind velocity (positive values indicate downward movement). Omega data at the 500 hPa level obtained from atmospheric reanalysis datasets were examined for a gridded domain

centered over the main Hawaiian Islands. Four reanalysis datasets have been identified for this study (Table 3.1); they include the National Centers for Environmental Prediction-National Center for Atmospheric Research (NCEP/NCAR) 40-year reanalysis product (NNRP; Kalnay et al., 1996), the NCEP-Department of Energy (NCEP/DOE) Atmospheric Model Intercomparison (AMIP-II) reanalysis product (NDRP; Kanamitsu et al., 2002), the European Center for Medium-Range Weather Forecasts (ECMWF) 40-year reanalysis (ERA40; Uppala et al., 2005), and the National Oceanic and Atmospheric Administration Cooperative Institute for Research in Environmental Sciences (NOAA/CIRES) 20th-century reanalysis version 2 (20CR; Compo et al., 2011).

Reanalysis datasets were chosen based on several criteria: the availability of the omega variable at 500 hPa; the period of record of available data (the analysis of TWI data begins in 1973 and, of the available reanalysis products, only NNRP, ERA40 and 20CR include this start date), and for the spatial consistency among datasets (all four of the selected datasets were available at a horizontal resolution at either 2˚ x 2˚ (20CR) or 2.5˚ x 2.5˚ (ERA40, NNRP, NDRP) grid cell size; Table 3.1). It should be noted that the 20CR does not incorporate any upper-air or satellite observations. Omega values were averaged for a 10˚ x 10˚ grid centered over the main Hawaiian Islands (17.5 to 25 N latitude, and -160° to -152.5°W longitude for 2.5˚ x 2.5˚ horizontally resolved data and 18 to 24 N latitude, and -160° to -152°W longitude for the 2.0˚ x 2.0˚ horizontally resolved data. In addition, I analyze omega, sea level pressure (SLP) and outward longwave radiation (OLR) data from the NNRP reanalysis data for a larger spatial domain (10˚ to 30˚N latitude; -135 to -180 ˚W longitude).

The Mulitvariate ENSO Index (MEI) is used to define ENSO status in this study (Wolter and Timlin, 1998). The MEI incorporates six observed fields (SLP, zonal and meridional surface

wind, SST, and total cloudiness) in the classification of ENSO modes. Data were obtained from the National Oceanic and Atmospheric Administration (NOAA) (http://www.esrl.noaa.gov/psd/enso/mei/table.html). PDO index values were obtained from the Joint Institute for the Study of the Atmosphere and Ocean (JISAO) at the University of Washington (http://jisao.washington.edu/pdo/PDO.latest).

Historical rainfall data from 21 high elevation climate stations were obtained from the Rainfall Atlas of Hawai‘i (Giambelluca et al., 2013). A dataset that had been screened for outliers and inhomogeneities, and had all data gaps filled during the period 1973 to 2007 is used (Giambelluca et al., 2011). These high elevation climate stations are located above 1900 m on the islands of Maui and Hawai‘i (Figure 3.1).

3.4 Methods

3.4.1 Trade Wind Inversion Identification

To identify TWI characteristics, sounding data were analyzed using a modification of the criteria proposed by Cao et al. (2007). The following six criteria were used to identify the TWI: 1) the TWI height is assumed to be found within the 950 – 650 hPa pressure range, which excludes inversions caused by radiative surface cooling below the 950 hPa level and inversions caused by the melting of cloud ice particles at altitudes above 650 hPa; 2) the TWI is identified as a layer with a positive vertical air temperature gradient and a drop in relative humidity at the same or the next (immediately higher) level; 3) apparent superadiabatic layers caused by enhanced cooling of temperature sensors emerging from the cloud zone were addressed using the method of Grindinger (1992); 4) for profiles with more than one inversion, the one with the greatest decrease in relative humidity with height is defined as the TWI layer (decreases in relative humidity were calculated as the average of the four relative humidity measurements

including and immediately above the initial relative humidity drop; 5) the inversion top is identified as the bottom of the first layer above the TWI in which temperature decreases with height; 6) inversions with dT > 8°C and/or thicker than 1000 m were excluded because they are considered to be unrealistic outliers (Cao et al., 2007)

The TWI is characterized using three monthly-interval metrics. TWI base height is identified as the mean elevation of the bottom inversion layer in each month. TWI frequency of occurrence is calculated as the number of days with an inversion present divided by the number of days of available data in each month (months with less than 15 days of data were excluded from the time series). TWI strength is calculated as the mean vertical temperature gradient within the TWI layer.

3.4.2 Data Aggregation and Temporal Assessment.

Hawai‘i has two distinct 6-month seasons (Giambelluca and Schroeder, 1998): dry (May – October) and wet (November – April). TWI and omega time series were each aggregated to a seasonal time step by averaging the six monthly values within each season. For rainfall data, the six monthly values were summed for each season. Wet seasons were identified according to the year of the beginning of the season (e.g., the wet season value for 1990 consists of data from 11/1990 to 4/1991). Because the TWI time series has gaps, only seasons with > 75% of the data (based on the number of daily measurements available) were averaged to get a 6-month seasonal value. Most of the missing periods in the TWI time series occurred prior to 1979, and based on the minimum data criterion, the years 1975-1977 were excluded from the time series. After 1979 at least 92% of the data were available for all seasonal means.

An assessment of seasonal climate variability is conducted in three ways: 1) time series data were tested for linear trends using a linear regression model. In a preliminary analysis, 64

climate variable time series were tested for temporal autocorrelation using the Durbin-Watson statistical test (Durbin and Watson, 1971). Of the 64 time series tested, 7(10.9%) we significant at $\alpha = 0.05$ and 2 (3.1%) were significant at $\alpha = 0.01$ and no consistent patterns among stations or variables were identified. Based on these results it was decided to not include a temporal autocorrelation correction in the regression model; 2) change-point analysis (Chen and Gupta, 2011) is used to identify significant shifts within each time series (change-point detection is the name given to a procedure for estimating a point in a time series when a statistically significant shift in the observations occurs; for the TWI time series, change-point detection is applied to the period 1979 to 2013, because of data gaps in the earlier period record (1975-1978); for other data, change-point detection is applied for the whole period of record of each dataset; 3) I tested for long-term change by comparing variable means between two different periods, delimited on the basis of the TWI change-point results as the periods before and after the start of the 1991 dry season and referred to as P1 (1973-1990) and P2 (1991-2013 for the dry season and 1991-2012 for the wet season). Note that the rainfall time series ends in 2007, therefore, the P2 sample size is 17 and 16 for the dry and wet seasons, respectively. Time series data were tested for normality using the Shapiro-Wilk statistical test (α=0.05; Shapiro and Wilk, 1965). For datasets determined to be normally distributed, the Welch two sample t-test.is used to determine if there is a significant difference in the means of the two periods (Welch, 1947). All TWI and omega time series are normally distributed. Some rainfall time series have non-normal distributions and, therefore, the Wilcoxon Rank Sum test (Wilcoxon, 1950) is used to determine if there is a significant difference in means of the two periods. Statistical tests were conducted using R open source statistical software. Statistical significance is assessed at the 90% significance level (α = 0.1) for all of the statistical tests with the exception of the Shapio and Wilk test for normality and

the Durbin Watson test for autocorrelation significance is assessed at the 95% level ($\alpha = 0.05$), using the null hypothesis that the trend is zero.

In addition to the time series method described above relationships between atmospheric variables for various time periods using a linear regression method were tested, and use the correlation coefficient (r) or the coefficient of determination (r^2) to assess the strength of the relationships between variables. Again, statistical significance is assessed at $\alpha = 0.1$.

3.5 Results

3.5.1 TWI Characteristics and Trend Assessment

The TWI is a persistent high elevation climate feature in Hawai‘i occurring on average 80 and 76% of the time for the dry and wet seasons, respectively (Table 3.2). The average TWI base height is 2077 m at Līhu‘e and 2241 m at Hilo. These results are in close agreement with those reported by Cao et al., (2007) who identified the TWI base height at 2076 m and 2255 m at Līhu‘e and Hilo respectively. In a side-by-side comparison for the overlapping time period, the annual average (Līhu‘e and Hilo) TWI frequency of occurrence was 6% lower and the annual mean TWI base height was 62 m lower than those reported by Cao et al. (2007; results not shown). These differences can be explained by the modifications that were made to the Cao et al. (2007) TWI identification criteria.

Trends in the TWI characteristics derived from the linear regression model for the dry and wet seasons at each of the two sounding stations are presented based on the 1973 to 2013 record of the 2 pm (HST) atmospheric sounding data (Figure 3.2). Slight increases in base height were observed for the dry season (0.5 to 1.9 m yr^{-1}), while slight decreases were observed for the wet season (-0.9 to -0.2 m yr^{-1}), but no base height trends were determined to be statistically significant (Table 3.3). The frequency of TWI occurrence was observed to have increased over

the period of record for both seasons. Statistically significant increases of 0.4 and 0.8% yr^{-1} (at Hilo and Līhuʻe, respectively) during the dry season and 0.4 and 0.6% yr^{-1} during the wet season were observed. Increases in TWI frequency were greater at Līhuʻe, which is located ~2˚ north of the Hilo station. Significant increases in TWI strength were observed at both sites in both seasons.

A change-point detection algorithm was applied to all of the TWI time series (1979 – 2013) to identify any significant change years. For the dry season, a TWI frequency change-point was identified at year 1993 (Hilo) and year 1989 (Līhuʻe). For the wet season, 1990 was identified as the change-point year for both stations (Table 3.3). Based on these findings and in an effort to maintain consistency throughout this analysis, the end of 1990 is chosen as the common change point for the time period comparison. TWI frequency data were separated into periods that correspond to observations occurring before (P1 = 1973 - 1990) and after (P2 = 1991 - 2013) the 1990 change-point. For the dry season, P2 means were found to be higher for TWI base height (0.3 and 1.4% for Hilo and Līhuʻe, respectively; not significant), frequency of occurrence (9 and 22%; significant at both stations), and strength (16 and 12%; significant at Hilo) (Table 3.4). For the wet season, P2 means were found to be lower for TWI base height (-1.0 and -0.9%; not significant), and higher for TWI frequency of occurrence (14 and 19 %; significant at both stations) and strength (18 and 19%; significant at both stations). TWI frequency of occurrence was significantly higher during P2 than P1 at both stations for both wet and dry seasons (Figure 3.3).

3.5.2 Omega Trend Assessment

Gridded data obtained from four reanalysis products for vertical velocity of wind variable omega at the 500 hPa level were each averaged for a 10˚ x 10˚ field centered over the

Hawaiian Islands. In addition, a 4-model reanalysis ensemble mean was calculated. Regression analysis indicates a consistent increase in omega (enhanced subsidence) for both the dry and wet seasons for all reanalysis products and the ensemble mean (Figure 3.4). For the dry season, increases in omega range from 0.0001 to 0.0005 hPa s^{-1} yr^{-1} and were determined to be statistically significant for three of the four reanalysis products (the 20CR trend was not significant) and the ensemble mean (Table 3.5). For the wet season, increases ranged from 0.00002 to 0.0007 hPa s^{-1} yr^{-1} and only the ERA40 trend was statistically significant.

Change-point analysis applied to all of the omega time series did not reveal any significant shifts in the record. To maintain consistency, the year 1990 is used as the change point year for the time period comparison. Omega was found to be higher during P2 than P1 for all of the reanalysis time series for both the dry (8-32% higher) and wet (10-44% higher) seasons, and 19% significantly higher (dry season; $p = 0.021$) and 25% higher (wet season; not significant; $p = 0.122$) for the ensemble mean (ENS)(Figure 3.5 and Table 3.6). The difference between time periods was statistically significant for the ERA40 and NNRP products for both seasons and for the ensemble mean during the dry season.

To compare reanalysis products, the correlation coefficient (r) for each pair of omega time series during the time window common to all products (1979–2002; not shown) is used. In general, reanalysis products were well correlated ($r = 0.61$ to 0.94; $p \leq 0.002$). All of the time series show stronger correlation in the wet season than the dry season. The relationship between TWI frequency of occurrence (calculated as the average of Hilo and Līhuʻe TWI data) and omega is also assessed. Significant positive correlations were found between TWI frequency of occurrence data and the omega time series during a common period among models for both dry and wet seasons (Figure 3.6; Table 3.7).

Using the NNRP data set, an expanded field of seasonal omega for the time period comparison (10˚ to 30˚N latitude; -135 to -180 ˚W longitude) is examined. Clear evidence of higher P2 subsidence is apparent over Hawai‘i for both the dry and wet seasons then the difference between the two time periods is examined (Figure 3.7c,f). In general, higher P2 subsidence is found between ~14-24˚N for the dry season and between ~10-22˚N for the wet season for a majority of the longitudinal field analyzed. Additional verification of increases in atmospheric subsidence over the Hawai‘i region in recent decades were obtained by examining NNRP-derived fields of SLP and OLR. Higher P2 SLP (Figure 3.8a:b) and higher OLR (Figure 3.8c:d) are identified over the Hawai‘i region in both seasons. Increases in both SLP and OLR are indicative of increases in atmospheric subsidence (Song and Zhang, 2007; Hu and Fu, 2007).

3.5.3 ENSO and PDO Assessment

TWI frequency and omega data were tested against the MEI and PDO indices for the period 1979-2002. In general, correlations of TWI frequency or omega with either MEI or PDO had opposite signs for dry and wet seasons (Figure 3.9). Linear regression results indicate no significant correlation between the MEI and TWI frequency ($r^2 = 0.05$) or omega derived from the 4 reanalysis products ($r^2 = 0.01$ to 0.05) during the dry season (Table 3.7). Wet season correlations were slightly stronger for TWI frequency ($r^2 = 0.13$; significant) and omega ($r^2 =$ 0.06 to 0.16; significant only for the 20CR omega). When data were compared with the PDO index a similar pattern is observed. During the dry season, PDO is weakly but significantly correlated with TWI frequency ($r^2 = 0.16$), but not significantly correlated with the omega ($r^2 =$ 0.02 to 0.08). For the wet season, there was no significant correlations between PDO and TWI frequency ($r^2 = 0.06$) and correlations between PDO and omega were weak ($r^2 = 0.02$ to 0.13) but significant for the NNRP and 20CR omega time series.

Despite weak correlations, the ENSO and PDO clearly have some effect on the variability of TWI frequency; however, these effects have opposite signs in the dry and wet seasons (Figure 3.9). Considering this, phase changes to these Pacific centered modes do not explain the long-term increase in TWI frequency reported earlier, which were consistent in both seasons (Figure 3.2). In general, correlations between TWI frequency and both the MEI and PDO indices were improved when time series were compared for the shorter P1 and P2 time periods and not assessed for the complete period of record.

3.5.4 Rainfall Trend Assessment

Linear trends were calculated for the dry and wet season rainfall at 21 high elevation climate stations in Hawai‘i from 1973 to 2007. For the dry season regression slopes ranged from -5.6 to +12.2 mm yr^{-1} (Table 3.8, Figure 3.10). Seven stations showed decreases in rainfall over the period and only one of these decreases was statistically significant. For the wet season, negative regression slopes were found at all 21 stations (-0.46 to -42.2 mm yr^{-1}), seven of which were statistically significant.

Change-point detection analysis is applied to the 21 rainfall time series. Results varied widely among stations and between seasons (Table 3.8, Figure 3.10). For the dry season the most common change point year was 1976 (n=12), which corresponds to a large-scale shift in the climate of the Pacific (Miller et al., 1994). All of the dry season shifts identified at the 1976 change-point showed an upward shift in rainfall relative to the pre-shift period. For the wet season, common change-point years were 1981 (n = 9) and 1990 (n = 5), and rainfall shifts were downward for all time series. The years 1981 and 1990 also correspond with periods of low TWI frequency. Average TWI frequency during these years was 14% (1981) and 9% (1990) below the long-term wet season TWI frequency mean. Increases in TWI frequency after these years and

subsequent lower in rainfall may explain why these years were identified in the changepoint detection. The change point 1990 is consistent with the wet season TWI frequency changepoint detection results.

Rainfall was assessed using the time period comparison defined earlier. Again, to maintain consistency among time series, the end of 1990 is used as the change point (P1 = 1973-1990; P2 = 1991-2007). For the dry season, results varied with lower P2 rainfall (-3 to -37%; relative to P1 rainfall) found at eight stations and higher P2 rainfall (+0.4 to +14%; relative to P1 rainfall) found at the other 13 stations (Table 3.9). For the wet season, lower P2 rainfall (-10 to -40%; relative to P1) were found consistently at all 21 stations. Eleven of the 21 wet season P1 versus P2 rainfall comparisons found statistically significant differences. In general the magnitude of changes in rainfall were much greater in wet season (Figure 3.10)

Correlations between rainfall at the 21 climate stations and TWI frequency and the 4-model omega ensemble time series (Figure 3.11) were tested for significance. Dry season correlations ranged from $r^2 = 0.00$ to 0.31for the TWI comparison and seven of the 21 comparisons were significant. For the wet season, significant correlations between rainfall and TWI frequency were found at all stations ($r^2 = 0.10$ to 0.44). For the dry season, correlations between rainfall and omega ranged from $r^2 = 0.00$ to 0.34 and 12 of the 21 stations were significant. Wet season rainfall was significantly correlated with omega at all 21 stations ($r^2 =$ 0.14 to 0.58). Of the eight stations that showed lower P2 dry season rainfall (Table 3.9), seven were also significantly correlated with both TWI frequency and Omega (Figure 3.11).

3.6 Summary and Discussion

Using TWI data from two atmospheric sounding stations, omega data from four reanalysis products, and rainfall data from 21 high elevation climate stations, long-term changes

atmospheric subsidence over the Hawai‘i region and the subsequent effects that these changes have had on rainfall at high elevations were examine.

I have found a significant increase in TWI frequency and TWI strength over the past ~four decades for both the dry and wet seasons most notably defined by an abrupt upward shift in the early 1990s. Increases in the vertical velocity of wind variable omega have been identified in four reanalysis datasets and were in agreement with changes in the TWI. Considering that TWI frequency is significantly correlated with omega, I hypothesize that increases in the intensity of HC subsidence are driving increases in the TWI frequency of occurrence.

Determining the causes of increases in HC subsidence is not within the scope of this study. However, many modeling studies have suggested multiple climate forcings that could alter the width and intensity of the HC (see Lucas et al., 2013). A primary source of tropical climate variability is ENSO, but the influence of ENSO on the HC is still debated. Oort and Yienger (1996) showed that HC intensity has a tendency to increase during the warm phase of ENSO due to enhanced convection in the equatorial central Pacific resulting in more persistent subsidence in the subtropics during the winter (DJF) months. Quan et al. (2004) showed that HC responses to ENSO were much stronger during the warm (El Niño) phase than during the cool La Niña phase. More recently, Stachnik, and Schumacher (2011) found that various reanalysis datasets show a weak, but statistically significant increase in HC intensity in the Northern Hemisphere (NH) during El Niño. In contrast to these findings, Tanaka et al. (2004) and Mitas and Clement (2005) found little relationship between the NH wintertime HC intensity and ENSO, and Caballero (2007) found that more than 70% of HC variability was not related to ENSO. To my knowledge no study has attempted to connect fluctuations in HC intensity with changes in PDO

phase. However, the HC has been shown to widen during the cool phase of PDO (Grassi et al., 2012).

In this study I find that correlations between omega, and the ENSO and PDO indices are weak and not statistically significant (Table 3.7). In addition, the effects these Pacific-centered modes have on TWI frequency and omega were opposite for the dry and wet seasons (Figure 3.9) and are not consistent with the ~1991 positive shift in TWI frequency (Figure 3.3) and omega (Figure 3.5) identified over the Hawai‘i region in this study which occurs in both seasons. Cao et al. (2007) demonstrated that during the warm phase of ENSO, wet season TWI frequency is greater, resulting in drier conditions at high elevations. I agree that ENSO phase changes may play some role in the TWI frequency of occurrence, but statistical correlations were weak when the entire time series is considered and inconsistent between seasons (Figure 3.9). The relationship between wet season TWI frequency and ENSO phase change is statistically significant, but explains only about 13% of the variance in the time series (Table 3.7). When subsets of the period-of-record (P1 and P2, before and after the end of 1990, respectively) were assessed, correlations between TWI frequencies and the MEI index were greatly improved for both seasons. When these shorter time periods were assessed, ENSO phase change explains 41% (P1) and 26% (P2) of the variance in the wet season TWI frequency time series. In general, correlations with the PDO and TWI frequency were also improved when data were separated into pre- and post-shift periods. This body of evidence suggests that while both ENSO and PDO may explain some of the variability in TWI frequency they do not explain the longer-term change, i.e. the shift between the 1973-1990 and 1991-2013 periods, reported here. Correlations between omega and the ENSO and PDO indices were weak and not significant (Table 3.7), which suggests that alternative forcing mechanisms are driving the observed increase in HC

intensity. In addition to the results reported here, Merrifield (2011) has shown that the 20% increase in the amplitude of Pacific trade winds from 1990 to 2009 relative to the previous 40-year period is linked to an increase in atmospheric circulation and is not explained by ENSO and PDO phase changes. The fact that this reorganization of the wind system is not consistent with a Pacific-only SST driving mechanism, suggests that that changes outside the tropical Pacific might be important (McGregor et al., 2014). McGregor, et al. (2014) has concluded that the unprecedented acceleration of the Pacific trade wind system since the early 1990's is, in fact, driven by rapid warming of the Atlantic in relation to the Pacific. Yu et al., (2014) has suggested that a positive phase change in the Atlantic Multi-Decadal Oscillation (AMO) occurring in the early 1990s is responsible for a strengthening of the sub-tropical high in the Pacific and the subsequent increases in trade wind strength.

Climate forcing mechanisms unrelated to ENSO or PDO that may explain increased HC subsidence include warming due to enhanced GHG concentrations and associated SST increases, the indirect or direct effects of aerosols, and/or the depletion of stratospheric ozone, which have been hypothesized to affect HC width (Lucas et al., 2013). Global simulations of future climate show that the margins of Hadley cell circulation will move poleward in both hemispheres and in all seasons as a result of global warming (e.g. Kang and Lu, 2012). Cao et al. (2007) suggested that a global warming-related poleward shift in mid-latitude storm tracks (Yin, 2005) would cause fewer interruptions of Hadley cell subsidence over Hawai‘i, thus increasing TWI persistence at least for the wet season when storms are more prevalent. In general, an expansion of the HC due to climate change (Seidel et al., 2008) would make interruptions of subsidence less frequent in Hawai‘i for both the dry and wet seasons.

To identify the effects that increases in subsidence have on seasonal high elevation rainfall patterns I compared 21 rainfall time series with TWI frequency and omega data. The results indicate a mixed signal in the dry season and a consistent drying signal in the wet season. For the dry season, rainfall at 7 stations (Figure 3.11) was significantly correlated with both TWI frequency and omega and rainfall at these stations was 16% lower in P2 than in P1. The average P2 rainfall for the other 14 stations was 4% higher (not significant) in P2 than in P1. When rainfall is averaged for all 21 stations there is a -3% change in dry season rainfall from P1 to P2 (Table 3.9). These findings suggest that, in general, an increase in subsidence has contributed to a slight overall P2 decrease in high elevation dry season rainfall although decreases at some individual stations (significantly correlated with TWI frequency) P2 decreases were much more pronounced. For the wet season, rainfall at all of the 21 stations was significantly correlated with both TWI frequency and omega (Figure 3.11) and the average rainfall for the 21 stations analyzed was 40% lower in P2 than in P1 (Table 3.9).

The spatial dynamics and temporal trends in rainfall have been a topic of great interest to many researchers in Hawai‘i. Previous studies have examined rainfall variability on seasonal (Lyons, 1982; Chu, 1989; Frazier et al., 2013), inter-annual and decadal time scales (Chu and Chen, 2005; Timm and Diaz, 2009; Chu et al., 2010; Elison Timm et al., 2011; Diaz and Giambelluca, 2012; Frazier et al., 2013). Kurk and Levinson (2008) detected a statistically significant downward trend in rainfall since 1905 (see also Diaz and Giambelluca, 2012), and Elison Timm et al. (2011) and Chu et al. (2010) have shown a decrease in the frequency of moderate and extreme rainfall events.

In other studies, Diaz et al. (2011) found evidence of drying in vertical humidity profiles at higher elevations, and Krushelnycky et al. (2012) noted an increase in the number of zero

rainfall days at a leeward high elevation site. While it has been well established that rainfall patterns are influenced by phases changes in ENSO and PDO (e.g. Chu and Chen, 2005; Frazier 2012), recent evidence suggests rainfall patterns have decoupled from these modes in the last decade (Diaz and Giambelluca, 2012)

Sustained increases in the TWI frequency pose several threats to high elevation ecosystems including decreases in stream flow and groundwater recharge (Bassiouni and Oki, 2012). Diaz et al. (2011) noted an increase in the lifting condensation level since ~2000 on the Island of Hawai‘i, which combined with a increase in TWI frequency would reduce the thickness of the cloud zone thus decreasing rainfall and cloud water interception there (Giambelluca and Gerold, 2011). In addition, the increases in TWI frequency over the past ~two decades may have already altered biota at high elevations. Increases in temperature, solar radiation, and the number of zero rainfall days, all of which are products of increased inversion frequency, have been linked to the decline of an iconic high-elevation endemic species, the Haleakalā Silversword (Argyroxiphium sandwicense subsp. macrocephalum)(Krushelnycky et al., 2013).

It is unclear if reported increases in TWI frequency and the subsequent decreases in rainfall will persist in the future. I have demonstrated that at least some of these trends can be linked to broader circulation patterns, potentially caused by anthropogenic global warming (Dai, 2011). Lauer et al., (2013) has used future CMIP5 projections to determine that TWI frequency of occurrence will increase by 11%, and the TWI base height will decrease by ~160 m by 2100. If expected increases in the TWI frequency of occurrence hold true additional decreases in high-elevation rainfall can be expected in both seasons in the future.

Chapter 3 Tables

Table 3.1: Reanalysis datasets used in this study.

Dataset	Source	Period	Spatial Resolution
ERA40	ECMWF	1973- 2002	2.5˚ X 2.5˚ X 23
NNRP	NCEP/NCAR	1973 - 2013	2.5˚ X 2.5˚ X 17
NDRP	NCEP/DOE	1979 - 2013	2.5˚ X 2.5˚ X 17
20CR	NOAA/CIRES	1973 - 2012	2.0˚ X 2.0˚ X 24

Period is the range of reanalysis data used from each dataset; spatial resolution is the latitude, longitude and pressure levels available for each data set.

Table 3.2: Seasonal TWI characteristics at Hilo and Līhuʻe (1973-2013); Base Ht. is the average base height of the TWI; Frequency is the average Frequency of occurrence of the TWI, Strength is the average strength of the TWI.

	Dry-Season						Wet-Season					
Station	Base Ht. (m)		Frequency (%)		Strength (˚C m^{-1})		Base Ht. (m)		Frequency (%)		Strength (˚C m^{-1})	
	mean	sd	mean	sd	mean	sd	mean	sd	mean	sd	mean	sd
Hilo	2284 ±	83	80 ±	8	0.005 ±	0.001	2198 ±	89	74 ±	10	0.006 ±	0.001
Līhuʻe	2131 ±	85	79 ±	12	0.004 ±	0.001	2023 ±	92	78 ±	10	0.007 ±	0.001

Table 3.3: Linear regression results for TWI variables (1973 – 2013).

	Dry-Season					Wet-Season				
Base Height	**Trend (m yr^{-1})**	**r^2**	**SE**	**p**	**C-Y**	**Trend (m yr^{-1})**	**r^2**	**SE**	**p**	**C-Y**
Hilo	0.5	0.00	1.22	0.689	No	-0.1	0.00	1.36	0.944	No
Līhuʻe	1.9	0.07	1.20	0.118	2003	-0.9	0.01	1.39	0.525	No
Frequency	**Trend (% yr^{-1})**					**Trend (% yr^{-1})**				
Hilo	0.35	0.27	0.09	0.001	1993	0.40	0.20	0.14	0.006	1990
Līhuʻe	0.81	0.65	0.10	0.000	1989	0.59	0.43	0.12	0.000	1990
Strength	**Trend (˚C m^{-1} yr^{-1})**					**Trend (˚C m^{-1} yr^{-1})**				
Hilo	0.00005	0.18	2E-05	0.009	No	0.00005	0.27	1E-05	0.001	No
Līhuʻe	0.00003	0.08	2E-05	0.077	No	0.00005	0.26	2E-05	0.001	No

Trend is the slope of the regression line; r^2 is the coefficient of determination; SE is the standard error of the slope in the same units as "Trend" for each variable; p is a measure of statistical significance; C-Y is the year at which a statistically significant shift in the data occurs. For dry season n = 38; for wet season n = 37.

Table 3.4: Relative differences in TWI characteristics between time periods P1(1973 to 1990) and P2(1991 to 2013).

	Dry-season		Wet-season	
Base Height	**Diff (%)**	**p**	**Diff (%)**	**p**
Hilo	0.3	0.803	-1.0	0.516
Līhuʻe	1.4	0.232	-0.9	0.590
Frequency				
Hilo	9.3	0.001	14.4	0.002
Līhuʻe	21.7	0.000	19.1	0.000
Strength				
Hilo	16.0	0.021	18.0	0.003
Līhuʻe	12.1	0.114	19.1	0.001

Diff is the percent difference between the two time periods calculated as: Diff = (1 – (P1 mean / P2 mean)) *100

Table 3.5: Linear regression results for omega.

	Dry-Season						Wet-Season					
Dataset	**Trend (hPa s^{-1} yr^{-1})**	**n**	**r^2**	**SE**	**p**	**C-Y**	**Trend (hPa s^{-1} yr^{-1})**	**n**	**r^2**	**SE**	**p**	**C-Y**
ERA40	0.00053	30	0.23	2.E-04	0.008	No	0.00066	29	0.15	3.E-04	0.040	No
NNRP	0.00027	41	0.16	1.E-04	0.009	No	0.00024	40	0.05	2.E-04	0.155	No
NDRP	0.00015	35	0.08	9.E-05	0.098	No	0.00021	34	0.03	2.E-04	0.364	No
20CR	0.00010	40	0.05	7.E-05	0.146	No	0.00002	39	0.00	2.E-04	0.935	No
ENS	0.00019	41	0.14	8E-05	0.015	No	0.00020	40	0.03	2.E-04	0.252	No

Note: time series lengths differ for each dataset ERA40:1973 – 2002, NNRP: 1973 – 2013, NDRP: 1979 – 2013, 20CR: 1973 – 2012, ENS: 1973 – 2013.

Table 3.6: Differences in mean omega between time periods P1 (1973 to 1990) and P2 (1991 to 2013).

	Dry-season		Wet-season	
Dataset	**Diff (%)**	**p**	**Diff (%)**	**p**
ERA40	32	0.009	44	0.017
NNRP	25	0.035	29	0.094
NDRP	12	0.133	25	0.235
20CR	8	0.216	10	0.554
ENS	19	0.021	25	0.122

Table 3.7: Coefficient of determination (r^2) values derived from linear regression between omega, TWI Frequency and the MEI and PDO indices (1979 – 2002).

	Dry-season		Wet-season	
vs. TWI	**r^2**	**p**	**r^2**	**p**
ERA40	0.458	0.000	0.329	0.004
NNRP	0.283	0.007	0.227	0.019
NDRP	0.287	0.007	0.301	0.006
20CR	0.287	0.007	0.318	0.004
ENS	0.402	0.001	0.321	0.004
vs. MEI				
ERA40	0.011	0.627	0.096	0.150
NNRP	0.032	0.405	0.064	0.232
NDRP	0.009	0.651	0.083	0.171
20CR	0.047	0.309	0.159	0.054
ENS	0.008	0.684	0.108	0.117
TWI	0.048	0.305	0.134	0.079
vs. PDO				
ERA40	0.021	0.497	0.028	0.444
NNRP	0.078	0.187	0.119	0.099
NDRP	0.058	0.257	0.047	0.311
20CR	0.023	0.478	0.237	0.016
ENS	0.052	0.286	0.106	0.121
TWI	0.155	0.057	0.060	0.248

TWI is trade wind inversion frequency of occurrence, MEI is the Multivariate ENSO Index, PDO is the Pacific Decadal Oscillation index.

Table 3.8: Time trends in rainfall, based on least-squares linear regression for 21 high elevation rainfall time series (1973-2007).

		Dry-season					Wet-season				
SKN	Elev (m)	Trend (mm yr^{-1})	r^2	SE	p	C-Y	Trend (mm yr^{-1})	r^2	SE	p	C-Y
71	1905	-5.4	0.14	2.3	0.025	1997	-2.1	0.01	3.6	0.555	1996
82	1920	12.3	0.08	7.1	0.094	1976	-9.3	0.03	9.5	0.334	1979
121	1920	3.3	0.03	3.4	0.328	1976	-3.9	0.02	4.8	0.421	1979
125.1	1920	4.2	0.01	6.6	0.524	1976	-19.2	0.11	9.7	0.057	1990
259.3	1939	-0.7	0.00	8.3	0.937	1977	-42.2	0.12	19.8	0.041	1990
125	1958	0.6	0.00	4.1	0.894	1976	-10.6	0.07	6.7	0.123	1981
107	1984	0.6	0.01	1.0	0.543	1984	-0.5	0.00	1.8	0.791	1981
80	2045	1.4	0.01	2.7	0.605	1976	-7.0	0.09	3.9	0.080	1975
113	2121	0.3	0.00	2.1	0.868	1975	-1.0	0.00	3.3	0.764	1979
259.5	2134	2.6	0.03	2.5	0.306	1976	-11.9	0.05	8.9	0.191	1990
338	2143	3.4	0.07	2.2	0.131	1976	-16.6	0.09	9.0	0.076	1981
278	2195	-1.7	0.00	10.4	0.870	1977	-20.8	0.05	16.6	0.220	1990
259.4	2231	-1.5	0.01	2.6	0.581	1976	-14.7	0.07	9.2	0.120	1981
102.1	2268	1.4	0.02	1.5	0.374	2004	-0.7	0.00	2.4	0.781	1975
120	2362	0.2	0.00	3.3	0.955	1975	-12.8	0.11	6.4	0.053	1981
279	2459	3.5	0.02	4.8	0.471	1976	-2.5	0.00	9.1	0.782	1981
76	2530	-0.8	0.00	2.4	0.740	1976	-9.6	0.16	3.9	0.019	1981
339.5	2589	1.3	0.01	1.9	0.493	1976	-9.1	0.06	6.2	0.152	1990
111	2810	-0.1	0.00	2.4	0.972	1976	-11.5	0.14	5.0	0.027	1979
339.6	2989	1.5	0.02	2.1	0.475	1981	-6.8	0.02	7.6	0.377	1981
39	3397	-0.2	0.00	1.6	0.899	1977	-3.4	0.03	3.7	0.353	1981

SKN is the state key number used to identify rainfall stations; n = 28 for the dry season; n = 27 for the wet season

Table 3.9: Differences in mean rainfall anomalies between time periods P1 (1973 to 1990) and P2 (1991 to 2013).

		Dry-season		Wet-season	
SKN	ELEV (m)	Diff (%)	p	Diff (%)	p
71	1905	-36.6	0.089	-18.2	0.287
82	1920	12.7	0.152	-20.9	0.232
121	1920	11.2	0.503	-28.8	0.066
125.1	1920	6.8	0.404	-37.9	0.077
259.3	1939	-15.4	0.368	-59.9	0.045
125	1958	0.4	0.909	-36.6	0.066
107	1984	4.4	0.986	-17.6	0.442
80	2045	-2.8	0.552	-37.4	0.125
113	2121	0.7	0.895	-10.3	0.386
259.5	2134	1.2	0.986	-59.3	0.194
338	2143	7.6	0.807	-67.2	0.048
278	2195	-7.0	0.786	-31.2	0.066
259.4	2231	-34.7	0.151	-57.7	0.125
102.1	2268	7.8	0.756	-15.7	0.483
120	2362	1.0	0.987	-57.6	0.057
279	2459	2.7	0.909	-9.6	0.683
76	2530	-9.4	0.636	-63.6	0.014
339.5	2589	4.6	0.756	-58.8	0.026
111	2810	-3.1	0.832	-72.8	0.035
339.6	2989	6.7	0.883	-33.2	0.318
39	3397	-10.2	0.656	-47.3	0.273

Chapter 3 Figures

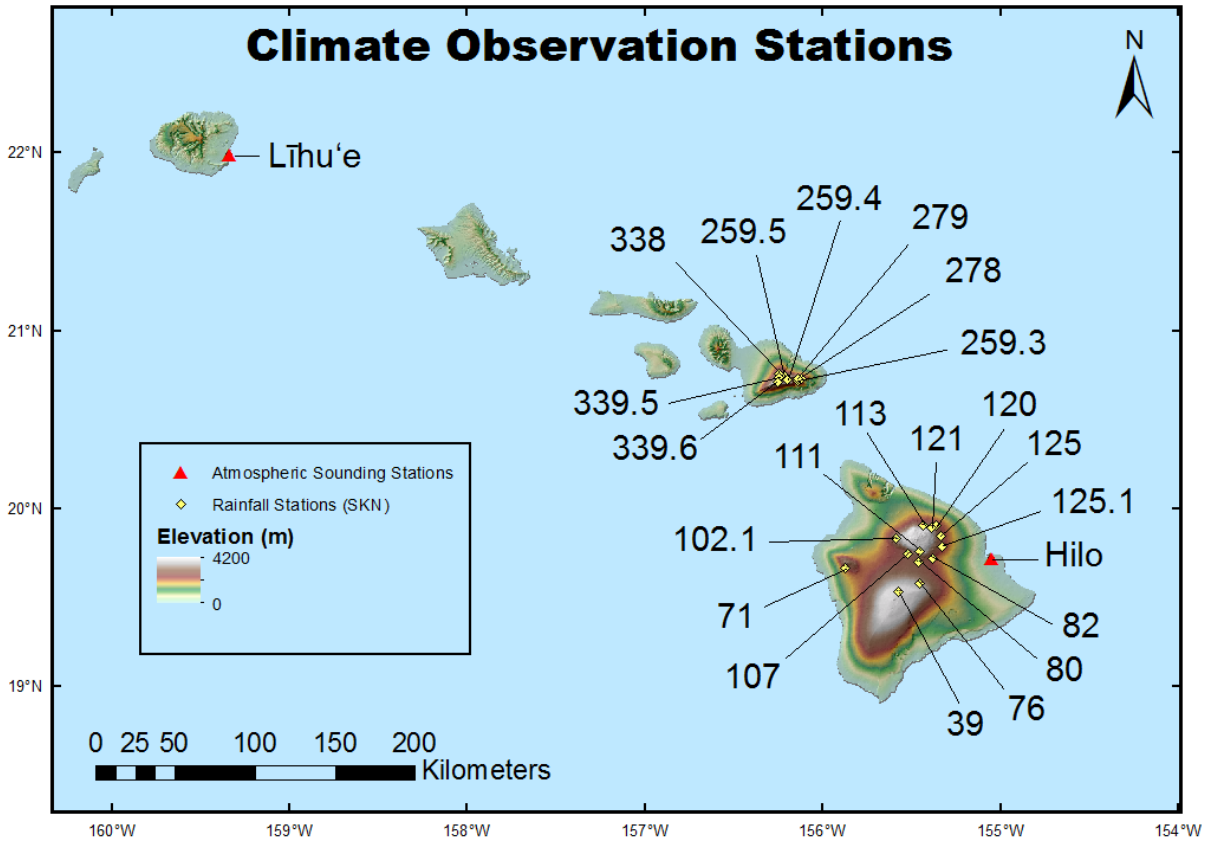

Figure 3.1: Atmospheric sounding and rainfall stations used in this study. Rainfall stations are referenced by the state key number found in the Rainfall Atlas of Hawai'i.

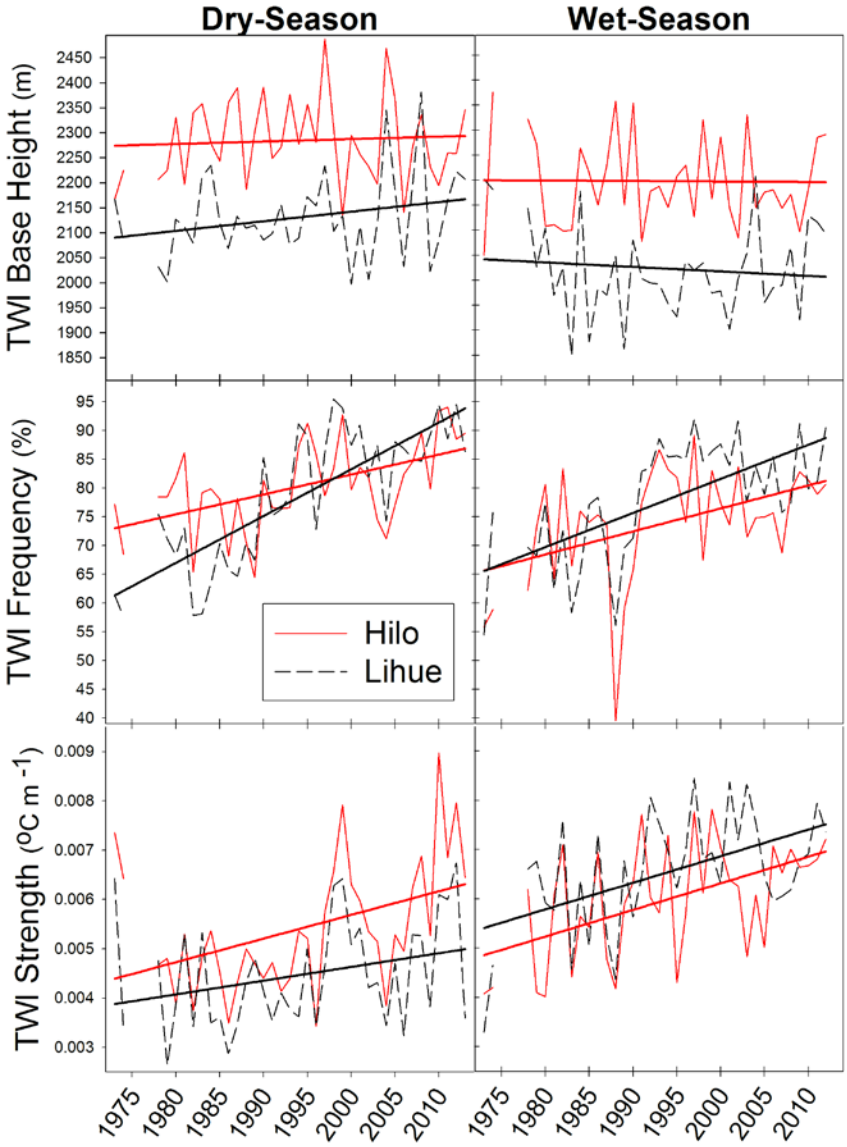

Figure 3.2: TWI characteristics; base height (top), frequency of occurrence (middle), and strength (bottom) for dry (left) and wet (right) seasons from 1973 – 2013.

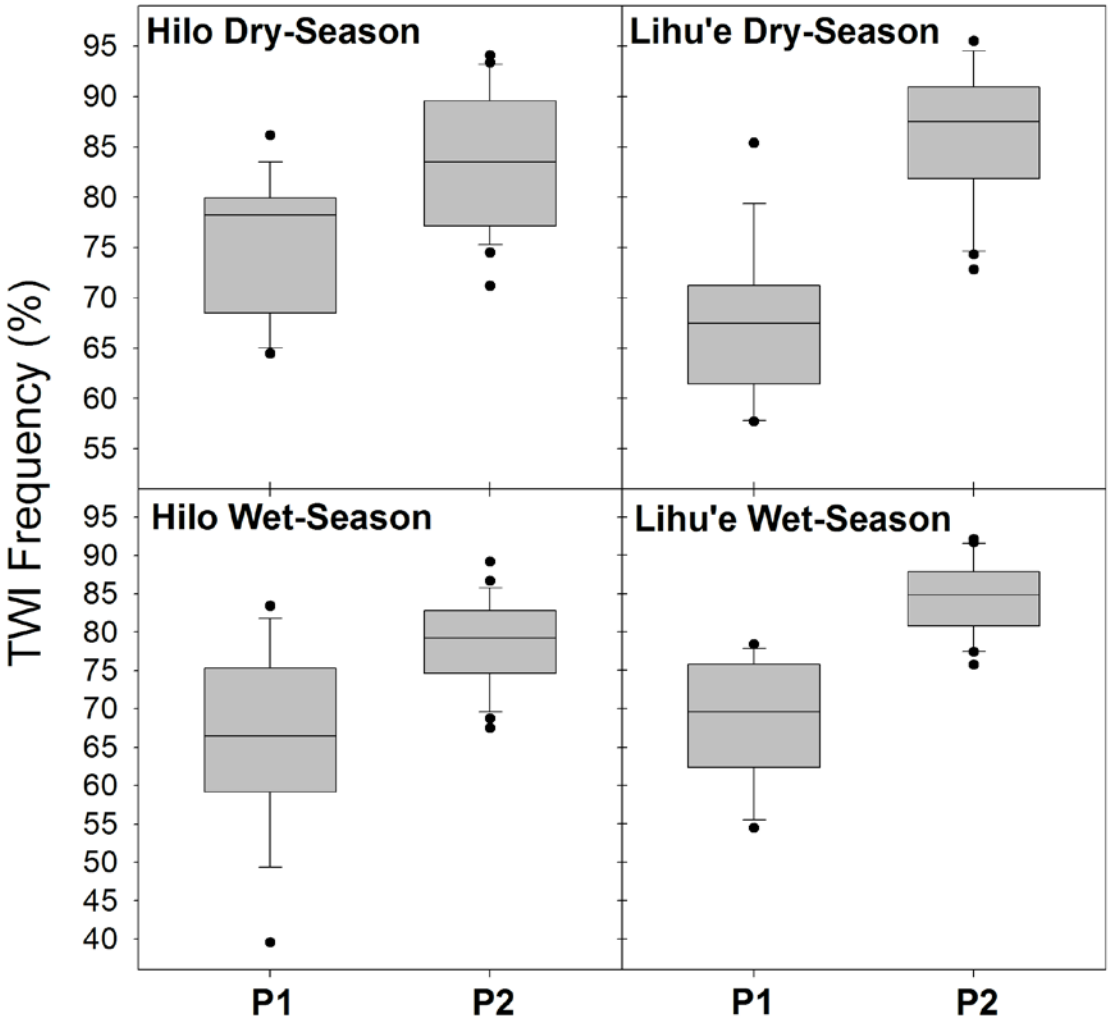

Figure 3.3: TWI frequency of occurrence for Hilo (left) and Līhuʻe (right) for the dry (top) and wet (bottom) seasons; P1 = 1973 – 1990; P2 = 1991 – 2013; the center line in the box is the median; hinge lines represent the 1st and 3rd quartile; horizontal lines on the top of the whiskers refer to the maxim and minimum values excluding outliers; outliners are defined as any point > or > 1.5 * the inter-quartile range (IQR)

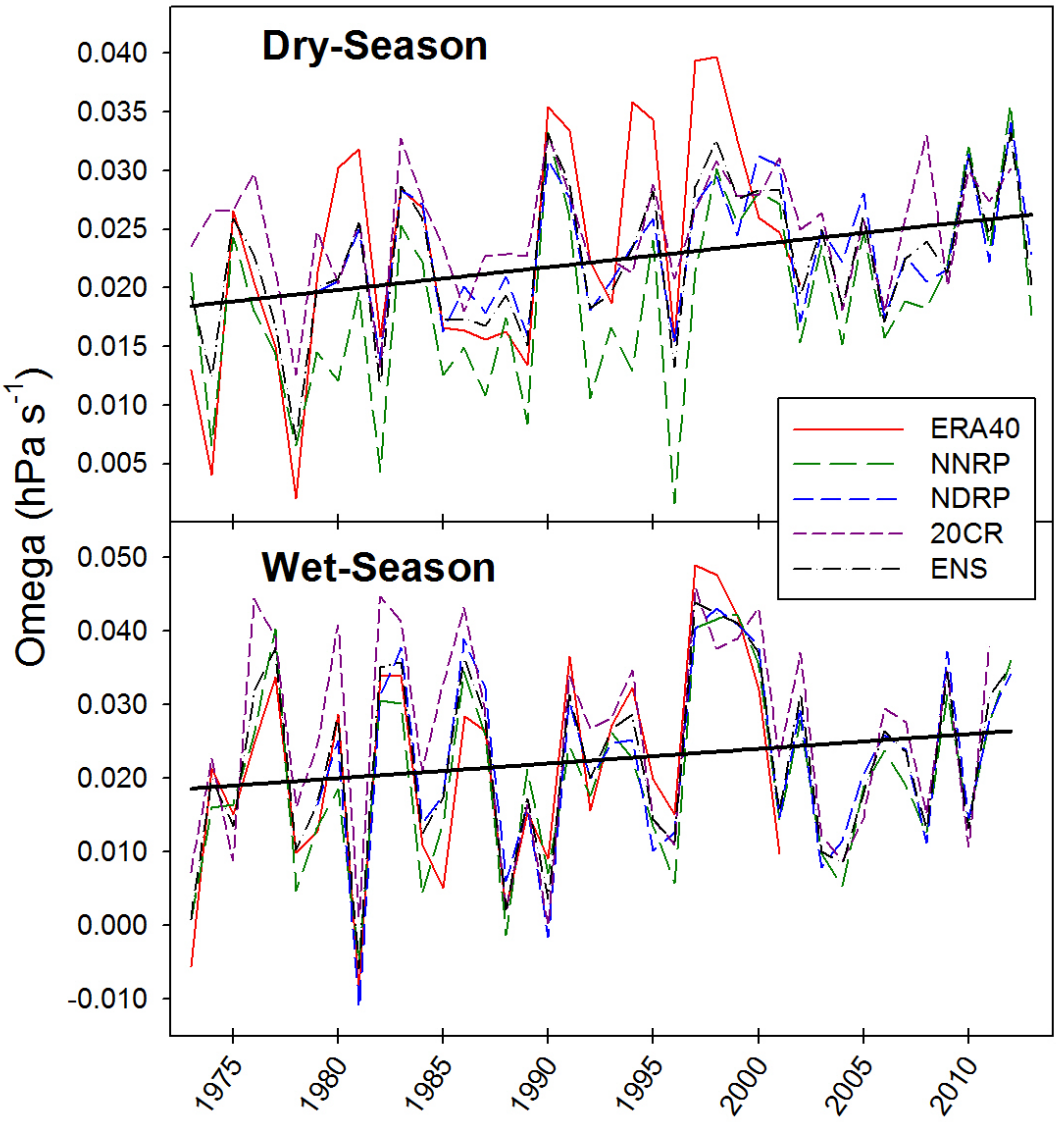

Figure 3.4: Average omega from four reanalysis products and 4-model reanalysis ensemble for dry (top) and wet (bottom) seasons; regression line is derived from the 4-model reanalysis ensemble.

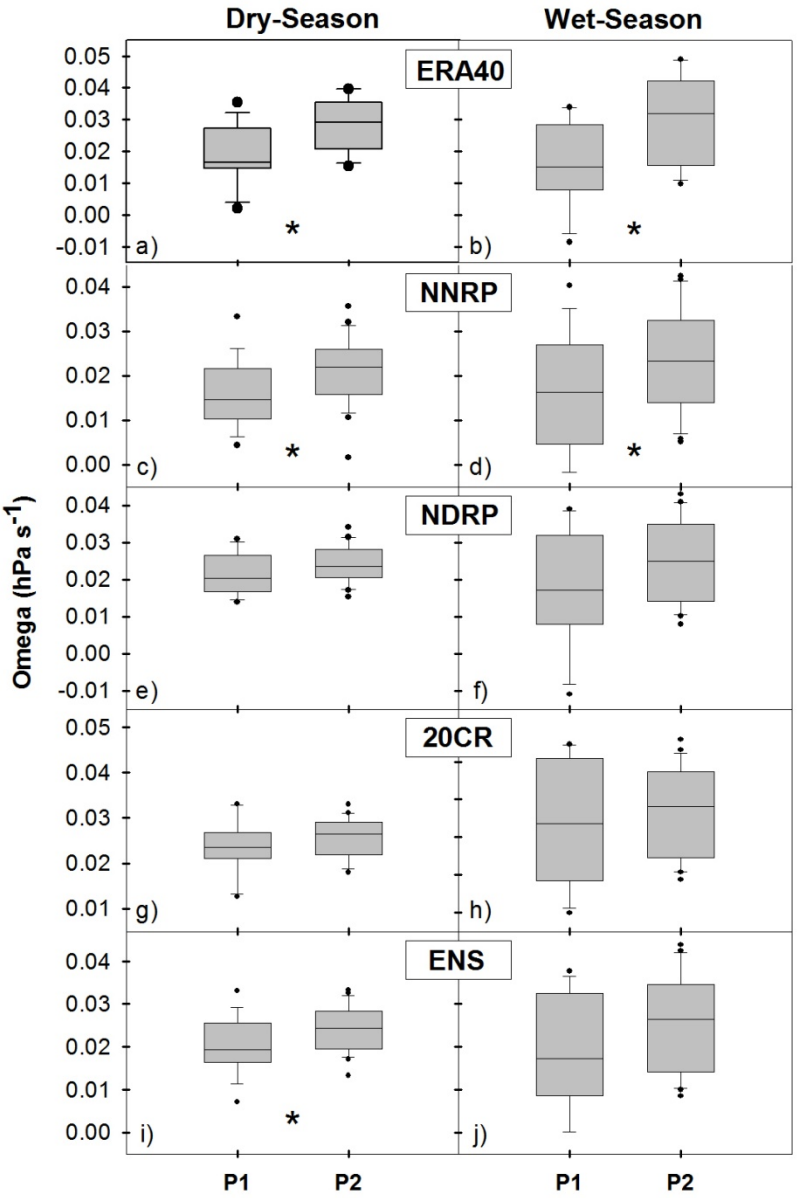

Figure 3.5: Omega time period assessment results for ERA40 (a,b), NNRP (c,d), NDRP (e,f), 20CR (g,h) reanalysis products and the 4-reanalysis ensemble (ENS; i,j) for the dry (left) and wet (right) seasons (asterisk indicates significant difference between periods).

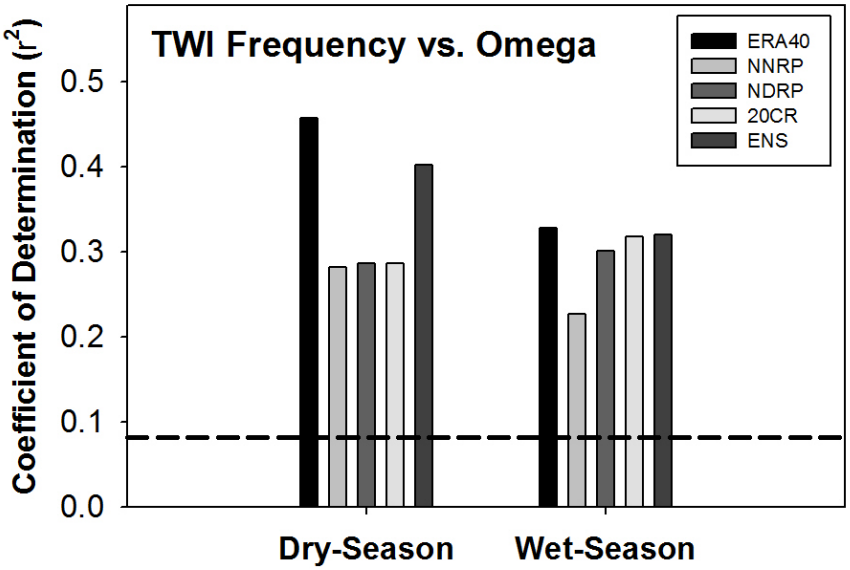

Figure 3.6: Coefficient of determination (r^2) between average TWI frequency (two station average) and omega time series between the period 1979-2002; dashed line represents the r^2 critical value at α =0.10 for a fixed sample size of 34 (df = 32), values above this threshold are considered statistically significant.

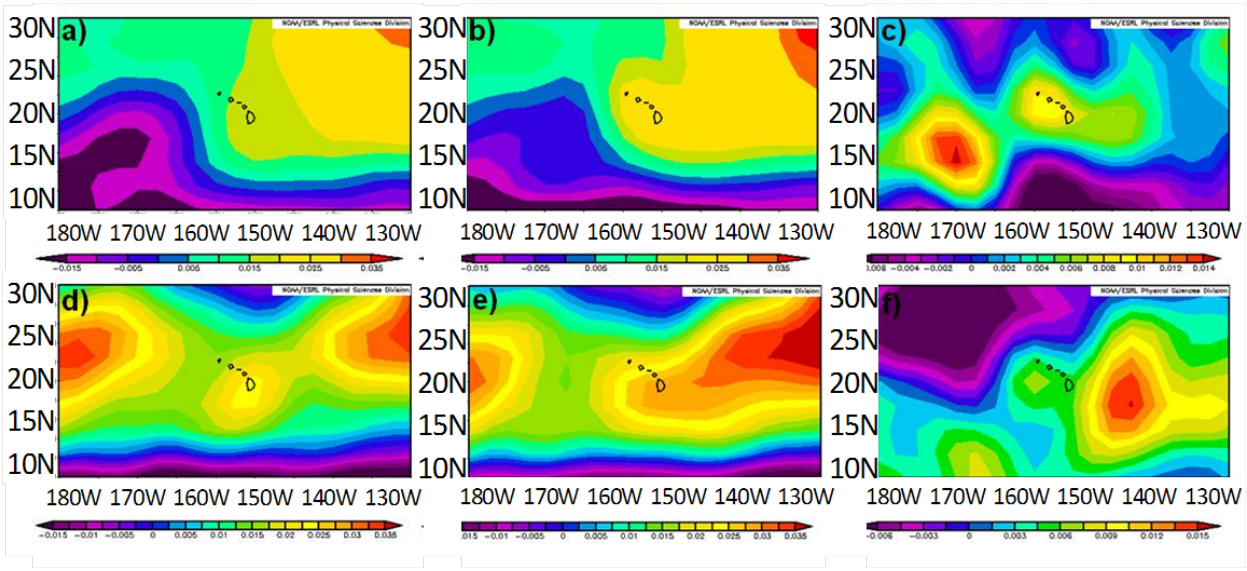

Figure 3.7: Composite mean NNRP-derived omega at the 500 hPa level for dry (top panel) and wet (bottom panel) seasons for P1 (a,d), P2 (b,e) and differences between P1 and P2 c,f; calculated as P2 mean minus P1 mean).

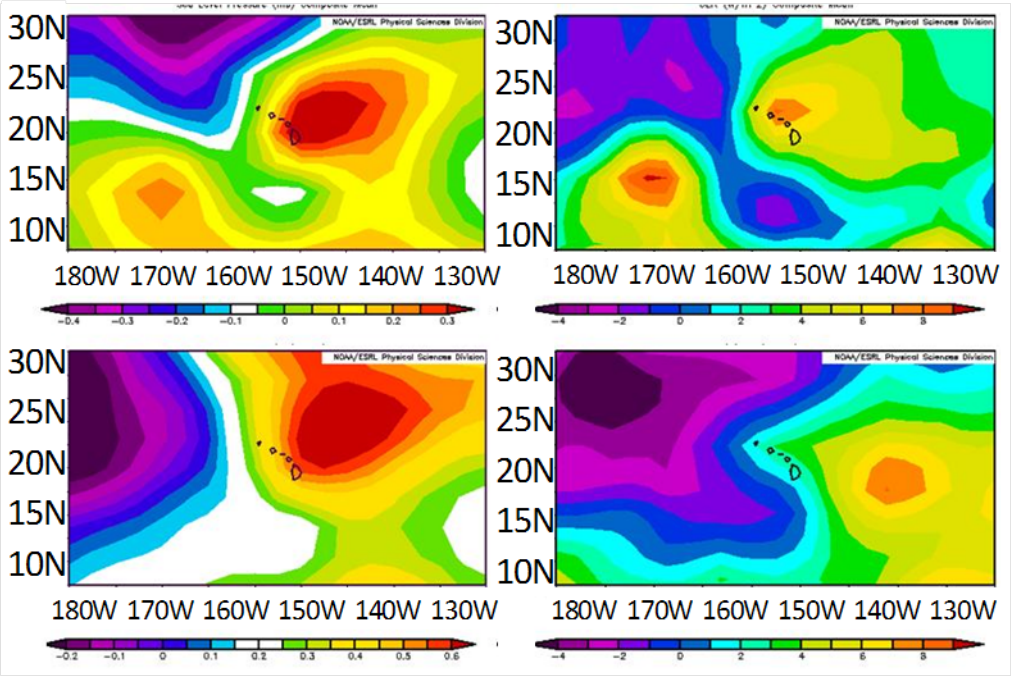

Figure 3.8: Differences in the mean SLP (left panel) and OLR (right panel) for the dry (top) and wet (bottom); calculated as P2 mean minus P1 mean.

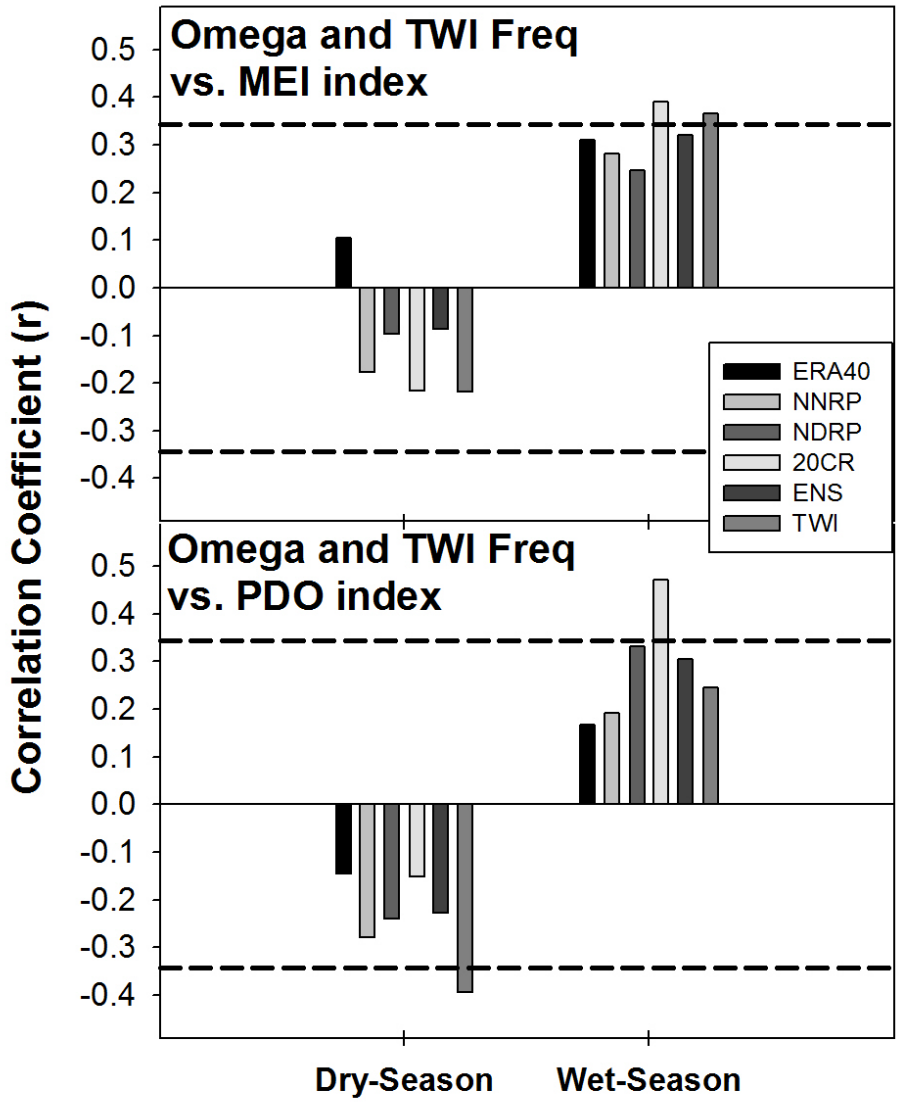

Figure 3.9: Correlation (r) between omega and TWI frequency, and the MEI index (top), the PDO index (bottom) during 1979-2002; dashed line represents the r critical value at α =0.10 for a fixed sample size of 34 (df = 32), values above (upper) and below (lower) this threshold are considered statistically significant.

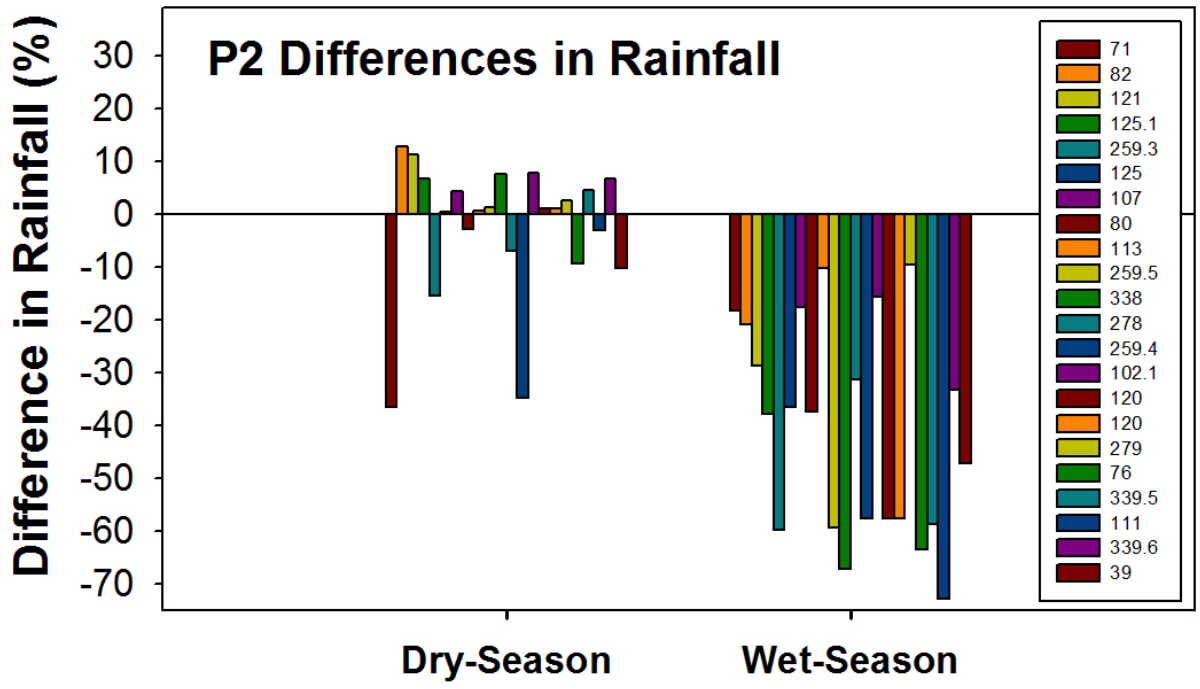

Figure 3.10: Changes in rainfall between 1973-1990 (P1) and 1991-2007 (P2) calculated as P2 mean minus P1 mean at high elevation stations for dry (left) and wet (right) seasons.

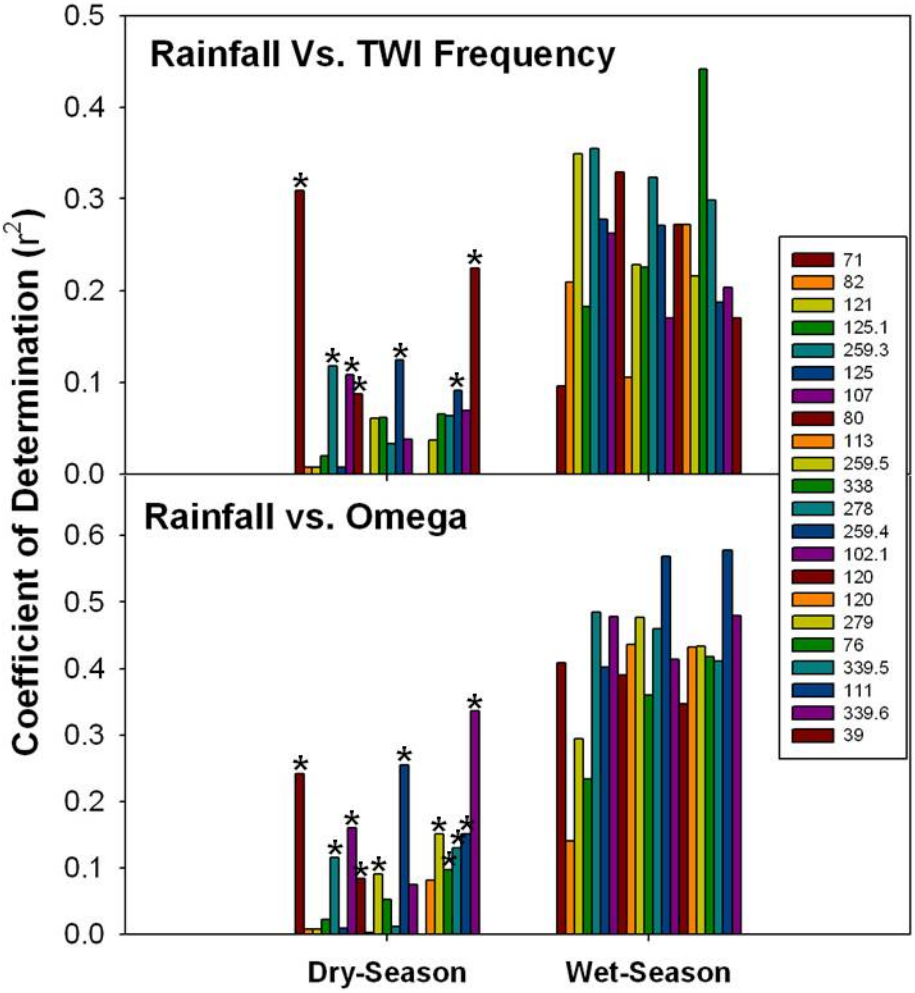

Figure 3.11: Amount of variance in seasonal rainfall at 21 individual stations explained by variations in two station seasonal mean TWI frequency (top) and the omega 4-model ensemble (bottom) for wet and dry seasons (1979-2002). Note: stations are positioned in order of increasing elevation (left to right) for each season; dry season stations with a asterisk and all wet season stations are considered significantly correlated with TWI frequency ($p \leq 0.1$).

CHAPTER 4. THE EFFECTS OF ENSO AND PDO ON MONTANE CLIMATES IN HAWAIʻI

4.1 Abstract

The trade wind inversion (TWI) is a prominent feature in the climate system of Hawaiʻi. On average the TWI is present in 78% of the year, however, the frequency of TWI occurrence can fluctuate on annual, seasonal, inter-annual and inter-decadal time scales. The primary objective of this research is to determine how Pacific centered modes of climate variability affect TWI frequency and to show how variations in TWI frequency influence energy and moister regimes at high and mid-elevations in Hawaii. In this study, the multivariate El Niño Southern Oscillation (ENSO) index and Pacific Decadal Oscillation (PDO) were used to determine how modes of natural climate variability affect the TWI frequency of occurrence during the 6-month dry and wet seasons of Hawaiʻi. Observations of solar radiation, rainfall and relative humidity obtained from HaleNet (Maui, Hawaiʻi) were used to determine how TWI frequency variability affects the climate at high and mid elevations on Maui, Hawaiʻi. Results show that the responses of TWI occurrence frequency to ENSO and PDO are significant and the dry season response is opposite of that in the wet season. For the dry season, mean TWI frequency of occurrence is 8.4% and 6.8% higher (significant at $p = 0.02$) during the cool phase of ENSO and PDO, respectively, relative to the warm phase means. For the wet season, mean TWI occurrence frequency is 4.6% lower (significant at $p = 0.1$) and 2.6% lower (not significant at $p = 0.19$) during cool phase of ENSO and PDO, respectively, relative to the warm phase means. The frequency of the TWI was determined to be significantly correlated with the climate variables; solar radiation, rainfall and relative humidity during the dry and wet seasons at high elevations and with solar radiation and rainfall at mid-elevation stations during the wet season. Linear

regression is used to determine how ENSO- and PDO-driven changes to TWI frequency affect the climate variables over the period 1991 to 2013. Results show that the general tendency toward more negative ENSO and PDO phase conditions over the study period has resulted in a 4.2% increase and a 1.8% decrease in mean TWI frequency for the dry and wet seasons, respectively. Dry season increases in TWI frequency are related to the observed increases in solar radiation (3% decade^{-1}; significant at $p = 0.03$; 4 stations) and decreases in rainfall (-5 decade^{-1}; significant at $p = 0.10$; 3 stations) and decreases in relative humidity (-6 % decade^{-1}; significant at $p = 0.09$; 3 stations) found at high elevation. For the wet season, decreases in TWI frequency is related to the observed decadal decreases in solar radiation (2% decade^{-1} significant at $p = 0.06$; 2 stations) and increases in relative humidity (9% decade^{-1}; significant at $p = 0.03$; 2 stations) at high elevations.

4.2 Introduction

The steep topography of the Hawaiian Islands interacts with general and local atmospheric circulation to form complex spatial climate gradients along high mountain slopes in Hawai‘i (Giambelluca et al., 2014). The highest elevations in Hawai‘i (above about 2000 m) are strongly influenced by the trade wind inversion (TWI), which is the result of the interaction between subsiding air from the upper troposphere and convection-driven mixing at lower levels (e.g. Cao et al., 2007). The TWI is a prominent feature in the climate system of Hawai‘i occurring on average 78% of the year at a mean base height of 2159 m (Chapter 3) based on a ~40 year climatology. The actual characteristics of the TWI have been shown to vary on monthly, seasonal, annual, inter-annual and decadal time scales (e.g. Cao et al., 2003; Chapter 3). When the TWI is present, the vertical development of clouds is suppressed and the transport of moisture to high elevation ecosystems above the inversion on Hawai‘i’s highest mountains is

inhibited (Giambelluca, 2005). Locations above the mean TWI level have higher solar radiation (Giambelluca and Nullet, 1991), higher potential evapotranspiration (Longman et. al., 2012), higher vapor pressure deficit (Gotsch et al., 2014) and lower rainfall (Giambelluca et al., 2013) compared with sites below the TWI.

In Chapter 3 of this dissertation I showed that a 16% (±6% s.d.) average increase in TWI frequency of occurrence has occurred between the periods 1973-1990 and 1991-2013 (Figure 4.1). This Change in the TWI frequency was found to be associated with an increase in Hadley Cell subsidence over Hawai‘i. Neither the increased subsidence nor the increased TWI frequencies were explained by Pacific-centered modes of climate variability such as the El Niño Southern Oscillation (ENSO; e.g Rasmusson and Carpenter, 1982) or the Pacific Decadal Oscillation (PDO; Mantua et al., 1997). However, these climate modes may help to explain some of the inter-annual variability in the TWI. Cao et al. (2007) identified ENSO-related differences in TWI occurrence frequency using a TWI time series from 1979 to 2003. They found that the frequency of TWI occurrence during El Niño (positive phase) years was higher for December through April and lower for May to September compared with non-El Niño (negative and neutral phase) years. In Chapter 3 I found that the strength of the relationships between the ENSO and PDO indices and TWI frequency were improved when data were subdivided into pre- (1973-1990) and post- (1991-2013) TWI-shift periods and examined independently. Prior work has not examined the differences in TWI frequency during the three phases of ENSO (positive, negative and neutral) and two phases of PDO (positive and negative). Therefore, the effects of ENSO- and PDO-driven changes in TWI frequency on high- and mid-elevation climate in Hawai‘i are not well understood.

Longman et al. (2014) identified a statistically significant increase ($\alpha \leq 0.05$) in dry season (May - October) solar radiation at four high elevation climate stations in Maui, Hawai‘i over the period 1988 to 2013. This analysis concluded that observed increases in solar radiation were explained by a decrease in cloud cover during the period 1998 to 2013. In contrast, the results for the wet season showed that solar radiation decreased during the wet season (November – April) at these same locations. Two subsequent research questions have emerged from the work of Longman et al. (2014): 1) what are the processes driving decreases in dry season cloud cover and the subsequent increases in solar radiation at high elevation? 2) Why is the observed dry season signal of change inconsistent with the wet season signal of change?

In this analysis, I hypothesize that the observed changes to dry season high elevation cloud cover and the subsequent effects on solar radiation reported by previously are linked to an increase in the TWI frequency of occurrence. The upward shift in TWI frequency, which occurred in the early 1990’s (Chapter 3) may partially explain some of the increases in dry season solar radiation reported by Longman et al. (2014). However, the solar record used in the earlier study only captures at most three years of the pre-shift time series (1988-1990) at the stations analyzed. The upward shift in TWI frequency does not explain the dry season decreases in high elevation cloud cover found only within the post-TWI-shift period (1991-2013). Reported increases in solar radiation and decreases in cloud cover at high elevation suggest a potential increase in dry season TWI occurrence frequency over the most recent ~2 decade period of record. Decreases in solar radiation over this same period suggest that wet season TWI occurrence frequency has potentially decreased.

In this study, a composite of the TWI occurrence time series obtained from two atmospheric sounding stations, solar radiation, rainfall and relative humidity data from as many

five high-elevation (>2000 m) and three mid-elevation (>950 m and <2000 m) climate stations and both the ENSO and the PDO indices over period 1991-2013 are analyzed. The main objectives of this analysis are to: 1) characterize and compare the TWI frequency of occurrence during the three unique phases of ENSO and two unique phases of the PDO for the dry and wet seasons, 2) Determine the relationships between TWI occurrence frequency anomalies and solar radiation, rainfall, and relative humidity anomalies obtained from high and mid-elevation locations, for the 6-month dry and wet seasons. 3) assess temporal changes in the climate indices ENSO and PDO and the climate variables, TWI frequency of occurrence, solar radiation, precipitation and relative humidity over the period 1991 – 2013, and 4) quantify the effects that ENSO and PDO driven changes in TWI frequency have on solar radiation, rainfall and relative humidity at high and mid-elevations over time.

4.3 Data

Temperature, relative humidity and elevation data obtained from two atmospheric sounding stations in Hawai‘i are used to identify the TWI. These stations are located at: Līhu‘e (21.97˚N, 159.333˚W) on the Island of Kaua‘i and Hilo (19.72˚N, 155.05˚W) on Hawai‘i Island (Figure 4.2). The TWI is identified using methods described in Chapter 3 which is a modified version of the TWI identification criteria proposed by Cao et al. (2007). The TWI base is assumed to be found within the 950 – 650 hPa pressure range, which excludes inversions caused by radiative surface cooling below the 950 hPa level and inversions caused by the melting of cloud ice particles at altitudes above 650 hPa. The TWI is identified as a layer with a positive vertical air temperature gradient and a drop in relative humidity at the same or the next (immediately higher) level. For, vertical profiles showing multiple inversions, the inversion with the greatest decrease in relative humidity with height is defined to be the TWI layer. TWI

frequency of occurrence is calculated as the number of days with an inversion present divided by the number of days of available data in each month. The average 2:00 PM HST (0:00 UTC) TWI frequency data from the two atmospheric sounding stations over the period 1991-2013 is used in this analysis. Atmospheric sounding data are maintained by the University of Wyoming and can be accessed at (http://weather.uwyo.edu/upperair/sounding.html).

Climate data, consisting solar radiation (K_d), rainfall (RF) and relative humidity (RH), are obtained from as many as eight climate stations located within the HaleNet climate network located on Haleakalā Volcano, Maui, Hawai‘i (https://sites.google.com/a/hawaii.edu/ecohydrology_lab/current-research/halenet) (Figure 2). Five of the climate stations are located on the leeward side of the island and cover a 1330 m vertical elevation gradient (960 to 2990 m). The three remaining stations are located on the windward side of the island and cover an 820 m vertical elevation gradient (1640 to 2460 m). Stations are categorized as either high elevation (>2000 m; n=5) or mid-elevation (≥960 and <2000 m; n=3). Note that the variables K_d and RH are not assessed at HN-106 due to a 10 year data gap (1991-2013) in the record. At each of the HaleNet stations; K_d was monitored with an Eppley model 8-48 (Eppley Laboratory, Newport, RI, USA) thermopile pyranometer measuring global solar radiation from 1991 – 2011 and with a Hukseflux(Manorville NY, USA) model NR01 four-component net radiation sensor between 2011 - 2013. Solar data have been homogenized to reduce the uncertainty associated with the calibration drift, and shifts that occurred at times of sensor re-calibration or replacement (Longman et al., 2013). RF was measured with a Texas Electronics TE-525 tipping bucket (updated to model TR-525I, in July of 2011). RH was monitored with Vaisala Model (Helsinki, Finland) HMD-30-YB sensors and in July of 1999 these sensors were replaced with the Vaisala Model HMP-45-C. Data for all

variables were sampled at 10-s intervals and recorded hourly using LI-COR (Lincoln, NE, USA) LI-1000 data loggers (before mid-July 1999), Campbell Scientific, Inc. CR10X data loggers (mid-July 1999 to January 2011), and Campbell Scientific CR3000 data loggers (January 2011 to present).

The Mulitvariate ENSO Index (MEI) is used to define ENSO status in this study (Wolter and Timlin, 1998). The MEI incorporates six observed fields (SLP, zonal and meridional surface wind, SST, and total cloudiness) in the classification of ENSO modes. Data are obtained from the National Oceanic and Atmospheric Administration (NOAA; http://www.esrl.noaa.gov/psd/enso/mei/table.html). The PDO index values are obtained from the Joint Institute for the Study of the Atmosphere and Ocean (JISAO) at the University of Washington (http://jisao.washington.edu/pdo/PDO.latest).

4.4 Methods

4.4.1 Data Aggregation

Hawai‘i has two distinct 6-month seasons, the dry season (May to October) and wet season (November to April) (Giambelluca and Schroeder, 1998). Monthly anomalies are calculated as departures from the 1991-2013 mean for each month. TWI frequency, K_d, and RH data are aggregated to the seasonal time step by averaging the monthly anomalies in each 6-month season-year. Anomaly values were included for a given season-year if at least 50% of the data were available. A composite TWI frequency time series is calculated as the average in each season of TWI frequency obtained from the two atmospheric sounding stations. Measured rainfall was aggregated differently than the other variables in this analysis to avoid extreme biases associated with missing data. Monthly rainfall data (RF_{mon}) were adjusted for missing data as:

$$RF_{mon} = \frac{RF_{Sum}}{RF_{Cnt}} * mon_n \quad (4.1)$$

where RF_{mon} is adjusted monthly rainfall total, RF_{sum} is the sum of available daily rainfall for the month, RF_{Cnt} is the number of available daily rainfall observations in the month, mon_n is the total number of days in the month. Anomalies are then calculated using the same methods as described above. All of the climate data were converted to units of percent by dividing the aggregated seasonal anomalies by the period-of-record (1991-2013) seasonal mean. Note that wet season years are identified according to the year of the beginning of the season (e.g., the wet season value for 1991 consists of data from 11/1991 to 4/1992). ENSO data was obtained from the National Oceanic and Atmospheric Administration (NOAA) MEI database (http://www.esrl.noaa.gov/psd/enso/mei/table.html) and PDO data was obtained from the Joint Institute for the Sutdy of the Atmosphere and Ocean (JISAO) PDO database (http://research.jisao.washington.edu/pdo/PDO.latest).

4.4.2 Data Analysis

Observed climate variables and the ENSO and PDO indices are analyzed using several methods and statistical tests. The relationships between TWI frequency and the ENSO and PDO indices and the relationships between TWI frequency and the atmospheric variables K_d, RF, and RH were analyzed and assessed for significance using linear regression. Statistical significance was evaluated at the 90% confidence level ($\alpha \leq 0.1$).

The mean TWI frequency during each phase of ENSO and PDO are compared with one another to determine if phase changes within these modes have significant effects on TWI occurrence. To accomplish this, first, monthly data from the ENSO and PDO indices were averaged to the 6-month seasonal values. Second, years were grouped according to: the three ENSO phases (using MEI value criteria of: <-0.4 = La Niña Phase; >-0.4 and <0.4 = Neutral

Phase; >0.4 = El Niño Phase) and the two PDO phases (using positive and negative PDO index values). Finally, differences in the mean TWI frequency between each phase combination were assessed for significance using an appropriate statistical test. For the TWI-ENSO phase comparison, a one-way analysis of variance test (ANOVA) was used to determine significant differences in mean TWI frequency followed by the post-hoc Tukey's test was used to establish which combinations ENSO phase comparisons were significantly different. Differences in mean TWI frequency for positive and negative PDO phases were assessed using the Welch two sample t-test (Welch, 1947).

Observed seasonal climate anomalies are analyzed to determine their temporal trends over the past ~22 years. Trends are evaluated using a linear regression model. TWI frequency, K_d, RF and RH time series data from 1991 to 2013. For K_d, RF, and RH time series only the station variables that were significantly correlated with TWI frequency and that have at least 14 seasonal anomalies are analyzed for trends. Statistical tests were conducted using R open source statistical software. Statistical significance was measured at the 90% significance level ($\alpha \leq 0.1$), using the null hypothesis that the trend is zero.

4.5 Results

4.5.1 TWI Frequency vs. Central Pacific Modes of Climate Variability

A statistically significant relationship between the ENSO index and TWI frequency was identified in both seasons and ENSO explains 28 and 29% of the TWI variance (based on r^2 value derived from linear regression) for the dry and wet seasons, respectively; however, the sign of this relationship differed between seasons (Figure 4.3). For the dry season, mean TWI frequency during the La Niña (cool) phase was 8.4% higher (significant) than then during the El Niño (warm) phase (Table 4.1). For the wet season, mean TWI frequency was 4.6% lower during

the La Niña Phase (significant) than during the El Niño phase. No significant differences were identified for comparisons of mean TWI frequency between the neutral phase and La Niña or El Niño phases.

The relationship between TWI frequency and the PDO index was also significant in both seasons. PDO explains 38 and 26% of the TWI variance for the dry and wet seasons respectively; however, as with ENSO, the sign of this relationship was also opposite for the two seasons (Figure 4.4). For the dry season, mean TWI frequency during the negative (cool) phase of the PDO is 6.8% higher (significant) than during the positive (warm) phase. During the wet season mean TWI frequency is 2.6% lower (not significant) during the negative phase than during the positive phase (Table 4.1).

4.5.2 TWI Frequency vs. Climate Variables

The linear relationships between each of the climate variables K_d, RF and RH obtained from as many as eight climate stations and the TWI frequency of occurrence were assessed for the dry and wet seasons (Figure 4.5). K_d was positively and significantly correlated with TWI frequency at four of the five high elevation sites during the dry season (r^2 = 0.25 to 0.55), but no significant correlation was found at the two mid-elevation sites analyzed (Table 4.2). For the wet season significant correlations were identified at all of the high- and mid-elevation sites analyzed (r^2 = 0.18 to 0.51). On average, a 10% increase in inversion frequency corresponds to 4% and 7% increases in high-elevation K_d for the dry and wet seasons, respectively.

Correlations between TWI frequency and RF were negative in both seasons. For the dry season, significant relationships were identified at all of the high-elevation sites (r^2 = 0.20 to 0.53) and at one mid-elevation site that is located in the heart of the leeward cloud zone (HN-106: r^2 = 0.56). For the wet season, RF was significantly correlated with TWI frequency at all of

the high- and mid-elevation sites analyzed (r^2= 0.17 to 0.79). On average 10% increases in inversion frequency corresponds to average -8% decreases in rainfall at both high and mid elevations for both the dry and wet seasons.

RH was negatively correlated with TWI frequency of occurrence and significant relationships between these two variables were identified at four high elevation sites during the dry season (r^2 = 0.21 to 0.69) and five high elevation sites during the wet season wet season (r^2 = 0.17 to 0.54). On average, 10% increases in TWI frequency results in 12 and 14% decreases in RH at high elevation sites for the dry and wet seasons, respectively. The largest regression slopes were identified at the two highest leeward sites (HN-152, 2590 m and HN-153, 2990 m). RH is not significantly correlated with TWI frequency at mid elevation sites during either season.

4.5.3 Temporal Changes in Climate

The time trends of TWI frequency, the ENSO and PDO indices, and the climate variables K_d, RF and RH, were assessed from 1991 to 2013 for both dry and wet seasons. Trends based on linear regression for the ENSO and PDO indices were negative over this ~2 decade period for both seasons (Figure 4.6). The negative trends can be interpreted as a tendency toward more La Niña (cool) phase ENSO conditions and negative (cool) phase PDO conditions over this period of record.

TWI frequency data assessed over this same time period show opposite signals of change for the dry and wet seasons. For the dry season the regression slope was positive (4% decade^{-1}) and significant (p = 0.035) and for the wet season the slope was negative (-2% decade^{-1}) and not significant (p = 0.296; Table 4.3) .This result is not surprising considering opposite response of TWI frequency during the cool phases of the ENSO and PDO for the two seasons (Figures 4.3, 4.4).

Time series data for the climate variables K_d, RF, and RH were assessed only if the station/variable was significantly correlated with TWI frequency and at least 14 seasonal values were available in the time series (Table 4.2; Figure 4.7). Significant increases in dry season K_d (3 to 4% decade^{-1}) were identified at four high elevation sites (Table 4.4). During the wet season, decreases in K_d were observed at all of the stations and significant decreases were observed at the mid-elevation stations on both the leeward (HN-119) and windward (HN-164) side of the island (-4 and -8% decade $^{-1}$).

Significant decreases in dry season rainfall (1 to 9% decade^{-1}) were identified at all but one of the stations analyzed (HN-152, 2120 m; $p = 0.102$). For the wet season, trends were relatively small and not significant at any station.

Significant decreases in dry season RH were identified for three of the four high elevation stations (4 to 10 % decade^{-1}). During the wet season, significant increases in RH were observed at three of the four highest elevation stations (5 to 13% decade^{-1})

4.6 Discussion

The results presented here highlight the role that Pacific-centered modes of climate variability have on TWI frequency and the subsequent effects that TWI frequency variability has on the energy and moisture regimes at high and mid-elevations in Hawai‘i. The presence of the TWI suppresses the vertical development of clouds resulting in a thinner moist layer, a virtual absence of rainfall above the inversion, and lighter rainfall below the inversion (Chen and Feng, 2001). In addition a more frequent inversion also results in significant increases in solar radiation and significant decreases in relative humidity at high elevation. Variations in TWI frequency may explain at least some of the significant observed dry-season increases in solar radiation (Longman et al., 2014) and the frequency of zero rainfall days (Krushelnycky et al., 2013), and

decreases in precipitation (Frazier et al., 2013), cloud cover (Longman et al., 2014) and stream flow (Bassiouni and Oki, 2013) that have been identified at high elevations on Maui. Ecological impacts of increased dry season TWI frequency may have already been observed at high elevations on Maui. Krushelnycky et al. (2013) have reported on the decline of the Haleakalā silversword, an iconic high-elevation species endemic to the high elevations of Haleakalā. Reductions in available moisture and increases in energy are also likely to affect other species in the ecosystems atop Haleakalā and other high mountains in Hawai‘i.

By the end of the century, modeling studies using the Coupled Model Intercomparsion Project (CMIP5) RCP 8.5 data (Taylor et al., 2012) suggest an 11% average increase in annual TWI frequency and a 157 m decrease in TWI base height (results based on a 10-model ensemble) relative to the 2001-2003 mean (Lauer et al., 2013). Increased atmospheric stability around the 700 hPa level were also identified by Lauer et al. (2013) over this same time window and are consistent with decrease in TWI base height. Increases in atmospheric stability are assumed to reduce the number of cumulus clouds penetrating into the inversion layer and evaporation of clouds in the dry stable atmosphere above the inversion can weaken the inversion and raise the base height (Riehl et al., 1951; Malkus, 1958). Increases in atmospheric stability may be directly related to intensification or widening of the Hadley Cell (see review by Lucas et al., 2013). Changes in Hadley Cell intensity and width have been explained by multiple climate forcing mechanisms including ENSO and PDO phase change (e.g. Mitas and Clement, 2005; Grassi et al., 2012). In Chapter 3 I did not find a significant correlation between the ENSO and PDO indices and when using vertical velocity of wind variable “omega” a indicator of Hadley Cell subsidence over the ~40 year period (1973 – 2013) analyzed. It is possible that correlations between these variables could be improved if these data were assessed over shorter time

windows such as were used in this present analysis or perhaps by using a different variable to define Hadley Cell subsidence. Considering the significant relationship between both ENSO and PDO indices and TWI frequency it is logical to assume that these Pacific centered climate modes of natural variability are at least partially influencing the Hadley Cell circulation patterns in the Pacific. Whether or not ENSO events will be enhanced in the future is still not clear (Collins et al., 2010; Stevenson, 2012). However, the implications of enhanced ENSO events are important when considering the indirect effect they have on high elevation ecosystems.

4.7 Conclusions

For this analysis, average TWI frequency data derived from two atmospheric sounding stations, ENSO and the PDO index data, observations of the climate variables K_d, RF and RH obtained from as many as 8 HaleNet climate stations were used to characterize changes to high- and mid-elevation climates on Haleakalā Volcano during the 6-month dry and wet seasons over the period 1991-2013. I identified significant relationships between TWI frequency and the ENSO and the PDO indices and determined the response of TWI frequency to phase changes in these Pacific modes was opposite in the dry and wet seasons. For example: During the cool phases of ENSO and PDO mean TWI frequency is higher than in the dry season and lower during the wet season relative to the mean warm phase mean. Cool ENSO and PDO phase conditions which have dominated the most recent ~2 decade period of observations help to explain increases in energy and decreases in moisture at high and mid elevations during the dry season.

Some limitations of this study include the small sample size of seasonal ENSO and PDO phase events which were limited to this ~23 year period. Another limitation is the aggregation of data to the 6-month seasonal time step, which may have a smoothing effect on events that may

be more pronounced on monthly or 4-season time steps. Another source of uncertainty arises from incomplete time series data. Although a consistent methodology was established to assess linear relationships, missing data points, which influenced sample size were not accounted for in the regression models.

There are many unresolved questions that have arisen from this analysis. First, it is not clear why TWI frequency has an opposite response to ENSO and PDO phase changes in the dry and wet seasons. To address this question it will be important to examine the role that ENSO and PDO have on the Hadley cell subsidence in the Pacific over the same time windows analyzed in this study. Second, considering that ENSO and PDO phase changes only partially explain TWI variability it may be necessary to determine the additional driving forces, which affect this variable. Finally, given the role that TWI has on moisture at mid-elevations, it would be valuable to expand this analysis to additional rainfall stations outside of the HaleNet climate network to determine if TWI frequency affects mid and potentially low elevation stations on other islands with summits located well below the mean TWI base height.

Chapter 4 Tables

Table 4.1: Difference in mean TWI frequency during different phases of ENSO and PDO modes of climate variability, results of a one-way ANOVA test.

	Dry-Season			Wet-Season		
ENSO Phase	**Diff (%)**	**Sign (±)**	**p**	**Diff (%)**	**Sign (±)**	**p**
La Niña vs. El Niño	8.4	(+)	0.017	4.6	(-)	0.100
Neutral vs. El Niño	3.5	(+)	0.337	2.9	(-)	0.492
Neutral vs La Niña	5.0	(-)	0.221	1.7	(+)	0.757
PDO Phase						
Positive vs. Negative	6.8	(+)	0.003	2.6	(-)	0.192

Diff is the difference in mean TWI frequency between phases; Sign is the direction of the difference.

Table 4.2: Linear regression results for comparisons between TWI frequency and the climate variables; solar radiation (Kd) rainfall (RF) and relative humidity (RH).

		Dry-Season				Wet-Season			
Elev.(m)		**n**	**b (%)**	**r2**	**p**	**n**	**b (%)**	**r2**	**p**
Solar Radiation									
HN-119	960	22	-0.1	0.011	0.649	22	0.7	0.434	0.001
HN-106	1640	12				11			
HN-164	1650	20	0.1	0.006	0.740	20	1.4	0.436	0.002
HN-151	2120	21	0.3	0.247	0.022	20	0.5	0.183	0.060
HN-162	2260	15	0.3	0.085	0.291	18	1.1	0.351	0.010
HN-161	2460	20	0.6	0.510	0.000	16	0.8	0.505	0.002
HN-152	2590	23	0.5	0.485	0.000	22	0.7	0.457	0.001
HN-153	2990	22	0.4	0.552	0.000	20	0.7	0.382	0.004
Rainfall									
HN-119	960	23	-0.6	0.103	0.135	22	-0.9	0.214	0.030
HN-106	1640	20	-1.1	0.565	0.000	19	-1.0	0.204	0.053
HN-164	1650	18	-0.2	0.106	0.188	17	-0.5	0.365	0.010
HN-151	2120	20	-0.9	0.525	0.000	22	-0.6	0.166	0.060
HN-162	2260	17	-0.4	0.341	0.014	19	-0.6	0.514	0.001
HN-161	2460	21	-0.6	0.218	0.033	17	-1.0	0.792	0.000
HN-152	2590	22	-0.8	0.392	0.002	22	-1.0	0.344	0.004
HN-153	2990	20	-1.0	0.201	0.047	21	-1.0	0.317	0.008
Relative Humidity									
HN-119	960	23	-0.2	0.091	0.162	22	0.0	0.005	0.760
HN-106	1640	12				12			
HN-164	1650	17	0.1	0.040	0.440	16	-0.2	0.154	0.134
HN-151	2120	20	-0.6	0.321	0.009	22	-0.7	0.172	0.055
HN-162	2260	13	-0.2	0.082	0.344	14	-1.2	0.524	0.003
HN-161	2460	20	-0.6	0.214	0.040	17	-0.7	0.199	0.072
HN-152	2590	22	-1.7	0.648	0.000	22	-1.7	0.441	0.001
HN-153	2990	22	-2.0	0.687	0.000	21	-2.4	0.538	0.000

Elev. is elevation; n is the number of observations; b is the slope of the regression line; r^2 is the coefficient of determination; p is a measure of statistical significance.

Table 4.3: Linear regression results for TWI frequency time series (1991-2013).

TWI Variability	n	Trend (% yr^{-1})	r^2	SE	p
Dry Season	23	0.379	0.194	0.168	0.035
Wet-Season	22	-0.166	0.054	0.155	0.296

SE is the standard error of the average trend.

Table 4.4: Linear regression results for K_d, RF and RH time series (1991-2013).

		Dry-Season					Wet-Season				
Elev.(m)		n	Trend (% yr^{-1})	r^2	SE	p	n	Trend (% yr^{-1})	r^2	SE	p
Solar Radiation											
HN-119	960	Not Significantly Correlated with TWI					22	-0.4	0.296	0.26	0.009
HN-106	1640	Insufficient Data					Insufficient Data				
HN-164	1650	Not Significantly Correlated with TWI					20	-0.8	0.311	0.41	0.011
HN-151	2120	21	0.3	0.362	0.22	0.004	20	-0.1	0.009	0.37	0.691
HN-162	2260	Not Significantly Correlated with TWI					18	-0.5	0.131	0.59	0.140
HN-161	2460	18	0.4	0.372	0.33	0.004	15	-0.3	0.146	0.41	0.145
HN-152	2590	23	0.4	0.424	0.31	0.001	22	-0.1	0.035	0.37	0.405
HN-153	2990	22	0.2	0.192	0.31	0.041	20	-0.2	0.112	0.41	0.149
Rainfall											
HN-119	960	Not Significantly Correlated with TWI					22	0.0	0.000	1.11	0.991
HN-106	1640	20	-0.6	0.236	0.56	0.030	19	-0.2	0.018	1.56	0.588
HN-164	1650	18	-0.1	0.274	5.34	0.026	17	0.1	0.020	9.85	0.586
HN-151	2120	20	-0.4	0.145	0.70	0.098	22	0.0	0.002	1.70	0.849
HN-162	2260	16	-0.3	0.202	2.95	0.070	19	0.0	0.001	4.36	0.897
HN-161	2460	21	-0.4	0.168	1.59	0.065	17	0.0	0.001	3.14	0.893
HN-152	2590	22	-0.4	0.128	0.59	0.102	22	0.0	1.678	1.68	0.867
HN-153	2990	20	-0.9	0.215	0.90	0.039	21	0.0	0.000	2.11	0.948
Relative Humidity											
HN-119	960	Not Significantly Correlated with TWI					Not Significantly Correlated with TWI				
HN-106	1640	Insufficient Data					Insufficient Data				
HN-164	1650	Not Significantly Correlated with TWI					Not Significantly Correlated with TWI				
HN-151	2120	20	-0.5	0.348	0.11	0.006	22	0.0	0.001	0.16	0.920
HN-162	2260	Not Significantly Correlated with TWI					14	0.5	0.234	0.21	0.080
HN-161	2460	20	-0.4	0.242	0.13	0.027	17	0.5	0.182	0.16	0.088
HN-152	2590	22	-1.0	0.307	0.17	0.008	22	0.6	0.100	0.18	0.151
HN-153	2990	22	-0.6	0.097	0.19	0.159	21	1.3	0.281	0.20	0.014

Chapter 4 Figures

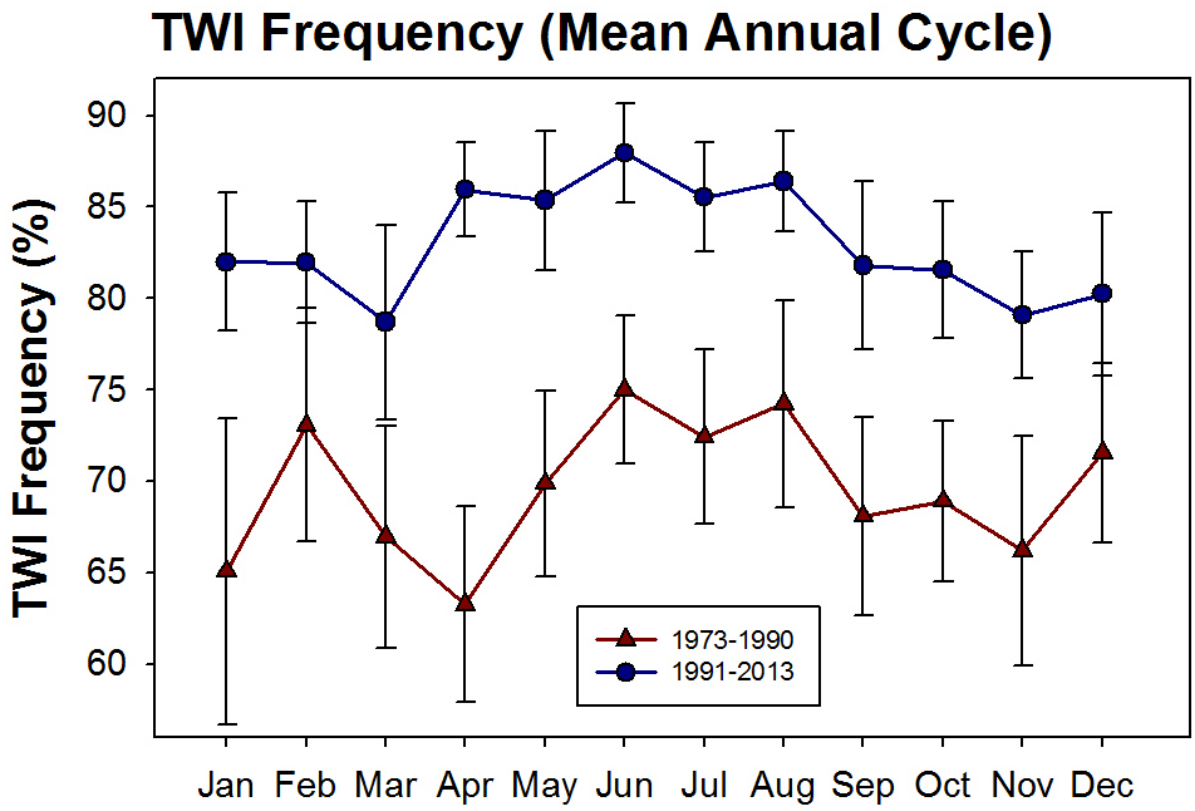

Figure 4.1: Mean monthly TWI frequency data pertaining to the pre-TWI-shift period(1973-1990; red line); post-TWI-shift period (1991-2013; blue line); error bars represent 95% confidence interval bands.

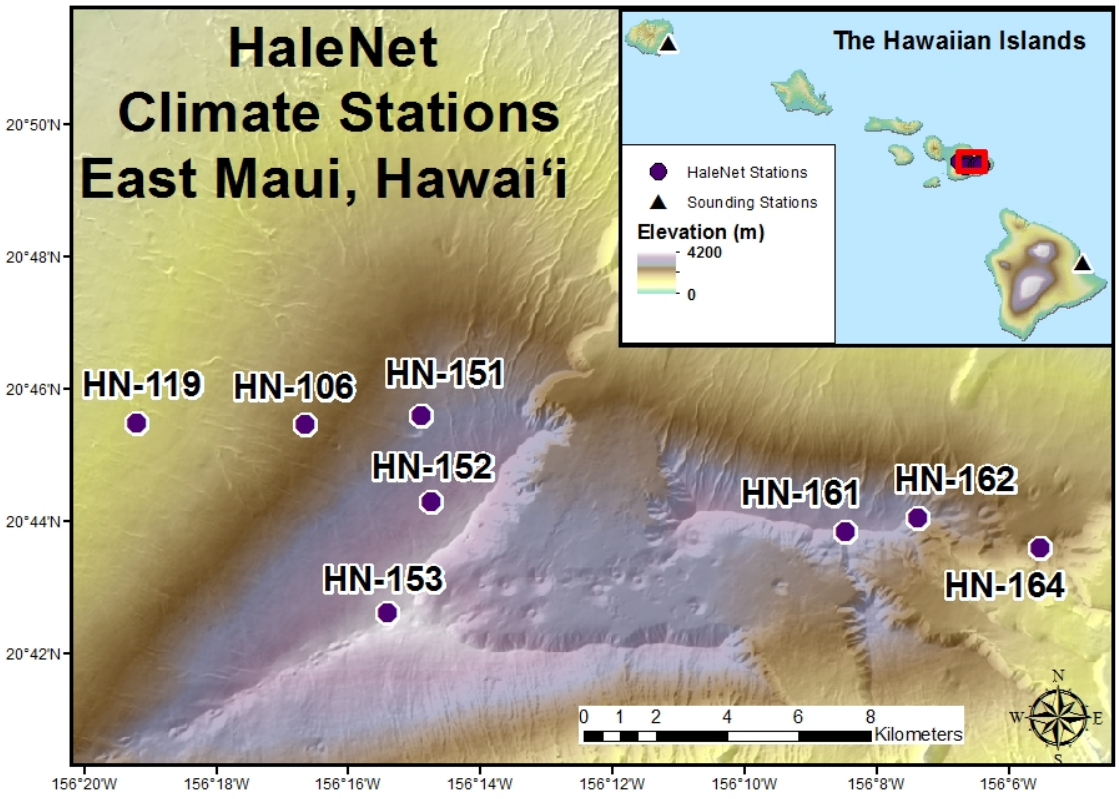

Figure 4.2: Map of the HaleNet stations used in this analysis; inset map shows the location of the atmospheric sounding stations used to calculate TWI characteristics.

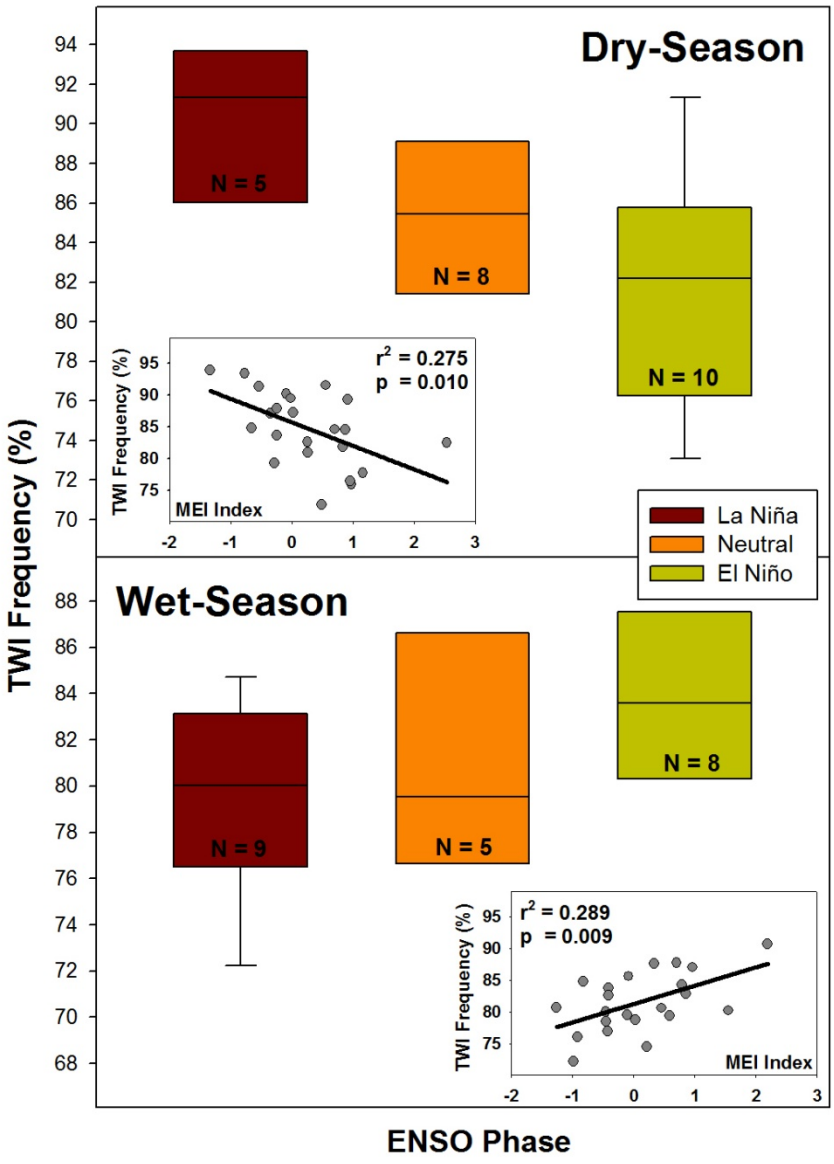

Figure 4.3: Box plot showing TWI frequency subdivided according to ENSO phase criteria for dry (top) and wet (bottom) seasons; subset graphs show the linear relationship between TWI frequency and the MEI index in each season.

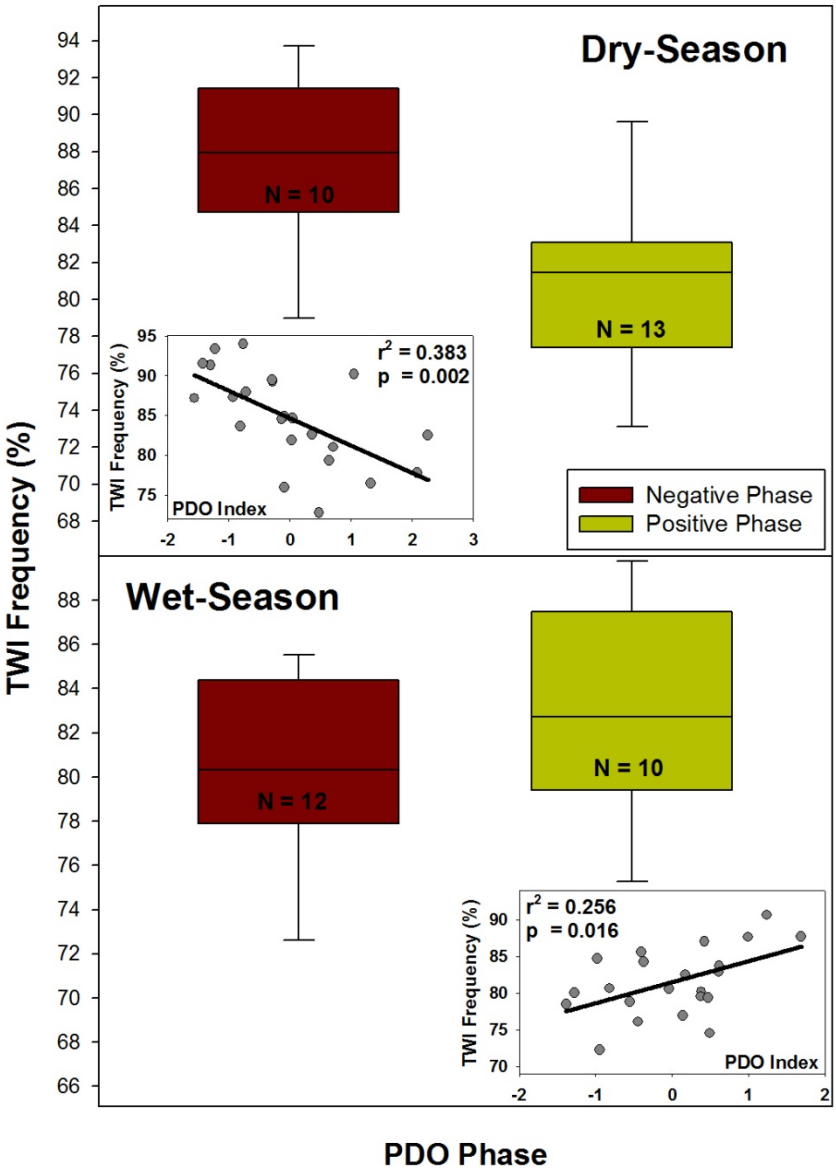

Figure 4.4: Box plot showing TWI frequency subdivided according to PDO phase criteria for dry (top) and wet (bottom) seasons; subset graphs show the linear relationship between TWI frequency and the PDO index.

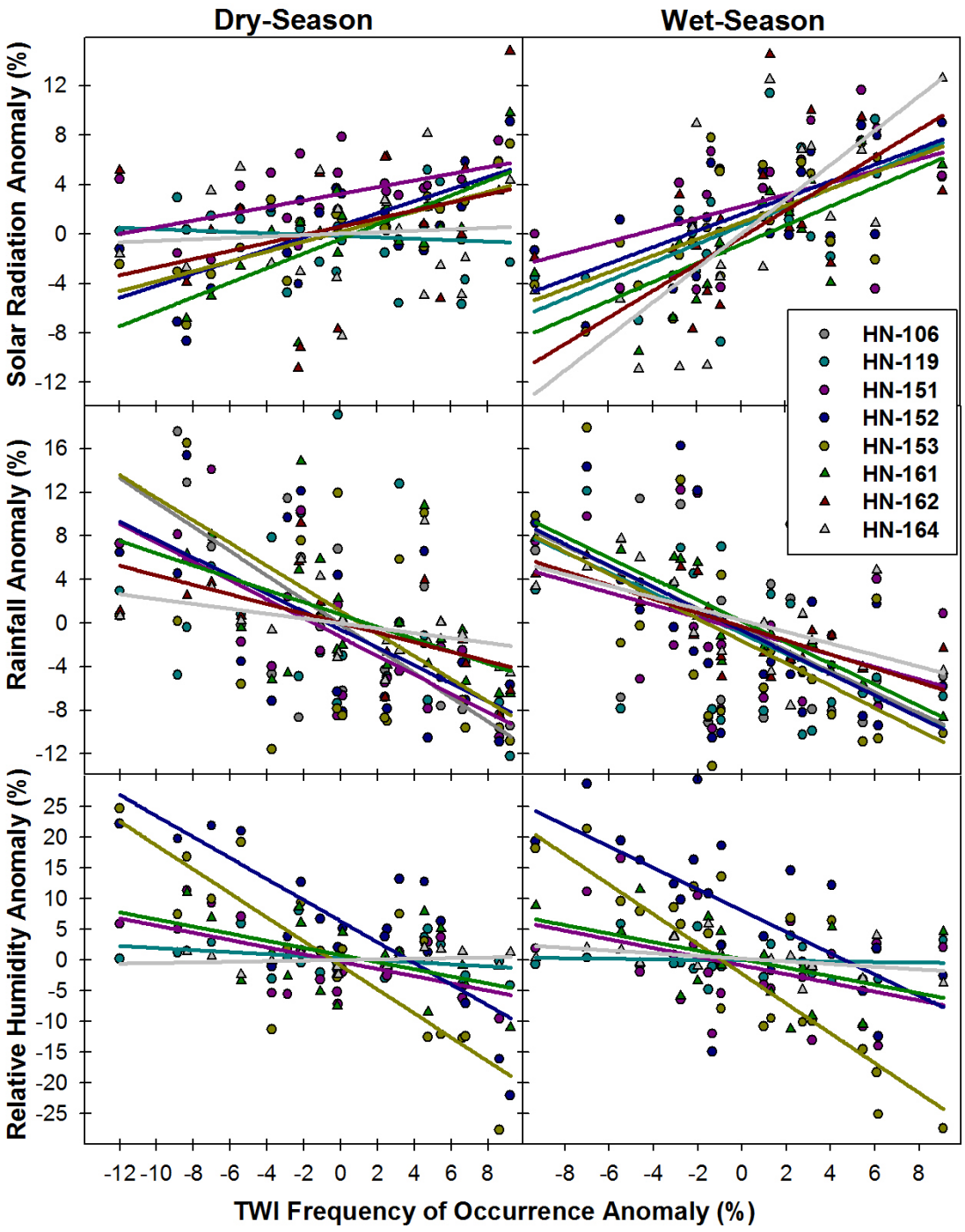

Figure 4.5: Linear relationships between solar radiation (top), rainfall (middle), relative humidity (bottom) anomalies and TWI frequency of occurrence anomalies (x-axis) for the dry (left) and wet (right) seasons; circle markers represent leeward stations and triangle markers represent windward stations.

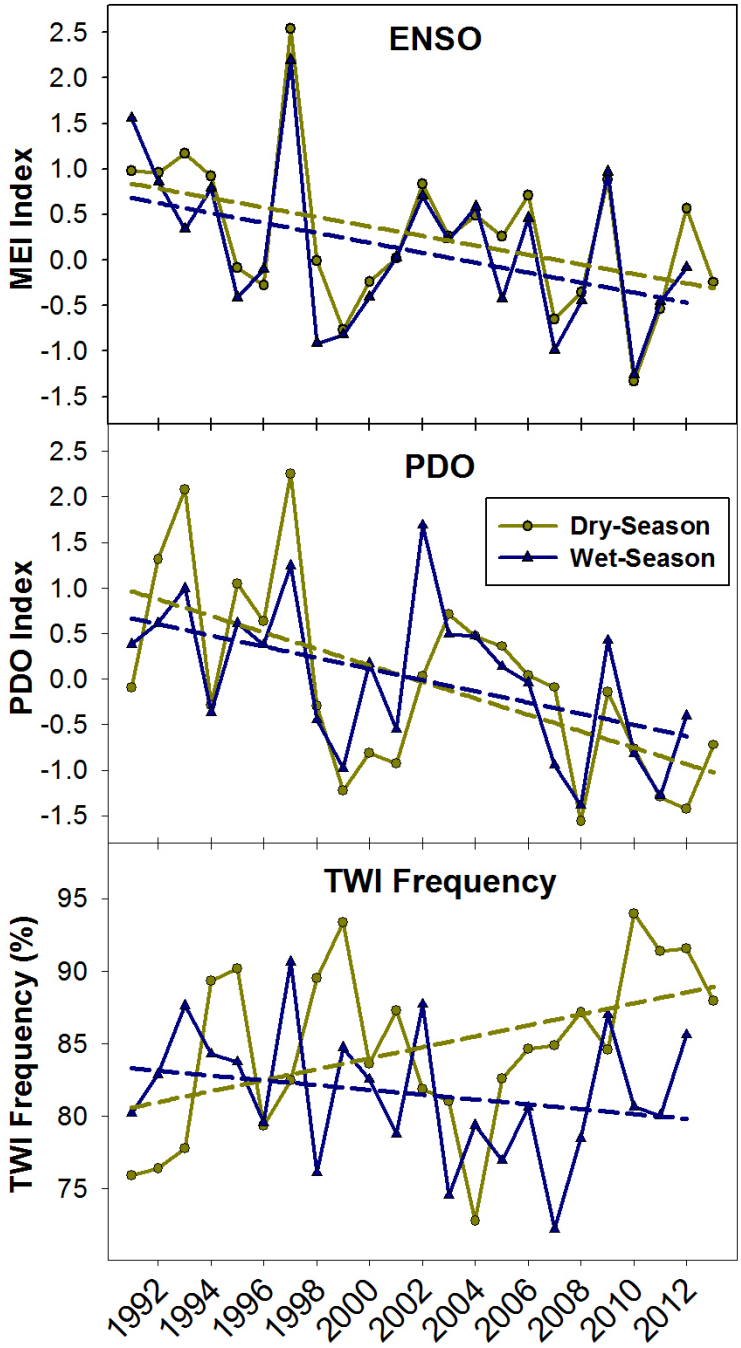

Figure 4.6: Dry (yellow line) and wet (blue line) season time series analysis from 1991 to 2013 for ENSO (MEI) index (top); PDO index (middle) and TWI frequency (bottom).

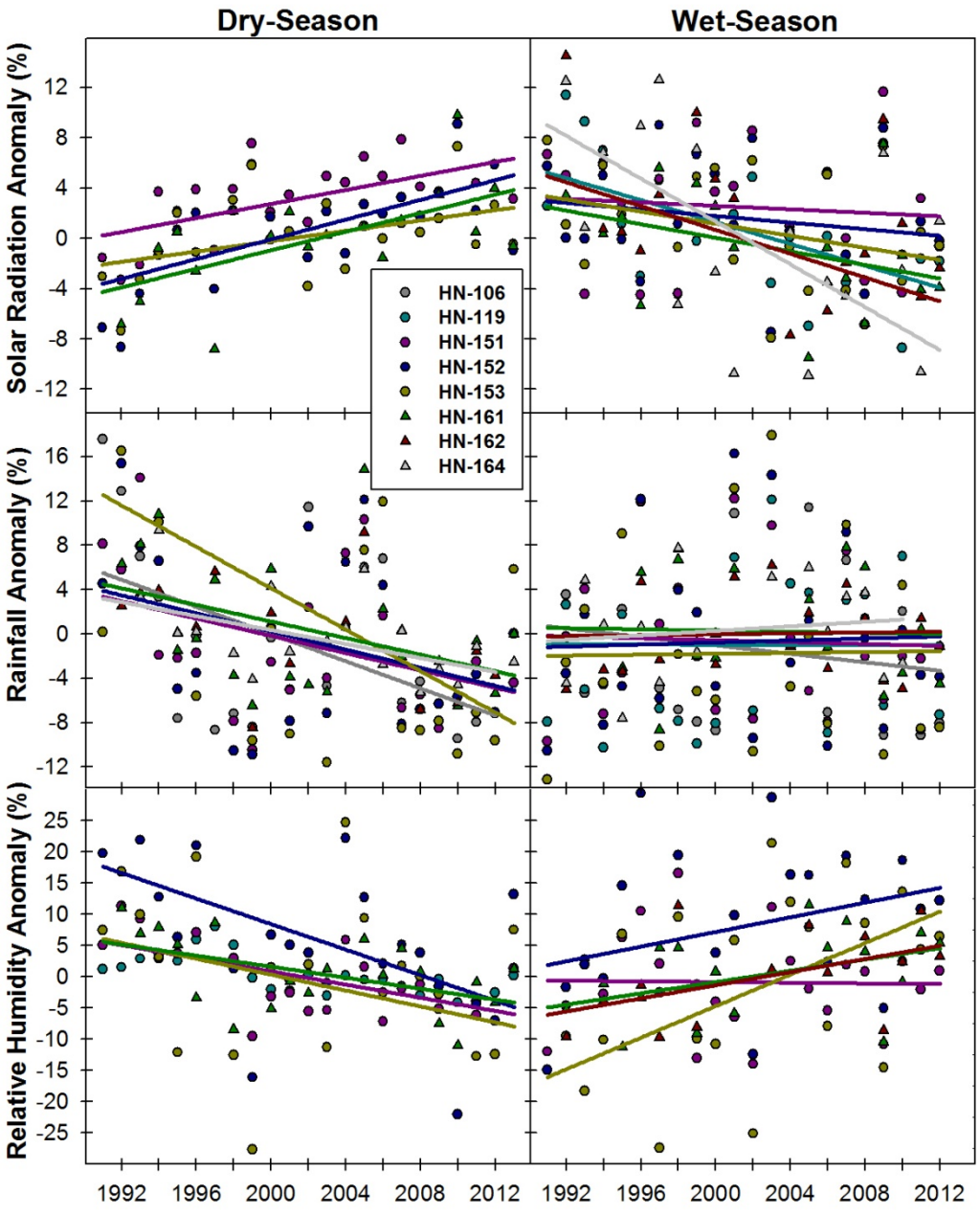

Figure 4.7: Temporal trends in solar radiation (top), rainfall (middle) and relative humidity (bottom) from 1991 to 2013 for dry season (left) and wet season (right).

CHAPTER 5. CONCLUSIONS

The high elevation climate of Hawai‘i is influenced by a number of interacting factors that change through space and time. In this study, I characterized the diversity of high elevation climates by analyzing the temporal and spatial patterns of various microclimatic variables along a leeward and windward elevation transect on Maui, Hawai‘i for the 6-month dry and wet seasons. I also examined ~40 years of TWI characteristic data to determine if previously identified increasing trends in TWI frequency and decreasing trends in TWI base height persisted for the most recent decade of observations (2004 to 2013). Finally, I attempted to identify the influence of Pacific-centered modes of climate variability on TWI frequency, and the effects that TWI frequency variability has on high- and mid-elevation climate parameters over the most recent two decades. In the following discussion I summarize my findings for each of the main chapters in this dissertation. Then I discuss the broader implications of my results and suggest potential future directions of study.

Based on the analysis presented in Chapter 2, I can make the following conclusions regarding the climatology of Haleakalā.

- Both leeward and windward microclimates above ~2000 m are strongly influenced by the presence of the TWI in both the dry and wet seasons.
- A leeward precipitation gradient was not identified, but other moisture variables such as potential evapotranspiration, relative humidity, vapor pressure deficit, and soil moisture decrease with height above the mean inversion base height.
- The windward slope has higher rainfall and higher humidity when compared with leeward locations at similar elevations.

- Period-of-record (up to 25 years) changes in the climate are apparent across both leeward and windward elevation gradients for both seasons.
- For the dry season, a decadal-scale drying trend was identified for all of the moisture variables analyzed at the stations located above 1000 m along both leeward and windward transects. Significant decreases in precipitation were found at four HaleNet stations located 1640 and 2990 m along the leeward transect. Significant decreases in relative humidity and significant increases in vapor pressure deficit, potential evapotranspiration and the occurrence of zero rainfall days were found at one or more of the three highest elevation (2120 – 2990 m) leeward observation sites. Along the windward transect, significant decreases in precipitation were found at all three stations across the 810 m gradient (1650 – 2460 m) and a significant decrease in relative humidity was identified at the windward summit station (2640 m).
- For the wet season, many of the climate variables showed a response over time that was opposite of their dry season trend. Regarding moisture variables, results were mixed and moister conditions were observed over the record although very few trends were significant.
- Most of the temperature trends were negative and not significant for both the dry and wet season, suggesting that the global warming temperature hiatus, which persisted for most of the period of HaleNet data, may have been captured in the temperature record.

Based on the analysis presented in Chapter 3, I can make the following conclusions regarding TWI characteristics over the past ~40 years.

- Mean TWI characteristics for the dry and wet season, respectively, are base height: 2200 and 2110 m (± 88 m s.d.); frequency: 80 and 76 % (± 10 % s.d.); and strength: 0.005 and 0.006 °C m^{-1} (± 0.001 °C m^{-1} s.d.).
- TWI frequency of occurrence has increased over the past ~4 decades for both seasons, most notably defined by an abrupt upward (16%) shift in the early 1990s.
- Increases in the vertical velocity of wind variable omega have been identified in four reanalysis datasets and are in agreement with changes in the TWI.
- TWI frequency data are significantly correlated with omega, which suggests that increases in the intensity of Hadley Cell subsidence are driving increases in the TWI frequency of occurrence.
- Correlations between omega, and the ENSO and PDO indices are weak and not statistically significant. In addition, the sign of these relationships is opposite for the dry and wet seasons which suggests that phase changes in Pacific-centered modes of climate variability do not explain the abrupt shift in TWI frequency.
- Rainfall records that were significantly correlated with TWI frequency data show decreases in rainfall during the TWI post-shift period (1991 to 2013) relative to the pre-shift period (1973 to 1990). On average, mean rainfall was 16 and 40% lower during this pre-shift period for the dry and wet seasons, respectively, for those stations at which rainfall was significantly correlated with TWI frequency.
- Dry-season rainfall at all of the 21 high elevation stations was significantly correlated with omega and TWI frequency.

Based on the analyses presented in Chapter 4, I make the following conclusions regarding the effects of ENSO and PDO on TWI variability and the relationship with TWI frequency and climate variables, solar radiation, rainfall, and relative humidity over the TWI post-shift time period (1991-2013).

- The ENSO (MEI) index is significantly correlated with TWI frequency during the dry and wet seasons.
- Mean TWI frequency during the dry (wet) season is 8% (5%) higher during La Niña (El Niño) phase conditions when compared to the mean TWI frequency during El Niño (La Niña) phase conditions.
- No significant differences were found when comparing mean TWI frequency during neutral phase with mean TWI frequency during the El Niño or La Niña phase.
- TWI frequency is significantly correlated with the PDO index during the dry and wet seasons.
- Mean TWI frequency during the dry (wet) season is 7% (3%) higher during positive (negative) PDO phase conditions when compared to the mean TWI frequency during negative (positive) PDO phase conditions.
- High-elevation observations of solar radiation, rainfall and relative humidity are all significantly correlated with TWI frequency during the dry and wet seasons.
- Mid-elevation observations of rainfall are significantly correlated with TWI frequency during the dry (1/3 sites) and wet (3/3 sites) seasons and mid-elevation observations of solar radiation are significantly correlated with TWI frequency during the wet season (2/2 sites).

- The ENSO and PDO time series show a predominantly negative (cool) pattern over the time period analyzed.
- The predominantly cool ENSO and cool PDO phase conditions may explain a 4% per decade significant increase in TWI frequency during the dry season and a 2% per decade decrease (not significant) in TWI frequency during the wet season over the time period analyzed.
- For the dry season, the 4% per decade average increase in dry season TWI frequency partially explains the average significant increase in solar radiation , and significant decrease in rainfall and relative humidity identified at high elevations and the decrease in rainfall identified at the leeward mid-elevation site.
- For the wet season, the 2% per decade decrease in TWI frequency partially explains the decreases in solar radiation observed at high and mid elevations and the high elevation increase in relative humidity.

Based on the results from this study, I can conclude that seasonal high elevation climates have shown change in Hawai‘i. However, the extent of these changes, and the causes of these changes are unique across multiple time scales. For example the TWI frequency of occurrence may explain much of the observed changes in rainfall, but the extent of magnitude changes is highly dependent on the period of record analyzed. The average 33-year (1973-2006) linear change in wet season rainfall at three high elevation leeward sites, HN-151 (SKN 338) 2020 m, HN- 152 (SKN 339.5) 2590 m, and HN-153 (SKN 339.6) 2990 m, on Maui was -16% per decade (Table 3.8). This period captured the upward shift in TWI frequency identified in the early 1990s. The average linear trend at these same three stations, assessed for a 24-year period (~1988 – 2012) is -2% per decade (Table 2.24). This period of record included up to 3 years of

the pre-TWI-shift period. When just the 21 years of the post-TWI-shift period are analyzed, the average rainfall trend at these same three stations is 0.0% per decade (Table 4.4). These findings highlight the importance of characterizing climate trends over the appropriate time periods. For example, assessments of climate variability that do not include data from the pre-TWI shift period may not accurately represent the behavior of a given variable that if the variable in question is assessed over a longer period of record (e.g. 30 years). Considering the profound affect that the TWI has on high elevation climate variables, this is an important factor to consider when making assessments of data that do not accurately represent the mid 1990 TWI shift. In general it may not be appropriate to draw conclusions about the behavior of the climate over periods that do not include data from the pre-TWI shift period.

The factors affecting TWI variability are also unique across multiple temporal scales. The shift in TWI frequency identified in Chapter 3 was not explained by variations of the Pacific-centered modes of climate variability (ENSO and PDO), whereas on the shorter time scales, TWI frequency was significantly correlated with these modes (Chapter 4). ENSO- and PDO-driven changes to TWI frequency are clearly connected to observed changes in high elevation climates. Interestingly, fluctuations in these modes have opposite effects on TWI frequency for dry and wet seasons, and thus an opposite signal of change is typically observed for the two seasons. This finding adds insight into the significant increases in high elevation solar radiation and decreases in cloud cover previously reported (Longman et al., 2014), which were found only in the dry season. Considering the significant correlation between TWI frequency and Pacific-centered modes of variability, it is not possible to confirm if observed changes in the climate over relatively short (~2 decade) time scales are linked to global climate change.

The causes of the observed shift in TWI frequency have not been clearly identified. I have demonstrated that at least some of these trends can be linked to broader circulation patterns, potentially caused by the phase change in the Atlantic Multi-Decadal Oscillation occurring in the early 1990s (Yu et al., 2014) or potentially caused by anthropogenic global warming (Dai, 2011). The question of what caused the apparent shift in TWI frequency of occurrence remains an interesting and important research question for future exploration.

Sustained increases in TWI frequency pose several threats to high elevation ecosystems including reductions in available water. These reductions, however, may not be limited to the high elevation environment. An interesting finding in this study was the significant negative relationship between TWI frequency and rainfall at HaleNet station (HN-106) positioned in the heart of the leeward cloud zone (1640 m). Located ~500 m below the mean inversion base height this station experienced negative rainfall anomalies during periods of increased TWI frequency. It has already been established that the presences of the TWI affects rainfall at locations both above and below the mean TWI (Tran, 1995) but the magnitude of these effects is not known. Considering this, reported decreases in stream flow and base flow (Bassiouni and Oki, 2012) and decreases in rainfall at elevations located below the mean TWI base height (Frazier et al., 2013) may partially be explained by the increased TWI frequency experienced over the past ~2 decades. A next step in determining how TWI variability directly affects rainfall regimes at mid- and low-elevation would be to expand the Chapter 4 analysis to include all of the available rainfall data for the state to show how the effects of TWI on rainfall vary with elevation.

A detailed knowledge of the climate at any given elevation is critically important for a variety of resource management issues, including ground water and surface water development and protection, controlling and eradicating invasive species, protecting and restoring native

ecosystems, and planning adaption strategies to address the effects of global warming (Giambelluca et al., 2014). Given the unique location of the Hawaiian archipelago, climate change signals identified here are extremely relevant to the discussion of the broader impacts to subtropical Pacific region and other island nations located at similar latitudes. The high mountains of Hawai‘i serve as some of the last remaining habitat to many native plant and animal species that reside there. Protecting these species and preserving these habitats is of great importance to resource managers. The HaleNet observation network is a valuable tool that has and will continue to aid the research community in identifying agents of change now and for future generations to come.

REFERENCES

Adler, R. F., G. J. Huffman, A. Chang, R. Ferraro, P. Xie, J. Janowiak, B. Rudolf, U. Schneider, S. Curtis, D. Bolvin, A. Gruber, J. Susskind, P. Arkin, 2003: The Version 2 Global Precipitation Climatology Project (GPCP) monthly precipitation analysis (1979-Present). *J. Hydrometeor*., **4**, 1147-1167.

Allen, R. G., L. S. Pereira, D. Raes, and M. Smith, 1998: Crop evapotranspiration-Guidelines for computing crop water requirements-FAO Irrigation and drainage paper 56. *FAO, Rome, 300,* 6541.

Allen, R. J., J. R. Norris, and C. S. Zender, 2012: Recent northern hemisphere tropical expansion primarily driven by black carbon and tropospheric ozone. *Nature*, **485**, 350-354.

Barnes M.L., 2013: An assessment of Diurnal and Seasonal Cloud Cover Changes Over the Hawaiian Islands using Terra and Aqua modis. MS thesis, Department of Natural Resource Management, University of Hawai‘i at Mānoa, Honolulu.

Bassiouni, M., and D. S. Oki, 2013: Trends and shifts in streamflow in Hawai ‘i, 1913–2008. *Hydrol. Process.*, **27**, 1484-1500.

Bonan, G., 2008: *Ecological Climatology* (2nd ed.). Cambridge: Cambridge University Press. 563 pp.

Burney, D., R.V. DeCandido, L. P. Burney, F. N. Kostel-Hughes, T. W. Stafford Jr. and H. F. James, 1995: A Holocene record of climate change, fire ecology and human activity from montane Flat Top Bog, Maui. *J. Paleolimnol.*, **13**, 209–217.

Caballero, R, 2007: Role of eddies in the interannual variability of Hadley cell strength. *Geophys. Res. Lett*, **34**,

Cabin, R. J., 2011: *Intelligent tinkering: bridging the gap between science and practice*. Island Press. Washington D.C. 240 pp.

Cao, G. G., T. W. Giambelluca, D. E. Stevens, and T. A. Schroeder, 2007: Inversion variability in the Hawaiian Trade Wind Regime. *J. Climate*, **20**, 1145–1160.

Caruso, S. J., and S. Businger, 2006: Subtropical cyclogenesis over the central North Pacific. *Weather Forecast*, **21**, 193-205

Chen, J., B. E. Carlson, and A. D. Del Genio, 2002: Evidence for strengthening of the tropical general circulation in the 1990s. *Science*, **295**, 838–841.

Chen, Y. L., and J. Feng, 2001: Numerical Simulations of Airflow and Cloud Distributions over the Windward Side of the Island of Hawaii. Part I: The Effects of Trade Wind Inversion*. *Mon. weather rev.*, **129**, 1117-1134.

Chen, J., and A.K. Gupta, 2011: *Parametric statistical change point analysis: With applications to genetics, medicine, and finance*. Springer Science and Business Media

Chu, P. S., 1989: Hawaiian drought and the southern oscillation. *Int. J. Climatol*., **9**, 619-631.

Chu, P.S., and H. Chen, H., 2005: Interannual and interdecadal rainfall variations in the Hawaiian islands. *J. Climate*, **18**, 4796-4813.

Chu, P. S., Chen, Y. R., and T. A. Schroeder, 2010: Changes in precipitation extremes in the Hawaiian Islands in a warming climate. *J. Climate*, **23**, 4881-4900.

Collins, M., S. I. An, W. Ca, A. Ganachaud, A., E. Guilyardi, F. F. Jin, M. Jochum, M. Lengaigne, S. Power, A. Timmermann, G. Vecchi, and A. Wittenberg, 2010: The impact of global warming on the tropical Pacific Ocean and El Niño. *Nat. Geosci*., **3**, 391-397.

Compo, G. P., and Coauthors, 2011: The twentieth century reanalysis project. *Quart. J. Roy. Meteor. Soc*., **137**, 1–28.

Crausbay, S.D. and S. C. Hotchkiss, 2010: Strong relationships between vegetation and two perpendicular climate gradients high on a tropical mountain in Hawai‘i. *J. Biogeogr*. **37**, 1160-1174.

Crausbay, S.D. and S.C. Hotchkiss, 2012: Pollen-vegetation relationships at a tropical cloud forest’s upper limit and accuracy of vegetation inference. *Rev. Palaeobot. Palyno.*, **184**, 1-13.

Crausbay, S. D., A. G. Frazier, T. W. Giambelluca, R. J. Longman, and S. D. Hotchkiss 2014: The addition of climate during a strong El Niño event improves distribution models of tropical montane cloud forest characteristics in Hawai‘i. *Oecologia* **175**, 273-284

Dai, A., 2011: Drought under global warming: a review. *Wiley Interdisc. Rev. Clim. Change*, **2**, 45-65.

Davis, S. M., and K. H. Rosenlof, 2012: A multidiagnostic intercomparison of tropical-width time series using reanalyses and satellite observations. *J. Climate*, **25**, 1061–1078.

DeLay, J. K., and T. W. Giambelluca, 2010: History of cloud water interception research in Hawai'i. *Tropical Montane Cloud Forests: Science for Conservation and Management*, Cambridge University Press, Cambridge, New York, N.Y., 332-341.

Diaz, H.F., T. W. Giambelluca, and J. K. Eischeid, 2011: Changes in the vertical profiles of mean temperature and humidity in the Hawaiian Islands. *Global. Planet. Change* **77**, 21–25.

Diaz, H. F and T. W. Giambelluca, 2012: Changes in atmospheric circulation patterns associated with high and low rainfall regimes in the Hawaiian Islands region on multiple time scales. *Global Planet Change*, **98-99**. 97-108.

Dunne, T. and Leopold L. B. , 1978: *Water in Environmental Planning.* New York: W.H. Freeman and Company. 814 pp.

Dutton, E. G., D. W. Nelson, R. S. Stone, D. Longnecker, G. Carbaugh, J. M. Harris, and J. Wendell, 2006: Decadal variations in surface solar irradiance as observed in a globally remote network, *J. Geophys. Res.* **111**, D19101.

Durbin J. and G.S. Watson, 1971: Testing for Serial Correlation in Linear regression III. *Biometrika*, **58**, 1–19.

Ekern, P.C. 1983: Measured evaporation in high rainfall areas leeward Koolau Range, O‘ahu, Hawai‘i, U. *Hawai‘i Water Resour. Res. Center Tech. Rpt. 156*, Honolulu Hawai‘i. 60 pp.

Elison Timm, O., H. F., Diaz, T. W. Giambelluca, M. Takahashi, 2011: Projection of changes in the frequency of heavy rain events over Hawai'i based on leading Pacific climate modes. *J. Geophys. Res.* **116**, D04109.

Elison Timm, O., M. Takahashi, T. W. Giambelluca, and H. F. Diaz, 2013: On the relation between large-scale circulation pattern and heavy rain events over the Hawaiian Islands: Recent trends and future changes. *J. Geophys. Res*., **118**, 4129-4141.

England, M. H., S. McGregor, P. Spence, G. A. Meehl G, A. Timmermann, W. Cai, A. S. Gupta, M. J. McPhaden, A. Purich, and A. Santoso 2014: Recent intensification of wind-driven circulation in the Pacific and the ongoing warming hiatus. *Nature Clim. Change*, **4**, 222-227.

Erdman, S., A. Medeiros, A. Durso, and L. L. Loope. 2000: Ranchers and biologists in Hawai'i: keeping a business strong and protecting native forests at Ulupalakua Ranch, Maui. *Rangelands*, **22**, 33-35.

Frazier, A.G., T. W. Giambelluca, and H. F. Diaz, 2012: Spatial rainfall patterns of ENSO and PDO in Hawai‘i, Abstract B13B-0502 presented at 2012 Fall Meeting, AGU, San Francisco, Calif., 3-7 Dec

Frazier, A.G., T. W. Giambelluca, and H. F. Diaz, 2013: Mapping Rainfall Trends in Hawai‘i, Abstract H43I-1580 presented at 2013 Fall Meeting, AGU, San Francisco, Calif., 9-13 Dec.

Giambelluca, T.W. 2005: Land use and water resources under a changing climate M.G. Anderson and J.J. McDonnell (eds.), Encyclopedia of Hydrological Sciences, Volume 5. John Wiley and Sons, Chichester, U.K.

Giambelluca, T. W., M. A. Nullet, and T. A. Schroeder, 1986: Rainfall atlas of Hawai'i. *Department of Land and Natural Resources*, Honolulu, 267.

Giambelluca, T.W. and D. Nullet, 1991: Influence of the trade-wind inversion on the climate of a leeward mountain slope in Hawai‘i, *Clim. Res.*, **1**, 207-216.

Giambelluca, T. W., and D. Nullet, 1992a: Evaporation at high elevations in Hawaii. *J Hydrol.*, **136**, 219-235.

Giambelluca, T.W., and D. Nullet, 1992b: An automated recording atmometer: 2. Evaporation measurement on a high elevation transect in Hawai‘i. *Agric. For. Meteorol.*, ***62***,127-138

Giambelluca, T. W. and G. Gerold, 2011: Hydrology and biogeochemistry of tropical montane cloud forests. *Forest Hydrology and Biogeochemistry*, Springer Netherlands, 221-259.

Giambelluca, T.W., D. L. McKenna, and P. C. Ekern, 1992: An automated recording atmometer: 1. Calibration and testing *Agric. For. Meteorol*., **62**, 109-125.

Giambelluca, T.W., T. A. Schroeder, 1998: The physical environment: climate. In: Juvik, S.P., Juvik, J.O. (Eds.), *Atlas of Hawai'i,* 3rd edition. University of Hawai'i Press, Honolulu. 49–59.

Giambelluca, T. W., H. F. Diaz, and M. S. A. Luke, 2008: Secular temperature changes in Hawai'i . *Geophys. Res. Lett.*, **35**, L12702.

Giambelluca TW, J. K. DeLay, M. A. Nullet, M. A. Scholl, and S. B. Gingerich, 2010: Interpreting canopy water balance and fog screen observations: separating cloud water from wind-blown rainfall at two contrasting forest sites in Hawai'i. In *Tropical Montane Cloud Forests: Science for Conservation and Management*, Bruijnzeel LA, Scatena FN, Hamilton LS (eds). Cambridge University Press: Cambridge, UK, 342–351.

Giambelluca, T. W., J. K. DeLay, M. A. Nullet, M, M. A. Scholl, and S. B. Gingerich, 2011: Canopy water balance of windward and leeward Hawaiian cloud forests on Haleakalā, Maui, Hawai'i. *Hydrol Process*, **25**, 438-447.

Giambelluca, T.W., Q. Chen, A. G. Frazier, J. P. Price, Y.-L. Chen, P.-S. Chu, J. K. Eischeid, and D. M. Delparte, 2013: Online rainfall atlas of Hawai'i. *Bull. Amer. Meteor. Soc.*, **94**, 313-316.

Giambelluca, T. W., X. Shuai, M. L. Barnes, R. J. Alliss, R. J. Longman, T. Miura, Q. Chen, A. G. Frazier, R. G. Mudd, L. Cuo, and A. D. Businger, 2014: Evapotranspiration of Hawai'i. Final report submitted to the U.S. Army Corps of Engineers—Honolulu District, and the Commission on Water Resource Management, State of Hawai'i.

Garza, J. A., P. S. Chu, C. W. Norton, and T. A. Schroeder, 2012: Changes of the prevailing trade winds over the islands of Hawaii and the North Pacific. *J. Geophys. Res.,* **117** (D11).

Gong, L., C. L. Xu, D. Chen, S. Halldin, and Y. D. Chen, 2006: Sensitivity of the Penman–Monteith reference evapotranspiration to key climatic variables in the Changjiang (Yangtze River) basin. *J. Hydrol.*, **329**, 620-629.

Gotsch S. G., S. D. Crausbay, A. Weintrab, T. W. Giambelluca, R. J. Longman, H. Asbjornesen, S. C. Hotchkiss and T. Dawson 2014: Water relations and microclimate around the upper limit of cloud forest in Maui, Hawai‘i. *Tree Physiol.,* **34**, 766-777.

Grassi, B., G. Redaelli, P. O. Canziani, and G.Visconti, G., 2012: Effects of the PDO phase on the tropical belt width. *J. Climate*, **25**, 3282-3290.

Grindinger, C. M., 1992: Temporal variability of the trade wind inversion: Measured with a boundary layer vertical profiler. M.S. thesis, Department of Meteorology, University of Hawaii at Manoa, 93 pp.

Gueymard, C. A., 2008: REST2: High-performance solar radiation model for cloudless-sky irradiance, illuminance, and photosynthetically active radiation–Validation with a benchmark dataset. *Sol. Energy*, **82**, 272-285.

Gueymard C. A., (2012) Clear-sky irradiance predictions for solar resource mapping and large-scale alications: Improved validation methodology and detailed performance analysis of 18 broadband radiative models. *Sol. Energy*, **86,** 2145–2169

Howell, T. A., and S. R. Evett, 2004: The Penman-Monteith Method. *USDA Agricultural Research Service. Bushland, Texas,* 12 pp.

Hu, Y., and Q. Fu, 2007: Observed poleward expansion of the Hadley circulation since 1979. Atmos. Chem. Phys., **7**, 5229–5236.

Juvik S. and J. Juvik , 1998: *Atlas of Hawai‘i, 3rd Edition.*University of Hawai‘i Press. 333 pp.

Kalnay, E., and Coauthors, 1996: The NCEP/NCAR 40-Year Reanalysis Project. *Bull. Amer. Meteor. Soc*., **77**, 437–471.

Kanamitsu, M., W. Ebisuzaki, J. Woollen, S. K. Yang, J. J. Hnilo, M. Fiorino, and G. L. Potter, 2002: NCEP-DOE amip-ii reanalysis (r-2). *Bull. Amer. Meteor. Soc*., **83**, 1631-1643.

Kang, S.M., and J. Lu, 2012: Expansion of the Hadley cell under global warming: Winter vs. summer. *Am. Meteorol. Soc*, **25**, 8387-8393.

Kitayama, K. and D. Mueller–Dombois, 1992: Vegetation of the wet windward slope of Haleakala, Maui, Hawaii. *Pac. Sci.*, **46**, 197-220.

Krushelnycky, P. D., L. L. Loope, T. W. Giambelluca, F. Starr, K. Starr, D. Drake, A. D. Taylor and R. H. Robichaux, 2013: Climate-associated population declines reverse recovery and threaten future of an iconic high-elevation plant. *Glob. Change Biol.* **19**, 911-922.

Kurk, M., and D. Levinson, 2008: Evaluating the impacts of climate change on rainfall extremes for Hawai'i and coastal Alaska. Extended Abstracts, 24th AMS Conference on Severe Local Storms, Savannah, GA.

Lauer, A., C. Zhang, O. Elison-Timm, Y. Wang, and K. Hamilton, 2013: Downscaling of climate change in the Hawaii region using CMIP5 results: On the choice of the forcing fields. *J. Climate*, **26**, 10006-10030.

Leopold, L. B., 1949: The interaction of trade wind and sea breeze, Hawaii. *J. Meteorol.*, **6**, 312-320.

Liley, J. B., 2009: New Zealand dimming and brightening. *J. Geophys. Res*., **114,** D00D10.

Liu, Z. 2012: Dynamics of interdecadal climate variability: A historical perspective, *J. Clim*ate, **25**, 1963-1995.

Longman R. J., 2011: Homogenization of long-term solar radiation time series using a clear-sky radiation model and assessment of solar radiation variability at upper elevations on Maui, Hawaii. Master's thesis, Department of Geography University of Hawai'i, Honolulu.

Longman, R. J, T.W., Giambelluca, and O. Elison Timm, 2012: The spatial dynamics of potential evapotranspiration in Hawai'i: How driving variables are influenced by the trade wind inversion. American Geophysical Union Fall Meeting, San Francisco, December 2012.

Longman, R. J., T. W. Giambelluca, and A. G. Frazier, 2012: Modeling clear-sky solar radiation across a range of elevations in Hawai'i: Comparing the use of input parameters at different temporal resolutions, *J. Geophys. Res.,* **117**, D02201.

Longman R. J., T. W. Giambelluca and M. A. Nullet 2013: Use of a clear-day solar radiation model to homogenize solar radiation measurements in Hawai'i., *Sol. Energy* **91**, 102-110.

Longman, R.J., T.W., Giambelluca, R.J., Allis and M. Barnes, 2014: Temporal solar radiation Change at High Elevations in Hawai'I, *J. Geophys. Res.*, **119** 6022-6033.

Longman R. J, H. F. Diaz and T. W. Giambelluca (In Review) Sustained increases in lower tropospheric subsidence over the central tropical North Pacific drives a decline in high Elevation rainfall in Hawai'i. Submitted to the *J. Clim.*, December 2014

Loope, L. L., A. C. Medeiros, and B. H., Gagné, 1991: Aspects of the history and biology of the montane bogs: Cooperative National Park Resources Studies Unit, Department of Botany University of Hawai'i at Mānoa, Honolulu. *PCSU Technical Report* **76**.

Loope, L. L., R. J. Nagata, and A. C. Medeiros, 1992: Alien plants in Haleakala National Park. Alien plant invasions in native ecosystems of Hawaii: management and research.

Cooperative National Park Resources Studies Unit, Department of Botany University of Hawai'i at Mānoa, Honolulu. *PCSU Technical Report* **NA,** 551–576.

Loope, L. L., and T.W. Giambelluca,1998: Vulnerability of Island Tropical Montane Cloud Forests To Climate change, with Special Reference to East Maui, Hawai‘i. *Climate Change*, **39**, 503-517

Loope L. L., and C. F. Crivellone, 1986: Status of the Haleakala silversword: Past and Present. Cooperative National Park Resources Studies Unit, Department of Botany University of Hawai'i at Mānoa, Honolulu. *PCSU Technical Report* **.**

Lowe, P. R., 1977: An approximate polynomial for the computation of saturation vapor pressure. *J. Appl. Meteorol.*, **16**, 100-102.

Lu, J., G. Sun, S. G. McNulty, and D. M. Amatya, 2005: A comparision of six potential evapotranspiration methods for regional use in the southeastern United States. *J. Am. Water Resour., As.* **41**, 621-633.

Lu, J., G. A. Vecchi, and T. Reichler, 2007: Expansion of Hadley cell under global warming. *Geophys. Res. Lett*., **34**, L06805.

Lucas, C., B. Timbal, and H. Nguyen, 2013: The expanding tropics: A critical assessment of the observational and modeling studies. Wiley Interdiscip. Rev.: *Climatic Change*, **5**, 89–112.

Lyons, S. W. 1982: Empirical orthogonal function analysis of Hawaiian rainfall. *J Appl. Meteorol.*, **21**, 1713-1729.

Malkus, J. S., 1958: On the structure of the trade wind moist layer. Massachusetts Institute of Technology and Woods Hole Oceanographic Institution Papers in Physical Oceanography and Meteorology, Vol. 13, No. 2, 47 pp.

Mantua, N. J., S. R. Hare, Y. Zhang, J. M. Wallace, and R. C. Francis, 1997: A Pacific interdecadal climate oscillation with impacts on salmon production. *Bull. Amer. Meteor. Soc.*, **78**, 1069-1079.

McGregor, S., A. Timmermann, M. F. Stuecker, M. H. England, M. Merrifield, F.F. Jin, and Y. Chikamoto, 2014: Recent Walker circulation strengthening and Pacific cooling amplified by Atlantic warming. *Nat. Clim. Change.*,**4**, 888-892.

Medeiros, A. C., L. L. Loope, and R. A. Holt, 1986: Status of native flowering plant species on the South slope of Haleakala, East Maui, Hawai‘i. Cooperative National Park Resources Studies Unit, Department of Botany University of Hawai'i at Mānoa, Honolulu. *PCSU Technical Report* **59.**

Medeiros, A. C., C. F. Davenport, and C. G. Chimera, 1998: Auwahi: Ethnobotany of a Hawaiian dryland forest. Cooperative National Park Resources Studies Unit, Department of Botany University of Hawai'i at Mānoa, Honolulu. *PCSU Technical Report* **117.**

Medeiros, A. C., 2003: The Pū ‘Olē ‘Olē Blows and ‘Awa Is Poured Maui Kumu Keli ‘i Tau ‘a Welcomes Hawaiian Seedlings Back to Auwahi. *Native Plants Journal*, **4**, 48-51.

Medeiros, A. C., and E. von Allmen, 2006: *Restoration of native Hawaiian dryland forest at Auwahi, Maui*. USGS Fact Sheet, 2006-3035.

Merrifield, M. A., 2011: A shift in western tropical Pacific sea level trends during the 1990s. *J. Climate*, **24**, 4126-4138.

Miller, A. J., D. R. Cayan, T. P. Barnett, N. E. Graham, and J. M. Oberhuber, 1994: The 1976–77 climate shift of the Pacific Ocean. *Oceanog.*, **7**, 21-26.

Minyard, W. P., T. W. Giambelluca, and D. Nullet, 1994: Elevational patterns of climate on the leeward slope of East Maui, Hawaii. Cooperative National Park Resources Studies Unit,

Department of Botany University of Hawai'i at Mānoa, Honolulu. *PCSU Technical Report* **92.**

Mitas, C. M., and A. Clement, 2005: Has the Hadley Cell been strengthening in recent decades? *Geophys. Res. Lett*., **32**, L03809.

Mitas, C. M., and A. Clement, 2006: Recent behavior of the Hadley cell and tropical thermodynamics in climate models and reanalyses. *Geophys. Res. Lett*., **33**, L01810.

Monteith, J. 1965: Evaporation and Environment. In: The State and Movement of Water in Living Organisms. *Soc. Exp. Biol.*, **19,** 205-234.

Mueller-Dombois, D, 1967: Ecological relations in the alpine and subalpine vegetation on Mauna Loa, Hawai‘i. *Journal of the Indian Botanical Society* **46**, 403-411.

Murray, Francis W., 1967: On the computation of saturation vapor pressure. *J. Appl. Meteorol.*, **6**, 203-204.

Nguyen, H., A. Evans, C. Lucas, I. Smith, and B. Timbal, 2013: The Hadley circulation in reanalyses: Climatology, variability, and change. *J. Climate*, **26**, 3357-3376.

National Park Service (NPS), 2015: Haleakalā National Park Island of Maui, Hawai‘i. National Park Service U.S. Department of Interior Foundation Document Part 1.

Nullet, D., 1989: Climate controls on evaporation in Hawai‘i. Ph.D. Dissertation, Department of Geography, University of Hawai‘i at Mānoa, Honolulu.

Nullet, D. And T. W. Giambelluca, 1990: Winter evaporation on a mountain slope, Hawaii. *J. Hydrol*., **112**, 257-265.

Oort, A. H., and J. J. Yienger, 1996: Observed interannual variability in the Hadley circulation and its connection to ENSO. *J. Climate*, **9**, 2751–2767.

Parmesan, C., 1996: Climate and species' range. *Nature*, **382**, 765-766.

Penman, H, 1948: Natural evaporation from open water, bare soil, and grass. *Proc. R. Soc.* **193**, 120-146.

Perkins, K. S., J. R. Nimmo, and A. C. Medeiros, 2012: Effects of native forest restoration on soil hydraulic properties, Auwahi, Maui, Hawaiian Islands. *Geophys. Res. Lett.* **39**, L05405

Polvani, L. M., D. W. Waugh, G. J. P. Correa, and S.-W. Son, 2011: Stratospheric ozone depletion: The main driver of twentieth century atmospheric circulation changes in the Southern Hemisphere. *J. Climate*, **24**, 795–812.

Priestley, C., and R. Taylor, 1972: On the assessment of surface heat flux and evaporation using large-scale parametters. *Mon. Weather Rev.,* **100**, 81-92.

Quan, X.-W., H. F. Diaz, and M. P. Hoerling, 2004: Change in the tropical Hadley cell since 1950. The Hadley Circulation: Past, Present and Future, H. F. Diaz and R. S. Bradley, Eds., Kluwer Academic, 85–120.

Quan, X. W., Hoerling, M. P., Perlwitz, J., Diaz, H. F., and Xu, T. 2014: How fast are the tropics expanding? *J. Climate*, **27**, 1999-2013.

Rasmusson, E. M., & Carpenter, T. H. 1982: Variations in tropical sea surface temperature and surface wind fields associated with the Southern Oscillation/El Niño. *Monthly Weather Review*, **110**, 354-384.

Riehl, H., 1979: *Climate and Weather in the Tropics*. Academic Press, London, 623 pp.

Riehl, H., T. C. Yeh, J. J. Malkus, and N. E. La Seur, 1951: The northeast trade of the Pacific Ocean, *Quart. J. Roy. Meteor. Soc.* **77**, 598-626.

Scholl M.A, T. W. Giambelluca, S. B. Gingerich, M. A. Nullet, and L. L. Loope, 2007: Cloud water in windward and leeward mountain forests: The stable isotope signature of orographic cloud water. *Water Resources Research,* **43**, WI2411.

Seidel, D. J., Q. Fu, W. J. Randel, and T. J. Reichler, 2008: Widening of the tropical belt in a changing climate. *Nat. Geosci.*, **1**, 21-24.

Shapiro, S. S., and M. B. Wilk, 1965: An analysis of variance test for normality (complete samples). *Biometrika*, **52**, 591-611.

Sherrod, D. R., J. M. Sinton, S. E. Watkins, and K. M. Brunt, 2007: Geologic Map of the State of Hawai`i: U.S. Geological Survey Open-File Report 2007-1089, 83 pp.

Sohn, B. J., and S.C. Park, 2010: Strengthened tropical circulations in past three decades inferred from water vapor transport. *J. Geophys. Res.,* **115**, D15.

Song, H., and M. Zhang, 2007: Changes of the boreal winter Hadley circulation in the NCEP–NCAR and ECMWF reanalyses: A comparative study. *J. Climate*, **20**, 5191–5200.

Stachnik, J. P., and C. Schumacher, 2011: A comparison of the Hadley circulation in modern reanalyses. *J. Geophys. Res*., **116**, D22102.

Stevenson, S. L., 2012: Significant changes to ENSO strength and impacts in the twenty-first century: Results from CMIP5. *Geophys. Res. Let.*, ***39*** L17703.

Staten, P.W., J. J. Rutz, T.Reichler, and J. Lu, 2011: Breaking down the tropospheric circulation response by forcing. *Climate Dyn*., **39**, 2361–2375.

Tanaka, H. L., N. Ishizaki, and A. Kitoh, 2004: Trend and interannual variability of Walker, monsoon and Hadley circulations defined by velocity potential in the upper troposphere. *Tellus*, **56A**, 250–269.

Taylor, K. E., R. Stouffer, and G. A. Meehl, 2012: An overview of CMIP5 and the experiment design. *Bull. Amer. Meteor. Soc.*, **93**, 485–498.

Timm, O. and H. F. Diaz, 2009: Synoptic-statistical approach to regional downscaling of IPCC twenty-first-century climate projections: seasonal rainfall over the Hawaiian Islands. *J. Climate*, **22**, 4261-4280.

Thomas, B. R., E. C. Kent, and V. R. Swail, 2005: Methods to homogenize wind speeds from ships and buoys. *Int. J. Climatol.*, **25**, 979-995.

Thorne, P. W., and R. S. Vose, 2010: Reanalyses suitable for characterizing long-term trends: Are they really achievable? *Bull. Amer. Meteor. Soc.*, **91**, 353-361.

Thornthwaite, C. 1948: An approach toward a rational classification of climate. *Geogr. Rev.,* **38**, 55-94.

Tran, L.T., 1995: Relationship between the Inversion and Rainfall on the Island of Maui. M.A. thesis. Department of Geography, University of Hawai'i at Mānoa, Honolulu.

Trenberth, K. E., D. P. Stepaniak, and J. M. Caron, 2000: The global monsoon as seen through the divergent atmospheric circulation. *J. Climate*, ***13***, 3969-3993.

Trenberth, K. E., J. T. Fasullo, G. Branstator, and A. S. Phillips, 2014: Seasonal aspects of the recent pause in surface warming. *Nat. Clim. Change*, **4**, 911-916.

Tu, C. C., and Y. L. Chen, Y. L., 2011: Favorable conditions for the development of a heavy rainfall event over Oahu during the 2006 wet period. *Weather Forcast.*, **26**, 280-300.

Uppala, S. M., and Coauthors, 2005: The ERA-40 Re-Analysis. *Quart. J. Roy. Meteor. Soc.*, **131**, 2961–3012.

Vecchi, G. A., and A. T. Wittenberg, 2010: El Niño and our future climate: where do we stand?. *WIREs Clim Change*, **1**, 260-270.

Vörösmarty, C. J., C. A. Federer, and A. L. Schloss, 1998: Potential evaporation functions compared on US watersheds: Possible implications for global-scale water balance and terrestrial ecosystem modeling. *J. Hydrol.*, **207**, 147-169.

Wang, C., 2002: Atmospheric circulation cells associated with the El Niño–Southern Oscillation. *J. Climate*, **15**, 399–419.

Welch, B. L., 1947: The generalization of student's' problem when several different population variances are involved. *Biometrika*, 28-35.

Wilcoxon, F., 1950: Some rapid approximate statistical procedures. *Ann. N.Y. Acad. Sci.*, **52**, 808-814.

Wolter, K., and M.S. Timlin, 1998: Measuring the strength of ENSO events: How does 1997/98 rank? *Weather*, **53**, 315-324.

Yu, J. Y., P. K. Kao, H. Paek, H. H. Hsu, C. W. Hung, M. M. Lu, and S. I. An, 2015: Linking Emergence of the Central Pacific El Niño to the Atlantic Multidecadal Oscillation. *J. Clim.*, **28,** 651-662.